MOLECULAR PHOTOELECTROCATALYTS FOR SOLAR FUEL PRODUCTION: DISCOVERY, MECHANISM, AND EXPLORATION

Catherine L. Pitman

A dissertation submitted to the faculty at the University of North Carolina at Chapel Hill in partial fulfillment of the requirements for the degree of Doctor of Philosophy in the Department of Chemistry.

Chapel Hill
2017

Approved by:

Alexander J. M. Miller

Michel R. Gagné

Maurice S. Brookhart

Joseph L. Templeton

Marcey L. Waters

ABSTRACT

Catherine L. Pitman: Molecular Photoelectrocatalyts for Solar Fuel Production: Discovery, Mechanism, and Exploration
(Under the direction of Alexander J. M. Miller)

An exploration of the chemistry of molecular photoelectrocatalysts, beginning with the Cp*Ir(bpy) framework, is presented. Chapter 1 covers approaches to hydrogen evolution with an eye towards solar fuel production. The importance of both metal-hydride species and methods to measure metal-hydride bond strength is discussed. In Chapter 2, the central complex of this dissertation, $[Cp^*Ir(bpy)(H)]^+$, is introduced when *in situ* electrochemical generation permits the construction of a photoelectrocatalytic cycle. Irradiation of neutral aqueous solutions containing $[Cp^*Ir(bpy)(H)]^+$ poised at cathodic potentials produces H_2 in high Faradaic efficiency. Chapter 3 presents a general synthetic scheme whereby precipitation of Cp*Ir(bpy) and analogues from water and subsequent reaction with electrophiles enabled access to a wide range of water-soluble metal-hydride and metal-alkyl complexes. Chapter 4 explores the hydricity—the hydride donor ability—of Cp*Ir(bpy)- and (arene)Ru(bpy)-based hydrides. The hydricity of $[Cp^*Ir(bpy\text{-}COO)(H)]^-$ is measured using a *potential-pK_a* cycle, and the hydricities of the metal-hydrides accessed in Chapter 3 are measured relative to this reference complex. The thermodynamic measurements presented explain why $[Cp^*Ir(bpy)(H)]^+$ is stable in neutral, aqueous solutions in the dark.

Chapters 5 and 6 present results of alterations to the $[Cp^*Ir(bpy)(H)]^+$ structure. In Chapter 5, Rh is exchanged for Ir, resulting in an entirely unexpected activation of Cp*.

Formation of the transient [Cp*Rh(bpy)(H)][Cl] complex leads to in the more stable species (Cp*H)Rh(bpy)(Cl). The implications of this structure on the reduction of NAD^+ are discussed. In Chapter 5, the hydride ligand is exchanged for a methyl ligand making $[Cp^*Ir(bpy)(CH_3)]^+$. This metal-methyl complex is characterized and its photochemical reactions are explored. Kinetic order, radical traps and clocks, and isotope labelling suggest that excitation results in homolysis of the $Ir–CH_3$ bond.

ACKNOWLEDGEMENTS

I put off writing my acknowledgments section because I was sure that I was going to get it wrong. I have probably forgotten to thank someone who I should—I'm sorry—and even those I have remembered, what I say here will not capture what you have meant to me.

First, to Alexander J. M. Miller, who took a chance on a first-year graduate student with scant research experience. You took me from an unsure student to an independent scientist, and I will never be able to thank you enough for what you have done for me. It has been a privilege to watch how quickly you adapted to and thrived in being a professor and mentor. When I could see no other reason to be in graduate school, I could rest easy in the knowledge that helping you get tenure was work worth doing. I am a better person for having worked for you, and I'm so glad that I worked for someone as ridiculous about diction and figure design as I am.

To the rest of the Miller lab: to Andrew Walden and Matt Kita, who were with me there in the very beginning. There is something about starting a lab together that I can't really put into words. To Matt Chambers, who is always happy to let me talk through my experiments. To LDoc, my job hunt and group meeting buddy, and to Seth, my desk buddy. To Kelsey Brereton, Jacob Brody Smith, Javier Grajeda, Ali Sullivan, Andrew Camp, and Brian Lindley, thank you for dogs, coffee, cupcakes, and comradery: I'm glad to be leaving the lab in such good hands. To Ann Marie, Bethany, and Quinton, good luck! It will be both better and worse than you think. To Teddy, Becca, Victoria, Ariana, and Olivia, my small

army of undergraduates, you have all been so different, and you have all taught me something unique.

To the many others in the chemistry department who have been an integral part of my time in graduate school: to Jillian Dempsey, Joe Templeton, and Brook Brookhart, you make the fourth floor of Kenan a special place to be. I hope that I will live up to the standard you have established, both as people and as scientists. To Brian McCarthy, for countless conversations, board games, and tea. To Eric Rountree, Alex Venning, Nate Romero, Meredith Zeller, and Melissa Gish, I can't really believe how far we've come since our first year. I am so sure that you will all go on to do great things. To Matt Goldfolgel, thank you for always being up for a movie. To Ross Beattie, Chris Turlington, Matty J, Tom Lyons, thank you for being friends and mentors.

To Katie Lavoie, Robin Knauf, Cortnie Roberts, and Katie Michaux. I can't really say how much better you made graduate school. When I was the only girl in my lab and in my inorganic cohort, you knew how that felt and kept me sane. Thank you for always letting me turn up at your desks and vent. Thank you for cheering me up. Thank you for being just generally awesome. Thank you for brunch and gelato martinis and being conference buddies.

To the people who keep this department running: to Peter White, Marc ter Horst, Brandie Ehrmann, and Kyle Brennaman for keeping the instruments on and for letting me pick your brains about them. To Ashley and Ann, for the tremendous amount of paperwork you do and did to keep us afloat. To Fred and Reggie, who do a lot more, for giving the friendliest hellos for five years.

To the greater UNC and Chapel Hill communities: to the Royster Society for keeping me connected to the university outside chemistry. To the Orange County Animal Shelter, for

letting me play with dogs once a week. To the Chapel Hill Library, where I write this now. To Anthony, Anthony, and Danielle, for your patience and dedication. To Kelley, Kelsey, Natalie, Paige, and all of Outdoor Fitness, for Sundays in the park. To Sarah Venning and Ribbit, for being good friends.

To the greater chemistry community: attending conferences and meeting so many of you has been one of the highlights of my graduate career. To Karen Goldberg and Melanie Sanford, for being such incredible and astounding role models. To Jim Mayer and Nilay Hazari, for lending an ear. To Mr. Nelson, Seth Brown, Olaf Wiest, Chris Timmel, Steve Davies, and John McGrady, without whom I never would have been a chemist or come to graduate school in the first place.

To my fellow chemists of the Notre Dame Class of 2011: to Andrea, Ryan, Laura, Jennifer, Jessica, Angela and on. You were always the best thing about late nights studying and long hours in labs that predictably didn't work.

To my family: to my Dad, for always being my first call when things go wrong. To my Mom, who somehow raised four children with Dad frequently deployed. I am in awe of you. To Chris, Mary, and Claire, for all the adventures. To my Grandparents. To the Camerons.

And finally, thank you to Neskowin, Carolina North Forest, and our National Parks because "everybody needs beauty as well as bread, places to play in and pray in, where nature may heal and give strength to body and soul alike."[1]

TABLE OF CONTENTS

LIST OF TABLES

LIST OF FIGURES

LIST OF SCHEMES

LIST OF SYMBOLS AND ABBREVIATIONS

•	radical
$^{13}C\{^{1}H\}$	proton decoupled carbon
^{1}H	proton
^{2}H	deuterium
A	absorbance
A/HA^{-}	hydride acceptor/hydride donor
Å	Angstrom
AcOH	acetic acid
aq	aqueous
atm	atmosphere
BH_4^-	borohydride
bpy	2,2’-bipyridine
bpy-X	4,4'-X-2,2'-bipyridine
C	Celsius
C	Coulomb
CA	chronoamperometry
cal	calories
cm^{-1}	wavenumber, inverse centimeters
Cp*	pentamethylcyclopentadienyl
CPE	controlled potential electrolysis
CV	cyclic voltammetry
cy	cyclohexyl

D	deuterium
DFT	density functional theory
DHMPE	1,2-bis(dihydroxymethylphosphino)ethane
dppe	1,2-bis-(diphenyl-phosphino)ethane)
e^-	electron
$E_{1/2}$	half wave potential
EC'	electron transfer, chemical catalysis
ECP	effective core potential
E^o	formal potential
eq	equation
EQE	external quantum efficiency
equiv	equivalent
erf	error function
ESI	electrospray ionization
Et	ethyl
eV	electron volt
f	oscillator strength
g	gram
GC	gas chromatography
GW	gigawatt
h	hour
H	hydrogen atom
H^-	hydride

H^+	proton
HER	hydrogen evolution reaction
HOMO	highest occupied molecular orbital
HPLC	high performance liquid chromatography
Hz	hertz
hν	light irradiation
i_{cat}	catalytic current
i_{diff}	diffusional current
$i_{p,a}$	peak anodic current
$i_{p,c}$	peak cathodic current
^{i}Pr	isopropyl
IrOx	iridium oxide
J	joule
K	Kelvin
K_a	acid dissociation constant
k_{cat}	catalytic rate constant
K_{eq}	equilibrium constant
KIE	kinetic isotope effect
k_{obs}	observe rate constant
LED	light emitting diode
L_nM	metal with n ligands
LUMO	lowest unoccupied molecular orbital
M	molar

m/z	mass over charge
mC	millicoulomb
Me	methyl
mg	milligram
MH	metal hydride
MHz	megahertz
min	minute
mL	milliliter
MLCT	metal to ligand charge transfer
mM	millimolar
mmol	millimole
mol	mole
MS	mass spectrometry
NAD^+	nicotinamide adenine dinucleotide
^{n}Bu	n-butyl
NHE	normal hydrogen electrode
nm	nanometer
NMR	nuclear magnetic resonance
^{n}Pr	n-propyl
^{o}	degree
OAc	acetate
OTf^-	triflate
OTs^-	tosylate

PCET	proton-coupled electron transfer
pD	-log([D^+])
pH	-log([H^+])
P_i	inorganic phosphate
pK_a	acidity
$P^{Ph}{}_2N^{Ph}$	1,3,6-triphenyl-1-aza-3,6-diphosphacycloheptane
ppm	parts per million
PS	photosensitizer
ps	picosecond
PV	photovoltaic
QY	quantum yield
RVC	reticulated vitreous carbon
s	second
t	time
TD-DFT	time-dependent density functional theory
TEMPO	(2,2,6,6-tetramethylpiperidin-1-yl)oxyl
THF	tetrahydrofuran
TMPS	tetrakis(3,5-disulfonatomesityl)porphyrin
TON	turnover number
tpy	2,2’:6’2”-terpyridine
TSPP	tetra(p-sulfonatophenyl)porphyrin
TW	terawatt
UV	ultraviolet

V	volts
v%	volume percent
Vis	visible
W	watt
wt%	weight percent
X-	halide
δ	chemical shift
ΔE	electronic energy
ΔG	free energy
ΔG_{ET}	free energy for electron transfer
ΔG_{H-}	free energy, hydricity
$\Delta G_{H-}(Y)$	effective hydricity for incoming ligand y
$\Delta G_{OH2 \rightarrow X}$	free energy to replace aquo ligand with x
ΔG_{ST}	free energy between singlet ground state and triplet excited state
ΔH	enthalpy
ΔS	entropy
$\Delta\Delta G_{H-}$	difference in hydricity
η	hapticity
λ	wavelength
λ_{max}	wavelength maximum
μ	bridging ligand
μA	microampere
μL	microliter

σ	sigma-type donor
σ_{p-}	Hammett parameter
ε	molar extinction coefficient

CHAPTER 1: MOLECULAR SOLAR FUEL PRODUCTION

1.1 Introduction to Solar Fuels

Energy use is projected to increase from our current average global consumption of 18.4 TW in 2012 to 27.3 TW by 2040.[2] Meeting this demand while limiting carbon accumulation in the atmosphere and oceans motivates exploration of alternative energy sources. The future energy portfolio will likely be comprised of a mixture of wind, solar, hydroelectric, nuclear, and petroleum sources, but of these, solar energy represents the greatest untapped potential. With an average of about 80,000 TW of solar radiation reaching the Earth's surface, there is a strong drive to develop technologies to harness this immense energy source.[3]

Photovoltaics (PV) and solar thermal heating have been the largest players on the solar stage. Solar PV that convert solar energy to electricity have seen a 8.3% yearly growth rate—the fastest growing renewable energy source—with global installed capacity reaching 90 GW in 2012.[2] Solar thermal systems are primarily used in residential water heating, but have been employed for electricity generation by boiling water with concentrated light to then drive steam-powered turbines, similar to those in coal fired plants. Globally, solar thermal plants produced 3.6 GW in 2013.[4]

Solar fuels are a third option for harnessing sunlight. Rather than transforming solar energy from sunlight into electrical or thermal energy, solar fuel systems store solar energy in the form of energy-rich chemical bonds. In order to use an intermittent energy source, like solar, as a major component of the energy economy, energy storage methods will need to be developed to level the gap between when energy is produced and when is it used. While there are a host of technologies to meet this need, from thermal storage to pumped hydroelectric to flow batteries, high energy density and low storage losses make fuels an ideal target.[5]

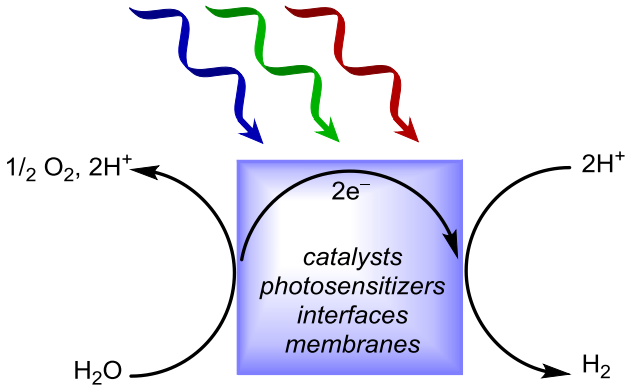

Figure 1.1. Black box depiction of water splitting, showing the many components required to split water with light.

Figure 1.1 depicts a generalized solar fuels device. A collection of catalysts, photosensitizers, interfaces, and membranes are assembled into a device that absorbs light and uses that energy to split water into oxygen and hydrogen, storing the captured energy. This process is often referred to as "artificial photosynthesis" because of its similarities to biological photosynthesis: both store the energy of sunlight in chemical bonds. In order to produce low-cost fuel, devices must optimize the oxidative and reductive catalysts and integrate light absorption to efficiently manage protons, photons, and electrons. Optimization and development of each component of an artificial photosynthesis device is complex;

consequently, this work will focus on the reductive half-reaction. The reductive half-reaction leads directly to the formation of a fuel, like hydrogen, or if water is replaced with CO_2, a carbon-based fuel.

1.2 Catalysts for Hydrogen Production

Light-promoted evolution of hydrogen from water is as an attractive route to solar fuels, and many approaches have emerged in order to reduce protons to H_2 with the aid of sunlight. Two general strategies have emerged: multi-component systems which combine a photosensitizer with an electrocatalyst to form H_2 (Scheme 1.1A) and photocatalysts which produce H_2 upon photon absorption (Scheme 1.1B). Examples of these strategies are described in this section.

In these schemes, the origin of the electrons used to form the H–H bond becomes a critical consideration. To split water, these electrons must come from oxidation of water, but in optimizing the reductive half-reaction, the electrons are typically drawn from sacrificial reductant—either added reductive quenchers or oxidation of the conjugate base of the acid. Incorporating these strategies into a water-splitting solar fuel device requires electron management that does not lead to stoichiometric consumption of a sacrificial reductant.

Scheme 1.1. Generalized representations of A) an electrocatalyst producing H_2 after reduction by a coupled photosensitizer (PS) and B) and photocatalyst producing H_2 by oxidizing a halide (X^-), a process which typically requires two photons.

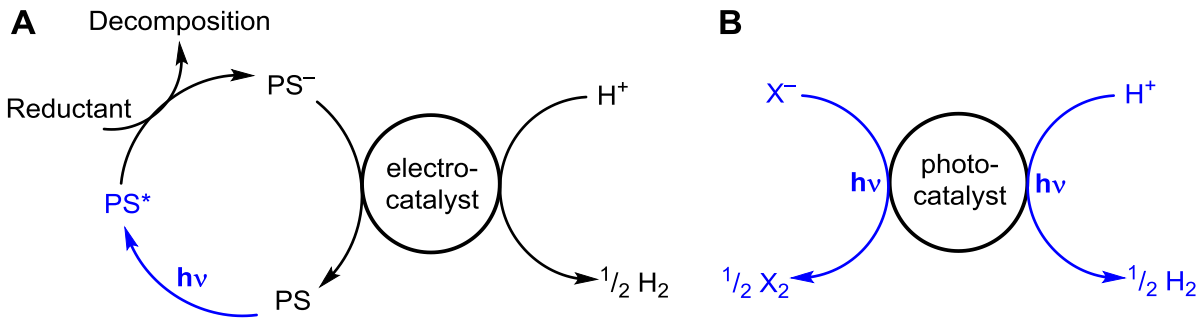

Fuel formation from electrocatalysts. Noble metals, platinum in particular, are the champion electrocatalysts for the hydrogen evolution reaction (HER). The adsorption of hydrogen to noble metals is strong enough to lower reaction barriers yet weak enough to permit product desorption, and therefore, noble metals catalyze the reaction at essentially no overpotential.[6] With many catalysts, excess energy beyond the thermodynamic minimum is required to overcome kinetic limitations or high energy intermediates, with this excess called the overpotential. Noble metal expense and scarcity, however, have necessitated the search for cheap, abundant catalysts that mirror the activity of platinum. One strategy to accomplish this goal has been a detailed exploration and engineering of materials to maximize surface area and active sites that lead to H_2. Rapid progress has been made in recent decades, particularly with sulfides (e.g. MoS_2), selenides, carbides, phosphides, and nitrides, but as a function of material surface sites, these materials are still less active than Pt.[6,7]

Another strategy to replace Pt catalysis is to use highly active homogenous catalysts either freely diffusing in solution or supported on a cheaper electrode surface.[8] This strategy takes inspiration from biology where hydrogenase enzymes have developed NiFe and FeFe active sites that receive electrons from cluster chains in order to make H_2.[9,10] Structural mimics of these active sites typically show poor activity in the absence of the surrounding protein scaffold.[11]

A range of molecular electrocatalysts that are structurally unrelated to hydrogenase active sites has shown excellent HER activity. Considerable effort has been focused on the development of H_2 evolution electrocatalysts in acetonitrile, which is often a convenient solvent for evaluating the electrochemistry of organometallic complexes.[12] Dozens of complexes containing a variety of metals and ligand architectures have been investigated

yielding insight into the electrocatalytic mechanism and improvement of catalytic rates and efficiency.[8,13–15] The mechanism of HER from cobaloximes was investigated in detail, illustrating that additional activation of catalysts may be needed in the form of additional electrons (Scheme 1.2A).[16] Systematic study of group 10 bis-diphosphine electrocatlysts led to the development of DuBois's $[Ni(P^{Ph}_2N^{Ph})_2][BF_4]_2$, ($P^{Ph}_2N^{Ph}$ = 1,3,6-triphenyl-1-aza-3,6-diphosphacycloheptane, Scheme 1.2B), which catalyzes HER from protonated dimethylformamide in acetonitrile with a turnover frequency 106,000 s^{-1} in the presence of 1.2 M of water, a faster rate for H_2 evolution than hydrogenase itself.[17]

Scheme 1.2. Selected electrocatalysts for H_2 evolution.

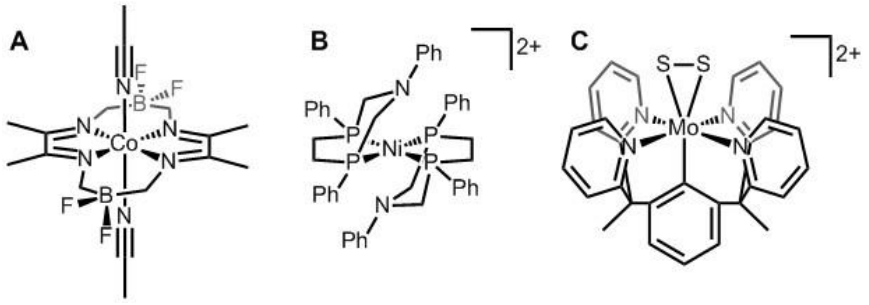

Though solar fuel generation will ideally take place in the most abundant solvent, water, aqueous media presents a unique challenge for the inorganic electrochemist. The electrochemical window is narrow: the abundance of protons in water leads to background H_2 evolution from the electrode at relatively positive potentials, making it difficult to study the electrocatalyst itself. Systems that can be studied under aqueous conditions are limited by their solubility and stability, which can be minimal for many organometallic complexes. Despite these challenges, many homogeneous electrocatalysts have been investigated in water.[14,18] Chang, for example, has developed Mo-based catalysts that mimic the activity of

MoS_2 materials in water (Scheme 1.2C).[19,20] Despite these successes, matching the rates of hydrogenase in aqueous conditions remains a challenge.[21]

To produce hydrogen using light as an energy input, these electrocatalysts must be coupled to a light-absorbing species, typically a molecular photosensitizer like $[Ru(bpy)_3]^{2+}$. Absorption of a photon produces high energy electrons and low energy holes. Quenching of the excited state with a sacrificial reductant produces a highly reducing species which can transfer an electron to the electrocatalyst and initiate H_2 evolution. To achieve high efficiencies, this electron transfer must be optimized, leading to the exploration of tethered systems which ensure spatial proximity of the chromophore and catalyst. Unfortunately, these linked systems have not improved efficiency, suggesting that the non-productive back-electron transfer is competitively improved by proximity.[22] The challenge with this approach is that while the catalyst and chromophore can be optimized individually, those benefits do not necessarily extend to the integrated system.

Fuel formation from photocatalysts. An alternative approach to light-driven hydrogen production is to merge the catalyst and the light absorber into one discrete species which collects energy from absorbed photons and then produces H_2. Photocatalysts of this kind have been developed which generate H_2 from a variety of sources. There is an extensive literature of photochemical dehydrogenations of alkanes, alcohols, and other organic substrates.[23] Several different mechanisms and photochemically active steps have appeared in the literature.[24] Many of these, like Cole-Hamilton's $Rh(P^iPr_3)_2(CO)(H)$ driven decomposition of methanol[25] and Goldman's $Rh(PMe_3)_2(CO)(Cl)$ dehydrogenation of cyclooctane,[26] are initiated by photochemical CO dissociation. After ligand loss, the elementary steps that lead to H_2 production, then, are those that would be observed for any

low-coordinate organometallic fragment in the dark. In other systems, like Crabtree's $Ir(H)_2(CF_3CO_2)(PCy_3)_2$ dehydrogenation of cyclooctane,[27] the photochemical step is proposed to be H_2 reductive elimination from a dihydride intermediate.

When the substrate is an acid, many systems require two photons to close the catalytic cycle: one to facilitate the release of H_2 and the other to assist in dissociation of the conjugate base from the catalyst. Hexachloroiridate can photocatalytically cleave H–Cl with one photon producing $H^{\bullet}$ and another producing $Cl^{\bullet}$ which go on to form H_2 and Cl_2.[23] Nocera's late-metal bimetallic H–X splitting schemes eliminate H_2 on absorbing one photon and then Cl_2 or Br_2 equivalents upon absorbing a second photon. Often, an external halide trap is included in functional catalytic systems to drive halogen elimination to completion.[28]

$$\boldsymbol{CO + H_2O \xrightarrow{hv} CO_2 + H_2} \qquad \textbf{(1.1)}$$

Of particular interest was a report in the literature from Ziessel of the photochemical water-gas shift with Cp*Ir(bpy)-based (Cp* is pentamethylcyclopentadienyl, bpy is 2,2'-bipyridine) catalysts. In this reaction (eq. 1.1), CO is oxidized to CO_2 while the protons from water are reduced to evolve H_2. Ziessel showed that the reduction of CO with H_2O transforms a $[Cp^*Ir(bpy)(Cl)]^+$ precursor to $[Cp^*Ir(bpy)(H)]^+$ with loss of CO_2 (and a proton, Scheme 1.3). This iridium hydride intermediate was proposed to be the photoactive species that releases H_2 on absorbing a photon.

Scheme 1.3. Ziessel's mechanism for the photochemical water-gas shift.

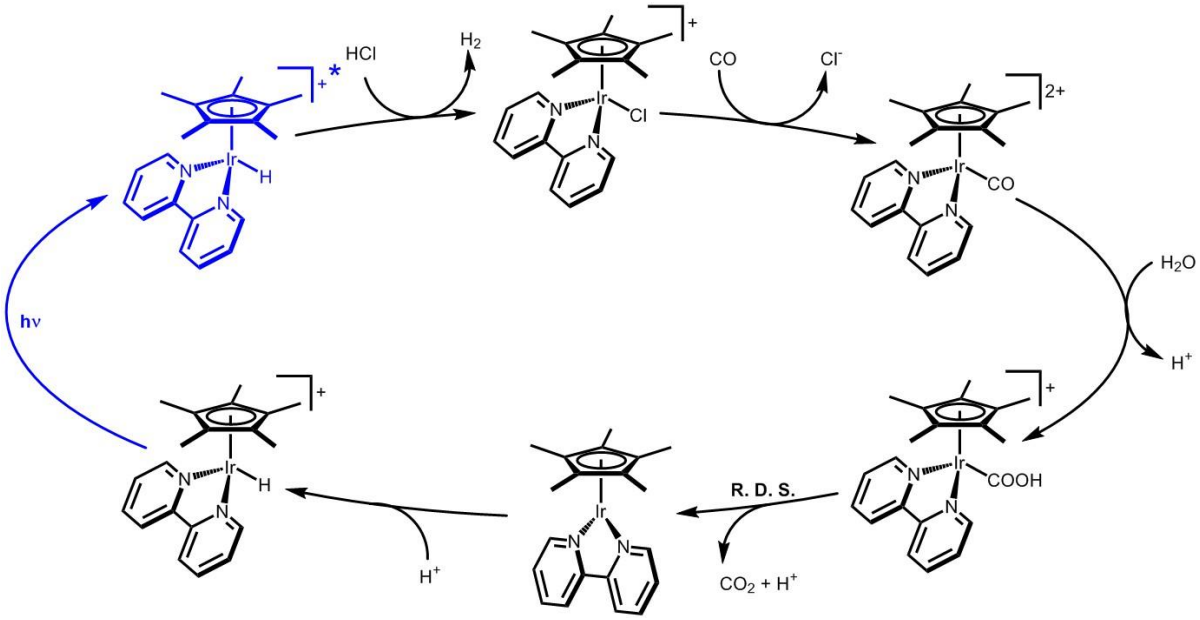

Scheme 1.4. Generalized scheme for a molecular photoelectrocatalyst.

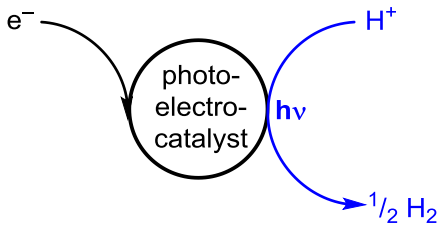

Drawing on the mechanism of Ziessel's photochemical water-gas shift, we envisioned a photoelectrochemical approach, in which H_2 evolution is facilitated by a single molecule acting *both* as light absorber and electrocatalyst, as described in Chapter 2. Unlike the water-gas shift and other multi-component hydrogen evolution strategies, no sacrificial reagent is required, enabling this half-reaction to be coupled to any favorable oxidative half-reaction, like water oxidation.

The mechanism of hydrogen evolution from [Cp*Ir(bpy)(H)]$^+$. In the course of our lab's investigation of [Cp*Ir(bpy)(H)]$^+$ as a photoelectrocatalyst, we became interested in the photochemical mechanism that leads to H_2 release. To elucidate this mechanism,

Chambers undertook a detailed investigation of the reaction of $[Cp^*Ir(bpy)(H)]^+$ with acids in acetonitrile.[29] From the decrease in lifetime of the excited state with increasing complex concentration, he deduced a self-quenching mechanism was operating, where electron transfer occurs between the excited state $[Cp^*Ir(bpy)(H)]^{+*}$ and a ground state $[Cp^*Ir(bpy)(H)]^+$ (Scheme 1.5). The source of H_2 was shown to be the resulting $Cp^*Ir^{II}(bpy)(H)$ and $[Cp^*Ir^{IV}(bpy)(H)]^{2+}$ pair: an initial burst of H_2 was observed even when deuterated acid sources where employed. Regeneration of the hydride $[Cp^*Ir(bpy)(H)]^+$ follows protonation of Cp*Ir(bpy) which is a product of H_2 release. This mechanism of self-quenching preceding bond formation had not been previously observed in the H_2 photochemistry literature.

Scheme 1.5. Mechanism for H_2 production from $[Cp^*Ir(bpy)(H)]^+$.

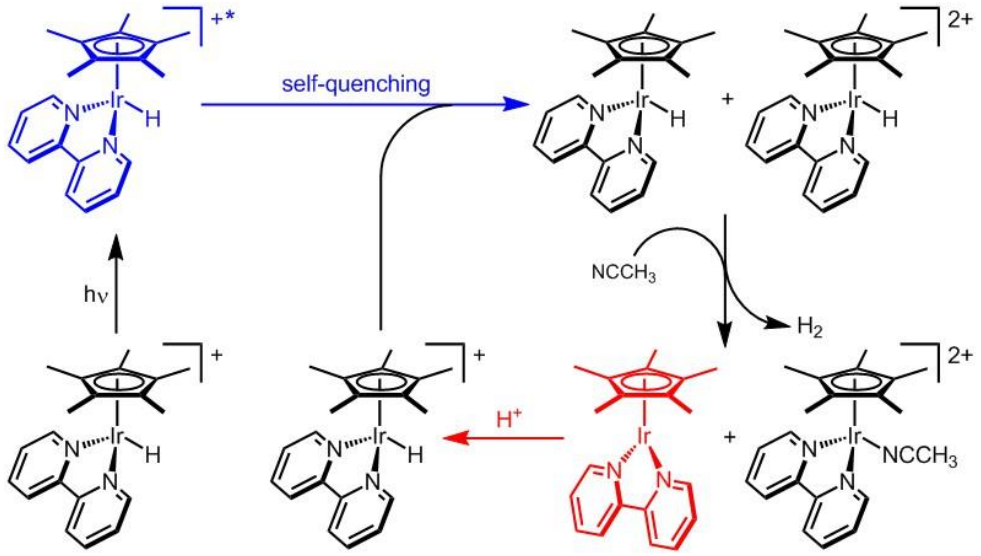

1.3 Transition Metal Hydrides in Aqueous Reactions

The various routes to hydrogen production have metal hydrides as a common intermediate. In nearly all of the HER reactions discussed above, there is, at some point on the catalytic cycle, a bond between a metal and a hydrogen atom. In addition to hydricity

being a useful parameter for understanding H_2 evolution from aqueous solution, transition metal hydrides are intermediates in a number of reactions in water outside of HER. Aqueous hydride transfer is an essential process in enzymatic catalysis,[30,31] in CO_2 reduction,[32,33] and in biphasic industrial catalysis.[34,35] Demonstrating the utility of metal hydrides in aqueous conditions, an aqueous-phase Rh hydride produces ~800,000 tons/year *n*-butyraldehyde for plastics.[34]

Given the prevalence of the metal-hydride bond, understanding and describing the strength and reactivity of these intermediates in order to modify and predict outcomes has become very desirable.

Measuring metal-hydride bond strength with hydricity. Thermochemical studies of metal hydrides provide a foundation for rational design of catalysts and for mechanistic studies of $2e^-$ proton-coupled electron transfer (PCET) reactions.[36,37] In acetonitrile, DuBois and Rakowski DuBois pioneered the determination of hydricity and its use as a powerful tool for reaction development in organic solvents.[38–40] DuBois's $[Ni(P^{Ph}_2N^{Ph})_2][BF_4]_2$ catalyst discussed above achieved its impressive rates through thermochemistry-guided catalyst design.[17,41]

As shown in Scheme 1.6, the metal hydride bond can be cleaved to a proton (H^+), a hydrogen atom (H•), or a hydride (H^-). Thermodynamic parameters have been determined for all three M–H bond-breaking reactions. As a thermodynamic measure of the energy required to break a bond, any of the reactions in Scheme 1.6 can be considered bond strengths. The heterolytic bond cleavage with proton dissociation is the acidity of the metal hydride, reported here as a pK_a value. *Thermodynamic hydricity*, ΔG^o_{H-}, is defined as the free energy required to remove a hydride anion (H^-) from a species, as shown in Scheme 1.6. Heterolytic

cleavage of a M–H bond to generate H^- is endergonic, and the magnitude of ΔG°_{H-} indicates how much energy is needed for bond cleavage. Species with large values of ΔG°_{H-} are therefore weak hydride donors, and species with small values of ΔG°_{H-} are strong hydride donors. Metal hydrides that are strong hydride donors can be described as being *hydridic*.

Scheme 1.6. Three L_nM–H bond cleavage reactions.

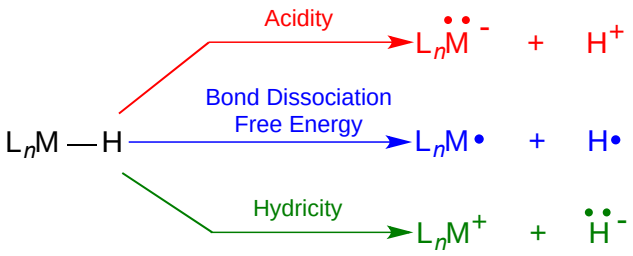

There are several methods that can be used to assess the hydricity of a complex. The most common of these are "*hydride transfer*," "*H_2 heterolysis*," and "*potential–pK_a*" methods for determining hydricity. These methods are discussed briefly here and in more detail in reference 15.

The "*hydride transfer*" method determines the hydricity of a metal hydride by measuring the equilibrium constant for the reaction of a hydride donor of unknown hydricity (MH) reacting with a reference hydride acceptor (A, where HA^- has a known hydricity), as illustrated in Scheme 1.7. NMR spectroscopy and UV-vis spectroscopy are the two most common techniques for the measuring the equilibrium constant for eq 1.2. The free energy of eq 1.2 is combined with the free energy of eq 1.3 to yield the hydricity of MH (eq 1.4). A reliably quantifiable equilibrium constant can typically only be achieved when the two hydride donors have hydricity values within ~3 kcal/mol of each other. This difference in hydricity is based on the assumption that a 1:10 ratio of the concentrations of two species is readily quantifiable. If equimolar amounts of a hydride donor and hydride acceptor react to

form a 10:1 equilibrium mixture, then K_{eq} is 100, and thereby $\Delta G^{o} = -1.364 \log(K_{eq}) \approx 2.7$ kcal/mol.

Scheme 1.7. Determination of Hydricity by Hydride Transfer.

$MH + A \rightleftharpoons M^+ + HA^-$	$\Delta G° = -1.364 \log(K_{eq})$	(1.2)
$HA^- \rightleftharpoons A + H^-$	$\Delta G°_{H-}$ of HA^-	(1.3)
$MH \rightleftharpoons M^+ + H^-$	$\Delta G°_{H-}$ of MH	(1.4)

The "*H_2 heterolysis*" method for hydricity determination relies on measuring the equilibrium constant for the reaction of a hydride acceptor, a base, and H_2 (eq 1.5 in Scheme 1.8) to form a metal hydride of unknown hydricity (MH).[39] The free energy for H_2 heterolysis can be combined with the pK_a value of the acid (reverse of eq 1.6) and the free energy for the heterolysis of H_2 in the same solvent (eq 1.7) to yield the hydricity of a metal hydride (eq 1.8). The H_2 heterolysis method is conceptually related to the relative hydricity method, in that the hydricity of a metal hydride is determined relative to the hydricity of H_2.

Scheme 1.8. Determination of Hydricity by Heterolysis of H_2.

$MH + H\text{–}Base^+ \rightleftharpoons M^+ + H_2 + Base$	$\Delta G° = -1.364 \log(K_{eq})$	(1.5)
$H^+ + Base \rightleftharpoons H\text{–}Base^+$	$\Delta G° = -1.364\ pK_a$	(1.6)
$H_2 \rightleftharpoons H^+ + H^-$	$\Delta G°_{1.7}$	(1.7)
$MH \rightleftharpoons M^+ + H^-$	$\Delta G°_{H-}$	(1.8)

The "*potential–pK_a*" method for hydricity determination of a metal hydride involves measuring the pK_a value of MH (eq 1.9) and the reduction potential of the conjugate hydride

acceptor (eq 1.10).[38] Combining these experimental free energies with the free energy for the two-electron reduction potential for reduction of H^+ to H^- (eq 1.11) provides the hydricity (eq 1.12). The reduction potential E^o is most commonly determined using cyclic voltammetry (CV), a method that can readily identify reversible reductions that reach equilibrium at the electrode surface. The $E_{1/2}$ value from a CV experiment is a good approximation of $E°$ if the electrochemical wave is reversible.[42]

Scheme 1.9. Determination of Hydricity from Two-Electron $E°$ Value and a pK_a.

$$MH \rightleftharpoons M^- + H^+ \qquad \Delta G° = 1.364\ pK_a \qquad (1.9)$$

$$M^- \rightleftharpoons M^+ + 2e^- \qquad \Delta G° = 46.12\ E° \qquad (1.10)$$

$$H^+ + 2e^- \rightleftharpoons H^- \qquad \Delta G°_{1.11} \qquad (1.11)$$

$$MH \rightleftharpoons M^+ + H^- \qquad \Delta G°_{H-} \qquad (1.12)$$

The "*H_2 heterolysis*" and "*potential–pK_a*" methods require one or more of the thermodynamic constants that relate H^+, H•, H^-, and H_2, shown in Table 1.1. The constants in Table 1.1 provide the basis for thermochemical cycles that can be used to quantify the favorability of each of the possible M–H bond cleavage reactions. The origins of these constants in acetonitrile[43–46] and water[47] have been previously described. Eq 1.7 is of particular importance as an expression for three different thermodynamic parameters: the free energy to heterolyze H_2, the acidity of H_2 (given as a free energy), and the hydricity of H_2. Consistency in the implementation of these values ensures that any systematic error introduced in their formulation will not impact the prediction of reactivity trends.

Table 1.1. Thermodynamic Constants for H^+, H•, H^-, and H_2 in Acetonitrile and in Water. [a]

Reaction	$\Delta G°$ in MeCN (kcal·mol^{-1})	$\Delta G°$ in H_2O (kcal·mol^{-1})	eq
$2H^+ + 2e^- \rightleftharpoons H_2$	3.6[b]	0.0[c]	(1.13)
$H_2 \rightleftharpoons 2H^\bullet$	103.6	105.7	(1.14)
$H^+ + e^- \rightleftharpoons H^\bullet$	53.6[b]	52.8[c]	(1.15)
$H^\bullet + e^- \rightleftharpoons H^-$	26.0[b]	–18.6[c]	(1.16)
$H^+ + 2e^- \rightleftharpoons H^-$	79.6[b]	34.2[c]	(1.11)
$H_2 \rightleftharpoons H^+ + H^-$	76.0	34.2	(1.7)

[a] These values correspond to a 1 atm standard state for H_2 and a 1 M standard state for H^+, $H^\bullet$, and H^-. [b]Referenced to the $FeCp_2^{+/0}$ couple in MeCN. [c]Referenced to NHE.

In light of the benefits that thermochemical understanding could have in the development of hydride-mediated catalysis in water, the aqueous hydricity of metal hydrides has been, until recently, surprisingly unexplored. Creutz's seminal efforts relied on experimentally challenging approach-to-equilibrium kinetics under CO_2.[47,48] The groups of Yang and Berben each reported the hydricity of one metal hydride based on the thermodynamics of H_2 cleavage reactions.[49,50] Our interest in the aqueous reactivity of Cp*Ir-based catalysts motivated us to develop a general and expedient method for hydricity determination in water, discussed in Chapter 4.

1.4 Beyond Transition Metal Hydrides

Metal-hydride bonds are not the only intermediates for proton and electron management that have been utilized in the HER and other reactions the require PCET. For example, the mechanism for H_2 evolution from $Cp^*Mo(\mu\text{-}S)_4MoCp^*$ has been extensively studied and involves no metal-hydride intermediates.[51] The dimolybdenum system supports a wide range of oxidation and protonation states, but protons are localized on the sulfide bridges while the electrons may be on either sulfur or molybdenum.

Biology has made extensive use of the carbon-based hydride donor NADH (the reduced form of NAD^+, nicotinamide adenine dinucleotide) to manage the $1H^+/2e^-$ transfer of a hydride. Indeed, enantioselective enzymatic reductions of carbonyls that rely on NADH as a cofactor are extremely successful. In order to take advantage of the selectivity of enzymatic catalysis without incurring the penalty of stoichiometric consumption of the expensive NADH cofactor tandem catalytic systems that regenerate NADH from NAD^+ using inexpensive terminal reductants have become an area of research.[52–55] Of the organometallic catalysts that have been shown to regenerate NADH, Cp*Rh(bpy)-based complexes have emerged as selective and efficient catalysts for reduction at the 4-position of nicotinamides, spurring innovation in tandem bio-organometallic catalysis (Scheme 1.10).[53]

Scheme 1.10. Tandem catalytic cycle for Rh, NAD^+, and enzyme mediated reductions

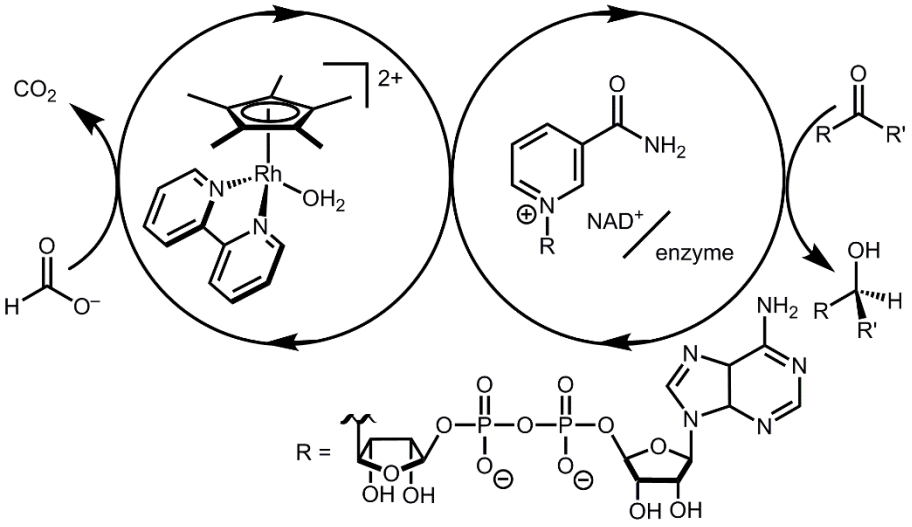

After considering the hydricity of the iridium analogues $[Cp^*Ir(bpy)(H)]^+$ in Chapter 4, we were interested in the comparison to $[Cp^*Rh(bpy)(H)]^+$, one of the best NAD^+ reduction catalysts. We found, surprisingly, that rather than the expected Rh–H, the stable

hydride donor was (Cp*H)Rh(bpy)(Cl), making this species, like NADH, a carbon-based hydride donor. Our investigation of the structure and hydricity of this complex is presented in Chapter 5.

Moving farther away from metal-hydrides, for the formation of heavier fuels like propane and butane, future solar fuel systems may need to mediate C–C bond formation. Thinking of the simplest substitution for the hydride, we investigated the methyl analogue $[Cp^*Ir(bpy)(CH_3)]^+$. Given that the Cp*Ir(bpy) scaffold exhibited an unexpected mechanism for H_2 evolution, we questioned whether substitution of a methyl group for the hydride would form C–C bonds through the analogous reaction to that of the hydride. Our investigation into the characterization, photochemistry, and mechanism of alkane formation from a methylated Cp*Ir(bpy) complex is discussed in Chapter 6.

1.5 Summation

Transition metal hydrides are key intermediates in many catalytic cycles, both for the formation of hydrogen and other fuels and for other reductions in biology and in industry. Designing systems that produce chemical bonds from these hydrides with the help of sunlight is a fundamental challenge for solar fuels. This work begins by integrating light absorption and electrocatalysis in a single molecule. The fundamental thermodynamics of hydride transfer were investigated to understand these reactions. With our understanding of this system, we broadened our scope to understand what happens when you perturb the catalyst by changing the metal and the ligands.

Discovering solutions to the energy needs of our planet is a multifaceted problem being approached from many different directions. By following this research path, though much

work remains, we have shed light on alternative strategies for the development of fuels from light.

CHAPTER 2: MOLECULAR PHOTOELECTROCATALYSTS FOR VISIBLE LIGHT-DRIVEN HYDROGEN EVOLUTION FROM NEUTRAL WATER

2.1 Introduction

Light-promoted evolution of hydrogen from water is an attractive route to solar fuels. Though there are many strategies to achieve this goal, as previously discussed, most involve many components. In multi-component schemes, the catalyst is often identified and optimized using electrochemical methods before integration with a light absorber.[56] The multi-component photoredox approach has seen widespread success in systems utilizing a molecular chromophore (e.g. $Ru(bpy)_3^{2+}$), a catalyst (e.g. Co diglyoximes), and a sacrificial reductant.[22] A light absorbing material (e.g. Si or small band gap semiconductors) can also be employed in such systems, leading to heterogeneous photoelectrochemical cells.[57]

We envisioned an alternative photoelectrochemical approach, in which H_2 evolution is facilitated by a *single* molecule acting *both* as light absorber *and* electrocatalyst. Such multifunctional catalysts (almost always $Ru(bpy)_3^{2+}$) have been used to produce "molecular photoelectrodes," but this strategy has not been applied to the synthesis of a chemical fuel, as in hydrogen evolution catalysis.[58–60] We report here that [Cp*Ir(bpy)(Cl)][Cl] (**1**) integrates light absorption and electrocatalysis in a single molecular framework. Aqueous solutions of **1** evolve negligible amounts of H_2 in the dark at pH 7, but illumination with visible light initiates sustained photoelectrocatalytic H_2 evolution with minimal applied potential (Scheme

2.1). Electron transfer occurs in the dark while H_2 release is light-triggered, consistent with previously observed reactivity pertaining to the photochemical water-gas shift reaction.[61–63] Unlike the water-gas shift and other multi-component hydrogen evolution strategies, no sacrificial reagent is required. Tuning the electronic nature of the ligand affords photoelectrocatalysts with good activity near the thermodynamic potential for H_2 evolution.

2.2 Results and Discussion

Sustained Photoelectrocatalytic Hydrogen Evolution. A molecular photoelectrocatalyst must be capable of electrochemical hydride formation and photochemical H_2 release. Detailed electrocatalytic studies of **1** in aqueous solution are lacking,[64] but H_2 evolution electrocatalysis in acetonitrile has been reported, albeit at very negative potentials (–1.6 V *vs.* Ag/Ag^+).[65] Considering this precedent, electrochemical studies in aqueous solution, in the dark and under visible light illumination, were undertaken.

Scheme 2.1. Photoelectrochemical water reduction conditions.

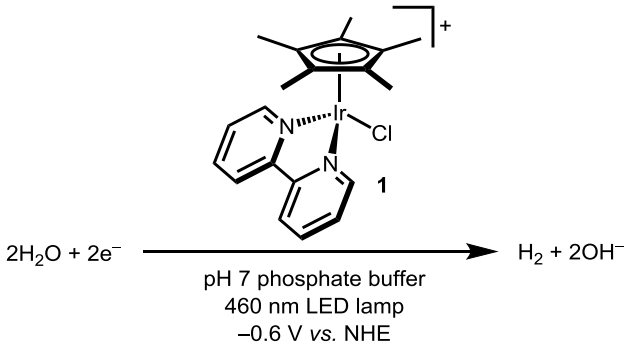

Water-soluble chloride complex **1** was prepared according to the previously reported procedure,[66] and cyclic voltammetry (CV) was performed as an initial probe for photoelectrocatalytic activity. In pH 7 phosphate buffer (0.1 M), protected from light, chloride complex **1** exhibited an irreversible reduction at –0.61 V on a glassy carbon working

electrode (Figure 2.1; all potentials reported *vs.* NHE unless otherwise noted). At scan rates of 25 $mV \cdot s^{-1}$ and faster, no current enhancement was observed upon illumination with a 460 nm LED lamp. At scan rates slower than 25 $mV \cdot s^{-1}$, however, illumination produced clear increases in current (Figure 2.1). At such slow scan rates convection can interfere with interpretation,[67] but the current enhancement is characteristic of catalysis.

Encouraged by the current response to light in CV experiments, controlled potential electrolysis (CPE) was carried out to provide further support for photoelectrocatalysis. In CPE experiments with the potential held at –1 V *vs*. NHE, a 1 mM solution of **1** in pH 7 phosphate buffer was irradiated at 460 nm. Sustained photocurrent around –600 μA was achieved over the course of the one-hour experiment (Figure 2.2A) and bubbles evolved from solution and accumulated on the electrodes. When protected from light, the current rapidly diminished to below –25 μA (Figure 2.2A). The CPE experiments confirm that while chloride **1** is an ineffective electrocatalyst in the dark, photolysis induces electrocatalytic activity. Visible light enhanced catalytic currents by a factor of roughly 25 after 60 min at –1 V, suggesting efficient and sustained photoelectrocatalysis.

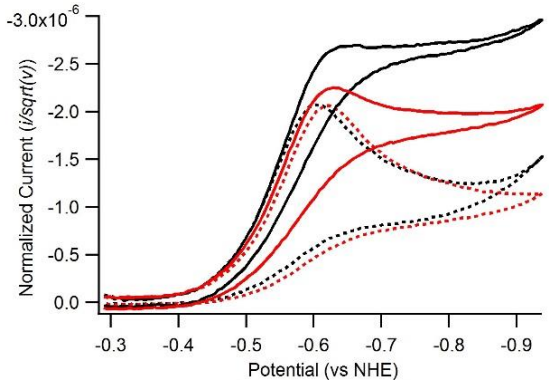

Figure 2.1. CV of 1 mM **1** in 0.1 M sodium phosphate buffer (pH 7) at 5 $mV \cdot s^{-1}$ illuminated (solid black) and dark (dashed black) and at 10 $mV \cdot s^{-1}$ illuminated (solid red) and dark (dashed red). Glassy carbon working electrode (3 mm disc), Pt wire counter electrode, Ag/AgCl (3M NaCl) reference electrode, 460 nm LED lamp. Current is scan-rate

normalized: normalized current of diffusion-controlled processes is constant with changing scan rate while normalized current of catalytic waves increases as scan rate decreases.

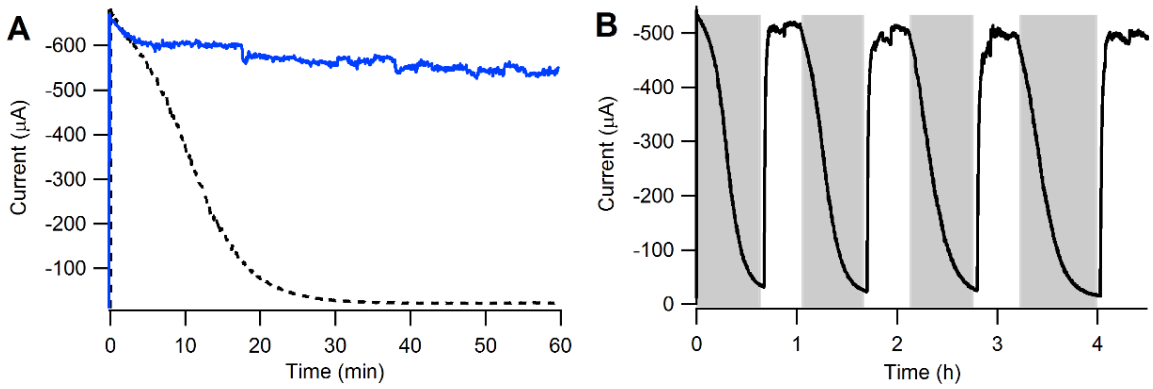

Figure 2.2. A) CPE at –1 V *vs.* NHE of 1 mM **1** in 0.1 M phosphate buffer (pH 7) in the dark (dashed black) and under 460 nm light (solid blue). B) CPE at –0.9 V *vs.* NHE of 1 mM **1** in 0.1 M phosphate buffer (pH 7) with light off (gray) and on (white). Reticulated vitreous carbon working electrode, Pt wire counter electrode, Ag/AgCl (3M NaCl) reference electrode.

The influence of light was further established by applying a shutter to CPE experiments (Figure 2.2B). In the dark, high levels of current are initially passed before rapidly decaying, consistent with complete electrochemical reduction of all **1** in solution. In the light, the current quickly rises and remains steady as photoelectrocatalytic H_2 evolution initiates. Applying a shutter halts catalysis, and the current immediately begins to drop. The large amount of charge passed after shuttering implies that $[Cp^*Ir(bpy)(H)]^+$ (**2**), which cannot be further reduced at the potential applied, is not the dominant species in the bulk solution during catalysis. The low proportion of hydride **2** in solution suggests that the photochemical steps are not limiting the reaction in this cell configuration. As a control reaction, the same experiment was performed in the absence of catalyst: no difference in current was observed when a cell containing only aqueous phosphate buffer was toggled between dark and light conditions.

The Faradaic efficiency of photoelectrocatalysis was quantified by monitoring the solution pH change *in situ* during photoelectrolysis. If H_2 is produced according to Scheme 2.1, proton consumption will lead to a pH increase. Faradaic efficiency was obtained by relating the measured pH change to the expected pH change if every two electrons produced H_2.[19] A weakly buffered solution (50 mM phosphate, initial pH 7.8) was irradiated while applying a potential of –0.9 V, and the pH was measured periodically. The pH increased as expected, with 100% Faradaic efficiency recorded at early times before a slight decrease to ~90% as the experiment proceeded and the pH increased (Figure 2.3).

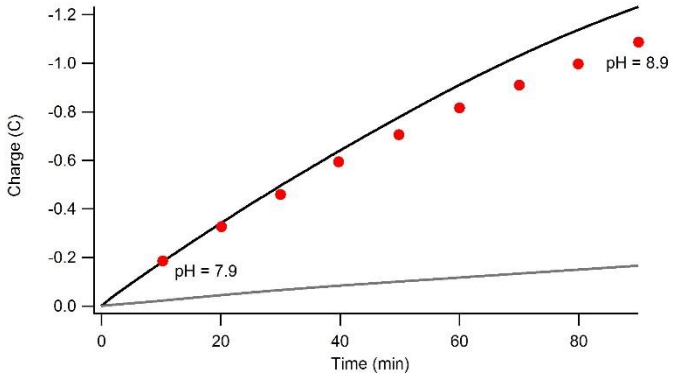

Figure 2.3. Total charge passed in the photoelectrolysis (–1.23 C, black) and charge that productively made H_2 according to the pH change (red circles) for 1 mM **1** in 50 mM sodium phosphate (initial pH = 7.8) at –0.9 V, and the charge passed in the absence of catalyst (–0.17 C, gray). Photoelectrolysis results in a seven-fold increase in total charge passed, and the pH change in the absence of catalyst was within the ±0.1 error of the probe. Faradaic efficiency drops from 100% to 90% over 90 minutes.

The photon-to-hydrogen efficiency is also of great interest in photoelectrocatalytic processes. This efficiency can be measured in a number of ways; the present system, in which the specific concentration of photoactive species at any given time is unknown, is best treated by "external quantum efficiency" ($EQE = \frac{moles\ H_2\ produced}{moles\ incident\ photons}$). The moles of incident photons in an area ~2 mm^2 greater than the electrode planar surface area were

measured using a Si photodiode. Based on the current passed and the Faradaic efficiency, EQE = 10(5)% in three separate controlled potential electrolysis experiments. This value is similar to a previous molecular photoelectrochemical cell based on photoredox quenching,[59] and similar to the H_2 quantum yield in photochemical water-gas shift reactions involving **2**.[63] It is expected that the EQE value obtained here will be sensitive to a variety of factors such as the light source and geometric position, electrode surface area (variations in which we believe to be responsible for the relatively large uncertainty in our value), catalyst concentration, and applied potential. The EQE is useful for practical catalytic applications; the mechanistically more insightful quantum yield, which measures the efficiency of H_2 evolution based on the number of photons actually *absorbed* by hydride **2**, will be assessed in future studies.

In prolonged photoelectrocatalysis experiments, photocurrent was relatively stable until the buffer was exhausted after 5.5 h. The total catalyst turnover number (TON) for H_2 production in this extended experiment was 16.5 (TON ~ 3.9 in a typical 1 h experiment). Photoelectrocatalytic activity was restored upon addition of acid, but steadily diminishing current over the course of 48 h suggests some catalyst degradation (Figure 2.4). In dark electrolyses under the same conditions, no H_2 was detected by GC. Similarly, when phosphate solutions (no catalyst) were subjected to photoelectrolysis, minimal charge passed (–0.17 C without catalyst, –1.23 C with catalyst) and the pH change did not change.

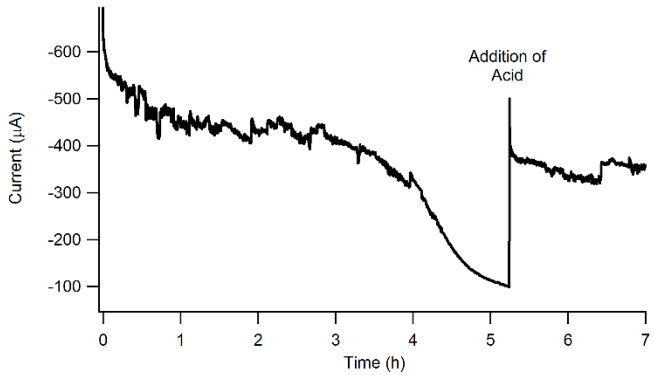

Figure 2.4. CPE of 1 mM **1** in 0.1 M sodium phosphate buffer (pH 7) at –0.9 V under 460 nm LED irradiation. After exhaustion of the buffer, addition of 100 μL 1 M H_3PO_4 restored current.

Separating the Electrochemical and Photochemical Steps. In order to establish that catalyst **1** was responsible for both the photochemical and electrochemical processes, they were studied independently. First, the electrochemical properties of **1** were probed in the absence of light. As described above, CV of **1** in pH 7 phosphate buffer (0.1 M) displays an irreversible reduction around –0.61 V that appears to be composed of multiple peaks. In contrast, solutions of **1** in pH 7 water with NaCl electrolyte (0.1 M) exhibited a single irreversible reduction feature (Figure 2.5A). The initial reduction features are assigned as $2e^-$ processes on the basis of previous reports and CPE experiments (*vide infra*).[64,65] The distinct behavior observed in chloride and in phosphate electrolytes indicates partial chloride displacement in phosphate buffer to form $[Cp^*Ir(bpy)(H_2O)]^{2+}$,[64,68] and $[Cp^*Ir(bpy)(H_2PO_4)]^+$,[69–71] as further evidenced by ^1H and $^{31}P\{^1H\}$ NMR studies that showed two minor species (<10% of total Ir) in D_2O containing ~0.1 M pD 7 NaH_2PO_4/Na_2HPO_4. In pure D_2O, **1** was the only species observed.

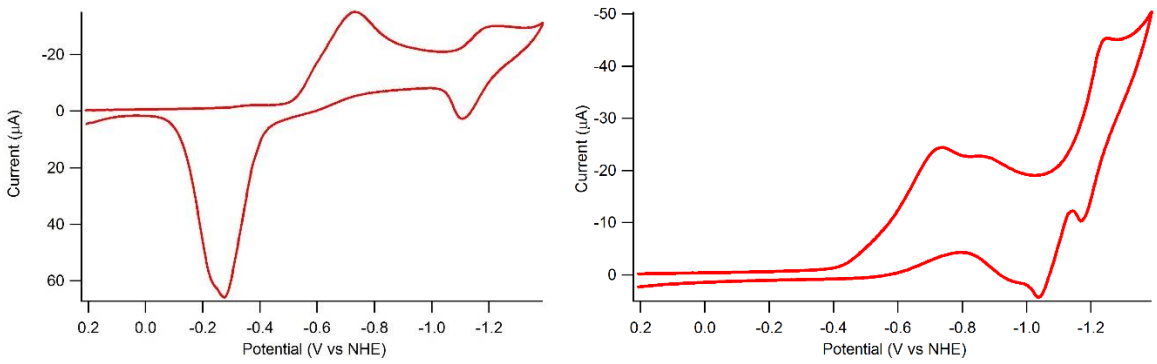

Figure 2.5. A) CV of 1 mM **1** in 0.1 M NaCl at a scan rate of 250 $mV \cdot s^{-1}$. B) CV of 1 mM **1** in 0.1 M sodium phosphate buffer (pH 7) at a scan rate of 250 $mV \cdot s^{-1}$.

Regardless of electrolyte, aqueous solutions of **1** show a second, quasi-reversible $1e^-$ reduction at –1.25 V (Figure 2.5B). This feature is assigned to the $Ir^{III}–H^+/Ir^{II}–H$ couple of hydride **2**, suggesting that $2e^-$ reduction of **1** to form $Cp^*Ir^{I}(bpy)$ (**3**) is followed by rapid protonation. Consistent with this assignment, the peak current at –1.25 V diminishes as the solution pH increases: as **3** becomes the dominant product upon reduction of **1**, the feature corresponding to the reduction of **2** disappears. Above pH 10, a new oxidation feature is also observed around –0.25 V, assigned as a $2e^-$ oxidation of **3**. At these high pH values, the voltammetric response is indicative of the neutral complex **3** adsorbing on the electrode. Similar adsorption is observed at pH < 10 when scanning beyond –1.3 V, at which point another neutral species, Cp*Ir(bpy)(H) is formed. Conditions in subsequent experiments were chosen to avoid such adsorption (see below for a discussion on homogeneity).

A stepwise electrolysis-photolysis experiment was undertaken to separately probe the role of electron transfer and photon absorption. Controlled potential electrolysis of **1** was carried out protected from light, in pH 7 phosphate buffer. The product of dark electrolysis was confirmed to be hydride **2** by ^1H NMR spectroscopy and by comparison of the UV-vis spectrum to an isolated sample of **2** (Figure 2.6, λ_{max} = 410 nm). From the electrochemically

formed **2**, ε_{410} = 2400 M^{-1} cm^{-1} which is consistent with the extinction coefficient determined from an isolated sample. The first reduction wave of **1** had also essentially disappeared, while the hydride redox couple remained. In a typical electrolysis with 2.5 mL 1 mM **1**, the total charge passed during dark CPE was –433 mC (1.8 e^-/Ir), consistent with 2e^- reduction of **1** followed by protonation to form hydride **2**.

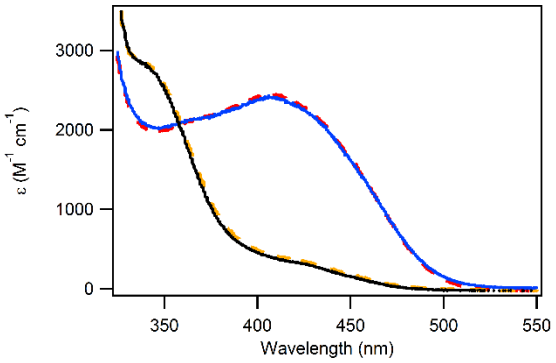

Figure 2.6. UV−vis spectra of 0.3 mM **1** in 0.1 M phosphate buffer (solid black), after 90 min of electrolysis at −0.9 V to form **2** (solid blue), and after 90 min of 460 nm photolysis to reform **1** (dashed orange). Subsequent electrolysis reformed **2** (dashed red) and photolysis reformed **1** (omitted for clarity). The molar extinction coefficient (ε) of each species was calculated assuming clean conversion (see text for details). Reticulated vitreous carbon working electrode, Pt wire counter electrode, Ag/AgCl (3 M NaCl) reference electrode.

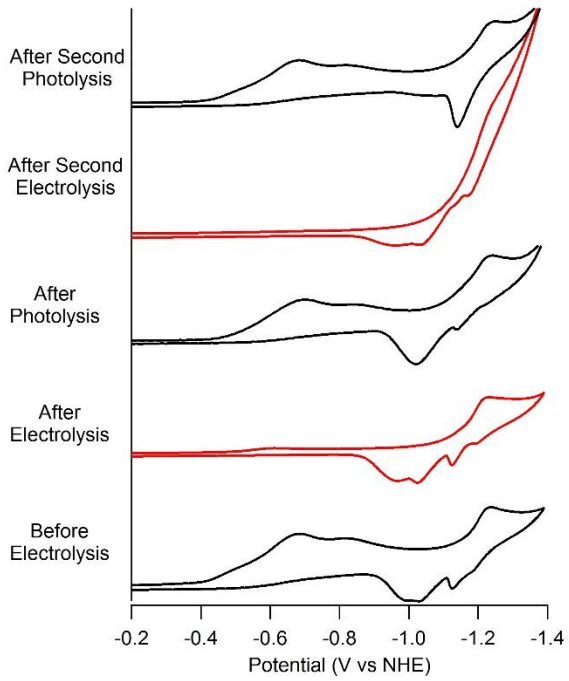

Figure 2.7. CV (scan rate of 250 $mV \cdot s^{-1}$) performed during stepwise electrolysis (–0.9 V) and photolysis (460 nm LED) of 1 mM **1** in 0.1 M sodium phosphate buffer (pH 7).

Next, the electrolysis solution containing *in situ*-generated hydride **2** was photolyzed. Whereas solutions of hydride **2** in neutral water are stable in the dark over several hours, irradiation with a 460 nm LED array leads to rapid consumption of **2**, as judged by UV-vis (Figure 2.6) and CV (Figure 2.7). Photolysis returned the Ir-containing species to pale yellow **1**. Re-subjecting the solution to CPE cleanly produced golden hydride **2**, which was again consumed upon photolysis, indicating stepwise catalysis. The evolved gas, confirmed to be H_2 by GC headspace analysis, was formed with 70% Faradaic efficiency. Faint orange luminescence was apparent to the naked eye during photolysis, suggesting the involvement of the previously reported excited state of $[Cp^*Ir(bpy)(H)]^+$, **2***, which has been reported to have a 80 ns lifetime at 298 K in MeCN.[72,73] Scheme 2.2 depicts a broad mechanism for photoelectrocatalytic H_2 evolution that is consistent with the stepwise studies. Later work

from our lab showed that the mechanism for H_2 evolution with **2** and acids in acetonitrile follows a bimolecular self-quenching pathway.

Scheme 2.2. Proposed photoelectrocatalytic cycle.

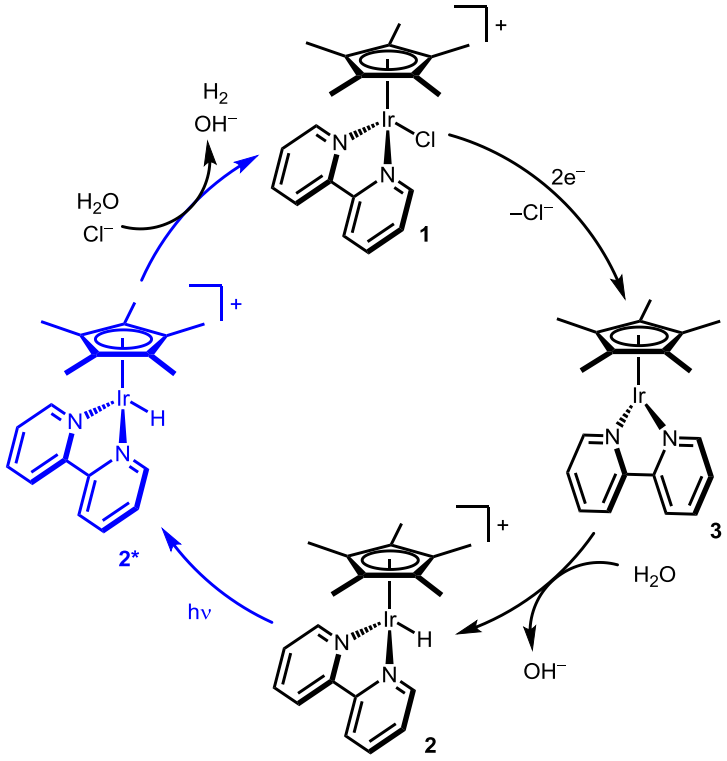

A slew of recent studies on the homogeneity of Cp*Ir-based catalysts compelled us to consider the possibility of Ir nanoparticles.[13,74,75] Without undertaking an exhaustive study, three lines of evidence suggest that a molecular catalyst is likely to be responsible for the observed behavior. First, the stepwise electrolysis/photolysis study described above shows that all of the chloride complex **1** in the bulk solution is cleanly converted to the hydride complex **2** electrochemically. If the electrochemical current was leading to deposition of nanoparticles or other decomposition, the yield of molecular species **2** should be low. Further, upon photolysis, H_2 gas and chloride **2** are formed in high yield; this cycle can be

repeated three times without noticeable degradation. It is noteworthy that the study was monitored by optical spectroscopy, as IrOx nanoparticles are highly colored; no absorption in the 600-800 nm range was observed. Second, a "rinse test" was performed: when the electrode was gently rinsed with water after a typical photoelectrocatalytic run and placed in a fresh phosphate solution containing no catalyst, only current attributed to glassy carbon background was observed, suggesting that adsorbed species are not the active catalyst. Finally, the kinetics of catalysis showed no induction period, with controlled potential electrolyses maintaining steady photocurrent for hours. These observations, coupled with the reductive, anaerobic conditions (as opposed to oxidizing, aerobic conditions under which Cp*Ir water oxidation catalysts have been shown to decompose), suggest that catalyst degradation to nanoparticles is not a major factor.

Optimization of Photoelectrocatalytic Performance. Optimization of the photoelectrocatalytic hydrogen evolution reaction was carried out with the aid of kinetic studies. As discussed above, the initial rates were too slow for reliable data to be extracted from CV experiments. Reaction rate constants were therefore measured using chronoamperometry (CA). While not commonly used to assess electrocatalysts, Delahay and Stiehl showed that CA data can provide an apparent rate constant for catalytic reactions.[76] The model assumes that electron transfer is fast, such that the observed rate constant is a reflection of a rate-determining chemical catalytic step (EC' mechanism). While the influence of light on the reaction may complicate such analysis, we have found CA convenient for obtaining an apparent rate constant, k_{obs}, for comparisons. Chronoamperometry of **1** was carried out at –1.0 V for 20 seconds both in the dark and under 460 nm illumination. Irradiated samples passed significantly more current than those protected from light (Figure

2.9A). The ratio of the dark and light currents was fit between 5 and 10 seconds to give k_{obs} = 0.037(9) s^{-1}. The observed rate constant varied linearly with light intensity (Figure 2.8), supporting the notion that photon fluence is a key parameter.

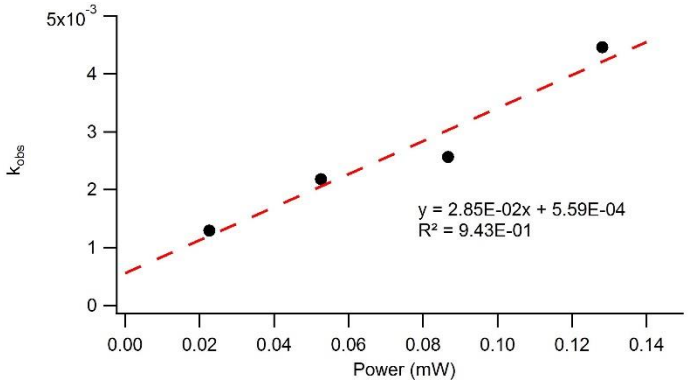

Figure 2.8. Plot showing rate dependence on lamp power. The apparent catalytic rate constants were obtained from CA experiments at different LED lamp power, each with 1 mM **1** in 0.1 M sodium phosphate buffer (pH 7) held at –0.9 V for 20 seconds. A variable power supply controlled the power of the incident light (470 nm LED strips).

The impact of potential on photoelectrocatalysis was investigated by varying the applied CA potential between –0.6 and –1.0 V (Figure 2.9A, black squares). The observed rate constant increased with increasing overpotential,[42,77] remaining steady with k_{obs} = 0.039(4) s^{-1} after –0.8 V. The catalytic onset potential is consistent with the notion that the key intermediate in H_2 evolution photoelectrocatalysis is the Ir^{III}–H^+ intermediate **2**, which is formed electrochemically at similar potentials. Further reduction to the neutral Ir(II)–H is not required. A hydrogen evolution overpotential of only 190 mV (–0.60 V *vs.* NHE at pH 7) is required to achieve half of the maximum catalytic rate, k_{obs} = 0.02(1) s^{-1}; this potential corresponds nicely to the relevant reduction wave of **1** (–0.61 V).[77] In contrast, aqueous solutions of **1** *protected from light* do not show conclusive evidence of catalysis even upon subsequent reduction of **2** to the Ir^{II}–H intermediate. A related catalyst with pyrrole

substituents, when electropolymerized onto an electrode surface, was reported to evolve H_2 *via* the Ir^{II}–H state under acidic conditions: pH 3 at –1.31 V, an overpotential of approximatly 1.1 V.[65] When a photochemical step is harnessed, **1** catalyzes H_2 evolution at a more positive reduction potential and at neutral pH.

A variety of media were screened as supporting electrolytes for water reduction across a wide pH range. Sustained catalytic current over background was observed when 1 mM solutions of **1** in 0.1 M citrate buffer underwent CPE at –0.9 V (pH adjusted to 4, 5, and 6 in separate experiments). A phosphate solution at pH 8 and borate buffer solutions at pH 9 and 10 also showed sustained CPE photocurrents (–1 V).

Facile tuning by ligand substitution is a key feature of many molecular catalysts, and indeed the photoelectrocatalytic H_2 evolution behavior is not unique to complex **1**. A large variety of substituted bipyridine analogues are known, and complexes of a few of these were screened in initial studies. Sustained currents over one hour were observed when electrochemical cells containing solutions of [Cp*Ir(bpy-OMe)(Cl)][Cl] (**1-OMe$_2$**) and [Cp*Ir(bpy-COOH)(Cl)][Cl] (**1-COOH$_2$**) (bpy-X = 4,4'-X-2,2'-bipyridine, X = OMe, COOH) were held at –1.0 V and irradiated with a 460 nm LED in pH 7 phosphate buffer.

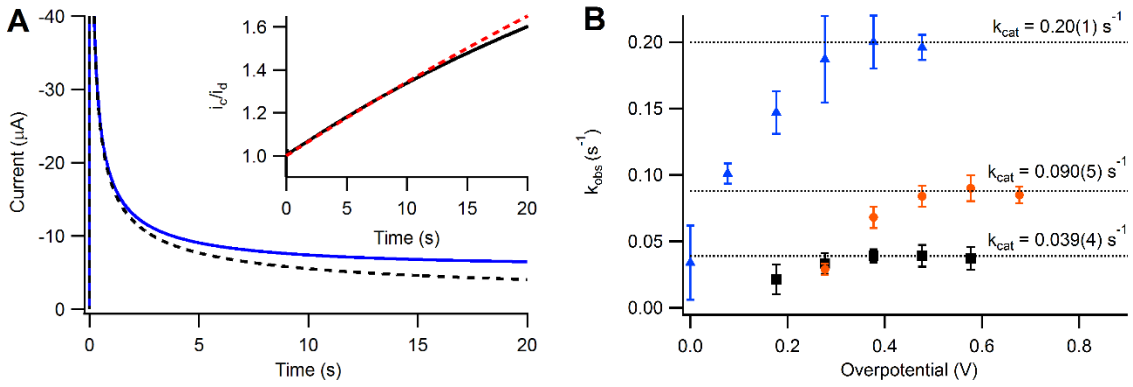

Figure 2.9. A) Chronoamperometry of 1 mM **1** in pH 7 phosphate buffer in the dark (dashed black) and under 460 nm LED irradiation (solid blue) at –1 V *vs.* NHE. Inset: ratio of the two CA traces (black) and fit (dashed red) with k_{obs} = 0.036 s^{-1}. B) Apparent catalytic rate

constants for **1** (black squares), **1-OMe2** (orange circles), and **1-COOH2** (blue triangles) as a function of potential. Error bars reflect two standard deviations in both directions as determined by between 3 and 7 experiments. Glassy carbon working electrode (3 mm disc), Pt wire counter electrode, Ag/AgCl (3M NaCl) reference electrode.

Surprisingly, the observed rate constants obtained from chronoamperometry did not follow the trends expected for electrocatalysts. The catalyst reduced at the most negative potential, **1-OMe2**, gave k_{obs} = 0.090(5) s^{-1} at –1 V while the catalyst reduced at the most positive potentials, **1-COOH2** (deprotonated under the experimental conditions), outperformed both catalysts, with k_{obs} = 0.20(1) s^{-1} at –0.8 V (Figure 2.9B). Carboxylate-substituted catalyst **1-COOH2** also operates at lower overpotentials than **1**, and CV traces show the onset of catalysis occurs *just prior to* the thermodynamically required potential for H_2 evolution (Figure 2.10). This situation is only possible when photon energy is being utilized and suggests that further catalyst optimization may lead to significant energy storage.

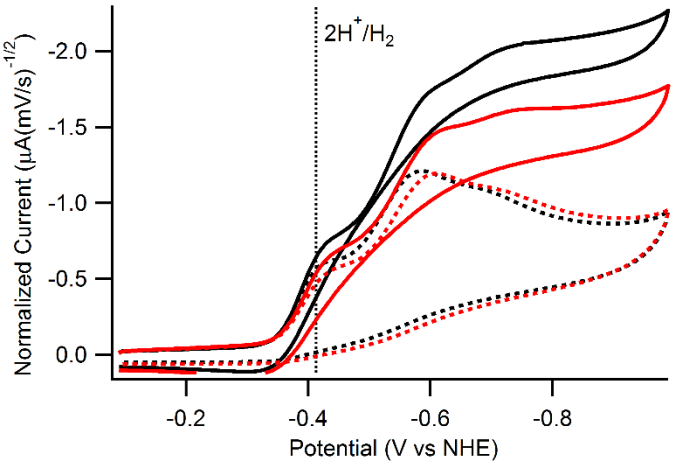

Figure 2.10. CV of 1 mM **1-COOH2** in 0.1 M sodium phosphate buffer (pH 7) at 25 $mV \cdot s^{-1}$ under 460 nm LED light (solid black) and dark (dashed black) and at 50 $mV \cdot s^{-1}$ in the light (solid red) and dark (dashed red). Dotted line indicates thermodynamic potential for hydrogen evolution at pH 7. Current is scan-rate normalized: normalized current of diffusion-controlled processes is constant with changing scan rate while normalized current of catalytic

waves increases as scan rate decreases. Glassy carbon working electrode (3 mm disc), Pt wire counter electrode, Ag/AgCl (3M NaCl) reference electrode.

It is remarkable that **1-COOH$_2$** is both the fastest catalyst *and* features the lowest overpotential, in light of the general trend for molecular electrocatalysts that larger overpotentials produce faster reactivity. Inspection of the absorption spectrum reveals that [Cp*Ir(bpy-COOH)(H)]$^+$ has excellent overlap with the 460 nm LED lamp used in these studies (Figure 2.11). This presumably leads to an increased external quantum efficiency, perhaps explaining the superior photoelectrochemical performance of **1-COOH$_2$** at low overpotential.

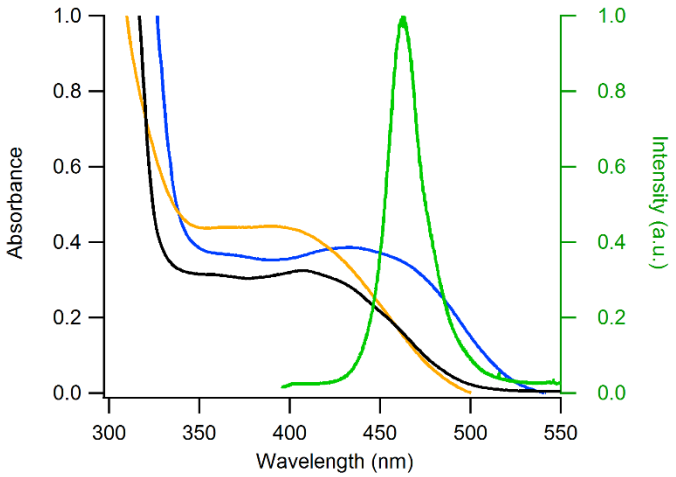

Figure 2.11. Absorption spectra of electrochemically generated [Cp*Ir(bpy)(H)]$^+$ (black), [Cp*Ir(bpy-OMe)(H)]$^+$ (orange), and [Cp*Ir(bpy-COOH)(H)]$^+$ (blue) in 0.1 M sodium phosphate buffer (pH 7) with the spectrum of the 460 nm LED lamp (green).

2.3 Conclusions

A novel approach to H_2 evolution using molecular photoelectrocatalysts has been introduced. A single molecular catalyst undergoes electrochemical hydride formation followed by photochemical H_2 release. Water reduction is facilitated by three different Ir

catalysts and visible light over a wide pH range at low overpotentials. Hydrogen evolution at the thermodynamic potential was observed, with rate constants of ~0.1 s^{-1} at ~100 mV electrochemical overpotential.

Combining aspects of photocatalysis and electrocatalysis leads to a number of interesting observations. In comparison to typical hydrogen evolution electrocatalysts, visible light excitation leads to a dramatic reduction in electrochemical applied overpotential, as the required energy comes from light instead of electricity. Further, electrocatalysts typically feature trade-offs between the required potential for catalytic onset and catalytic activity. By incorporating a photochemical step, this linear correlation is broken, and the more easily reduced catalyst **1-COOH$_2$** also was found to be the most active, due to better photon absorption ability. In comparison to typical photocatalysts, the use of an electrode lifts the requirement for sacrificial reducants. Whereas a complex mixture of light absorbers, redox mediators, catalysts, and sacrificial reagents are often required for photocatalytic H_2 evolution, the present system features a single component that acts as light absorber and catalyst.

Based on the approach presented here, further improvements can be envisioned: for example, the 460 nm (2.6 eV) lamp provides substantial excess photon energy that is currently not fully utilized. Future work will focus on elucidating the detailed mechanism of the reaction and developing new catalysts capable of sustaining faster hydrogen evolution rates even while absorbing lower energy light.

2.4 Experimental Section

General Considerations. Procedures were carried out under nitrogen except where noted. 2,2'-bipyridine (bpy) and 4-4'-dimethoxy-2-2'-bipyridine (bpy-OMe), 4,4'-carboxyl-2,2'-bipyridine (bpy-COOH), sodium hydroxide, phosphoric acid, and pentamethylcyclopentadiene (Cp*H) were obtained from either Alfa Aesar or Sigma-Aldrich. Sodium phosphate monobasic hydrate was obtained from Mallinckrodt. $IrCl_3 \bullet 3H_2O$ was obtained from J&J Materials Inc. Commercial HPLC-grade water was used as a solvent. Deuterium oxide was purchased from Cambridge Isotope Laboratories, Inc. Electrochemical experiments were performed on a Pine WaveNow potentiostat or Pine WaveDriver bipotentiostat controlled by Aftermath software. Details on specific electrochemical experiments are described below. Solution pH was recorded using an OrionStar A111 pH meter with a Beckman-Coulter pH probe. UV-Vis spectra were obtained using an Agilent Cary 60 spectrophotometer or an Ocean Optics USB2000+ spectrometer with a DT-MINI-2GS deuterium and tungsten halogen light source controlled by OceanView software. Photolysis was conducted using a 500 lumen blue LED lamp from Eagle Lights. The wavelength of maximum intensity was 460 nm, as measured with an Ocean Optics USB2000+ controlled by Overture software. In the power dependence experiment, a 460 nm LED light strip from Super Bright LEDs was used. An estimate of the external quantum efficiency was obtained by measuring photon flux with a Coherent LM-2VIS photodiode in conjunction with a Coherent $FieldMax_{II}$ Laser Power/Energy Meter. The photodiode was positioned at the same distance from the lamp as the electrode and a piece of curved glass was used to approximate the conditions of the cell.

A Varian 450-GC with a pulsed discharge helium ionization detector was used to quantify H_2. A calibration curve was constructed from samples of 0.5, 1.0, 3.0, and 5.0 v/v % H_2 in air. All gas transfers were performed with a 1.0 mL or 10 mL Vici Pressure-Lok® Precision Analytical Syringe. As much as possible, septa were pierced only once. NMR spectra were obtained on 400 or 600 MHz spectrometers. ^{1}H NMR spectra were referenced to the residual solvent signals (or with acetone or sodium tosylate as an internal standard in D_2O).[78] Spectra were processed using the MestReNova software suite from Mestrelab Research S. L. The solution acidity in NMR experiments is reported as pD, obtained by addition of +0.4 to the reading of a pH electrode that was calibrated using H_2O standards.[79]

Synthesis. The catalysts [Cp*Ir(bpy)(Cl)][Cl],[66] [Cp*Ir(bpy-OMe)(Cl)][Cl],[66] [Cp*Ir(bpy-COOH)(Cl)][Cl],[63] and $[Cp^*Ir(Cl)_2]_2$[80] were prepared according to literature procedures. Catalyst identity and purity (>99%) was established by ^{1}H NMR spectroscopy. The spectroscopic features closely matched the published data.

Electrochemistry. Unless otherwise noted, all electrochemical experiments were performed in a divided H-cell with a 3-electrode configuration. A carbon working electrode (specific material varied with experiment, see below) and platinum wire counter electrode were positioned on either side of the fine frit. A Ag/AgCl (3M NaCl) reference electrode was placed in the counter electrode compartment in a small glass tube fitted with a Vycor glass frit. Solutions were thoroughly degassed by sparging with nitrogen for at least 15 minutes before beginning an experiment. All potentials are reported relative to NHE, with values obtained by adding 0.21 V to the experimentally observed potential *vs.* Ag/AgCl.[81] Overpotentials (to achieve a certain catalytic efficiency) were calculated by subtracting the

formal potential for H_2 evolution ($E^o_{H+/H2} = 0 - 0.059 \cdot pH$) from the applied potential at which catalysis was experimentally observed.[82]

Cyclic voltammetry experiments were carried out with a 3 mm diameter glassy carbon disc working electrode (polished with 0.05 micron alumina powder between scans). For experiments under irradiation, the 460 nm LED lamp was placed directly below the glass carbon electrode at a fixed distance.

Controlled potential electrolysis experiments were carried out with reticulated vitreous carbon (RVC) impaled on a graphite rod wrapped with copper wire (above the water line) as the working electrode. In the illuminated experiments, a 460 nm lamp was placed approximated one inch away from the cell. In the dark experiments, the cell was wrapped in aluminum foil. In the shutter experiment, the light was turned on and off periodically; the cell was not wrapped in aluminum foil during the dark stages.

Faradaic efficiency was determined by monitoring the pH change over the course of a CPE experiment. A solution of 1 mM [Cp*Ir(bpy)(Cl)][Cl] in 50 mM phosphate was held at –0.9 V while being irradiated with 460 nm LED light for 90 minutes, with the pH probe inserted into the working electrode compartment of the H-cell. For each molecule of H_2 formed, two OH^- ions are produced. The amount of hydroxide corresponding to the observed pH change was determined by titration of an identical sample with 0.1 M NaOH.[19] A control experiment, in which a pH 7 phosphate buffer with *no catalyst* was held at –0.9 V, showed minimal charge accumulation. Whereas the solution pH changed by 1.0 unit when the catalyst was present, without catalyst the pH changed by < 0.1 unit, suggesting little or no H_2 production at the electrode under the standard photoelectrolysis conditions.

Headspace detection of H_2 by gas chromatograph was performed in the same cell that was used for CV and CPE experiments. Every effort was made to configure the cell such that any leaks were minimized. After controlled potential electrolysis at –0.9 V for 30 minutes, a headspace sample was obtained before and after photolysis using a gastight 1.0 mL syringe. The volume % hydrogen was quantified by comparison to a calibration curve. Before photolysis, no H_2 peak was observed by GC. After photolysis, a prominent H_2 peak was observed in the GC trace. Integration and comparison to the calibration curve established a 70% Faradaic efficiency.

To show stepwise catalysis by UV-Vis (Figure 2.6), a 200 mL capacity divided cell was used. The Pt wire was positioned in 3 mL in 0.1 M pH 7 phosphate buffer across a frit from the RVC working electrode and Ag/AgCl reference electrode. A 0.3 mM solution of **1** (40 mL 0.1 M pH 7 phosphate buffer) was added to the working electrode chamber and degassed. UV-Vis were obtained by syringing 3 mL of solution into septa-capped cuvettes under N_2. The samples were returned to the cell after the spectra were taken. Spectra were collected at five points: initially, after exhaustive electrolysis at -0.9 V, after exhaustive photolysis, after a second electrolysis, and after a final photolysis.

Chronoamperometry was carried out in the standard H-cell, electrode configuration, and lamp positioning described above for CV. The potential was held between –0.4 and –1.1 V, based on the location of the reduction wave observed by cyclic voltammetry. At each potential, two traces were obtained in the light and in that dark with electrode polishing between each experiment. The ratio of the current in the light (i_{cat}) to the current in the dark (i_{diff}) was fit to the following equation:

$$i_{cat}/i_{diff} = (k_{obs}t)^{1/2}\left[\pi^{1/2}\mathrm{erf}((k_{obs}t)^{1/2}) + \frac{\exp(-k_{obs}t)}{(k_{obs}t)^{1/2}}\right]$$

where k_{obs} is the rate constant for the turnover-limiting chemical step and t is time.[42,76] The data was least-squares fit between 5 and 10 s using the Excel solver function. Though deviations from k_{cat} are suggestive of mechanistic complexity, the CA traces at low applied potentials are still indicative of catalysis.

A control reaction to test whether adsorbed species might be the true catalyst was performed as follows: a standard CA experiment was carried out at –0.9 V in phosphate buffer, followed by gently rinsing the carbon electrode with water and repeating the CA experiment in a fresh phosphate buffer solution containing no catalyst. When moved to a fresh electrolyte solution containing no catalyst, no current over background was observed in the CA experiment, and no current enhancement under photolysis was observed, suggesting that catalyst adsorption is not a factor in this system.

CHAPTER 3: FACILE SYNTHESIS OF (PENTAMETHYLCYCLOPENTADIENYL)-(2,2'-BIPYRIDINE)-IRIDIUM, ANALOGUES, AND REACTIONS WITH ELECTROPHILES

3.1 Introduction

We were motivated to arrive at an alternative synthesis of Cp*Ir(bpy) **1** because of our need to produce water-soluble metal hydride species The conjugate base of $[Cp^*Ir(bpy)(H)]^+$ (**1**H), **1** has previously been synthesized, though yields were poor. Ladwig and Kaim reduced [Cp*Ir(bpy)(Cl)][Cl] (**1**Cl) in dry THF with $[^nBu_4N][BH_4]$ at –20°C. Crystallization afforded 23% yield of Cp*Ir(bpy).[83] In our hands, successive crystallization was required to remove unreacted $[^nBu_4N][BH_4]$, resulting in much lower yields.

. Typically, hydride **1**H has been prepared by precipitation from water with PF_6^- or OTf^- leading to $[Cp^*Ir(bpy)(H)][PF_6]$ and [Cp*Ir(bpy)(H)][OTf], which were insoluble above 2 mM in water.[84] From our electrochemical studies in Chapter 2, we knew that the hydride was soluble in water when paired with an appropriate counterion and that, therefore, counterion selection was playing a critical role in solubility. We hypothesized that Cp*Ir(bpy) would be a useful synthetic intermediate: a water-soluble hydride could be produced by protonation with HCl to give [Cp*Ir(bpy)(H)][Cl] and reactions with other electrophiles could generate other Ir(III) complexes of interest.

3.2 Results and Discussion

***In situ* generation of Cp*Ir(bpy).** Determination of the hydricity of the parent complex $[Cp^*Ir(bpy)(H)]^+$ (**1**H) was targeted through the "potential−pK_a" thermodynamic cycle discussed in Chapter 1. This approach, however, was stymied by the water-insolubility of the conjugate base **1**, which precluded measuring acidity using a traditional bulk scale pK_a titration.

Electrochemical reduction allowed for the observation of base **1** generated *in situ*. Two electron reduction of [Cp*Ir(bpy)(Cl)][Cl] in 0.1 M pH 7 sodium phosphate (NaP_i) initially produces **1**, followed by protonation to form the hydride **1**H.[85] As the pH is increased by addition of NaOH, less protonation of **1** occurs and the oxidation wave for **1** grows in at –0.26 V. At high pH, the current of the oxidation is constant with increasing pH. By assuming that the current at high pH corresponded to complete production of **1** with no protonation of the hydride **1**H, the relative concentrations of **1** and **1**H at each pH were determined. These concentrations led to an estimate of pK_a = 10.6 (Figure 3.1). This estimate, however, varied with scan rate indicating that protonation is not fast enough for the solution near the electrode to achieve equilibrium on the electrochemical time scale. Additionally, the shape of the oxidation and its linear dependence (at high pH) on scan rate are indicative of product adsorption onto the electrode, which prevents accurate determination of $E_{1/2}$, as well.

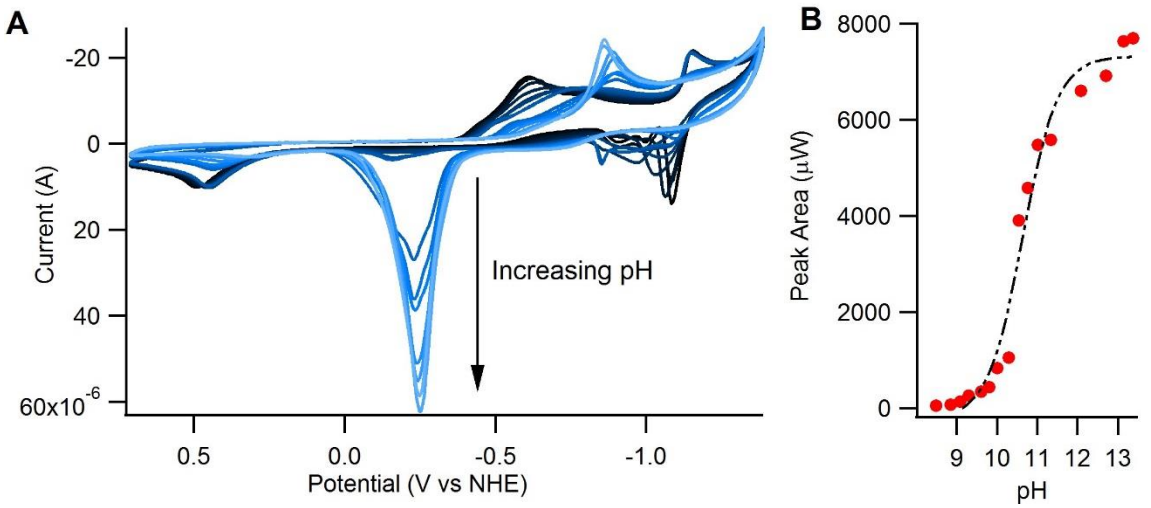

Figure 3.1. A) Cyclic voltammetry of [Cp*Ir(bpy)(Cl)][Cl] in 0.1 M pH 7 NaP_i titrated with solutions of NaOH showing the growth of the oxidation of Cp*Ir(bpy) with increasing pH. B) Fit (dashed black) of oxidation peak area (red dots) to the Henderson-Hasselbalch equation, suggesting a pK_a of 10.6 for $[Cp^*Ir(bpy)(H)]^+$.

Synthesis and Structure of Cp*Ir(bpy) and Analogues. The insolubility of **1** proved to be a major obstacle to detemining the pK_a of **1**H and oxidation potential of **1**, but this insolubility became the inspiration for a facile synthesis of Cp*Ir(bpy), with the goal of producing **1** cleanly from precipitation from water. The chloride salt of **1**Cl was reduced by excess $NaBH_4$ in 1 M NaOH and allowed to stir for 3 h, resulting in precipitation of purple **1** in 98% yield (Scheme 3.1, ^{1}H NMR spectrum: Figure 3.3). The solids were washed with water to remove residual salts and extracted into benzene.

Scheme 3.1. Synthesis of Cp*Ir(bpy) by precipitation from basic water.

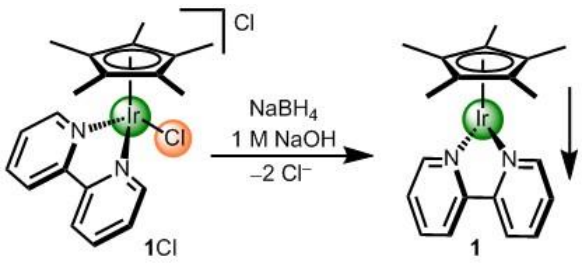

Though previously synthesized, **1** had not been crystallographically characterized. A large purple block crystal suitable for X-ray diffraction was produced by slow evaporation of a solution of **1** in THF (Figure 3.2). Crystallographic data and refinement details are given in Table 3.1. The report of this crystal structure completes the Group 9 Cp*M(bpy) series (M = Co, Rh, Ir).[86–88] Like its lighter metal congeners, **1** adopts a near-perpendicular orientation of the Cp* and bpy planes (84.68°). The C–C bond connecting the pyridine rings of bpy (C5–C6 1.403(5) Å) shows the characteristic contraction observed in these electron-rich species, attributed to electron delocalization into bpy resulting in partial double bond character in the interpyridyl bond. In free bipyridine, this distance is 1.49 Å and contracts to 1.43 Å in $bpy^{\bullet-}$ and to 1.39 Å for bpy^{2-}.[89] In the Ir complex **1**, however, this bond is shorter than in either of its lighter brethren (M = Co, 1.419 Å[86]; M = Rh, 1.423 Å[87,88]), suggesting more electron density resides on bpy when M = Ir.

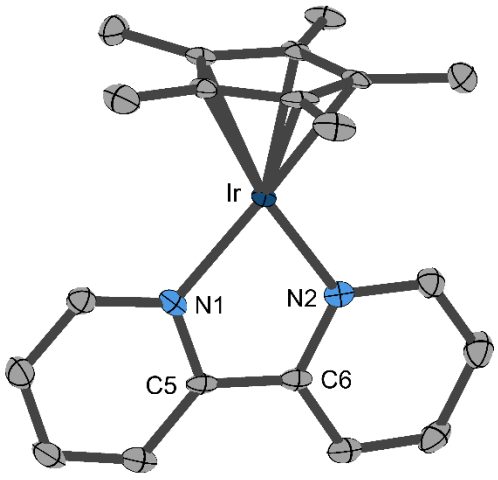

Figure 3.2. Structural representation of **1** with ellipsoids drawn at the 50% probability level. Hydrogen atoms omitted. Selected distance (Å): C5-C6 1.403(5).

Table 3.1. Crystal data and structure refinement for 1.

Empirical formula	$C_{20}H_{23}IrN_2$
Formula weight	483.60
Temperature/K	100.15
Space group	$P2_1/n$
a/Å	9.1987(2)
b/Å	9.2369(2)
c/Å	20.1231(5)
Volume/Å^3	1691.67(7)
Z	4
μ/mm^{-1}	15.265
Crystal size/mm^3	0.19 × 0.179 × 0.106
Radiation	CuKα (λ = 1.54178)
Reflections collected	30282
Independent reflections	3218 [R_{int} = 0.0321, R_{sigma} = 0.0147]
Goodness-of-fit on F^2	1.211
Final R indexes [I>=2σ (I)]	R_1 = 0.0232, wR_2 = 0.0585
Final R indexes [all data]	R_1 = 0.0238, wR_2 = 0.0589

Precipitation of reduced half-sandwich species from water following the standard conditions of Scheme 3.1 proved to be quite general: several Ir, Ru, and Rh complexes were made this way (Table 3.2). In addition to Ir(I) complex **1**, three of these species—(cymene)Ru(bpy), (C_6Me_6)Ru(bpy), and Cp*Rh(bpy)—have been previously reported with reductions performed in rigorously dry organic solvents with Na, K, or TlO_2CH. In some cases, the current synthesis represents a marked improvement in yield, but in all cases, the synthetic conditions in this work with $NaBH_4$, NaOH, and H_2O are milder than those previously reported.

Table 3.2. Complexes synthesized by precipitation from water and literature precedent.

Complex	Lit. Yield	This work	Modifications
Cp*Ir(bpy)	23%[83]	quantitative	
Cp*Ir(bpy-Me)	Not reported	quantitative	5 M NaOH
Cp*Ir(bpy-CO_2Me)	Not reported	47%	pH 7 NaP_i, NaO_2CH
(cymene)Ru(bpy)	60–80%[90]	quantitative	
(C_6Me_6)Ru(bpy)	60–80%[90]	quantitative	
Cp*Rh(bpy)	15%[88], 87%[87]	88%	

Two complexes, Cp*Ir(bpy-Me) and Cp*Ir(bpy-CO_2Me) (bpy-X is 4,4'-X-2,2'-bipyridine), were prepared that have not been previously reported. This required slight modifications of the standard conditions. For Cp*Ir(bpy-Me), a 5 M NaOH solution was used to ensure full deprotonation. Indeed, Cp*Ir(bpy-OMe) could not be prepared this way. Donation from the –OMe substituents increases the electron density at Ir and, therefore, increases the pKa of $[Cp^*Ir(bpy\text{-}OMe)(H)]^+$. No conditions tested were sufficient to deprotonate the hydride to lead to precipitation. $[Cp^*Ir(bpy\text{-}COOMe)(H)]^+$, by contrast, is quite acidic and can easily be deprotonated ($pK_a \sim 5$, by electrochemical titration). Saponification of the esters to form $[Cp^*Ir(bpy\text{-}COO)]^{2-}$, however, occurs readily under basic conditions, so a neutral solution was used in an attempt to limit the side reaction. Preliminary results indicate that CpIr(bpy) (Cp is cyclopentadienyl) can also be formed following this method.

Scheme 3.2. Synthesis of [Cp*Ir(bpy)(H)][Cl] by precipitation from ether.

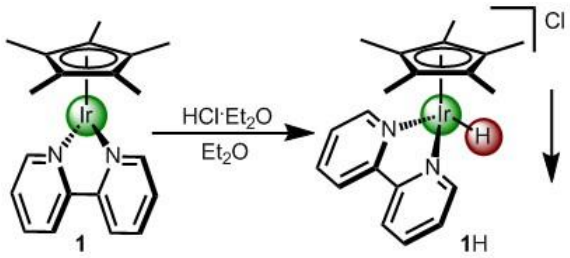

Functionalization via Electrophilic Attack. These Ir(I), Rh(I), and Ru(0) species are electron rich and react readily with electrophiles. Grätzel noted that Cp*Rh(bpy) formed adducts with Lewis acids and oxidatively added electrophiles.[91] Reactions with electrophiles allowed quick access to a variety of oxidized species. Metal-hydrides, for example, were readily obtained by protonation with HCl. Dropwise addition of 40 mM HCl·Et_2O to a stirring solution of **1** in Et_2O prompted precipitation of the golden yellow chloride salt of hydride **1**H (Scheme 3.2). The solvent was removed *in vacuo* giving [**1**H][Cl]. Small amounts (<10%) of overprotonation products were observed, giving **1**Cl impurities. For use in water, extraction and filtration of solids into water removed any unreacted Ir(I) complex **1**. For use in other solvents, **1** could be removed by filtration of the solids and washing with ether. The hydride peak (δ –11.54) can be observed in pD 7 0.1 M NaP_i, but we have observed this hydride NMR signal moves with changing concentrations of **1**H.

Table 3.3. ^{1}H NMR Shifts of Metal-Hydrides in pD 7 0.1 M NaP_i

Complex	δ
[Cp*Ir(bpy)(H)][Cl]	–11.54
[Cp*Ir(bpy-Me)(H)][Cl]	–11.63
[Cp*Ir(bpy-CO_2Me)(H)][Cl]	–12.28
[(cymene)Ru(bpy)(H)][Cl]	–6.32
[(C_6Me_6)Ru(bpy)(H)][Cl]	–7.48

HCl·Et_2O protonation in Et_2O permitted access to [Cp*Ir(bpy-Me)(H)][Cl], [Cp*Ir(bpy-CO_2Me)(H)][Cl], [(cymene)Ru(bpy)(H)][Cl], and [(C_6Me_6)Ru(bpy)(H)][Cl] (Table 3.3). [(C_6Me_6)Ru(bpy)(H)][OTf] has been previously isolated,[92,93] and [(cymene)Ru(bpy)(H)][OTf] has been observed in a mixture.[94] For all of the Ir(I) and Ru(0) species formed, this protonation procedure resulted in the formation of the metal-hydride product.

Scheme 3.3. Reactions of Cp*Ir(bpy) with electrophiles.

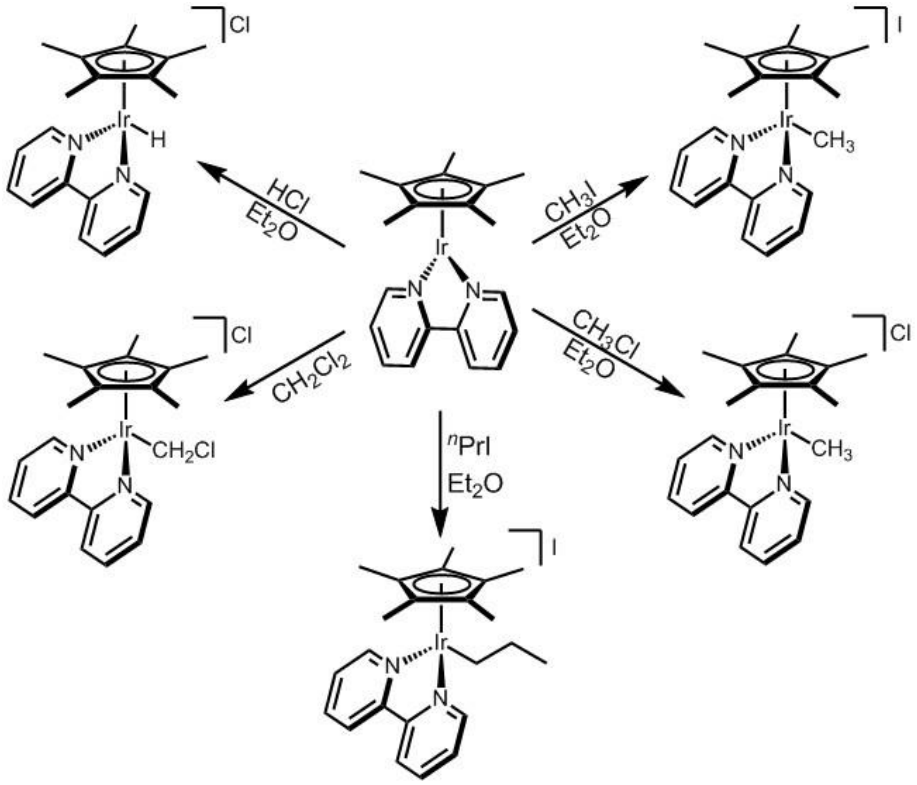

Electrophiles other than protic acids can also be used in this reaction. Scheme 3.3 depicts the reactions of Cp*Ir(bpy) with electrophiles that have been carried out. Methyl iodide readily methylates Cp*Ir(bpy) ethereal solutions to form [Cp*Ir(bpy)(CH_3)][I]. Stripping the solvent gives the air-stable product in 95% yield. While the reaction with acid is instantaneous, the methyl species precipitates over the course of minutes. Chloromethane was a competent electrophile for methylation of Cp*Ir(bpy): allowing a solution of **1** to stir under an atmosphere of CH_3Cl produced [Cp*Ir(bpy)(CH_3)][Cl] as a yellow solid. Due to the gaseous nature of chloromethane, the reaction proceeded considerably more slowly than the methyl iodide reaction, taking hours, rather than minutes. Moving from methyl iodide to primary alkyl halides also increases reaction times: when Cp*Ir(bpy) and ^{n}PrI were allowed

to mix in Et_2O, goldenrod [Cp*Ir(bpy)(^{n}Pr)][I] precipitated over the course of hours. Cp*Ir(bpy) will oxidatively add CH_2Cl_2, and dissolving **1** in CH_2Cl_2 will result in the solution slowly changing from purple to brown to yellow as [Cp*Ir(bpy)(CH_2Cl)][Cl] is formed in solution

Reactions of Cp*Rh(bpy) present a contrast to its heavier congener Cp*Ir(bpy). Some of the reactions proceed analogously: stirring Cp*Rh(bpy) with CH_3I in Et_2O results in precipitation of [Cp*Rh(bpy)(CH_3)][I]. Grätzel observed oxidative addition of CH_2Cl_2 by Cp*Rh(bpy) to give [Cp*Rh(bpy)(CH_2Cl)][Cl].[91] Protonation, however, proceeds quite differently: addition of 40 mM $HCl{\cdot}Et_2O$ to a stirring solution of Cp*Rh(bpy) in Et_2O results in a homogenous red solution. While $[Cp^*Rh(bpy)(H)]^+$ is initially formed, it is not stable and rapidly reacts (Chapter 5).

3.3 Conclusions

The facile synthesis of Cp*Ir(bpy) as well as other Ir(I), Rh(I) and, Ru(0) species permitted quick access to a variety of Ir(III), Rh(III), and Ru(II) species. These synthetic routes lead to hydrides that were water-soluble, critical for our aqueous hydricity investigation in Chapter 4. The generality of the synthetic techniques permitted a large collection of hydricities to be readily measured without extensive synthesis. The predictability of the protonation permitted the unusual characteristics of the protonation of Cp*Rh(bpy) to be immediately recognized, leading to the investigation into Cp* non-innocence in Chapter 5. The ease of preparation of $[Cp^*Ir(bpy)(CH_3)]^+$ permitted investigations into its photochemistry in analogy to $[Cp^*Ir(bpy)(H)]^+$, as seen in Chapter 6.

3.4 Experimental Section

General Considerations. Procedures were carried out under nitrogen except where noted. All solutions containing metal hydride species were protected from ambient light during preparation to prevent excited state reactions. All reagents were commercially available and used without further purification. Organic solvents were dried and degassed with argon using a Pure Process Technology solvent system. Deuterated solvents were purchased from Cambridge Isotope Laboratories, Inc and degassed with three freeze-pump-thaw cycles before storing over sieves in a N_2 glovebox. UV−vis spectra were obtained using an Ocean Optics USB2000+ spectrometer with a DTMINI-2GS deuterium/tungsten halogen light source controlled by OceanView software. NMR spectra were obtained on 400, 500, or 600 MHz spectrometers. ^{1}H and ^{13}C NMR spectra were referenced to the residual solvent signals or a dioxane internal standard for D_2O. Spectra were processed using the MestReNova software suite from Mestrelab Research S. L. Single-crystal X-ray diffraction data were collected on a Bruker APEX-II CCD diffractometer at 100 K with Cu Kα radiation (λ = 1.54175 Å). Using Olex2,[95] the structures were solved with the olex2.solve[96] structure solution program using Charge Flipping and refined with the XL[97] refinement program using least squares minimization.

Synthesis. The complexes [Cp*Ir(bpy)(Cl)][Cl] (**1**Cl), [(cymene)Ru(bpy)(Cl)][Cl], [(C_6Me_6)Ru(bpy)(Cl)][Cl], [Cp*Ir(bpy-Me)(Cl)][Cl], and [Cp*Ir(bpy-OMe)(Cl)][Cl] were prepared following the method of Dadci et al., with final precipitation from MeOH/ether.[66] [Cp*Ir$(Cl)_2]_2$,[80] and [Cp*Ir(bpy)(H)][OTf][84] were prepared following literature procedures.

*Cp*Ir(bpy) (**1**).* In a nitrogen filled glovebox, [Cp*Ir(bpy)(Cl)][Cl] (16 mg, 0.028 mmol) and excess $NaBH_4$ (8.5 mg, 0.22 mmol) were allowed to stir in 2 mL of 1 M NaOH.

Dark purple solids quickly formed. After letting the solution stir for four hours, the solid was filtered off, washed 3× with water, collected in benzene, and evaporated to dryness, yielding 13 mg of **1** (0.21mmol, 98 % yield). The ^{1}H NMR spectrum of **1** prepared in this way matched previously reported data (Figure 3.3).[83]

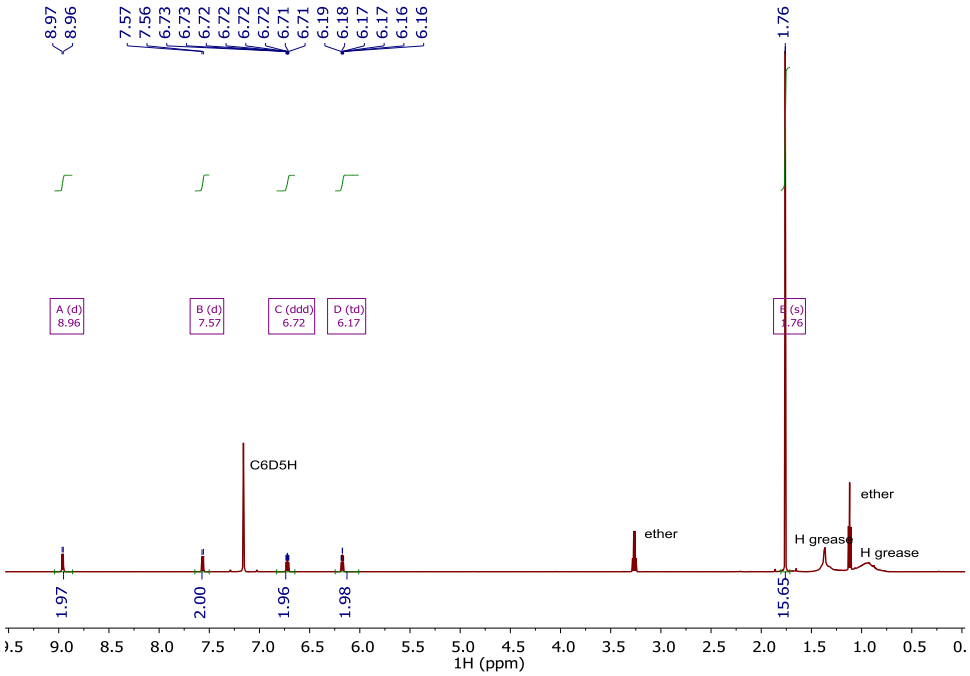

Figure 3.3. ^{1}H NMR spectrum of Cp*Ir(bpy) (**1**) in C_6D_6.

*[Cp*Ir(bpy)(H)][Cl] (**1**H).* To a stirring solution of **1** (13.3 mg, 0.028 mmol) in ether, a dilute solution of HCl·Et_2O (40 mM) was added dropwise until a change from a dark purple solution to bright yellow solids was observed. Typically, 1-1.5 eq of HCl were added with the excess acid immediately pumped off after completion of the addition. Samples of hydride prepared in this way typically contained small amounts (<5%) of [Cp*Ir(bpy)(Cl)][Cl] (formed by protonation of hydride releasing H_2), and the ^{1}H NMR spectrum (Figure 3.4) is consistent with previously reported $[Cp^*Ir(bpy)(H)]^+$.[85]

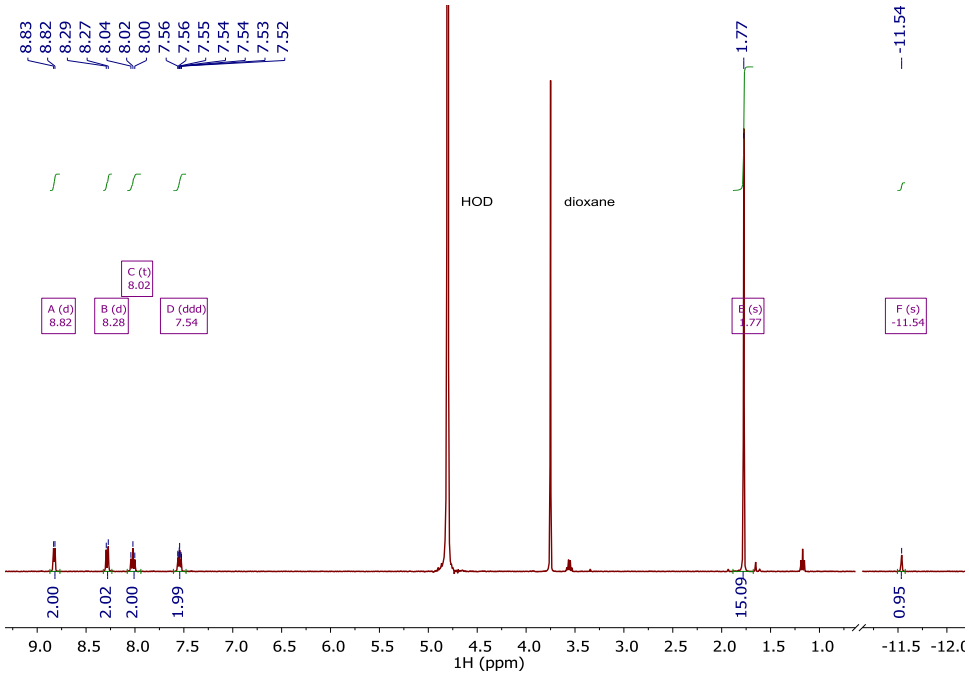

Figure 3.4. ^{1}H NMR spectrum of [Cp*Ir(bpy)(H)][Cl] (**1**H) in 0.1 M pD 7 NaP$_i$ (referenced to dioxane).

*(cymene)Ru(bpy) (**4**).* Deep purple **4** was prepared in quantitative yield from the chloride salt of **4**Cl, according to the procedure used in the synthesis of **1**. The ^{1}H NMR spectrum matched the previously reported data (Figure 3.5).[90]

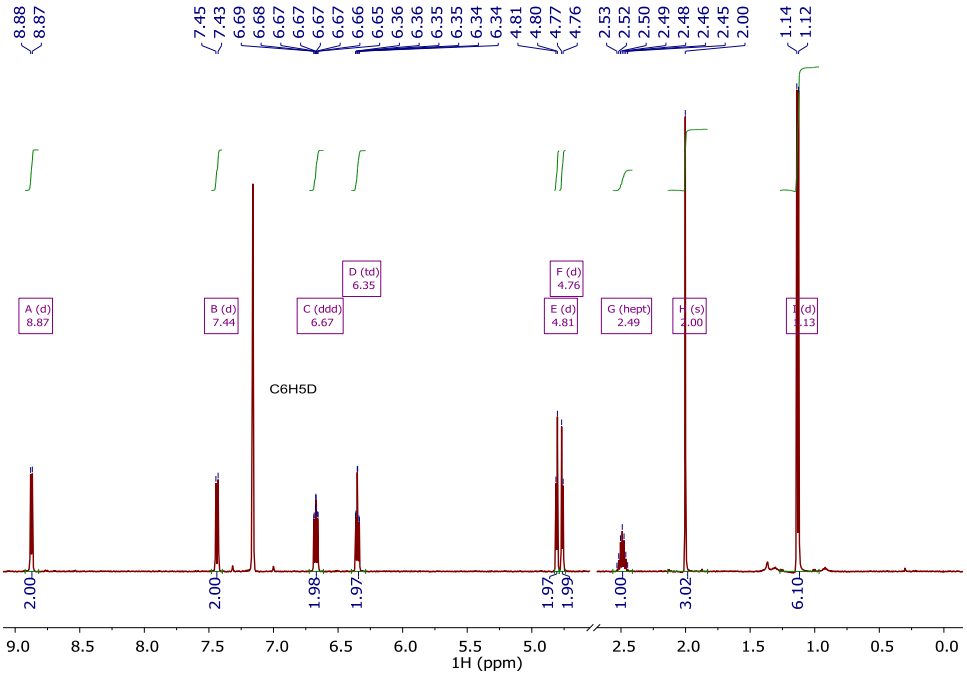

Figure 3.5. ^{1}H NMR spectrum of (cymene)Ru(bpy) (**4**) in C_6D_6.

*[(cymene)Ru(bpy)(H)][Cl] (**4**H).* The chloride salt of **4**H was prepared from **4**, according to the procedure used in the synthesis of the chloride salt of **1**H. ^{1}H NMR (600 MHz, D_2O + dioxane, Figure 3.6) δ 8.78 (d, *J* = 4.1 Hz, 2H), 8.09 (d, *J* = 8.2 Hz, 2H), 7.87 (t, *J* = 7.8 Hz, 2H), 7.32 (dd, *J* = 7.3, 5.8 Hz, 2H), 5.56 (d, *J* = 6.0 Hz, 2H), 5.36 (d, *J* = 6.0 Hz, 2H), 2.53 (sept, *J* = 7.1 Hz, 1H), 2.10 (s, 3H), 0.99 (d, *J* = 6.9 Hz, 6H), -6.32 (s, 1H).

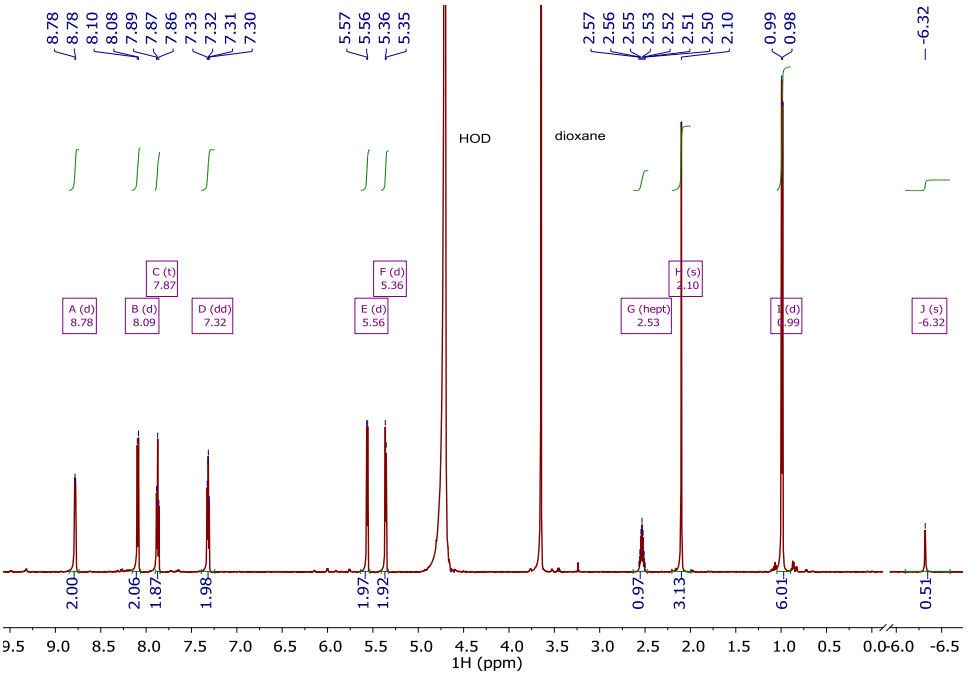

Figure 3.6. ^{1}H NMR spectrum of [(cymene)Ru(bpy)(H)][Cl] (**4**H) in 0.1 M pD 7 NaP_i (referenced to dioxane). The hydride signal at -6.32 moderately underintegrates because of scrambling with D_2O.

*(C_6Me_6)Ru(bpy) (**5**).* Deep purple **5** was prepared in quantitative yield from the chloride salt of **5**Cl, according to the procedure used in the synthesis of **1**. The ^{1}H NMR spectrum matched the previously reported data (Figure 3.7).[90]

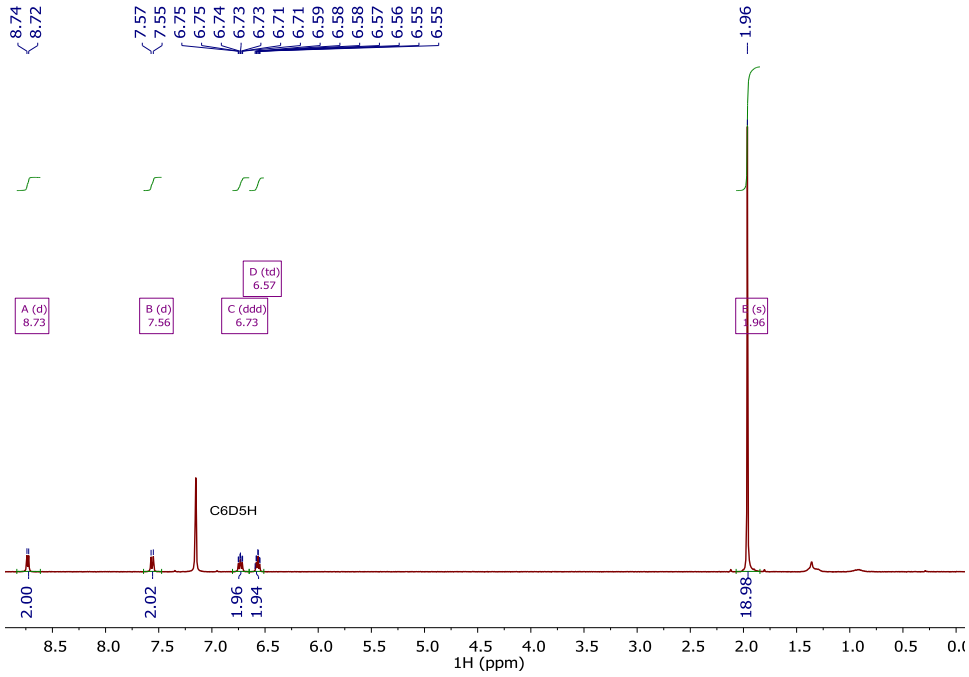

Figure 3.7. ^{1}H NMR spectrum of (C_6Me_6)Ru(bpy) (**5**) in C_6D_6.

*[(C_6Me_6)Ru(bpy)(H)][Cl] (**5**H).*The chloride salt of **5**H was prepared from **5**, according to the procedure used in the synthesis of the chloride salt of **1**H. The ^{1}H NMR spectrum is consistent with the reported spectrum for the triflate salt of **5**H in water (Figure 3.8).[92]

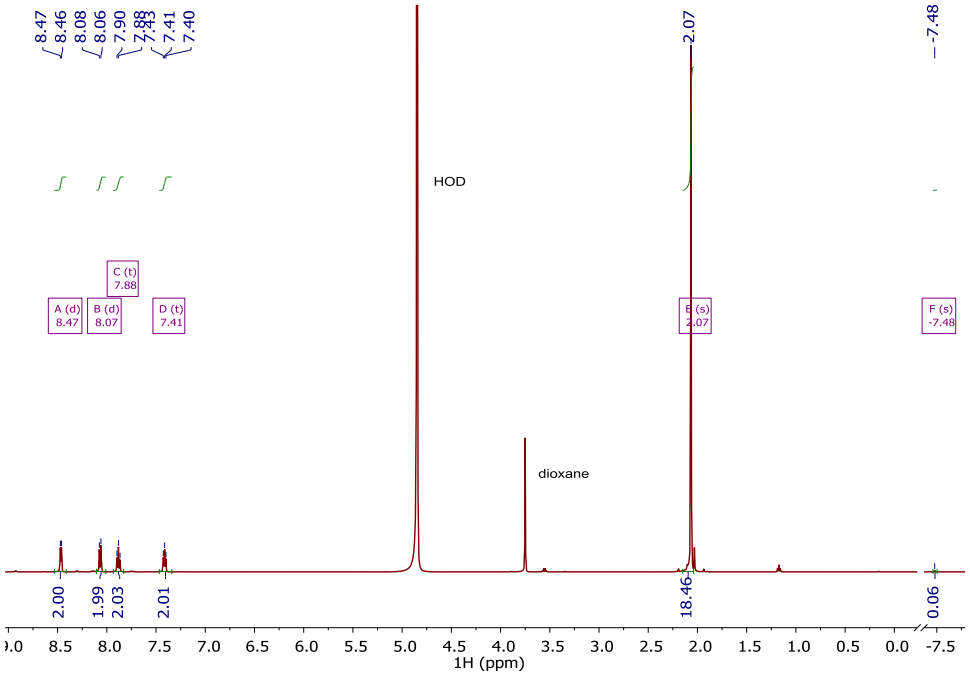

Figure 3.8. ^{1}H NMR spectrum of [(C_6Me_6)Ru(bpy)(H)][Cl] (**5**H) in 0.1 M pD 7 NaP_i (referenced to dioxane). The hydride signal at -7.48 dramatically underintegrates because of scrambling with D_2O.

*Cp*Ir(bpy-Me) (**6**).* In a nitrogen filled glovebox, [Cp*Ir(bpy-Me)(Cl)][Cl] (5.8 mg, 0.010 mmol) and excess $NaBH_4$ (5.1 mg, 0.135 mmol) were allowed to stir in 2 mL of 5 M NaOH, and a dark violet solid quickly forms. After letting stir for four hours, the solid was extracted into C_6H_6, dried over $MgSO_4$, and evaporated to dryness, yielding **6** in quantitative yield. ^{1}H NMR (600 MHz, C_6D_6, Figure 3.9) δ 8.91 (d, J = 6.8 Hz, 2H), 7.44 (s, 2H), 6.06 (dd, J = 6.8, 2.1 Hz, 2H), 2.02 (s, 6H), 1.82 (s, 15H). ^{13}C NMR (151 MHz, C_6D_6, Figure 3.10) δ 148.20, 141.06, 127.59, 122.82, 117.92, 83.32, 21.44, 10.24. $\lambda_{abs,max}$ (C_6H_6, Figure 3.11) = 499, 641, 687 nm.

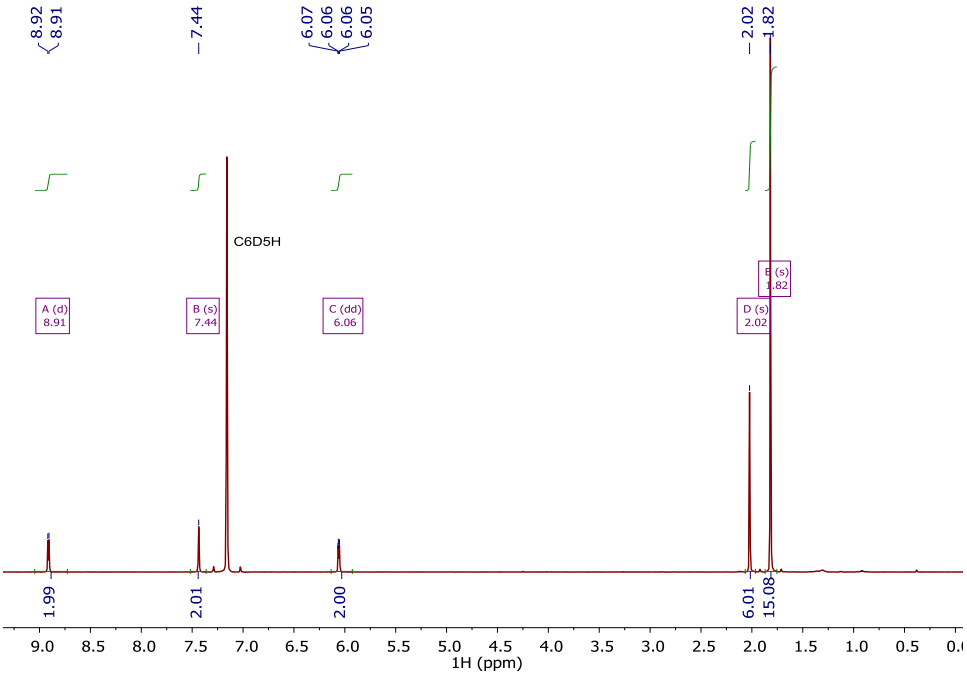

Figure 3.9. ^{1}H NMR spectrum of Cp*Ir(bpy-Me) (**6**) in C_6D_6.

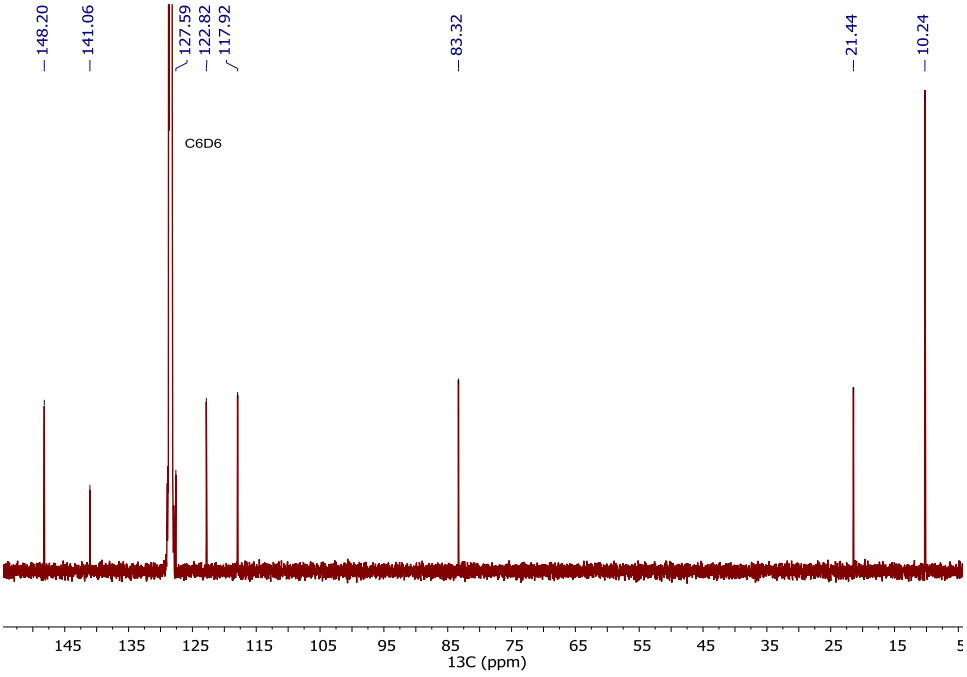

Figure 3.10. ^{13}C{^{1}H} NMR spectrum of Cp*Ir(bpy-Me) (**6**) in C_6D_6.

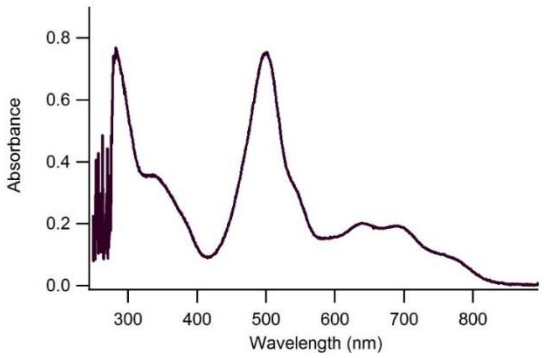

Figure 3.11. UV-Vis spectrum of Cp*Ir(bpy-Me) (**6**) in C_6H_6.

*[Cp*Ir(bpy-Me)(H)][Cl] (**6**H).* The bright yellow chloride salt of **6**H was prepared from **6**, according to the procedure used in the synthesis of the chloride salt of **1**H. ^{1}H NMR (600 MHz, D_2O + dioxane, Figure 3.12) δ 8.42 (d, J = 5.9 Hz, 2H), 7.80 (s, 2H), 7.18 (d, J = 5.9 Hz, 2H), 2.38 (s, 6H), 1.61 (s, 15H), -11.63 (s, 1H). ^{13}C NMR (151 MHz, D_2O + dioxane, Figure 3.13) δ 155.51, 151.61, 150.78, 128.53, 124.12, 90.75, 20.85, 8.97. $\lambda_{abs,max}$ (pH 7 0.1 M NaP_i, Figure 3.14) = 394 nm (2900 $M^{-1}\cdot cm^{-1}$).

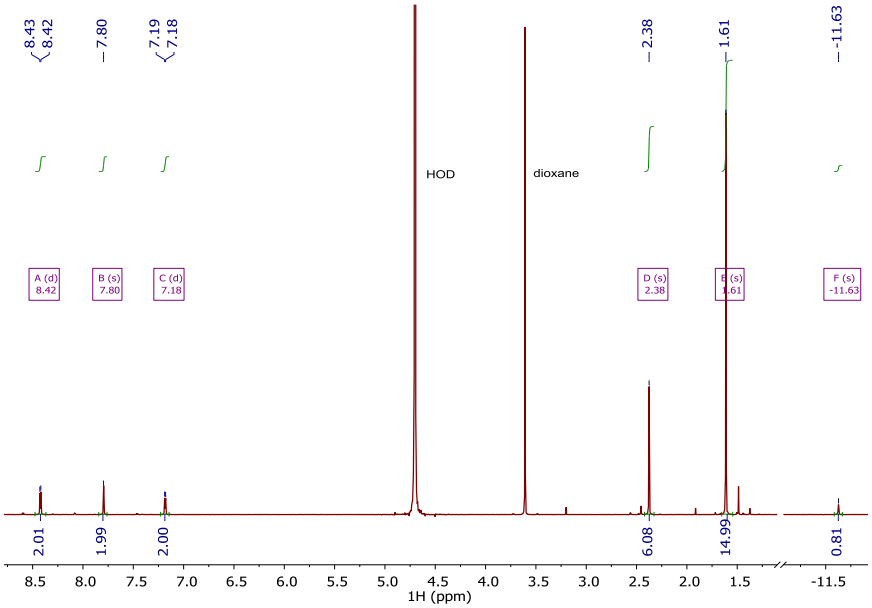

Figure 3.12. ^{1}H NMR spectrum [Cp*Ir(bpy-Me)(H)][Cl] (**6**H) in 0.1 M pD 7 NaP_i (referenced to dioxane). The hydride signal at -7.48 moderately underintegrates because of scrambling with D_2O.

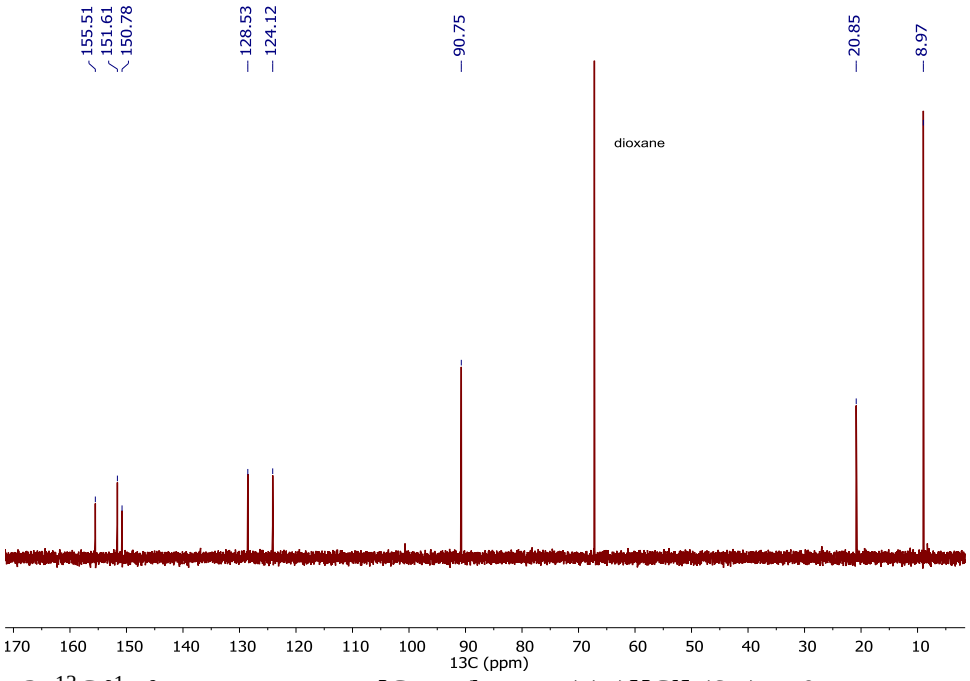

Figure 3.13. $^{13}C\{^{1}H\}$ NMR spectrum [Cp*Ir(bpy-Me)(H)][Cl] (**6**H) in 0.1 M pD 7 NaP_i (referenced to dioxane).

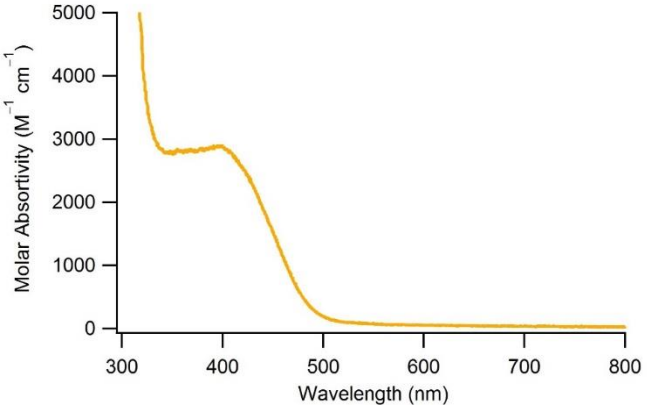

Figure 3.14. UV-Vis spectrum [Cp*Ir(bpy-Me)(H)][Cl] (**6**H) in 0.1 M pH 7 NaP_i.

*Cp*Ir(bpy-COOMe) (**8**).* In a nitrogen filled glovebox, 8.1 mg (0.012 mmol) [Cp*Ir(bpy-COOMe)(Cl)][Cl] and 4.7 g (0.069 mmol) NaO_2CH were stirred in 2 mL pH 7 0.1 M NaP_i. While stirring for four hours, a royal purple solid precipitated from solution. The solution was filtered, and the solids were washed 3× with water, collected by dissolving in benzene, and evaporating under vacuum to yield **8** (3.4 mg, 47 % yield). ^{1}H NMR (600 MHz,

C_6D_6, Figure 3.15) δ 8.78 (d, *J* = 7.0 Hz, 1H), 8.69 (d, *J* = 2.1 Hz, 1H), 7.20 (dd, *J* = 7.0, 2.0 Hz, 1H), 3.52 (s, 2H), 1.55 (s, 6H). ^{13}C NMR (151 MHz, C_6D_6, Figure 3.16) δ 166.76, 147.22, 142.02, 125.72, 115.04, 85.57, 51.76, 9.68. $\lambda_{abs,max}$ (C_6H_6, Figure 3.17) = 328, 389, 552 nm.

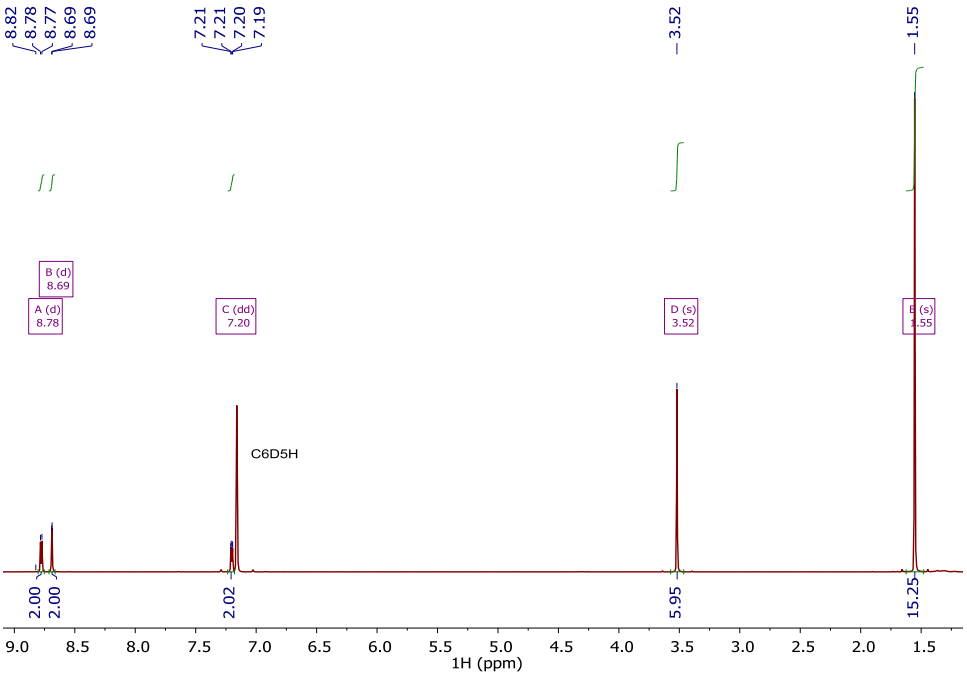

Figure 3.15. ^{1}H NMR spectrum of Cp*Ir(bpy-COOMe) (**8**) in C_6D_6.

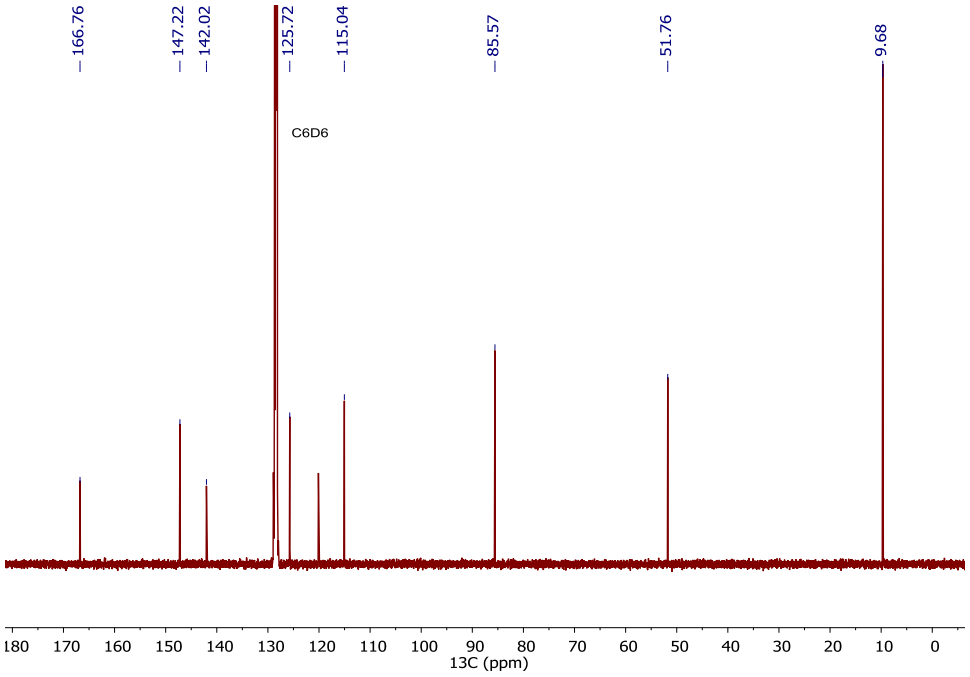

Figure 3.16. $^{13}C\{^{1}H\}$ NMR spectrum of Cp*Ir(bpy-COOMe) (**8**) in C_6D_6.

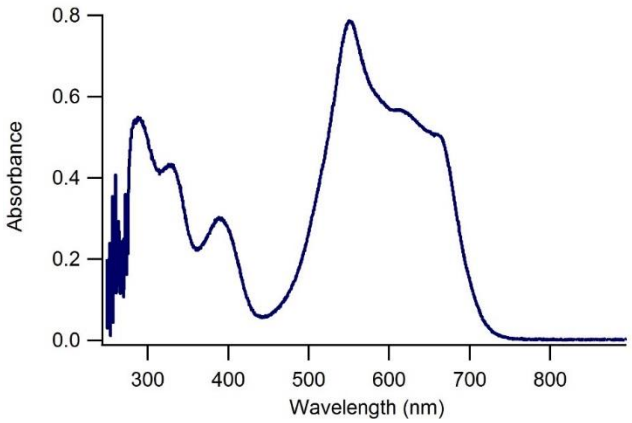

Figure 3.17. UV-Vis spectrum of Cp*Ir(bpy-COOMe) (**8**) in C_6H_6.

*[Cp*Ir(bpy-COOMe)(H)][Cl] (**8**H).* The scarlet chloride salt of **8**H was prepared from **8**, according to the procedure used in the synthesis of the chloride salt of **1**H. ^{1}H NMR (600 MHz, D_2O + dioxane, Figure 3.18) δ 8.89 (d, *J* = 5.9 Hz, 2H), 8.69 (s, 2H), 7.92 (d, *J* = 5.9 Hz, 2H), 4.10 (s, 6H), 1.80 (s, 15H),-12.28 (s, 1H). ^{13}C NMR (151 MHz, D_2O + dioxane, Figure 3.19) δ 165.82, 155.95, 153.00, 138.06, 126.69, 123.19, 92.70, 54.39, 8.94. $\lambda_{abs,max}$

(pH 3 0.1 M NaP$_i$, Figure 3.20) = 388 nm (4200 $M^{-1}\cdot cm^{-1}$), 451 nm (4300 $M^{-1}\cdot cm^{-1}$), 481 nm (4400 $M^{-1}\cdot cm^{-1}$).

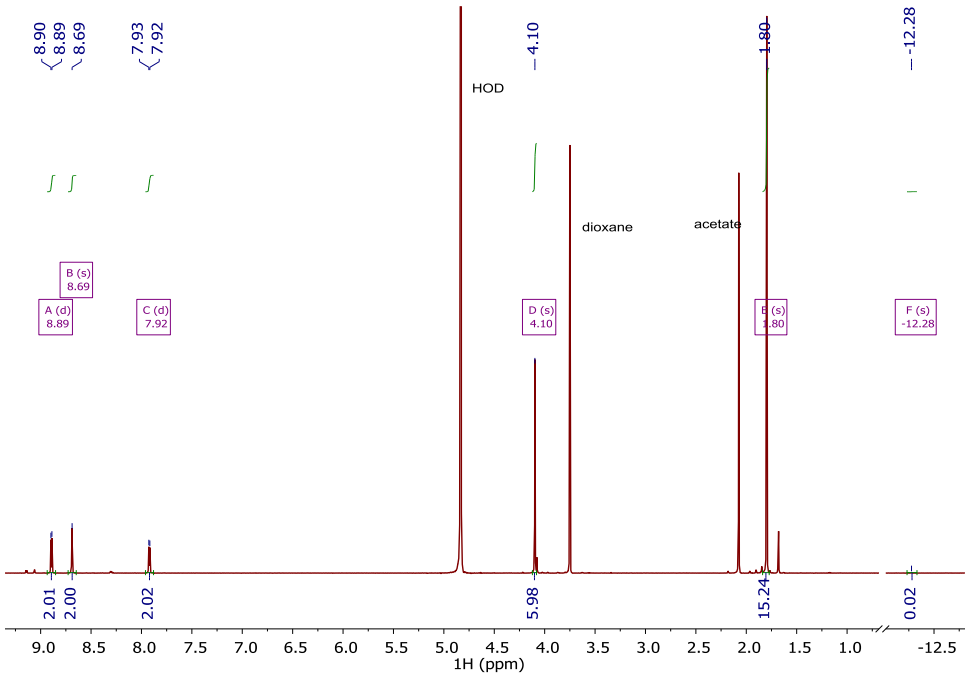

Figure 3.18. ^{1}H NMR spectrum of [Cp*Ir(bpy-COOMe)(H)][Cl] (**8**H) in 20 mM pD 4.3 NaOAc (referenced to dioxane). The hydride signal at -12.28 dramatically underintegrates because of scrambling with D_2O.

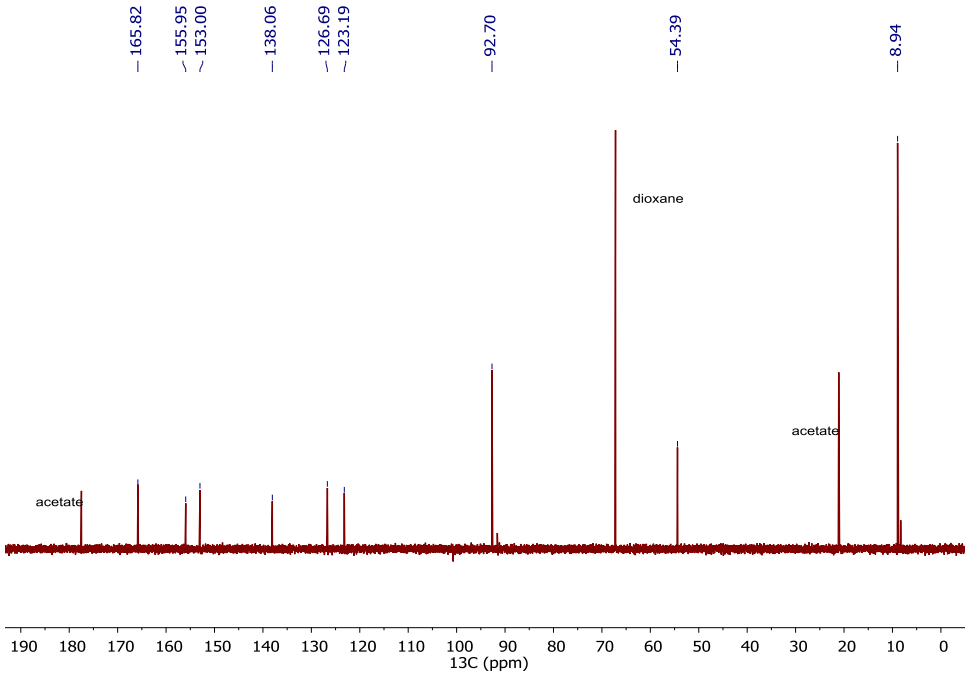

Figure 3.19. $^{13}C\{^{1}H\}$ NMR spectrum of [Cp*Ir(bpy-COOMe)(H)][Cl] (**8**H) in 20 mM pD 4.3 NaOAc (referenced to dioxane).

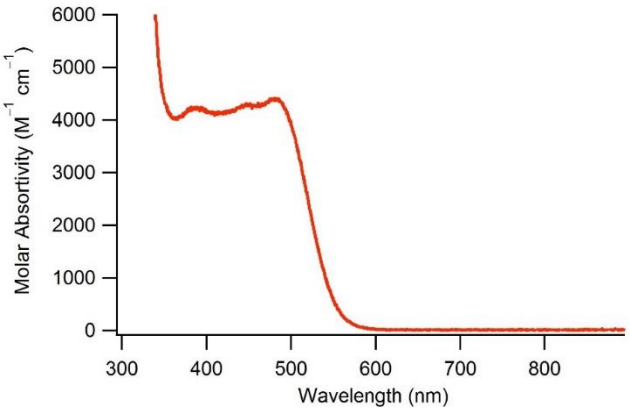

Figure 3.20. UV-Vis spectrum of [Cp*Ir(bpy-COOMe)(H)][Cl] (**8**H) in 0.1 M pH 3 NaP_i.

*Cp*Rh(bpy).* In a nitrogen filled glovebox, [Cp*Rh(bpy)(Cl)][Cl] (15.6 mg, 0.034 mmol) and excess $NaBH_4$ (10.3 mg, 0.272 mmol) were allowed to stir in 3 mL of 1 M NaOH. Dark purple solids quickly formed. After stirring for two hours, the solid was filtered off, washed 3× with water, collected in benzene, and evaporated to dryness, yielding Cp*Rh(bpy)

(11.6 mg, 88 % yield). The ^{1}H NMR spectrum of **1** prepared in this way matched previously reported data (Figure 3.22).[88]

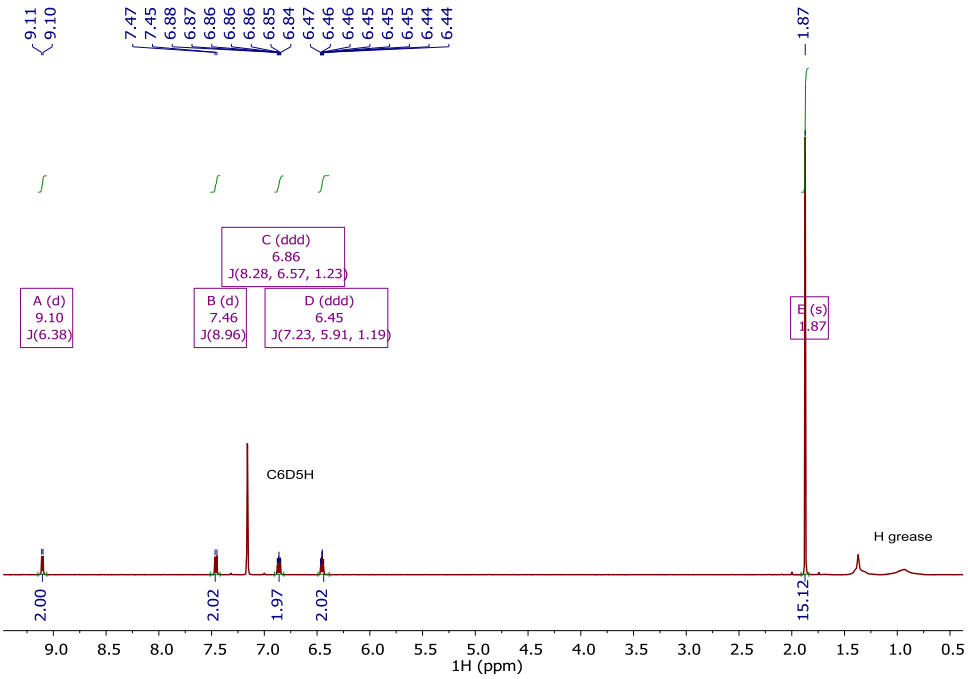

Figure 3.21. ^{1}H NMR spectrum of Cp*Rh(bpy) in C_6D_6.

*[Cp*Ir(bpy)(CH$_3$)][I]*. A slight excess of a 50 mM solution of CH_3I in Et_2O (1.2 mL, 0.060 mmol) was added dropwise to a stirring saturated purple solution of Cp*Ir(bpy) (28.0 mg, 0.058 mmol). The fluffy yellow solid precipitated over the course of several minutes. The solid was separate by filtration and washed with Et_2O resulting in 34.4 mg of air-stable [Cp*Ir(bpy)(CH_3)][I] (0.055 mmol, 95% yield). ^{1}H NMR (600 MHz, CD_3CN, Figure 3.22) δ 8.67 (ddd, J = 5.8, 1.5, 0.8 Hz, 2H), 8.43 (dt, J = 8.2, 1.1 Hz, 2H), 8.08 (ddd, J = 8.1, 7.5, 1.5 Hz, 2H), 7.60 (ddd, J = 7.4, 5.7, 1.4 Hz, 2H), 1.68 (s, 15H), -0.04 (s, 3H). ^{13}C NMR (151 MHz, CD_3CN, Figure 3.23) δ 156.01, 152.44, 139.08, 129.00, 125.32, 90.85, 8.70, -6.35. $\lambda_{abs,max}$ (CH_3CN) = 418 nm.

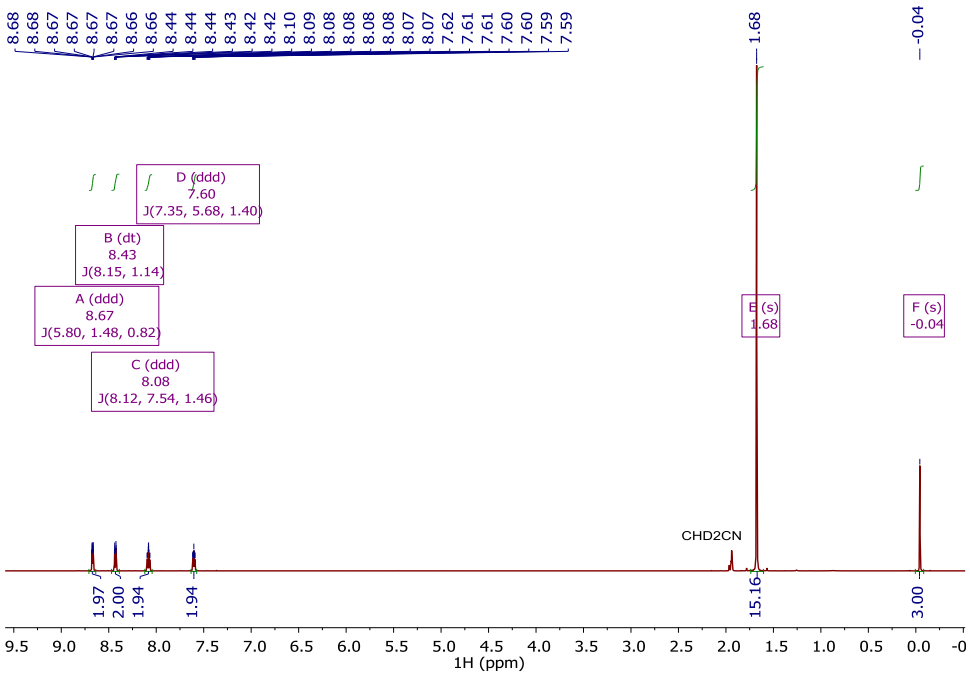

Figure 3.22. ^{1}H NMR spectrum of [Cp*Ir(bpy)(CH_3)][I] in CD_3CN.

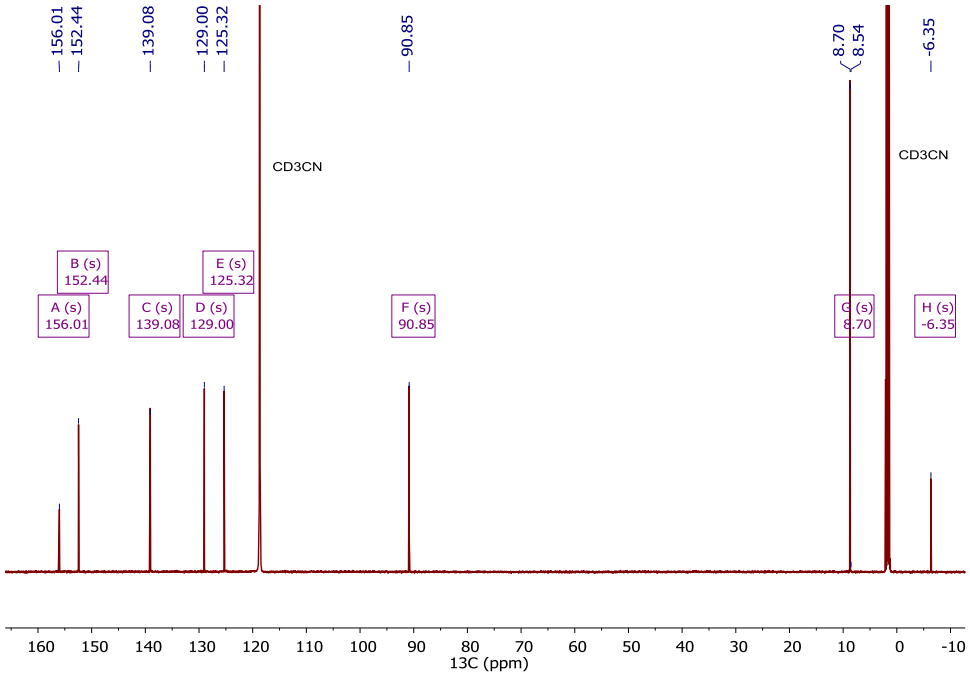

Figure 3.23. $^{13}C\{^{1}H\}$ NMR spectrum of [Cp*Ir(bpy)(CH_3)][I] in CD_3CN.

*[Cp*Rh(bpy)(CH$_3$)][I]*. A slight excess of a 50 mM solution of CH_3I in Et_2O was added dropwise to a stirring saturated purple solution of Cp*Rh(bpy) (4.5 mg). The fluffy yellow solid precipitated over the course of five minutes. The solid was separate by filtration and washed with Et_2O resulting [Cp*Rh(bpy)(CH_3)][I]. ^{1}H NMR (600 MHz, CD_3CN, Figure 3.24) δ 8.57 (ddt, J = 5.7, 1.6, 0.8 Hz, 2H), 8.43 (dt, J = 8.2, 1.0 Hz, 2H), 8.13 (td, J = 7.8, 1.5 Hz, 2H), 7.67 (ddd, J = 7.3, 5.5, 1.4 Hz, 2H), 1.64 (s, 15H), 0.18 (d, J = 2.4 Hz, 3H). ^{13}C NMR (151 MHz, CD_3CN, Figure 3.25) δ 153.44, 151.72, 138.40, 127.21, 123.62, 96.03 (d, J = 6.26 Hz), 7.67, 6.78 (d, J = 24.24 Hz)

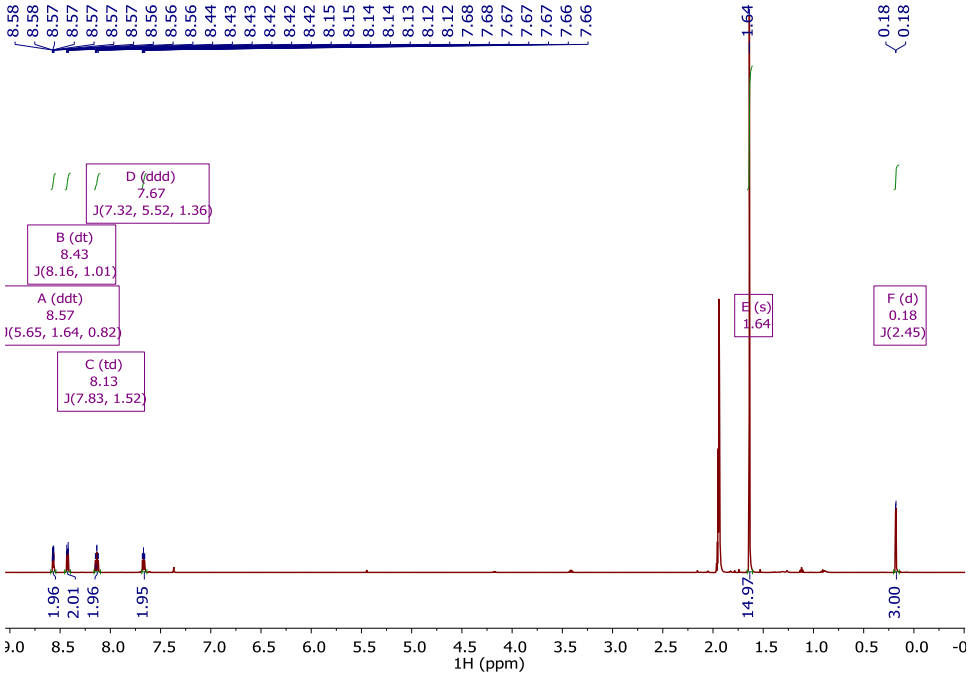

Figure 3.24. ^{1}H NMR spectrum of [Cp*Rh(bpy)(Me)][I] in CD_3CN.

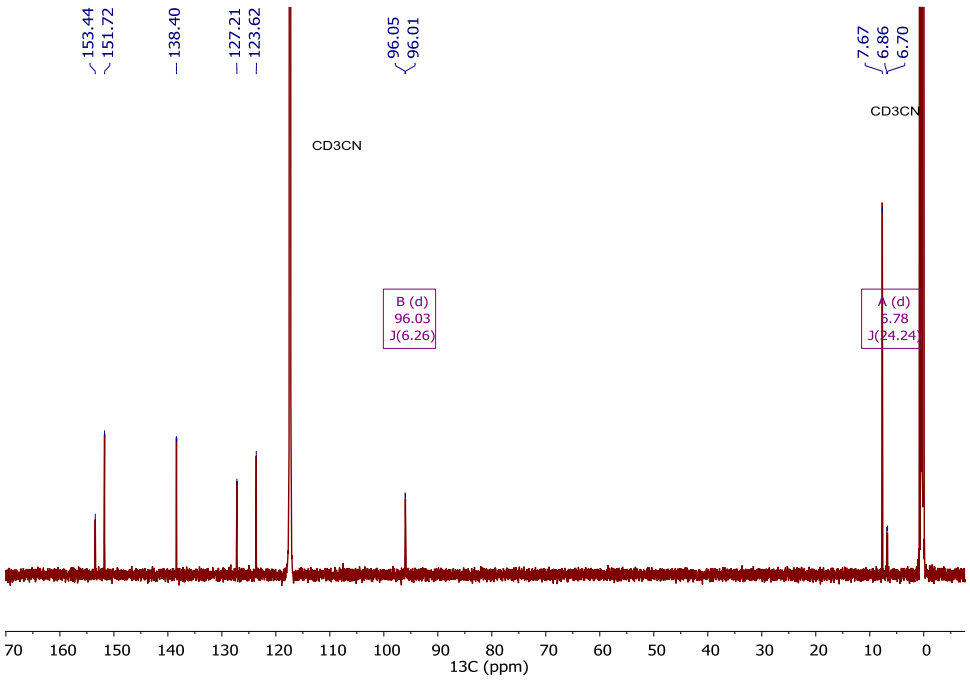

Figure 3.25. $^{13}C\{^{1}H\}$ NMR spectrum of [Cp*Rh(bpy)(CH_3)][I] in CD_3CN.

*[Cp*Ir(bpy)(CH_3)][Cl]*. A purple solution of Cp*Ir(bpy) was allowed to stir in the dark under a headspace of CH_3Cl. Over the course of several hours, a yellow precipitate formed. The solvent was dried *in vacuo* yielding [Cp*Ir(bpy)(CH_3)][Cl] in 95% purity. ^{1}H NMR (500 MHz, CD_3CN, Figure 3.26) δ 8.67 (d, J = 4.9 Hz, 2H), 8.48 (d, J = 8.3 Hz, 2H), 8.08 (t, J = 8.0 Hz, 2H), 7.61 (t, J = 6.3 Hz, 2H), 1.68 (s, 15H), -0.04 (s, 3H).

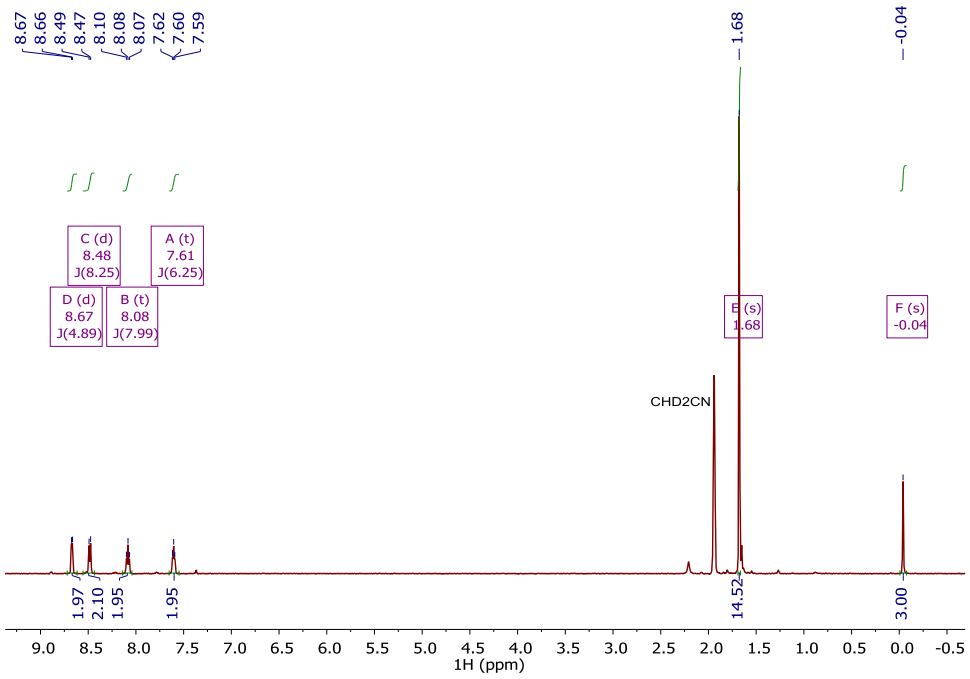

Figure 3.26. ^{1}H NMR spectrum of [Cp*Ir(bpy)(CH_3)][Cl] in CD_3CN.

*[Cp*Ir(bpy)(^{n}Pr)][I]*. To a stirring purple solution of Cp*Ir(bpy) (3.5 mg) in Et_2O was added excess ^{n}PrI (10 uL). Over the course of 4 hours, a yellow precipitate formed, which was isolated by filtration and washed with Et_2O. ^{1}H NMR (600 MHz, CD_3CN, Figure 3.27) δ 8.68 (ddd, J = 5.7, 1.4, 0.8 Hz, 2H), 8.49 (dt, J = 8.0, 0.9 Hz, 2H), 8.12 (ddd, J = 8.1, 7.5, 1.4 Hz, 2H), 7.64 (ddd, J = 7.4, 5.7, 1.4 Hz, 2H), 1.68 (s, 15H), 0.87 – 0.72 (m, 4H, *CH_2CH_2*CH_3), 0.61 (t, J = 6.9 Hz, 3H, CH_2CH_2*CH_3*).

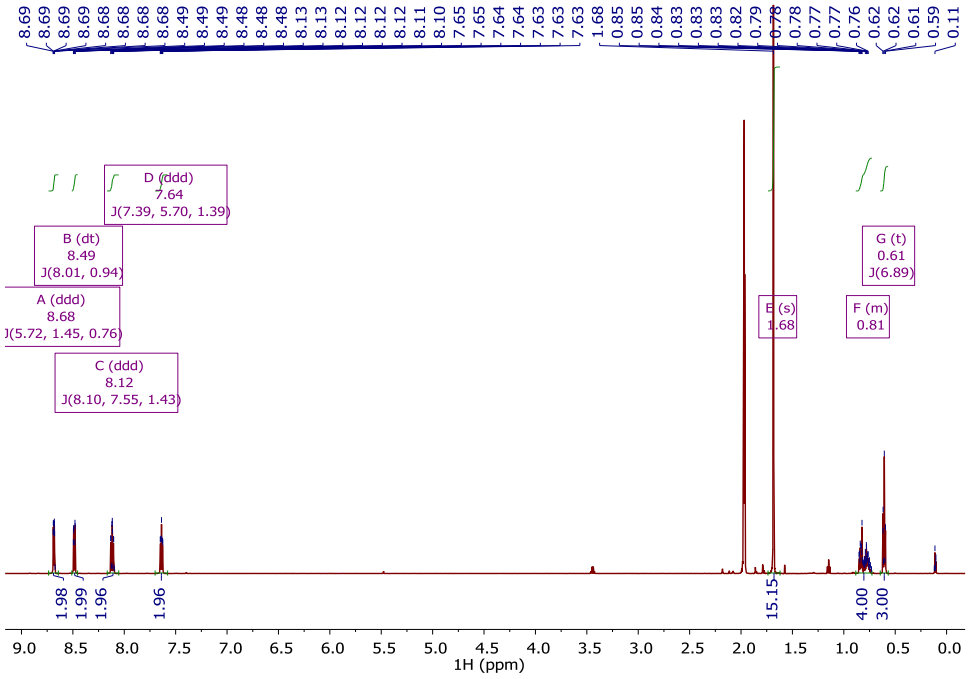

Figure 3.27. ^{1}H NMR spectrum of [Cp*Ir(bpy)(^{n}Pr)][I] in CD_3CN.

*[Cp*Ir(bpy)(CH₂Cl)][Cl]*. Solid Cp*Ir(bpy) (5.0 mg) was dissolved in CH_2Cl_2. The solution lightened from purple to yellow over the course of minutes. The solvent was removed *in vacuo* yielding [Cp*Ir(bpy)(CH_2Cl)][Cl]. ^{1}H NMR (600 MHz, CD_3CN, Figure 3.28) δ 8.65 (ddd, J = 5.7, 1.5, 0.8 Hz, 2H), 8.56 (dt, J = 8.0, 1.1 Hz, 2H), 8.16 (td, J = 7.9, 1.5 Hz, 2H), 7.67 (ddd, J = 7.4, 5.6, 1.4 Hz, 2H), 3.60 (s, 2H), 1.68 (s, 15H).

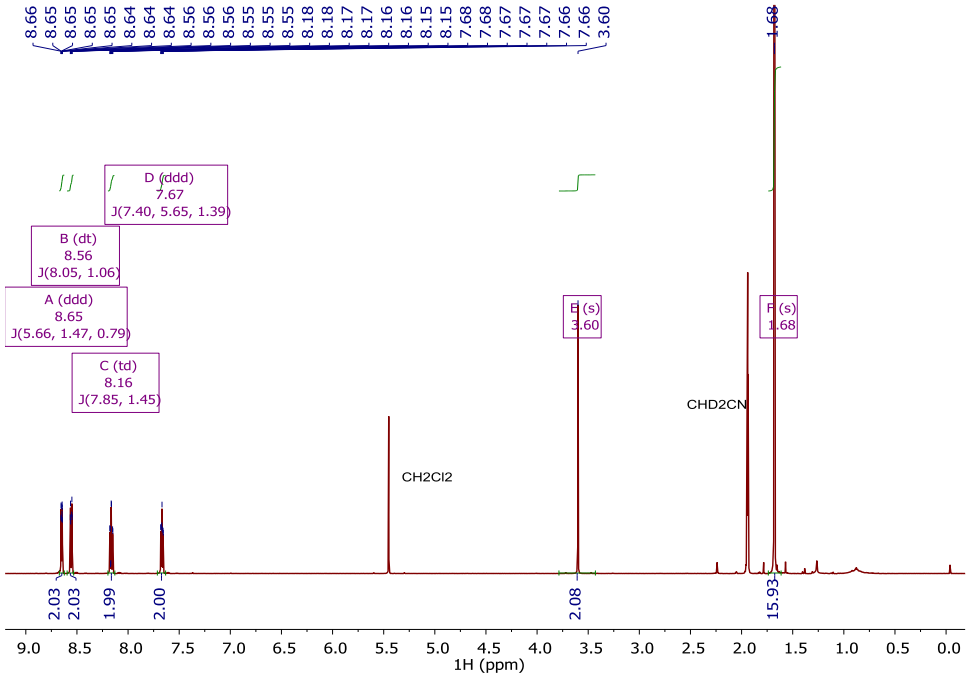

Figure 3.28. ^{1}H NMR spectrum of [Cp*Ir(bpy)(CH_2Cl)][Cl] in CD_3CN.

CHAPTER 4: AQUEOUS HYDRICITY OF LATE METAL CATALYSTS AS A CONTINUUM TUNED BY LIGANDS AND THE MEDIUM

4.1 Introduction

While the importance of metal-hydrides in the HER and other reactions in water is recognized (and discussed in Chapter 1) and while methods for measuring the strength of the M–H bond have been pioneered by DuBois and Rakowski DuBois in acetonitrile,[38–40] applying these tools to the aqueous environment has lagged behind their use in organic solvents. The discrepancy is partially due to the solubility and stability challenges that hinder the investigation of organometallic species in water. A renewal of interest in catalysts compatible with water has led to increasingly frequent reports of hydricities in water in recent years: Creutz, Wayland, Yang, and Berben have published isolated studies into the hydricities of a handful of complexes.[47–50] Our interest in a family of Cp*Ir-based catalysts motivated us to develop a general and expedient method for aqueous hydricity determination in this series of complexes.

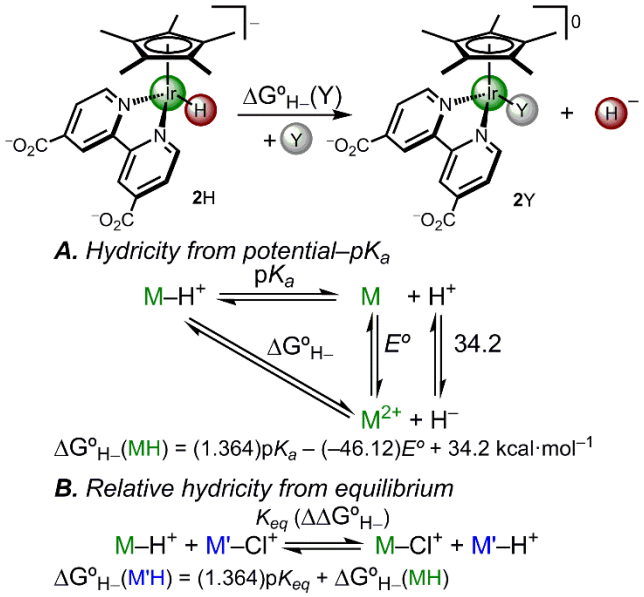

Figure 4.1. Scheme illustrating the hydricity of reference complex $[Cp^*Ir(bpy\text{-}COO)(H)]^-$ (**2**H) and thermochemical cycles that establish aqueous hydricity of Ir and Ru hydrides.

Preliminary studies on the parent complex $[Cp^*Ir(bpy)(H)]^+$ (**1**H; Cp* is pentamethylcyclopentadienyl and bpy is 2,2'-bipyridine) were stymied by the water-insolubility of the conjugate base Cp*Ir(bpy) (**1**, see Chapter 3), so we charted a course utilizing carboxylate groups on the ligand to confer water solubility. We would first establish the hydricity of a reference complex using a potential-pK_a thermochemical cycle in water (Figure 4.1A) and then map the relative hydricity of other complexes based on hydride transfer equilibria (Figure 4.1B). The potential-pK_a thermochemical cycle has been used extensively in acetonitrile,[98] but has not been systematically applied in water.

The strategy depicted in Figure 4.1 has enabled the construction of an extensive, self-consistent aqueous hydricity scale. The broad range of Ir and Ru hydricity values reveals how the polar, protic aqueous environment impacts hydride transfer thermodynamics. Substantial shifts in the hydricity values are observed relative to acetonitrile, with electronic changes to supporting ligand correlated strongly to the Hammett parameter σ_p^-. A dramatic

impact of water was also observed in the primary coordination sphere: a variety of suitable ligands present in aqueous media can bind the Ir or Ru centers after hydride transfer, shifting the effective hydricity substantially. Describing the complexities of hydride transfer in water allows interpretation of previously reported catalytic reactions and predictions that can guide improvements in the hydrogenation of carboxylic acids,[99] the disproportionation of formic acid to methanol,[100] and other metal hydride-mediated reactions such as H_2 evolution[85,101–103] and CO_2 reduction.[101,104]

4.2 Results and Discussion

Characterization of Reference Complexes. The first "reference" hydride investigated was $[Cp^*Ir(bpy\text{-}COO)(H)]^-$ (**2**H; bpy-X = 4,4'-X-bpy), with carboxylate groups installed on the bipyridine ligand to confer good water solubility over a wide pH range, independent of metal ligation or oxidation state.[63] The potential–pK_a thermochemical cycle of Figure 4.1A was used to measure the hydricity of **2**H.

The reduction potential of $[Cp^*Ir(bpy\text{-}COOH)(Cl)][Cl]$ (**2**Cl) was initially assessed using cyclic voltammetry (CV) in 1 M NaOH. Under these conditions, the chloride is displaced by hydroxide to form $[Cp^*Ir(bpy\text{-}COO)(OH)]^-$ (**2**OH) based on NMR and MS data, and a $2e^-$ reduction forms the freely diffusing species $[Cp^*Ir(bpy\text{-}COO)]^{2-}$ (**2**). Unfortunately, a large peak-to-peak separation was observed between the reduction of **2**OH and the oxidation of **2**. This electrochemical irreversibility, attributed to slow electron transfer or ligand dissociation, prevented the use of CV to determine $E_{1/2}$ (Figure 4.2).

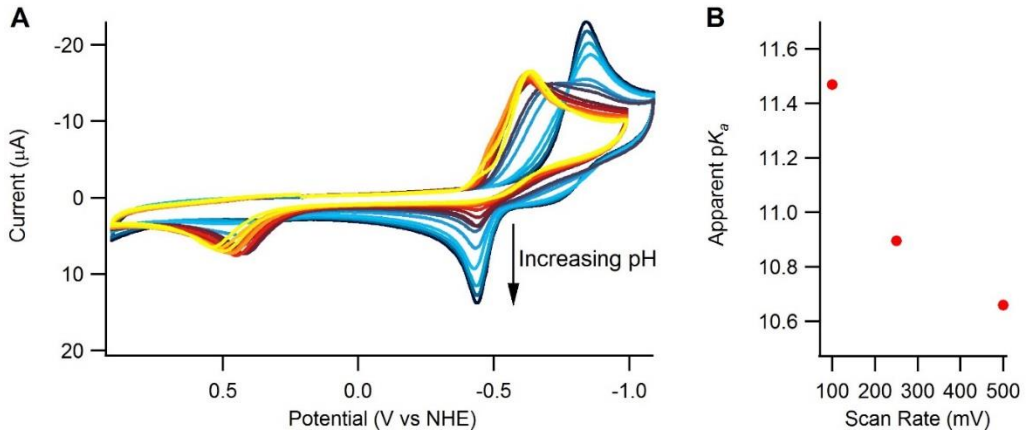

Figure 4.2 A) Cyclic voltammetry of [Cp*Ir(bpy-COOH)(Cl)][Cl] in 0.1 M pH 7 NaP_i titrated with solutions of NaOH showing the growth of the oxidation of Cp*Ir(bpy) with increasing pH and the large peak-to-peak separation between the reduction of $[Cp^*Ir(bpy\text{-}COO)(OH)]^-$ (under basic conditions) and the oxidation of $[Cp^*Ir(bpy\text{-}COO)]^{2-}$. B) The change in the apparent pK_a with scan rate indicating a slow protonation.

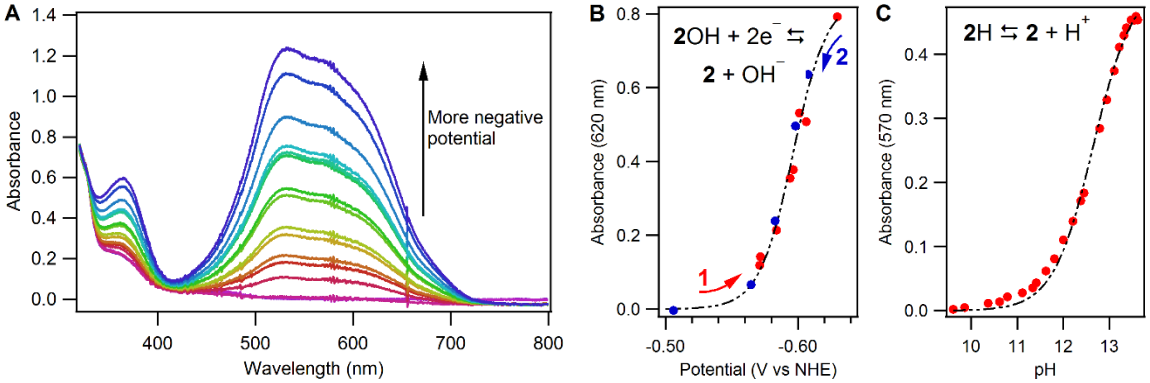

Figure 4.3. (A) Spectral changes of a pH 14 solution of $[Cp^*Ir(bpy\text{-}COO)(OH)]^-$ (2OH) as the solution potential is decreased by electrolysis to form $[Cp^*Ir(bpy\text{-}COO)]^{2-}$ (2). (B) Absorbance at 620 nm stepping in the negative potential direction (red dots), the positive potential direction (blue dots), and the fit to the Nernst equation (dot-dashed line) giving $E^{o\prime}$ = –0.60 V. The lack of hysteresis indicates that equilibrium was established. (C) Absorbance at 570 nm of a titration of $[Cp^*Ir(bpy\text{-}COO)(H)]^-$ (2H) forming 2 (red dots) and the fit to the Henderson-Hasselbalch equation (dot-dashed line) giving pKa = 12.4.

Biochemists have developed an electrochemical technique suitable for quantifying reduction potentials that are hampered by slow kinetics: *redox potentiometry*.[105] Solutions varying the relative concentrations of **2**OH and **2** were prepared by partial electrolysis of a

pH 14 solution of **2**OH. Between each stage of the electrolysis, the solution was allowed to reach equilibrium (as judged by a constant open circuit potential) and the concentrations of the Ir species were determined by UV-vis (Figure 4.3A). This method provided $E^{o\prime}$ = –0.60 V for the reduction of **2**OH to **2** at pH 14 (Figure 4.3B). As thermodynamic constants for proton reduction are determined at the standard state of pH 0,[36,47] this reduction was extrapolated to pH 0 by applying a 29.5 mV per pH unit shift ($2e^-$ reduction with loss of hydroxide), giving E^o = –0.19 V. Redox potentiometry is seldom used in organometallic chemistry,[106,107] but this method was essential for overcoming the slow kinetics that prevented the straightforward measurement of thermodynamic values.

With a reduction potential in hand, hydricity could be determined if paired with the metal hydride pK_a value. The water-soluble Ir complexes possess *several* acidic protons. Spectrophotometric titrations established the pK_a of the carboxylic acid groups in $[Cp^*Ir(bpy\text{-}COOH)(OH_2)]^{2+}$ and $[Cp^*Ir(bpy\text{-}COOH)(H)]^+$ as 1.9 and 2.7, respectively. The acidity of **2**H was then measured spectrophotometrically by addition of base to a yellow-orange solution of **2**H to produce a deep purple solution of **2** (Figure 4.3C), providing pK_a(**2**H) = 12.4. The relatively acidic carboxylic acid groups provide a doubly anionic supporting ligand at pH 7 and ensure that hydride donation will not be coupled to protonation changes at the ligand.

$$\mathbf{2}H \leftrightarrows \mathbf{2} + H^+ \qquad (4.1)$$

$$\mathbf{2} + OH^- \leftrightarrows \mathbf{2}OH + 2e^- \qquad (4.2)$$

$$\underline{H^+ + 2e^- \leftrightarrows H^-} \qquad (4.3)$$

$$\mathbf{2}H + OH^- \leftrightarrows \mathbf{2}OH + H^- \qquad (4.4)$$

The hydricity of reference complex **2**H was established by combining the pK_a of the metal hydride (Eq. 4.1), the oxidation potential of the conjugate base (Eq. 4.2), and the free energy of proton reduction to hydride (Eq. 4.3, 34.2 kcal·mol^{-1}).[47] This thermochemical cycle provides $\Delta G^{o}_{H-}(OH)$ = 42.4 kcal·mol^{-1} (Eq. 4.4), employing the conventional standard state of pH 0.

The hydricity $\Delta G^{o}_{H-}(OH)$ is the free energy of hydride transfer from **2**H with formation of the hydroxo complex **2**OH. Hydroxide binding is involved in the experimentally measured reduction potential, so thermochemistry involving this ligand is obtained directly. The free energy of hydride transfer from **2**H with formation of the aquo complex **2**OH_2 can also be determined by taking into account the pK_a of **2**OH_2 (Eq. 4.5, pK_a = 7.6 by spectrophometric titration): $\Delta G^{o}_{H-}(OH_2)$ = 32.0 kcal·mol^{-1}.

$$\mathbf{2}OH + H^{+} \leftrightarrows \mathbf{2}OH_2 \qquad (4.5)$$

An unusual situation arises when taking into account the metal aquo acidity: there two *different* hydricity values for **2**H, $\Delta G^{o}_{H-}(OH)$ and $\Delta G^{o}_{H-}(OH_2)$. Formal hydride transfer initially results in a 16e^{-} complex with a vacant coordination site, and this hydride dissociation process (ΔG^{o}_{H-} in Scheme 4.1) is most commonly associated with hydricity. But in many cases the coordinatively unsaturated complex rapidly binds a ligand (e.g. solvent or a counterion) during the net hydride transfer process. In organic solvents, solvation of the metal center after hydride transfer is commonly ignored in the thermochemistry: the activity of the solvent is taken as unity.[108–111] *In water, several species beyond the solvent itself can ligate the final product after hydride release — and different thermochemical values are expected for water, hydroxide, phosphate, and chloride complexes.*

The obtained thermodynamic values $\Delta G^{o}_{H-}(OH)$ and $\Delta G^{o}_{H-}(OH_2)$ include the formal hydricity *and* the binding affinity for the incoming ligand (Scheme 4.1). A similar situation arises for acidities when following proton loss, aggregation through hydrogen-bonding interactions, e.g. homoconjugation, influence effective acidity.[112] To distinguish the different effective hydricity values that couple hydride transfer and ligand association, the nomenclature $\Delta G^{o}_{H-}(Y)$ is used, where Y is the incoming ligand.

Scheme 4.1. Effective hydricity including ligand association.

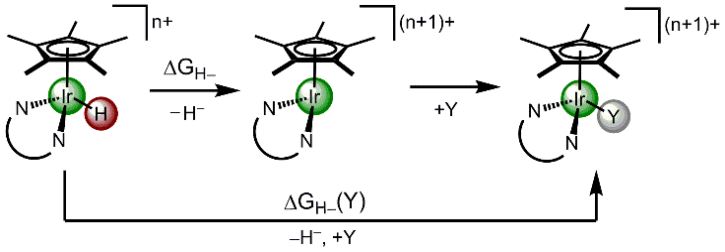

To better understand the role of incoming ligands, we explored the effect of other common aqueous salts on hydricity. Effective hydricity values were determined by measuring the free energy of ligand exchange with **2**OH_2 (Figure 4.4A) and adding that thermodynamic value to $\Delta G^{o}_{H-}(OH_2)$. The relative free energy of chloride substitution was determined by NMR titration of NaCl into a pD 7 solution of **2**OH_2, $\Delta G_{OH2\rightarrow Cl}$ = –4.4 kcal·mol^{-1} (Eq. 4.6). Because ligand exchange is slow on the NMR timescale, the concentrations of the iridium species could be determined directly. The hydricity of **2**H to form the chloride product is thus $\Delta G^{o}_{H-}(Cl)$ = 27.6 kcal·mol^{-1}.

$$\mathbf{2}OH_2 + Cl^- \leftrightarrows \mathbf{2}Cl + H_2O \qquad (4.6)$$

$$\mathbf{2}OH_2 + H_nPO_4^{m-} \leftrightarrows \mathbf{2}H_nPO_4 + H_2O \qquad (4.7)$$

The phosphate buffer presents both $H_2PO_4^-$ and HPO_4^{2-} ligands at pH 7, either of which can bind Ir(III).[85] Phosphate binding is apparent by NMR spectroscopy in pH 7 phosphate buffer, but rapid proton exchange prevents precise identification of the ligand. The

relative binding affinity of the phosphate mixture ($\Delta G_{OH2 \rightarrow Pi}$ = –1.9 kcal·mol^{-1} at pH 7, Eq. 4.7) provides $\Delta G_{H-}(P_i)$ = 30.1 kcal·mol^{-1} (n = 1 or 2; m = 3 – n). This hydricity is strictly accurate only at pH 7, where the measurement was made for the specific $H_2PO_4^-/HPO_4^{2-}$ mixture which P_i^- represents. The concentrations of $H_2PO_4^-$ and HPO_4^{2-} will change based on the solution pH, however, which could impact hydride transfer.

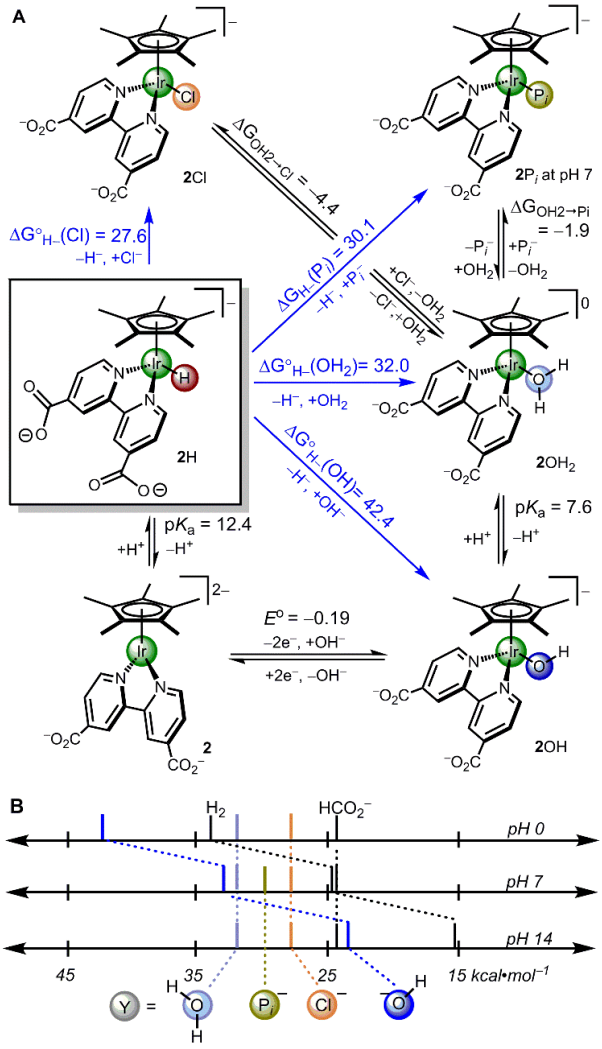

Figure 4.4. (A) Summary of thermochemical values of [Cp*Ir(bpy-COO)(H)]$^-$ (**2**H). Free energies (kcal·mol^{-1}) and reduction potentials (V vs. NHE) are cited at the standard state of pH 0, 1 M reagents, and 1 atm gases, except for $\Delta G_{OH2 \rightarrow Pi}$ and $\Delta G_{H-}(P_i)$ values that refer to pH 7. (B) Summary of the pH dependence of $\Delta G^o_{H-}(Y)$ with the H_2O/H_2 and CO_2/HCO_2^- couples.

Complex **2**H is substantially more hydridic in water (smaller $\Delta G^{o}_{H-}(OH_2)$ value) than in acetonitrile, consistent with prior studies.[49,50,110] The large differences in hydricity as a function of the ligands present in aqueous solution, however, were previously unexplored and suggest that water plays a role in hydride transfer reactions beyond simply providing a high polarity medium. Transition metal hydride transfer can be described by a *manifold of hydricity values* comprised of the heterolytic M–H bond strength (to release H^-) and the dative metal−ligand bond strength of any aqueous buffer components or salts.

The effective hydricity, $\Delta G^{o}_{H-}(Y)$, is expected to be experimentally relevant to catalysis. Hydride transfer reactions for d^6 hydrides during catalysis will involve ligand association, so understanding the overall thermodynamics of that process is vital.[1] For example, in a typical pH 7 phosphate buffer solution used in photoelectrocatalytic H_2 evolution,[85] hydride **2**H reacts with water to release H_2 and generate an equilibrium mixture of Ir(III) chloride, aquo, and phosphate complexes—representing three different H_2 release pathways with three different hydricity values.

In water, pH also becomes an integral factor in hydricity (Figure 4.4B). For one, the H_2O/H_2 potential will shift to lower values as pH increases (1.36 $kcal \cdot mol^{-1} \cdot pH^{-1}$), indicating that as protons become scarcer, stronger hydrides are required to evolve H_2. Yet while H_2 is shifting, $\Delta G^{o}_{H-}(Cl)$ and $\Delta G^{o}_{H-}(OH_2)$ remain constant across the accessible pH range, altering net H_2 release thermodynamics. On the other hand, $\Delta G^{o}_{H-}(OH)$ is influenced by pH as the concentration of ligand available for binding changes with pH. At pH 0, hydroxide ligation is unfavorable, leading to $\Delta G^{o}_{H-}(OH) > \Delta G^{o}_{H-}(OH_2)$; while chemical intuition might suggest

[1]Many of the transition metal hydride studied in MeCN have been d^8, which can minimize the influence of solvation through a geometry change after hydride transfer. See ref. 39.

that hydride transfer to form an aquo complex would be a less favorable than hydride transfer to form a complex with the more basic hydroxide ion, the extremely low concentration of hydroxide at pH 0 leads to unfavorable energetics. As the solution pH increases, however, formation of the hydroxide complex will become more favorable, and the value $\Delta G^{o}_{H^-}(OH)$ will shift smoothly. Figure 4.4B illustrates that at pH 14, $\Delta G^{o}_{H^-}(OH) < \Delta G^{o}_{H^-}(OH_2)$ and complex **2**H becomes a much stronger hydride donor.

Establishing a Second Reference Point. Though the differences caused by different ligands in the aqueous medium are striking, their impact is best assessed by comparison to the effect of changing the metal center and supporting ligands. Modification of the structure of the hydride is the most common route to tune hydricity, and these synthetic strategies are typically assumed to have a greater influence than solvation of the product. To make these comparisons, we sought to explore a wider range of metal complexes and began by determining the hydricity of another soluble "reference" hydride, [(cymene)Ru(bpy-COO)(H)]$^-$ (**3**H). Hydride **3**H hails from a family of (arene)Ru(diimine) catalysts that carry out aqueous transfer hydrogenation, water splitting, and CO_2 reduction.[104,113,114]

The reduction potential of [(cymene)Ru(bpy-COO)(OH)]$^-$ (**3**OH) between pH 8 and 12 was measured by CV. The quasi-reversible **3**OH/**3** couple (ΔE_p = 60 mV) shifted 26 mV per pH unit, close to the ideal value of 29.5 mV expected for a $1OH^-/2e^-$ process (Figure 4.5). Extrapolating the trend in $E_{1/2}$ to pH 0 provided the standard reduction potential E^o = –0.30 V.

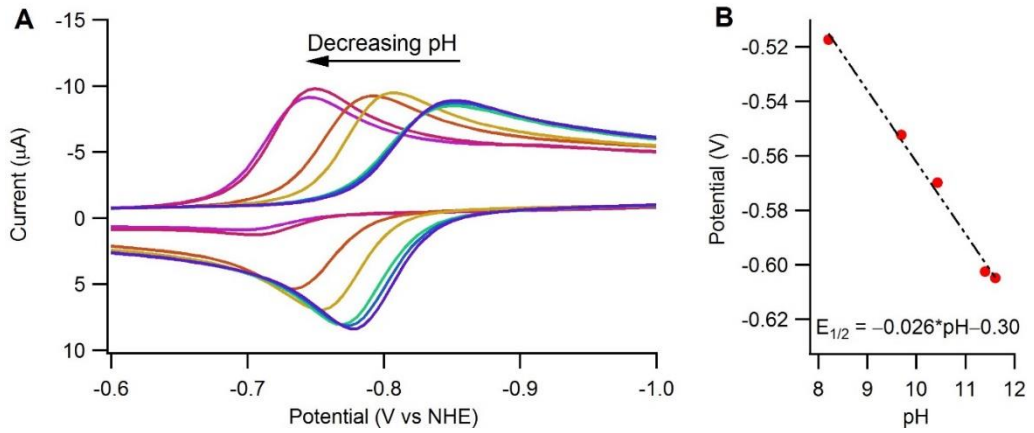

Figure 4.5. (A) Cyclic voltammetry of [(cymene)Ru(bpy-COOH)(OH_2)][$OTf]_2$ in 1 M NaOH titrated with solutions of H_3PO_4 at 50 mV/s. (B) To determine E^o, $E_{1/2}$ between pH 8 and 12 were extrapolated to zero giving E^o = –0.30 V (assuming oxidized and reduced species have similar diffusion properties). Though at lower pH (purple trace), the oxidation is very poorly resolved as Ru^0 is protonated, the extrapolation is consistent with the best estimate of $E_{1/2}$(pH 7.8) ~ –0.51 V, or –0.28 V accounting for the deprotonation of the aquo to form the hydroxo.

Spectrophotometric titrations provided the acidity of the hydride **3**H, pK_a(**3**H) = 11.8. From the pK_a and E^o, $\Delta G^o_{H-}(OH)$ = 36.5 kcal·mol^{-1} can be determined. Including the aquo pK_a = 7.7 gives $\Delta G^o_{H-}(OH_2)$ = 26.0 kcal·mol^{-1}. (All the relevant pK_a and $\Delta G°_{H-}$ values for this system are collected in Table 4.1). The relative aquo–chloride association free energy, $\Delta G_{OH2\rightarrow Cl}$ = –2.9 kcal·mol^{-1}, was significantly smaller than that of the Ir complex. Taken together, the hydricity to form the chloride was determined to be $\Delta G^o_{H-}(Cl)$ = 23.1 kcal·mol^{-1}.

Table 4.1. Summary of Thermodynamics

	Reaction	Cp*Ir(bpy-COO)	(cymene)Ru(bpy-COO)
E^{oa}	$[M^{III}(OH)]^- \leftrightarrows [M^{I}]^{2-} + 2e^- + OH^-$	–0.19	–0.30
pK_a	$[M^{III}(H)]^- \leftrightarrows [M^{I}]^{2-} + H^+$	12.4	11.8
	$[M^{III}(OH_2)]^0 \leftrightarrows [M^{III}(OH)]^- + H^+$	7.6	7.7
	$[M^{III}(bpy\text{-}COOH)(OH_2)]^{2+} \leftrightarrows [M^{III}(bpy\text{-}COO)(OH_2)]^0 + H^+$	1.9	2.2
	$[M^{III}(bpy\text{-}COOH)(H)]^+ \leftrightarrows [M^{III}(bpy\text{-}COO)(H)]^- + H^+$	2.7	—
X^{-b}	$[M^{III}(OH_2)]^0 + Cl^- \leftrightarrows [M^{III}(Cl)]^- + OH_2$	–4.4	–2.9
	$[M^{III}(OH_2)]^0 + P_i^- \leftrightarrows [M^{III}(P_i)]^- + OH_2$	–1.9[c]	–1.2[c]
$\Delta G_{H^-}{}^b$	$[M^{III}(H)]^- + Cl^- \leftrightarrows [M^{III}(Cl)]^- + H^-$	27.6	23.1
	$[M^{III}(H)]^- + P_i{}^- \leftrightarrows [M^{III}(P_i)]^- + H^-$	30.1[c]	24.8[c]
	$[M^{III}(H)]^- + OH_2 \leftrightarrows [M^{III}(OH_2)] + H^-$	32.0	26.0
	$[M^{III}(H)]^- + OH^- \leftrightarrows [M^{III}(OH)]^- + H^-$	42.4	36.5

[a]V vs NHE at pH 0. [b]kcal·mol^{-1}. [c]at pH 7.

Building a Scale through Equilibria. Having established two well-defined reference hydricity values, we set out to determine the hydricity of related hydrides, including the parent bpy complexes. To probe hydride transfer equilibria between Ir and Ru hydrides, however, a reliable synthetic route to these species was required. Chloride counter ions were

sought to increase water solubility (the previously reported PF_6^- and $CF_3SO_3^-$ salts of **1**H were insoluble above 2 mM in water)[84] and to reduce speciation.

Electrochemical and chemical synthetic methods were developed to provide rapid access to a wide range of water-soluble metal hydrides. In a representative controlled potential electrolysis, the chloride salt of **1**Cl was converted to >20 mM of **1**H in 0.1 M pH 7 NaP_i. If the pH and electrolysis potential were appropriately controlled to facilitate a reduction–protonation sequence, the electrolysis method was quite general. Chemical syntheses were also carried out, as needed, according to a newly developed procedure. For example, reduction of the chloride salt of **1**Cl by $NaBH_4$ in 1 M NaOH resulted in precipitation of purple **1** in nearly quantitative yield. Dropwise addition of $HCl{\cdot}Et_2O$ to a stirring solution of **1** in Et_2O prompted precipitation of the golden yellow chloride salt of hydride **1**H. This procedure is also generally applicable, except when the metal hydride cannot be deprotonated in water or the conjugate base does not precipitate from water.

With a collection of hydride complexes (see Figure 4.6 for numbering scheme), relative hydricity could be determined by mixing a hydride donor and a hydride acceptor and allowing the system to reach an equilibrium distribution of both hydrides and acceptors. The concentrations of each species were determined by NMR, and the equilibrium constant provided the difference in hydricity ($\Delta\Delta G^\circ_{H-}$) between the two complexes, according to Figure 4.1B.[115] Figure 4.6 depicts the relative hydricity of each hydride complex, with each reaction representing a hydride/chloride exchange.

In a representative hydride equilibration, a solution of **2**Cl in pD 7 0.1 M NaP_i (produced electrochemically in 84% yield, with 16% unreacted **2**Cl) was mixed with **1**Cl. After the reaction was allowed to reach equilibrium, the concentrations of **1**H, **1**Cl, **2**H, and

2Cl were measured by ^{1}H NMR spectroscopy. The equilibrium constant, K_{eq} = 0.35, provided $\Delta\Delta G^{o}_{H-}$ = 0.6 kcal·mol^{-1} (Eq.4.8) and established the hydricity of **1**H in a single experiment: ΔG^{o}_{H-}(Cl) = 26.3 kcal·mol^{-1}. It is noteworthy that equilibration was established in < 15 min, and though our present focus is on *thermodynamic* hydricity, this contrasts with the frequently kinetically slow hydride transfer reactions reported in acetonitrile.[110,115]

$$\mathbf{2}\text{H} + \mathbf{1}\text{Cl} \leftrightarrows \mathbf{2}\text{Cl} + \mathbf{1}\text{H} \qquad (4.8)$$

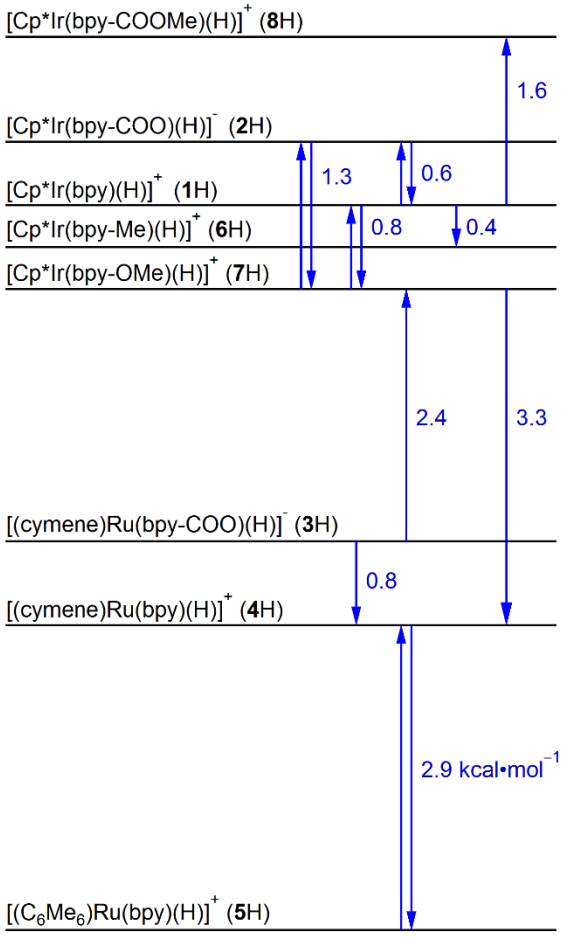

Figure 4.6. Relative hydricity values of Ir and Ru complexes (blue). The equilibria used to determine hydricity are represented by blue arrows.

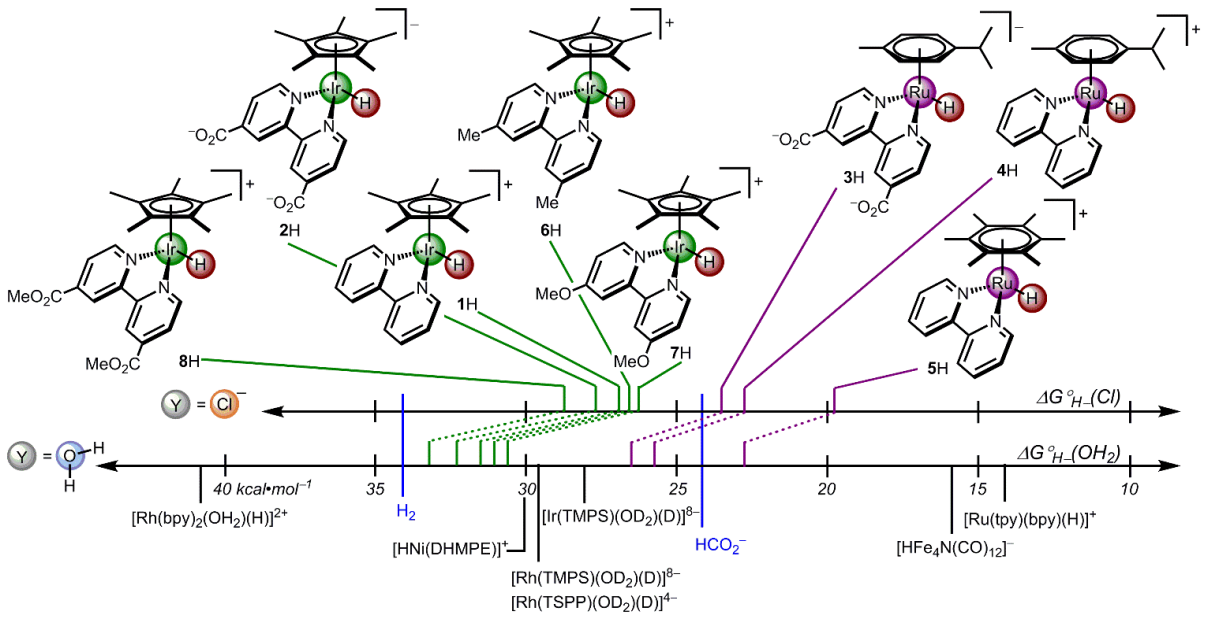

Figure 4.7 Aqueous hydricity scale of the complexes we report along with those previously reported in the literature. Y represents the incoming ligand such that the top scale shows $\Delta G^{o}_{H-}(Cl)$ and the bottom scale shows $\Delta G^{o}_{H-}(OH_2)$. TSPP = tetra(p-sulfonatophenyl)porphyrin; TMPS = tetrakis(3,5-disulfonatomesityl)porphyrin; tpy = terpyridine; DHMPE = 1,2-bis(dihydroxymethylphosphino)ethane.[47,49,50,116]

A series of hydride transfer equilibrium experiments established the relative hydricity scale of Figure 4.6. Equilibrium could be established from either direction to give $\Delta\Delta G°_{H-}$ values that were identical within experimental uncertainty (±0.1 kcal·mol^{-1}, see Experimental Section). Hydricity values were determined from these relative hydricities by comparison to the $\Delta G^{o}_{H-}(Cl)$ of reference **2**H for Ir complexes and reference **3**H for Ru complexes, and the scale is self-consistent within the ±1 kcal·mol^{-1} estimated uncertainty of the measurements.[98,115,117] The $\Delta G^{o}_{H-}(OH_2)$ for all complexes was determined by measuring the aquo chloride exchange energy of each of these species (Table 4.2).

Table 4.2. Aquo-chloride exchange free energy and hydricity to form ligated products in kcal·mol^{-1}.

Complex	$\Delta G^{o}_{H-}(Cl)$	$\Delta G^{o}_{H-}(OH_2)$	$\Delta G_{OH2\rightarrow Cl}$
1	27.0	31.5	-4.5
2	27.6	32.0	-4.4
3	23.1	26.0	-2.9
4	22.3	25.6	-3.3
5	19.4	22.9	-3.5
6	26.6	31.1	-4.5
7	26.2	30.8	-4.6
8	28.6	33.4	-4.7

Our values are also consistent with one of the few other well-defined hydricity values available in the literature: the hydricity of $[(C_6Me_6)Ru(bpy)(H)]^+$ (**5**H) with formation of **5**OH_2 was reported by Creutz, $\Delta G^{o}_{H-}(OH_2)$ = 22.2 kcal·mol^{-1},[47,48] which we independently determined to be $\Delta G^{o}_{H-}(OH_2)$ = 22.9 kcal·mol^{-1}.

In Figure 4.7, our continuum of hydricity values is contextualized against previously reported hydricity values ($\Delta G^{o}_{H-}(OH_2)$) for transition metal hydrides and substrates relevant to alternative energy pursuits (H^+ and CO_2). The two parallel scales illustrate the role of the ligand bound to the product and the influence of changes to the supporting ligands or metal center. In general, the hydricity values are much smaller in water than in acetonitrile.[84,110] Electron-donating groups promote hydride transfer, as evidenced by a strong correlation between $\Delta G^{o}_{H-}(Cl)$ and the Hammett parameter σ_{p-} (Figure 4.8A).[118] The ease with which each ligand can stabilize increased electron density is reflected in electronic spectroscopy: hydricity is correlated to the metal-to-ligand charge-transfer band around 400 nm that is present in each of the Ir hydride complexes (Figure 4.8B). Interestingly, the *activity* of aqueous hydrogen evolution catalysis involving Cp*Ir-based catalysts also correlates with

electron-donating ability of the bipyridine ligand,[103] suggesting that perhaps the increase in rate is due to an increase in the hydricity of the metal hydride intermediate.

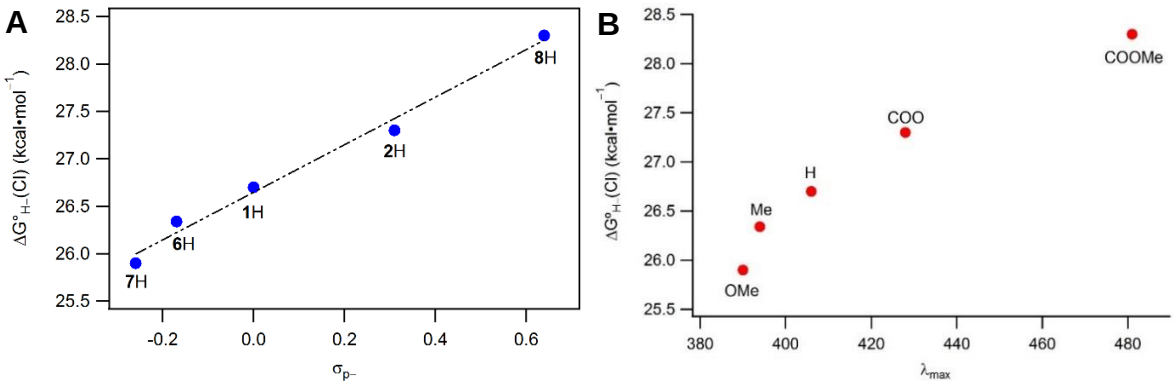

Figure 4.8. A) Correlation between σ_{p^-} and $\Delta G°_{H-}(Cl)$. B) Correlation between λ_{max} of the hydride with the hydricity of that hydride.

Electronic changes to the bipyridine ligands affect the *acidity* of the metal hydride more dramatically than the hydricity. The hydricity difference between methoxy-substituted **7**H (pH > 14) and methylester-substituted **8**H (pH ~ 5) is only 2.4 kcal·mol^{-1}, while the acidity difference between these complexes spans ~9 orders of magnitude (~12 kcal·mol^{-1}). The hydricity calculation tends to moderate electronic effects as increased electron density increases pK_a and shifts $E°$ more negative which raise and lower hydricity, respectively.

Ligand effects on hydricity were more pronounced when changes were made to the arene rings.[115] Cymene complex **4**H and hexamethylbenzene complex **5**H displayed a ~3 kcal·mol^{-1} difference in hydricity that is larger than observed for bpy ligand modifications, but of a similar magnitude to the effect of chloride ligation. These differences warrant further studies into possible steric effects in these thermodynamic hydricity values.

The emerging picture of aqueous hydricity tunable by both ligands *and* the medium could impact catalysis. Electrocatalytic hydrogen evolution in water is usually carried out

with pH-stabilizing buffer bases,[56] and water splitting schemes that employ salt water must wrestle with an abundance of chloride[20,119]—which would lead to a ~5 kcal·mol^{-1} difference in the hydricity of Ir catalysts. The hydricity trends in Figure 4.7 also predict the pH at which H_2 evolution will occur, as a function of the ligand electronics and the presence of incoming ligands in solution. All of the complexes investigated, for example, are predicted to produce H_2 at pH 0 (ΔG^{o}_{H-} < 34.2 kcal·mol^{-1}), but at pH 10 only Ru complex **5**H is thermodynamically capable of forming H_2 (and only at high chloride concentration). Under basic conditions, hydroxide ligation could also start to impact hydride transfer reactivity.

At pH 7, parent Ir–H **1**H is not expected to make H_2, consistent with our observations in electrolysis experiments. Excitation by visible light is expected to result in a more potent hydride donor.[84] An estimation of the hydricity of the excited state can be gleaned from the extrapolation of the high energy edge of the emission of **1**H in water. This method suggests that the thermodynamic hydricity of the excited state of **1**H is –23 kcal·mol^{-1}, making **1**H more than capable of making H_2 in neutral water.

The ability of a hydride to reduce CO_2 to formate at pH 0 can also be predicted by inspection of Figure 4.7. Species more hydridic than formate (ΔG^{o}_{H-} < 24.1 kcal·mol^{-1}) are thermodynamically capable of CO_2 reduction. An intriguing prediction arises from Figure 4.7: CO_2 reduction by hydride transfer from (cymene)Ru complexes **3**H and **4**H should unfavorable in unbuffered water and favorable only when chloride anion is present. The less hydritic hydrides would require increased CO_2 pressure to enable hydride transfer to CO_2. In a prior report of CO_2 hydrogenation, the Ir hydride **1**H underwent slow, rate-limiting hydride transfer to CO_2, while the Ru hydride **5**H transferred hydride sufficiently quickly that hydride formation from H_2, instead, became rate-limiting.[104] Our studies show that **5**H is more

hydridic than the parent Ir complex **1**H; the hydricity scale correctly predicts that **5**H will more readily hydrogenate CO_2 (and less readily cleave H_2).

4.3 Conclusions

A general strategy for the determination of hydricity in water is presented. Comparisons across a range of well-known catalytic intermediates were enabled by both an electrochemical technique well suited to the complications of water and a new synthetic routes to water-soluble hydrides. Thermodynamic hydricity in water is not only influenced by the supporting ligands, but also by the range of ligands present in aqueous media. Rather than a single value defined in terms of the hydride donor, a continuum of hydricity values should be considered. Being cognizant of the resulting product after hydride transfer makes direct comparisons between catalysts and conditions possible.

The hydricity scales suggest new strategies in aqueous catalysis. The synthetic chemist instinctively tunes catalysts through ligand modifications, but tuning the medium itself can also effect changes in hydricity. The present findings will guide further thermodynamic studies of PCET events in water and guide aqueous catalyst development.

4.4 Experimental Section

General Considerations. Procedures were carried out under nitrogen except where noted. All solutions containing metal hydride species were protected from ambient light to prevent excited state reactions.[85] All reagents were commercially available and used without further purification. Commercial HPLC-grade water was used as a solvent, and organic solvents were dried and degassed with argon using a Pure Process Technology solvent

system. Deuterated solvents were purchased from Cambridge Isotope Laboratories, Inc. Electrochemical experiments were performed on a Pine WaveNow potentiostat or Pine WaveDriver bipotentiostat controlled by Aftermath software. Details on specific electrochemical experiments are described below. Solution pH was recorded using an OrionStar A111 pH meter with a Beckman-Coulter, Hanna, or Hach ISFET pH probe. UV-Vis spectra were obtained using an Ocean Optics USB2000+ spectrometer with a DT-MINI-2GS deuterium/tungsten halogen light source controlled by OceanView software.

NMR spectra were obtained on 400, 500, or 600 MHz spectrometers. ^{1}H NMR spectra were referenced to the residual solvent signals (or dioxane or NaOTs as an internal standard in D_2O).[78] Spectra were processed using the MestReNova software suite from Mestrelab Research S. L. The solution acidity in NMR experiments is reported as pD, obtained by addition of +0.4 to the reading of a pH electrode that was calibrated using H_2O standards.[79]

ESI-MS were obtained on a Thermo Scientific LTQ FT-ICR MS with samples introduced either through direct infusion or by LC. Inductively coupled plasma-mass spectrometry (ICP-MS, Agilent Technologies 7500x series) was employed to determine the precise Ir and Ru concentrations in UV-Vis samples (for molar extinction coefficient determination), with the aid of a calibration curve for 10-500 ppb Ir and Ru.

Electrochemistry. Electrochemical experiments were carried out with carbon working electrodes, platinum wire counter electrodes, and Ag/AgCl (3M NaCl) reference electrode in a small glass tube fitted with a Vycor glass frit. Solutions were thoroughly degassed by sparging with nitrogen for at least 15 minutes before beginning an experiment. All potentials

are reported relative to NHE, with values obtained by adding 0.21 V to the experimentally observed potential *vs.* Ag/AgCl.[81]

Cyclic voltammetry experiments were carried out with a glassy carbon working electrode (polished with 0.05 micron alumina powder between scans) in an undivided cell. Controlled potential electrolysis experiments were carried out with reticulated vitreous carbon (RVC) as the working electrode separated from the counter electrode and reference electrodes by a fine frit in an H-cell.

Potentiometric experiments were performed in a custom-made three-compartment cell divided by fine frits and with a 10 mm x 10 mm Pyrex glass cuvette affixed to the central working electrode chamber. The solution was stirred at the base of the cuvette and by slow bubbling of N_2 through the length of the cuvette to ensure sufficient mixing near the electrode. An RVC electrode was used as the working electrode for both the electrolysis and open circuit potential experiments. Reduction and oxidation of the analyte was achieved via short periods of electrolysis and after each pulse of current, sufficient time was allowed for the solution components to come into equilibrium (typically 5-10 min) as judged by an unchanging open circuit potential over 30 s. After equilibrium was established, UV-vis spectra were recorded.

Synthesis. $[Cp^*Ir(Cl)_2]_2$,[80] $[Cp^*Ir(bpy\text{-}COOH)Cl][Cl]$[63] and $[Cp^*Ir(bpy)(H)][OTf]$[84] were prepared following literature procedures. $[Cp^*Ir(bpy)(OH_2)][SO_4]$[100] (**1**$OH_2$), $[Cp^*Ir(bpy\text{-}COOH)(OH_2)][OTf]_2$[120] (**2**$OH_2$), and $[(cymene)Ru(bpy\text{-}COOH)(OH_2)][OTf]_2$[114] (**3**$OH_2$) were prepared following literature procedures with the appropriate silver salt.

*$[Cp^*Ir(bpy\text{-}COO)(H)]^-$ (**2**H) and $[Cp^*Ir(bpy\text{-}COO)]^{2-}$ (**2**).* Electrolysis of **2**Cl in NaP_i, Na_2SO_4, or NaOH electrolytes (depending on the desired use of the product) past the

first reduction feature (~ –1.0 V) resulted in conversion to reduced products, consistent with previously reported spectroscopic and electrochemical properties.[85] The form of these products (either **2**H or **2**) was highly dependent on solution pH, giving **2**H at neutral pH, **2** at high pH, and a mixture in between. To confirm the identities of these reduced products, **2**Cl (9.3 mg, 0.014 mmol) was reduced by excess $NaBH_4$ (3.7 mg, 0.98 mmol) by stirring for 30 min in MeOH. Filtration and evaporation produced a dark brown film. Dissolution in neutral water provided **2**H, and dissolution in basic water provided **2**. **2**H: ^{1}H NMR (600 MHz, D_2O + dioxane, Figure 4.9) δ 8.69 (d, *J* = 5.9 Hz, 2H), 8.55 (s, 2H), 7.72 (d, *J* = 5.9 Hz, 2H), 1.77 (s, 15H), -11.90 (s, 1H). $\lambda_{abs,max}$ (pH 7 0.1 M NaP_i, Figure 4.10) = 428 nm (3700 M^{-1} cm^{-1}) 2: ^{1}H NMR (400 MHz, D_2O + dioxane, Figure 4.9) δ 8.81 (d, J = 7.0 Hz, 1H), 8.42 (s, 1H), 6.82 (dd, J = 6.9, 2.0 Hz, 1H). 1.80 (s, 15 H). $\lambda_{abs,max}$ (1 M NaOH, Figure 4.10) = 292 nm (22000 M^{-1} cm^{-1}), 364 nm (10800 M^{-1} cm^{-1}), 535 nm (23000 M^{-1} cm^{-1}).

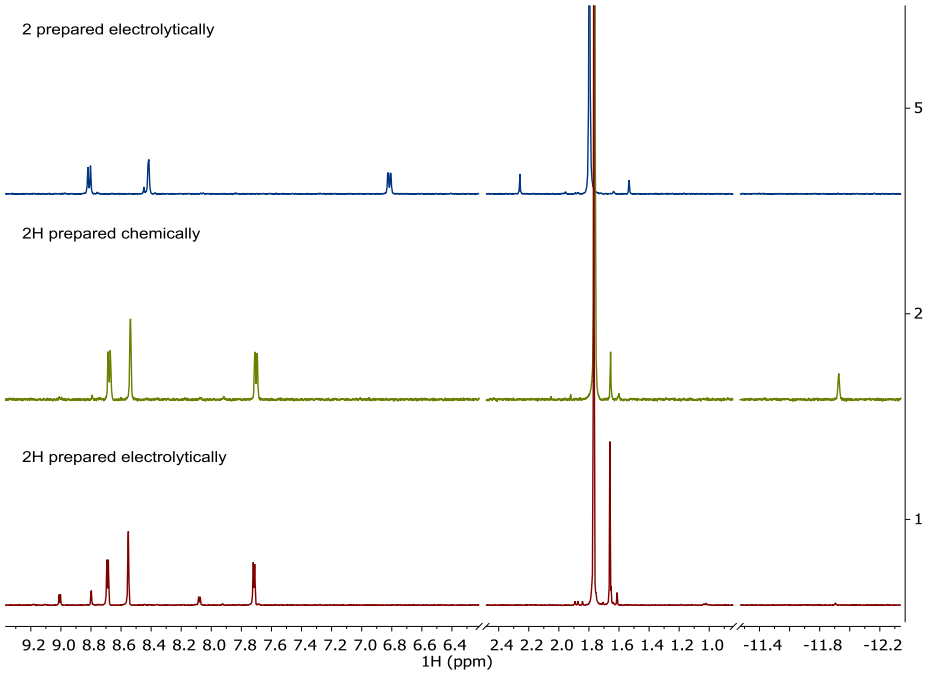

Figure 4.9. ^{1}H NMR spectra of the electrolytically produced $[Cp^*Ir(bpy\text{-}COO)(H)]^-$ (bottom) and synthetically produced $[Cp^*Ir(bpy\text{-}COO)(H)]^-$ (middle) in 0.1 M pD 7 NaP_i.

Both contain small $[Cp^*Ir(bpy\text{-}COO)(Cl)]^-$ impurities. Electrolytically produced $[Cp^*Ir(bpy\text{-}COO)]^{2-}$ in 1 M NaOH in D_2O is shown in the top panel.

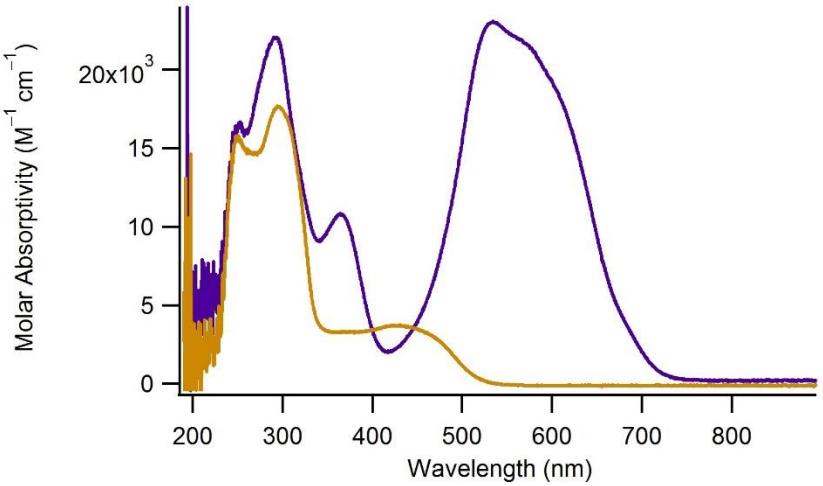

Figure 4.10. Molar absorptivities of $[Cp^*Ir(bpy\text{-}COO)(H)]^-$ (gold) and $[Cp^*Ir(bpy\text{-}COO)]^{2-}$ (purple). Samples were prepared by electrolysis and checked for purity by ^{1}H NMR before use. The Ir concentration in each sample was measured by ICP-MS.

*[(cymene)Ru(bpy-COOH)(Cl)][Cl] (**3**Cl).* Under nitrogen, $[(cymene)RuCl_2]_2$ (50.3 mg, 0.082 mmol) and bpy-COOH (40.3 mg, 0.165 mmol) were allowed to stir in 8 mL DMF at 60 °C for 3 h. After filtering the solution in air to remove unreacted ligand, the DMF was removed *in vacuo*. The resulting film was dissolved in MeOH, and yellow **3**Cl (83.4 mg, 92% yield) precipitated from solution on addition of ether. The ^{1}H NMR spectrum matched the previously reported data (Figure 4.11).[114]

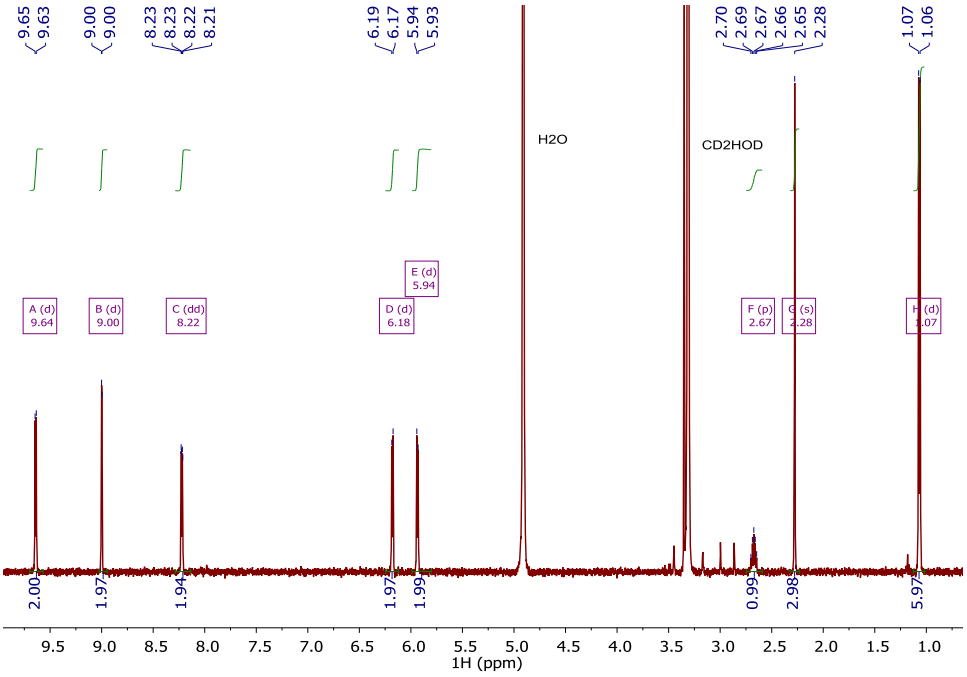

Figure 4.11. ^{1}H NMR spectrum of [(cymene)Ru(bpy-COOH)(Cl)][Cl] in CD_3OD.

*[(cymene)Ru(bpy-COO)(H)]$^{-}$ (**3**H) and [(cymene)Ru(bpy-COO)]$^{2-}$ (**3**).* The hydride **3**H and reduced complex 3 were prepared according to the procedures for **2**H and **2**. **3**H: ^{1}H NMR (600 MHz, D_2O + dioxane, Figure 4.12) δ 8.87 (d, *J* = 5.8 Hz, 2H), 8.53 (d, *J* = 1.5 Hz, 2H), 7.64 (dd, *J* = 5.9, 1.6 Hz, 2H), 5.70 (d, *J* = 6.2 Hz, 2H), 5.51 (d, *J* = 6.1 Hz, 2H), 2.63 (sept, *J* = 6.9 Hz, 1H), 2.24 (s, 3H), 1.07 (d, *J* = 6.9 Hz, 6H), -6.21 (s, 1H). $\lambda_{abs,max}$ (pH 7 0.1 M NaP_i, Figure 4.13) = 295 nm (20800 M^{-1} cm^{-1}), 434 nm (5500 M^{-1} cm^{-1}) **3**: ^{1}H NMR (600 MHz, D_2O + dioxane, Figure 4.12) δ 8.82 (d, *J* = 6.8 Hz, 2H), 8.37 (s, 2H), 7.12 (d, *J* = 6.7 Hz, 2H), 4.84 (d, *J* = 5.5 Hz, 2H), 4.81 (d, *J* = 5.7 Hz, 2H), 2.32 (sept, *J* = 7.7 Hz, 1H), 1.85 (s, 3H), 0.86 (d, *J* = 6.7 Hz, 6H). $\lambda_{abs,max}$ (1 M NaOH, Figure 4.13) = 298 nm (22600 M^{-1} cm^{-1}), 374 nm (13500 M^{-1} cm^{-1}), 506 nm (17600 M^{-1} cm^{-1}), 610 nm (14400 M^{-1} cm^{-1}).

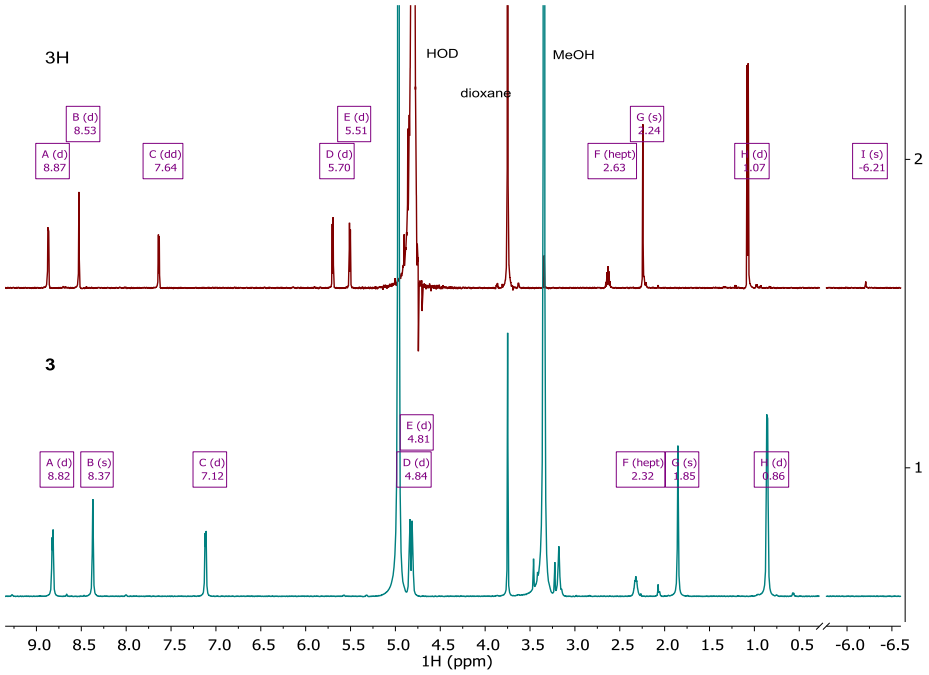

Figure 4.12. ^{1}H NMR spectra of the electrolytically produced [(cymene)Ru(bpy-COO)(H)]$^{-}$ in 0.1 M pD 7 NaP$_i$ (top) and synthetically produced [(cymene)Ru(bpy-COO)]$^{2-}$ in 1 M NaOH in D_2O (bottom). Both are referenced to dioxane.

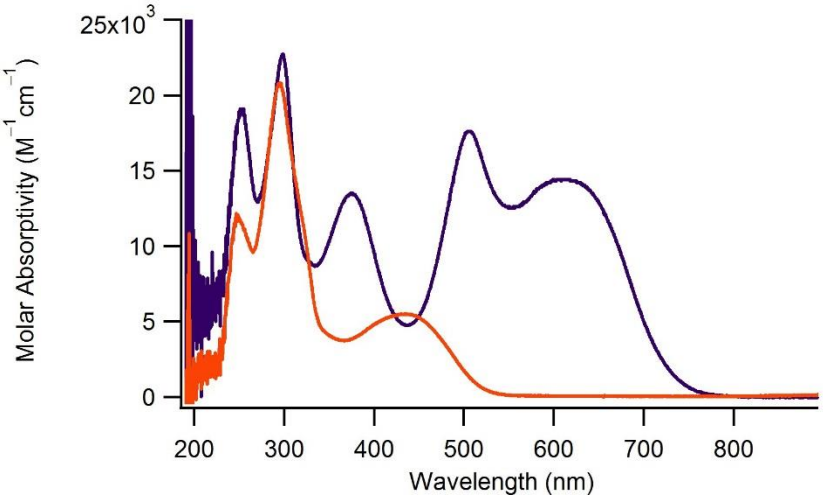

Figure 4.13. Molar absorptivities of [(cymene)Ru(bpy-COO)(H)]$^{-}$ (red-orange) and [(cymene)Ru(bpy-COO)]$^{2-}$ (purple-blue). Samples were prepared by electrolysis and checked for purity by ^{1}H NMR before use. The Ru concentration in each sample was measured by ICP-MS.

Thermodynamic Measurements. *Hydride Equilibrations.* In a typical equilibration experiment to determine relative hydricity according to Figure 4.1B, 19.3 mg **2**Cl was

dissolved by sonication in 2 mL pD 7 0.1 NaP_i, added to the working electrode compartment of an H-cell, and degassed for 15 min. The counter electrode compartment was charged with 2 mL pD 7 0.1 NaP_i. The solution was electrolyzed at –1.0 V for 6 h, transferred to a N_2 purged bomb flask, and brought into a glovebox. Different volumes of the electrolyzed solution (100, 200, and 300 μL) were added to three samples containing 3.5 mmol **1**Cl and dioxane, and the total volume was brought to 500 μL (Scheme 4.2). Samples were monitored by ^{1}H NMR, and equilibrium of the experimental samples was quickly achieved; though the samples were monitored over 25 h by ^{1}H NMR (Figure 4.14), equilibrium (K_{eq} = 0.35) was established by the first time point, giving $\Delta\Delta°G_{H^-}$ = 0.6±0.1 kcal·mol^{-1}.

Scheme 4.2. Representative hydride equilibration reaction.

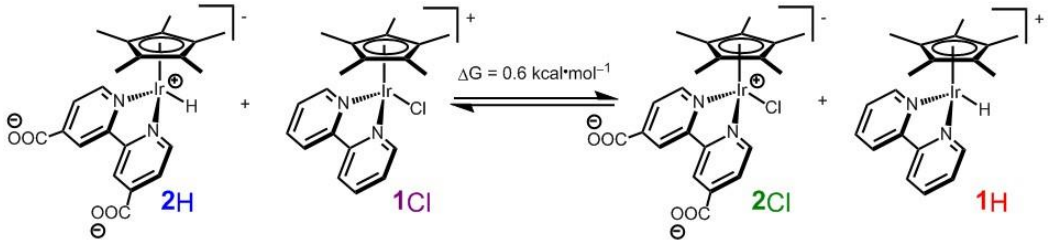

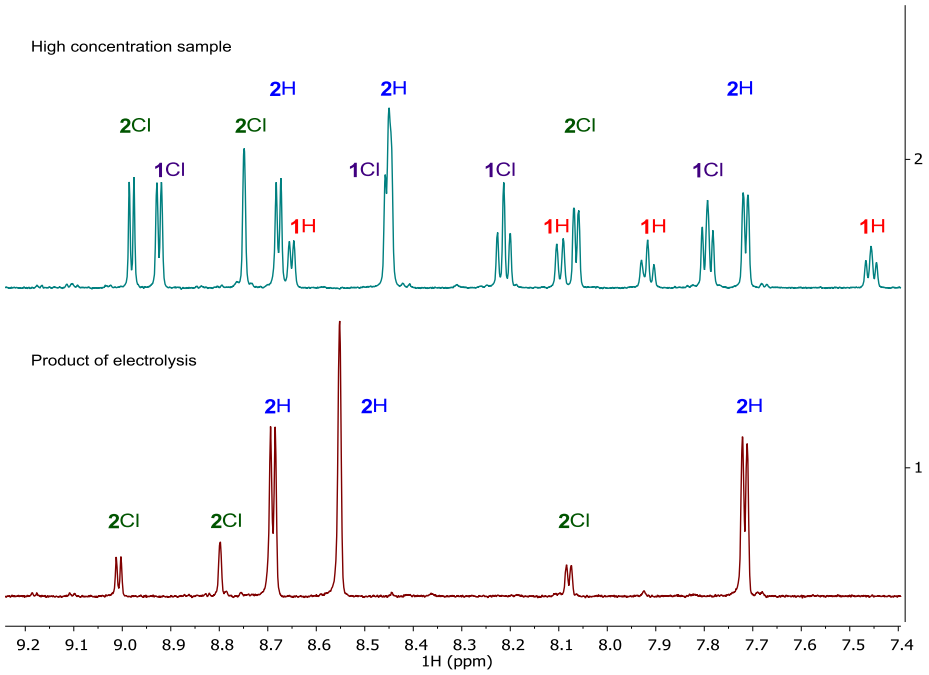

Figure 4.14. Representative ^{1}H NMR spectrum of a typical hydride equilibrium experiment. (top) Equilibrium mixture of **1**H, **1**Cl, **2**H, and **2**Cl formed from the addition of **1**Cl to the mixture of **2**H and **2**Cl formed from electrolysis (bottom).

Alternatively, following protonation with HCl·Et_2O, the solid hydride was extracted into the NMR solvent (either pD 7 0.1 M NaP_i or pD 4.3 20 mM NaOAc with dioxane internal standards), filtered to remove any residual Cp*Ir(bpy-X) or (arene)Ru(bpy-X), and combined with a hydride acceptor. Equilibration was followed by ^{1}H NMR. In a representative experiment (Scheme 4.3), 2.0 mg [Cp*Ir(bpy)(H)][Cl] (0.004 mmol) was dissolved in 490 µL pD 7 0.1 M NaPi with 10 µL 0.5 M dioxane as an internal standard. After confirming the purity of the hydride sample by ^{1}H NMR (Figure 4.15) 2.1 mg [Cp*Ir(bpy-Me)(Cl)][Cl] (0.004 mmol) was added to the NMR tube as a solid. $\Delta\Delta G°_{H-}$ was determined to be 0.4±0.1 kcal·mol^{-1}.

Scheme 4.3. Representative hydride equilibration reaction.

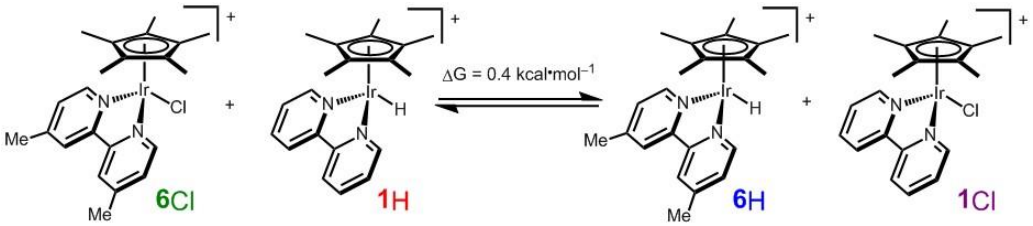

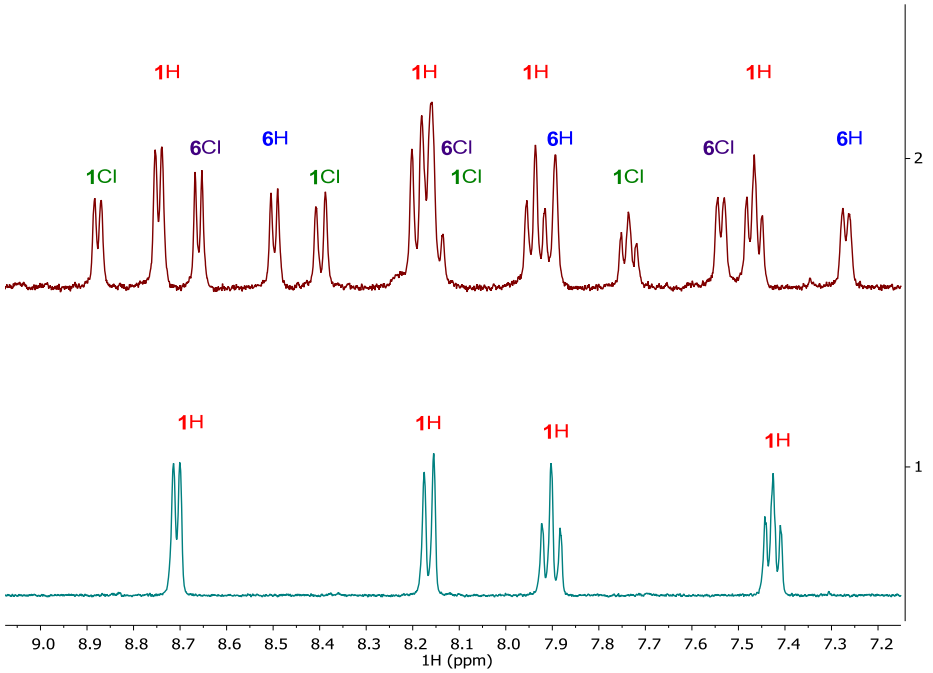

Figure 4.15. Representative ^{1}H NMR spectrum of a typical hydride equilibrium experiment. (top) Equilibrium mixture of **1**H, **1**Cl, **6**H, and **6**Cl formed from the addition of **6**Cl to **1**H formed synthetically (bottom).

Aquo-Chloride Association Equilibria. For each species, a series of solutions of known concentration of chloride were prepared in pD 7 NaP_i and monitored by NMR to ensure that the aquo, phosphate, and chloride species were in equilibrium. For example, in air, a 5.5 mM solution of $[Cp^*Ir(bpy\text{-}COOH)(OH_2)][OTf]_2$ in 50 mM pD 7 NaP_i with a dioxane internal standard was split between 6 samples each containing dry NaCl to produce final solutions with $[Cl^-]$ from 0 mM to 18 mM. The samples were monitored by ^{1}H NMR over 24 hours to ensure that equilibrium had been established between [Cp*Ir(bpy-

COO)(OH_2)]^0, [Cl^-] and [Cp*Ir(bpy-COO)(Cl)]$^-$. The initial [Cl^-] left from the halide abstraction with AgOTf was fit by minimizing the variance of ΔG of the 0 mM NaCl added sample with that of the remaining 5 samples. The free energy of the ligand exchange was found to be –4.4±0.2 kcal·mol^{-1}. The relative aquo-phosphate association free energy was determined similarly with solutions of increasing total [P_i] at pD 7.

CHAPTER 5: CYCLOPENTADIENE-MEDIATED HYDRIDE TRANSFER FROM RHODIUM COMPLEXES

5.1 Introduction

Transition metal catalysts capable of selective hydride transfer to the enzyme cofactor nicotinamide adenine dinucleotide (NAD^+) to form the 1,4-reduced product (1,4-NADH) are critical links between organometallic and enzymatic catalysis in emerging strategies in sustainable, enantioselective organic synthesis.[52–55] Biocompatible catalytic routes for 1,4-NADH regeneration provide access to the enzymatic hydride transfer reactivity without stoichiometric amounts of the complex molecule 1,4-NADH.[121] Of the organometallic catalysts that have been shown to regenerate NADH, rhodium complexes have emerged as selective and efficient catalysts for reduction at the 4-position of nicotinamides, spurring innovation in tandem bio-organometallic catalysis (Scheme 5.1).[53]

In the presence of a precatalyst like $[Cp^*Rh(bpy)(OH_2)]^{2+}$ (**2**; Cp* is pentamethylcyclopentadienyl and bpy is 2,2'-bipyridine), generation of 1,4-NADH can be accomplished using chemical reductants (e.g. formate) or by electrochemical methods (by $1H^+/2e^-$). The mechanism is typically proposed to proceed *via* $[Cp^*Rh(bpy)(H)]^+$ as rhodium hydride intermediate with selectivity directed by coordination of NAD^+ to the Rh centre after an η^5- to η^3-Cp* ring slip.[122] Drawing on this mechanism, Cp*Rh(bpy)-based catalysts have been applied in ketone and aldehyde reductions[123,124] and hydrogen evolution.[91,125]

After considering the hydricity, or hydride donor ability, of the iridium analogues $[Cp^*Ir(bpy)(H)]^+$ (Chapter 4),[126] we were interested in the comparison to $[Cp^*Rh(bpy)(H)]^+$. Relatively few hydricity values have been determined in water, and these Rh complexes provided an opportunity to learn more about an important catalytic intermediate and add new data to the emerging area of aqueous hydricity.[48–50,127]

Scheme 5.1. Tandem catalytic cycle for Rh, NAD^+, and enzyme mediated reductions

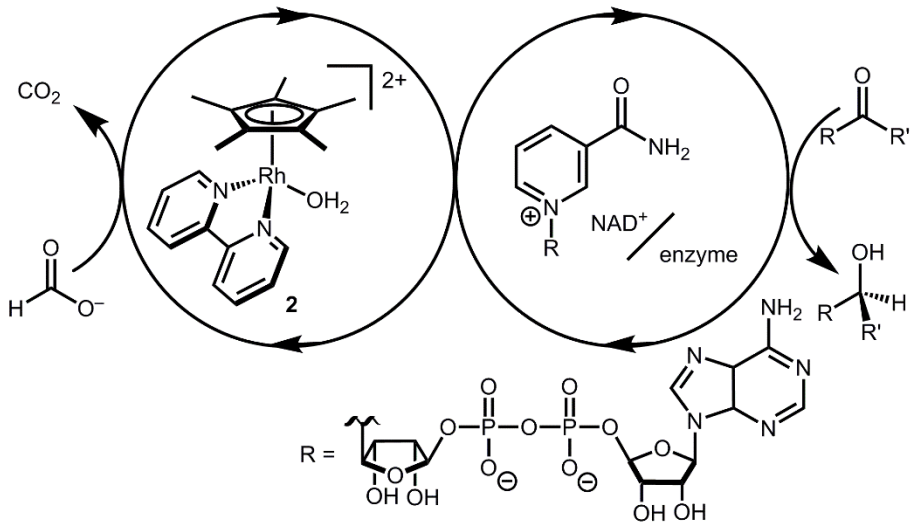

5.2 Results and Discussion

Formation of a (Cp*H)Rh complex. In order to determine the hydricity of the proposed $[Cp^*Rh(bpy)(H)]^+$ intermediate, we first needed a preparative route for this species, which had not previously been isolated. Reduction of $[Cp^*Rh(bpy)(Cl)][Cl]$ in a pH 5 formate solution (following a procedure that cleanly generates the Ir analogue $[Cp^*Ir(bpy)(H)][PF_6]$)[128] produces a dark red solution from which a green solid precipitates on addition of $[NH_4][PF_6]$. Dissolution of the solids in CD_3CN cleanly produced a red solution containing a new species. Surprisingly, the Cp* methyl resonances were not equivalent: two singlets (6H integration each) and a doublet (J = 6.2 Hz, 3H) presented in the

aliphatic region. A quartet (δ 2.31, J = 6.2 Hz, 1H) indicated a pentamethylcyclopentadiene (Cp*H) fragment containing a new C–H bond (Figure 5.1).

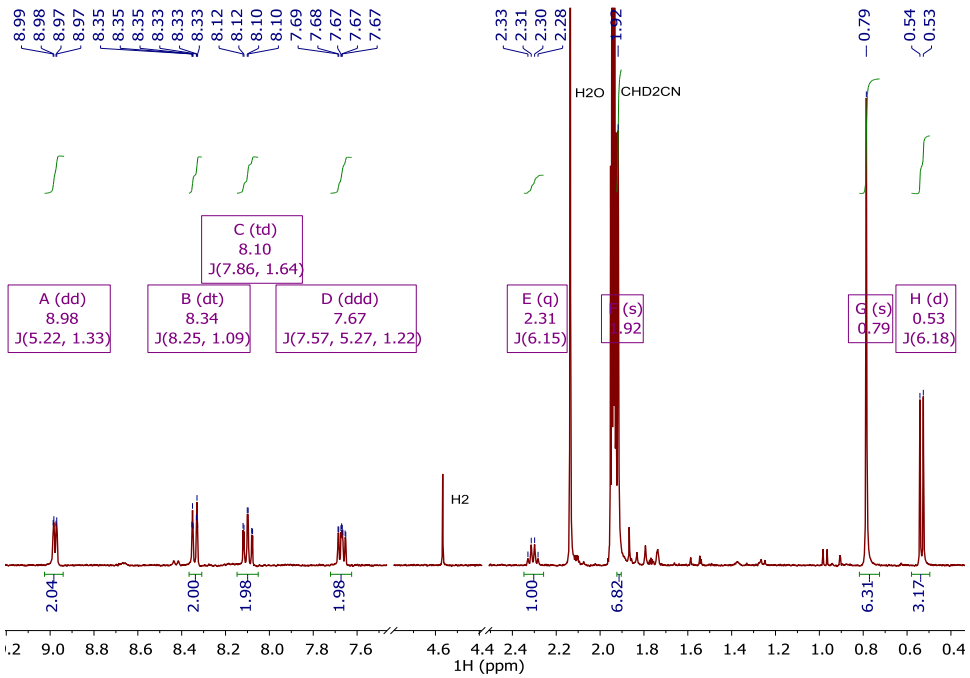

Figure 5.1. ^{1}H NMR spectrum of [(Cp*H)Rh(bpy)(NCCD$_3$)][PF$_6$] in CD$_3$CN.

An alternative procedure involving protonation of a reduced Cp*Rh(bpy) (**1**) species was also attempted. Reduction of [Cp*Rh(bpy)(Cl)][Cl] by NaBH$_4$ in 1 M NaOH led to precipitation of dark purple **1**. Dropwise addition of a dilute solution of HCl·Et$_2$O to an ethereal solution of **1** produced a Cp*H-containing product similar to the one described above.

Crystals suitable for X-ray diffraction were prepared by vapor diffusion of DCM and pentane. The resulting molecular structure revealed the product to be (Cp*H)Rh(bpy)(Cl) (**2**), a Rh(I) complex containing a η^4-pentamethylcyclopentadiene ligand with the new C–H bond endo with respect to the metal center (Figure 5.2). Crystallographic data and refinement

details are given in Table 5.1.The long C1–C2 distance (1.517(2) Å) compared to the short C2–C3 (1.440(3) Å) distance confirm that the species is a diene. In contrast, the crystal structure of complex **1** shows only a 0.034 Å difference amongst the cyclopentadienyl C–C bonds.[88] Aromaticity has clearly been broken with a C2'–C1–C2–C3 torsional angle of 31.9(2)° compared to 3.418° in **1**. Crystal data, data collection parameters, and structure refinement for **2** are listed in Table 5.1. The bromide analogue (Cp*H)Rh(bpy)(Br) was concurrently isolated by Winkler, Gray and Blakemore and was being investigated relating to H_2 evolution in acetonitrile.[129]

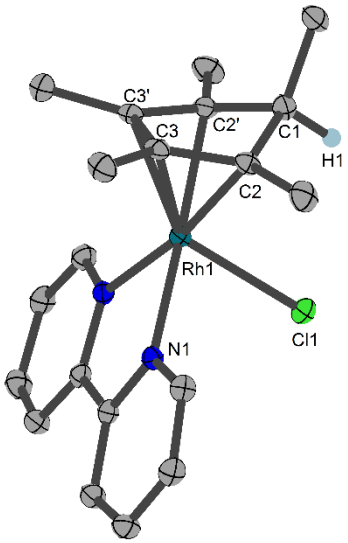

Figure 5.2. Structural representation of **2** with ellipsoids drawn at the 50% probability level (containing a mirror plane that bisects the Cp*H and bpy ligands). A co-crystallized CH_2Cl_2 solvent molecule and hydrogen atoms removed for clarity. Selected distances (Å) and angles (deg): C1–C2 1.517(2), C2–C3 1.440(3), Rh1–N1 2.1157(15), Rh1–Cl1 2.5440(6), C2'–C1–C2–C3 31.9(2)

Table 5.1. Crystal data and structure refinement for 2.

Empirical formula	$C_{21}H_{26}Cl_3N_2Rh$
Formula weight	515.70
Temperature/K	100
Space group	Pnma
a/Å	22.5211(11)
b/Å	12.1599(6)

c/Å	7.8427(4)
Volume/Å^3	2147.76(19)
Z	4
μ/mm^{-1}	9.921
Crystal size/mm^3	0.282 × 0.143 × 0.035
Radiation	CuKα (λ = 1.54178)
Reflections collected	18815
Independent reflections	2224 [R_{int} = 0.0258, R_{sigma} = 0.0153]
Goodness-of-fit on F^2	1.112
Final R indexes [I>=2σ (I)]	R_1 = 0.0220, wR_2 = 0.0549
Final R indexes [all data]	R_1 = 0.0224, wR_2 = 0.0552

Scheme 5.2. Alternative routes to diene 2.

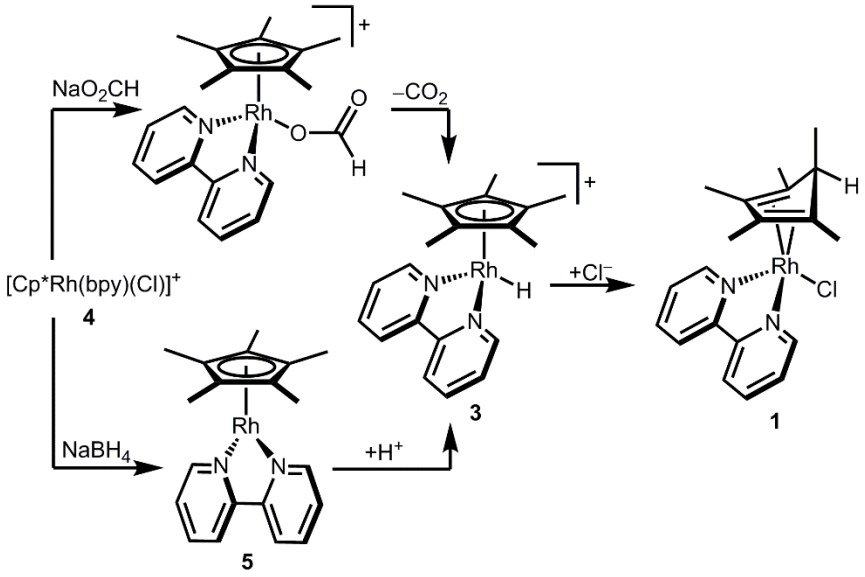

The structure of the complex yields clues about the probable mechanism of its formation. The endo orientation of the hydride is consistent with C–H bond-forming reductive elimination of Cp* and a Rh–H. Reductive elimination of Cp* with hydride ligands has been observed from Rh and Ir metal hydrides with dissociation of the free diene.[130,131] As shown in Scheme 5.2, a Rh hydride intermediate is also consistent with the observation that the Cp*H product is formed both by hydride transfer from formate and by protonation of **1**.

The intermediacy of a hydride was probed by low temperature NMR experiments. Indeed, protonation of **1** with HCl at 233 K allowed the observation of a Rh–H resonance in by ^{1}H NMR (δ –9.60, J_{RhH} = 19.9 Hz, Figure 5.3), which converted to diene complex **2** upon warming.

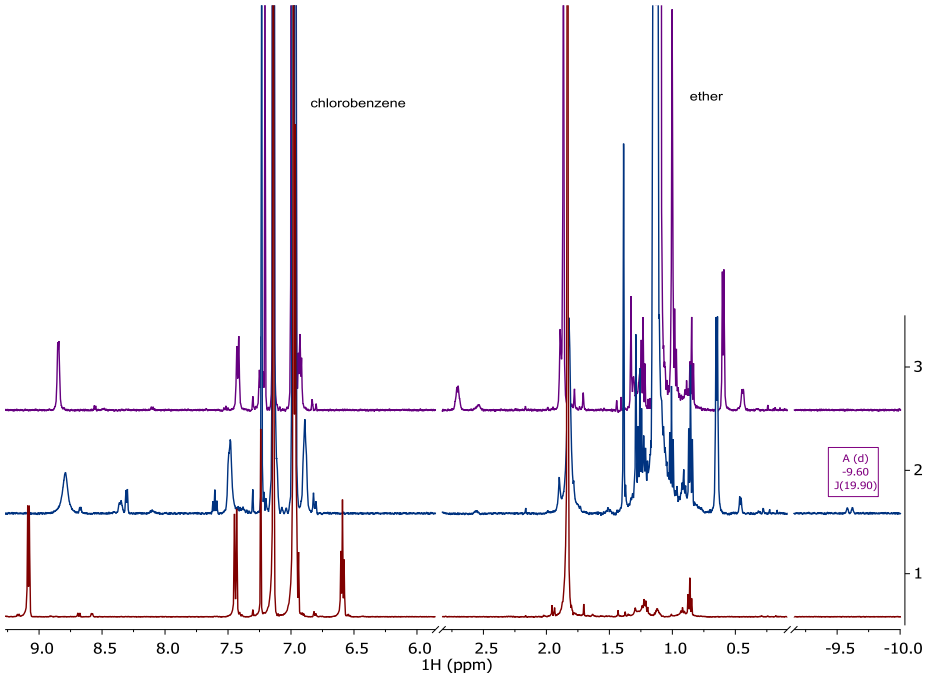

Figure 5.3. ^{1}H NMR spectra showing the low temperature protonation of Cp*Rh(bpy) (4.8 mg, 0.012 mmol) in C_6D_5Cl (red). After injection of 5.5 µL 2.0 M HCl·Et_2O in an acetonitrile/dry ice bath. Spectrum recorded at 238 K (blue). After warming to 293 K (purple). A hydride resonance at –9.60 ppm at low temperatures is evidence for the intermediacy of $[Cp^*Rh(bpy)(H)]^+$ in the formation of (Cp*H)Rh(bpy)(Cl).

Density functional theory (DFT) calculations are consistent with a Rh hydride intermediate that is unstable towards C–H reductive elimination. As illustrated in Scheme 5.3 and tabulated in Table 5.2, reductive elimination of the Rh hydride to form the Cp*H complex is favorable by –4.1 kcal·mol^{-1}. In contrast, for the Ir analogue $[Cp^*Ir(bpy)(H)]^+$, which has been isolated and structurally characterized,[128] formation of Cp*H is predicted to be unfavorable by 8.1 kcal·mol^{-1}. Interestingly, the only prior report of a similar bpy-

supported Rh hydride complex is the methyl-substituted complex [Cp*Rh(6,6'-Me-bpy)(H)]$^+$, which features steric bulk that might influence this equilibrium.[64]

Scheme 5.3. Relative free energies for reductive elimination of Cp*H from M–H (M = Rh, Ir) in acetonitrile solvent from DFT

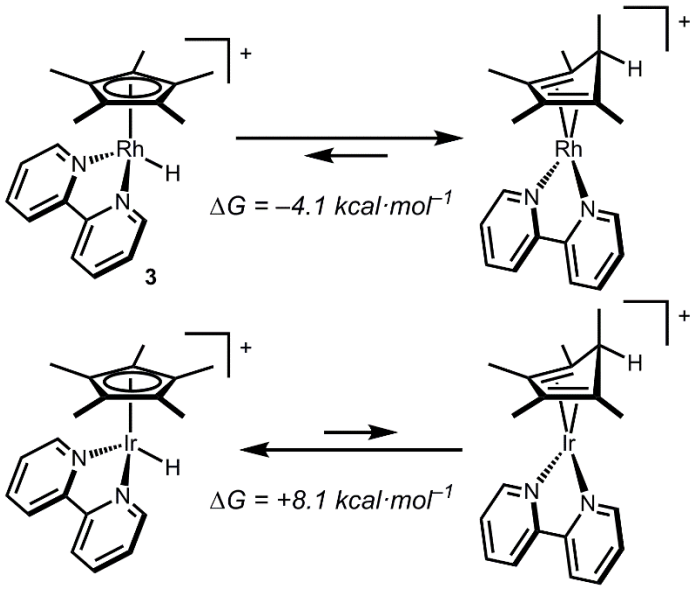

Table 5.2. Overview of calculated change in electronic energy (ΔE), enthalpy (ΔH), entropy (ΔS), and free energy (ΔG) for the isomerization of rhodium and iridium hydrides.

Reaction	ΔE (kcal·mol^{-1})	ΔH (kcal·mol^{-1})	ΔS (cal·mol^{-1}·K^{-1})	ΔG (kcal·mol^{-1})
[Cp*Rh(bpy)(H)]$^+$ → [(Cp*H)Rh(bpy)]$^+$	–6.17	–4.02	0.097	–4.05
[Cp*Ir(bpy)(H)]$^+$ → [(Cp*H)Ir(bpy)]$^+$	+5.91	+7.89	–0.62	+8.07

The apparent instability of the Rh hydride intermediate with respect to reductive elimination raises questions about how Cp*Rh-based catalysts mediate hydride transfer reactions. Diene **2** could undergo hydride transfer indirectly via a Rh–H intermediate, or *via* a C–H bond-breaking direct hydride transfer. The latter mechanism illustrates the similarity

between diene **2** and a variety of transition metal complexes ligated by organic hydride donors and acceptors that have been created.[132–134]

Reactivity of diene 2. To better understand complex **2**, we sought to measure the hydricity and establish hydride transfer reactivity. We focused on the closely related complex $[(Cp^*H)Rh(4,4'\text{-}COO\text{-}bpy)]^-$ (**2coo**) due to its favorable solubility profile in water. For Ir–H complexes, carboxylate substitution has a very minor impact on hydricity,[126] and with the additional distance to the substitution site, the impact on hydricity is expected to be similarly minor for (Cp*H)Rh complexes.

The hydricity ($\Delta G°_{H-}$, eq. 5.5) was established by determining the pK_a of the diene complex (eq. 5.1), the reduction potential of $[Cp^*Rh(bpy\text{-}COO)(OH)]^-$ (**3coo**) (eq. 5.2) and the pK_a of the Rh^{III} aquo complex $Cp^*Rh(bpy\text{-}COO)(OH_2)$ (eq. 5.3). Combining these experimental values with the constant free energy of 2e$^-$proton reduction (eq. 5.4)[47] provides $\Delta G°_{H-}$ according to Eq. 5.6.

$$\mathbf{2coo} \leftrightarrows \mathbf{1coo} + H^+ \quad (5.1)$$

$$\mathbf{1coo} + OH^- \leftrightarrows \mathbf{3coo} + 2e^- \quad (5.2)$$

$$\mathbf{3coo} + H^+ \leftrightarrows Cp^*Rh(bpy\text{-}COO)(OH_2) \quad (5.3)$$

$$H^+ + 2e^- \leftrightarrows H^- \quad (5.4)$$

$$\mathbf{2coo} \leftrightarrows Cp^*Rh(bpy\text{-}COO)(OH_2) + H^- \quad (5.5)$$

$$\Delta G°_{H-} = (1.364)pK_{a(1)} - (-46.12)E° - (1.364)pK_{a(3)} + 34.2\ \text{kcal}\cdot\text{mol}^{-1} \quad (5.6)$$

The reduction potential was measured by cyclic voltammetry (CV) in aqueous phosphate electrolyte. Above pH 9, the 2e⁻ reduction of [Cp*Rh(bpy-COO)(OH)]⁻ (**3coo**) to [Cp*Rh(bpy-COO)]$^{2-}$ is quasi-reversible (ΔE_p = 30-80 mV across the pH range) and $E_{1/2}$ shifts cathodically by 24.6 mV per pH unit, close to the ideal 29.5 mV per pH unit shift expected for a 1OH⁻/2e⁻ process (Figure 5.4). Extrapolating this trend to pH 0 (the standard state of aqueous thermodynamics in eqs. 5.1-5.5) provides the formal potential, $E°$ = –0.25 V, for the reduction of the hydroxide complex.

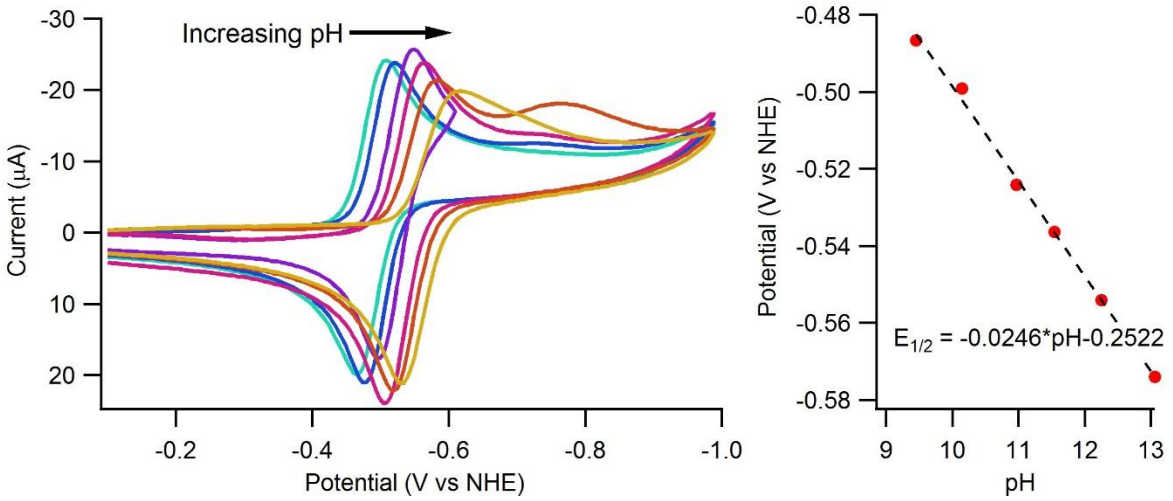

Figure 5.4. The shift of the 2e⁻ reduction of [Cp*Rh(bpy-COO)(OH)]⁻ at 100 mV/s as the pH increases from 9.5 to 13.0 (left). $E_{1/2}$ of the reduction plotted against pH to extrapolate to pH 0 (right).

To confirm that products of electrochemical reduction, controlled potential electrolysis (CPE) of hydroxide **3coo** was performed under basic conditions. CPE of **3coo** resulted in a midnight blue solution after passing 2e⁻ per Rh of charge (Figure 5.5). Upon addition of pD 7 0.1 M sodium phosphate buffer, the blue solution turned red and ^{1}H NMR spectroscopy confirmed formation of **2coo**, as indicated by the characteristic 6:6:3 pattern of the Cp* methyl resonances in the aliphatic region.

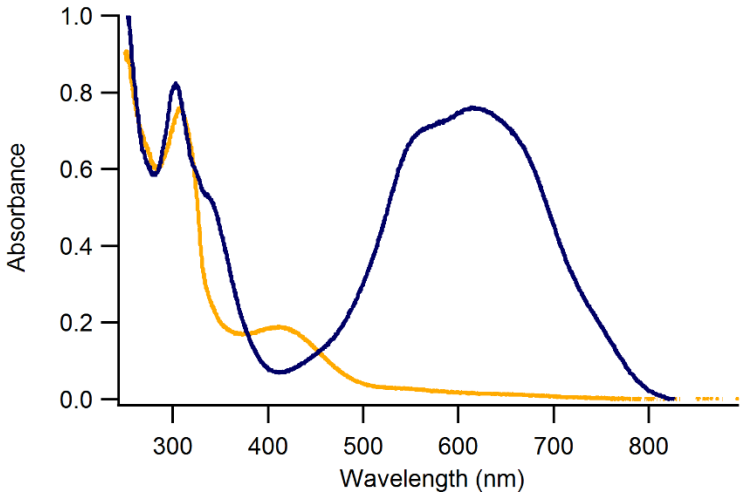

Figure 5.5 UV-vis spectra of $[Cp^*Rh(bpy\text{-}COO)]^{2-}$ formed electrochemically at pH 11.2 (blue) and added to a pH 7 0.1 M sodium phosphate buffer to protonate (yellow).

The acidity of diene complex **2coo** has an estimated pK_a < 10 based on a spectrophotometric titration adding acid to an aqueous solution of $[Cp^*Rh(bpy\text{-}COO)]^{2-}$ (Figure 5.6). Both the basic starting material and its conjugate acid were observed to react on the timescale of the experiment, which leads to lower than expected absorbance at 610 nm and produces an artificially low [Cp*Rh]/[(Cp*H)Rh] ratio — and thus an overestimate of the pK_a.

The relative instability of these Rh species led us to carry out a complementary electrochemical titration by monitoring the growth of the oxidation of **1coo** by CV as a function of solution pH, which provided pK_a > 8 (Figure 5.7). The scan rate dependence indicates that protonation is slow on the electrochemical time scale. As the scan rate decreases, the reaction has longer to approach equilibrium, leading to an increase in apparent pK_a — and therefore an underestimate of the true pK_a. Each method provides a limiting value, and we, therefore, estimate that **2coo** has pK_a = 9 ± 1.

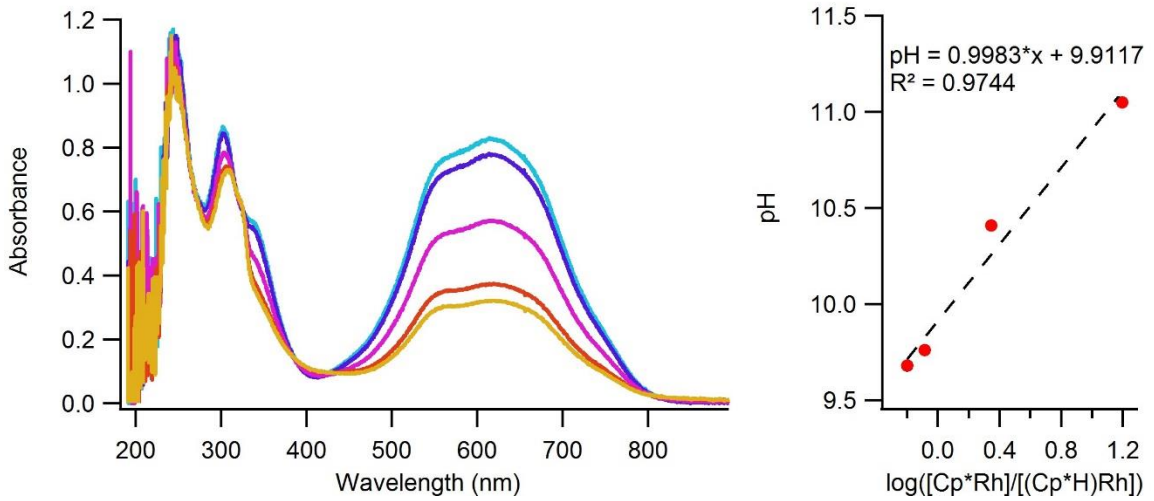

Figure 5.6. Spectrophotometric titration of $[Cp^*Rh(bpy\text{-}COO)]^{2-}$ with addition of acid to form $[(Cp^*H)Rh(bpy\text{-}COO)]^{-}$ (left) and analysis of the absorbance at 610 nm to the Henderson-Hasselbalch equation giving pK_a = 9.9 (right).

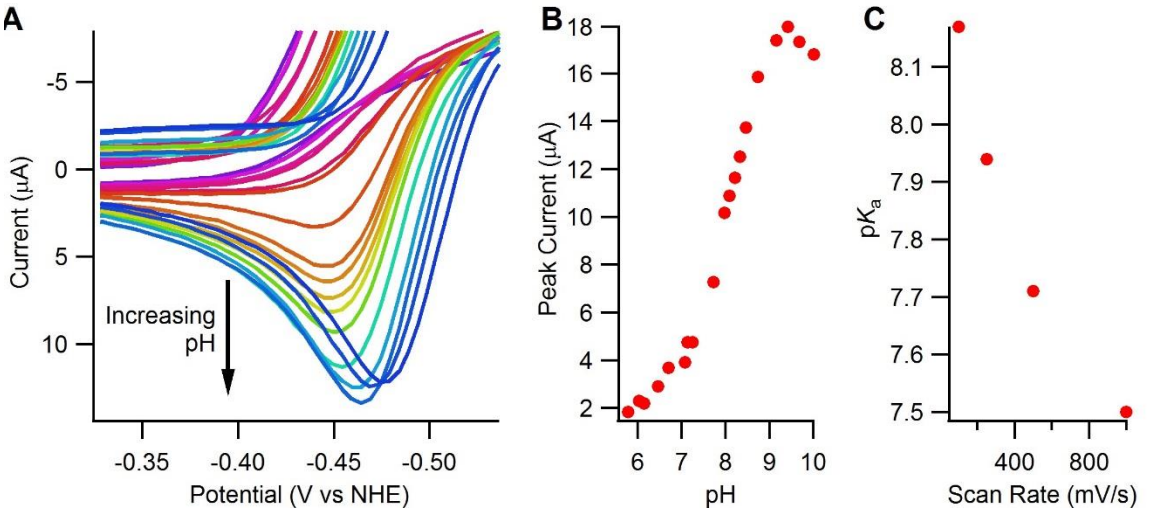

Figure 5.7. (A) CV of [Cp*Rh(bpy-COOH)(Cl)][Cl] in pH 5.8 to pH 10 phosphate electrolyte at a scan rate of 100 mV/s, expanded to highlight the return wave attributed to oxidation of $[Cp^*Rh(bpy\text{-}COO)]^{2-}$. In acidic water, $[Cp^*Rh(bpy\text{-}COO)]^{2-}$ is protonated to form $[(Cp^*H)Rh(bpy\text{-}COO)]^{-}$. The increasing oxidative peak current with increasing pH indicates higher concentrations of $[Cp^*Rh(bpy\text{-}COO)]^{2-}$ as pH increases. (B) Plot of oxidative peak current vs. pH. At each scan rate this sigmoid was fit to the Henderson-Hasselbalch equation to determine a pK_a. (C) Plot of apparent pK_a vs. scan rate.

The Rh^{III} species exists as the aquo Cp*Rh(bpy-COO)(OH_2), not the hydroxo **3coo**, under the neutral, aqueous conditions of most catalysis.[125] Incorporation of the pK_a of the aquo complex (8.8 by spectrophotometric titration) accounts for this protonation state.

Based on the experimentally determined $E°$ and pK_a values, Eq. 6 provides the aqueous hydricity of $[(Cp*H)Rh(bpy\text{-}COO)]^-$ to form Cp*Rh(bpy-COO)(OH_2): $\Delta G°_{H^-}(OH_2)$ = 23 ± 2 kcal·mol^{-1}.

Hydride transfer to complex Cp*Rh(bpy-COO)(OH_2) from species with $\Delta G°_{H^-}$ < 23 kcal·mol^{-1}, and hydride transfer to $[Cp*Rh(bpy)(OH_2)]^{2+}$ is expected to proceed with similar driving forces (*vide supra*). As expected, $[(C_6Me_6)Ru(bpy)(H)]^+$ ($\Delta G°_{H^-}(OH_2)$ = 22 ± 1 kcal·mol^{-1}) reacts with $[Cp*Rh(bpy)(Cl)]^+$ (Cl^- is displaced in water[125]) to produce the corresponding hydride transfer product **2** (Scheme 5.4). The product slowly decomposed, preventing the system from reaching equilibrium. Transfer does not occur from weaker hydride sources: combining $[Cp*Ir(bpy\text{-}COO)(H)]^-$ ($\Delta G°_{H^-}(OH_2)$ = 32.0 kcal·mol^{-1}) with $[Cp*Rh(bpy)(Cl)]^+$ results in no reaction. In accord with the hydricity values, in the reverse reaction (Cp*H)Rh(bpy)(Cl) reacted completely with $[Cp*Ir(bpy\text{-}COO)(Cl)]^-$ to form $[Cp*Ir(bpy\text{-}COO)(H)]^-$.

Scheme 5.4. Selected hydride transfer reactions.

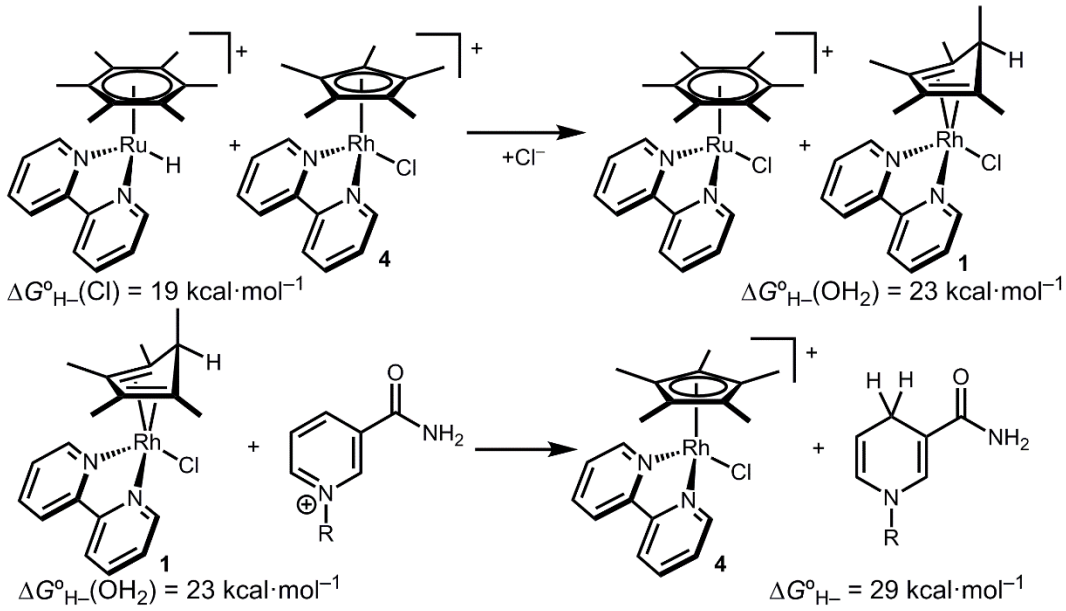

After establishing the viability of diene complex **2** in hydride transfer reactions with transition metal complexes, we turned our attention to hydride transfer involving NAD^+. The hydricity of NADH is 29 kcal·mol^{-1},[135,136] so the Rh diene complex **2** should be sufficiently hydridic to reduce NAD^+. A red solution of isolated (Cp*H)Rh(bpy)(Cl) quickly turned yellow on addition of NAD^+. ^{1}H NMR spectroscopy confirmed consumption of (Cp*H)Rh(bpy)(Cl) and selective production of 1,4-NADH within 15 minutes (Figure 5.8).

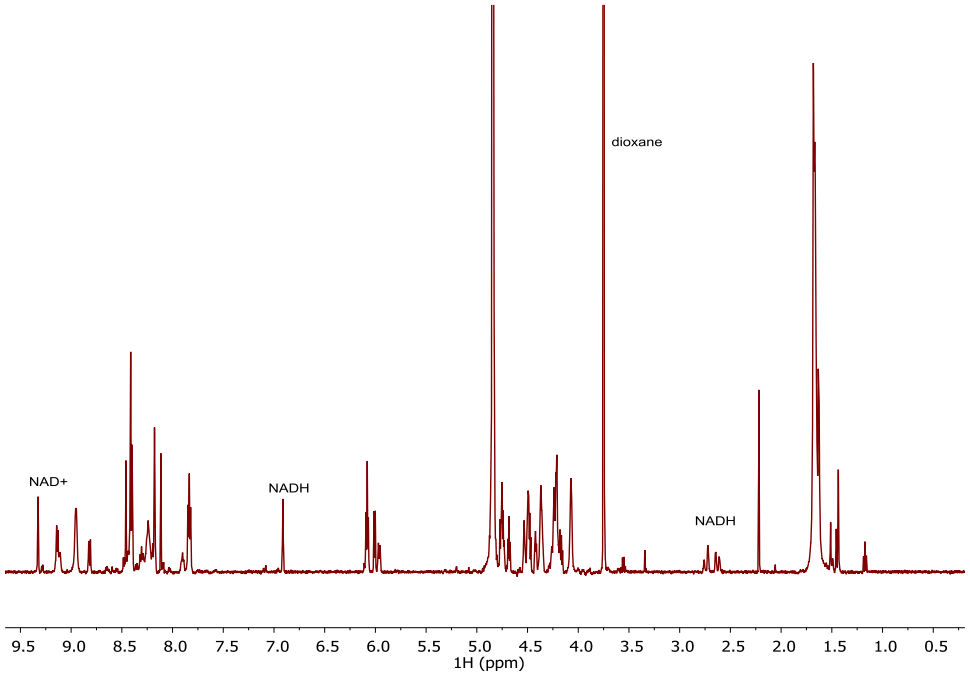

Figure 5.8. ^{1}H NMR spectrum of a solution of (Cp*H)Rh(bpy)(Cl) after addition of 2.7 mg NAD^+ (4.1 μmol) in pD 7 0.1 M NaP_i. The Rh species has reacted completely (best seen by the absence of any resonance at 0.7 ppm), and NADH has appeared. The nicotinamide singlet shifts from 9.3 ppm to 6.9 ppm upon reduction and a pair of diastereotopic protons appear at 2.6 and 2.7 ppm. Assignments where made by comparison to authentic samples in the same solutions and by comparison to ref. [137].

Finally, we assessed the viability of diene species **2** as an intermediate on the NAD^+ reduction cycle by mimicking various chemical and electrochemical catalytic conditions typically employed. Reduction of $[Cp^*Rh(bpy)(Cl)]^+$ in D_2O with 10 equiv formate forms the red hydride migrated complex immediately, as judged by the appearance of a 6:6:3 pattern in the Cp* region. The same species is also formed upon reduction of $[Cp^*Rh(bpy)(Cl)]^+$ at -0.64 V vs NHE in pD 7 0.1 M phosphate buffer. Even treatment of $[Cp^*Rh(bpy)(OH_2)]^{2+}$ with 1 atm H_2 in pD 7 0.1 M phosphate buffer produced diene **2** (Figure 5.9).

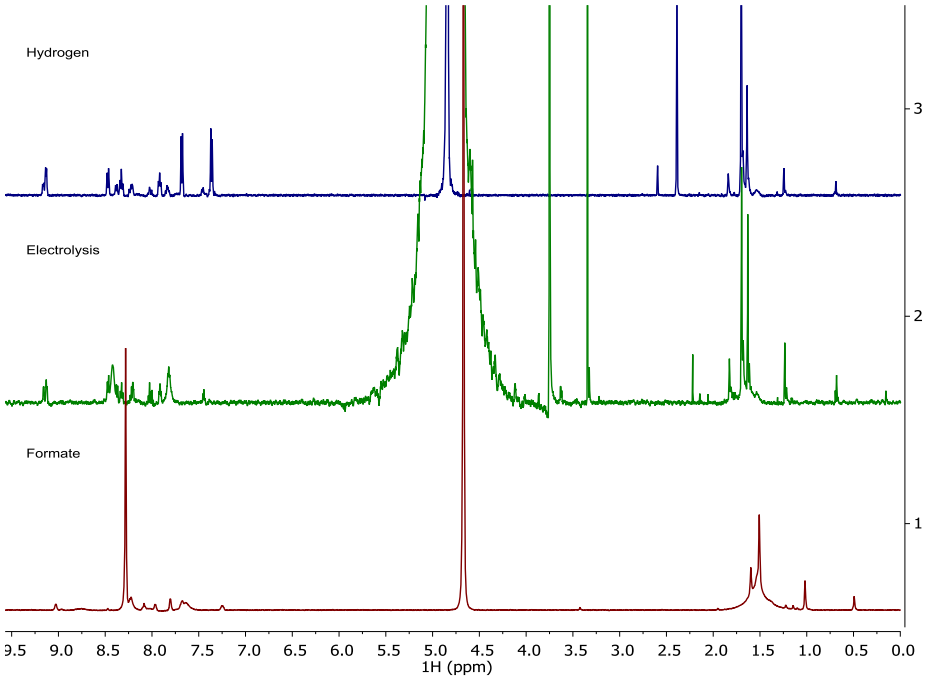

Figure 5.9. ^{1}H NMR spectra showing the formation of diene products (indicated by a 6:6:3 pattern in the aliphatic region) under catalytic conditions. (top) $[Cp^*Rh(bpy)(OH_2)]^{2+}$ under an atmosphere of H_2 in pD 7 0.1 M NaP_i, referenced to sodium tosylate. (middle) Product of electrolysis of $[Cp^*Rh(bpy)(Cl)]^{+}$ at –0.64 V in 80:20 pD 7:pH 7 0.1 M NaP_i, referenced to dioxane. (bottom) $[Cp^*Rh(bpy)(Cl)]^{+}$ in D_2O with 10 equiv of sodium formate, referenced to formate.

The presence of **2** under catalytically relevant conditions indicates that it is a viable intermediate. Complex **2** is not the only Rh species in these solutions, however, and this species does not exhibit long term stability under aqueous conditions. Bubbles formed on the walls of NMR tubes containing **2** in neutral aqueous solutions, indicating H_2 evolution. The Cp* methyl protons also scrambled H for D. Such scrambling has been observed for Cp* ligands and typically proceeds through a base-assisted mechanism *via* fulvene intermediates.[138,139] We have also observed the per-deuteration of Cp* in $[Cp^*Ir(bpy\text{-}COO)(H)]^{-}$ by ^{1}H, ^{2}H NMR and MS (Figure 5.10), but deuteration in the Ir manifold occurs over the course of weeks, while deuteration in the Rh manifold occurs over the course of

hours. Broad resonances shifted slightly upfield of each proteo Cp*H signal appear quickly before the signals slowly disappear altogether.

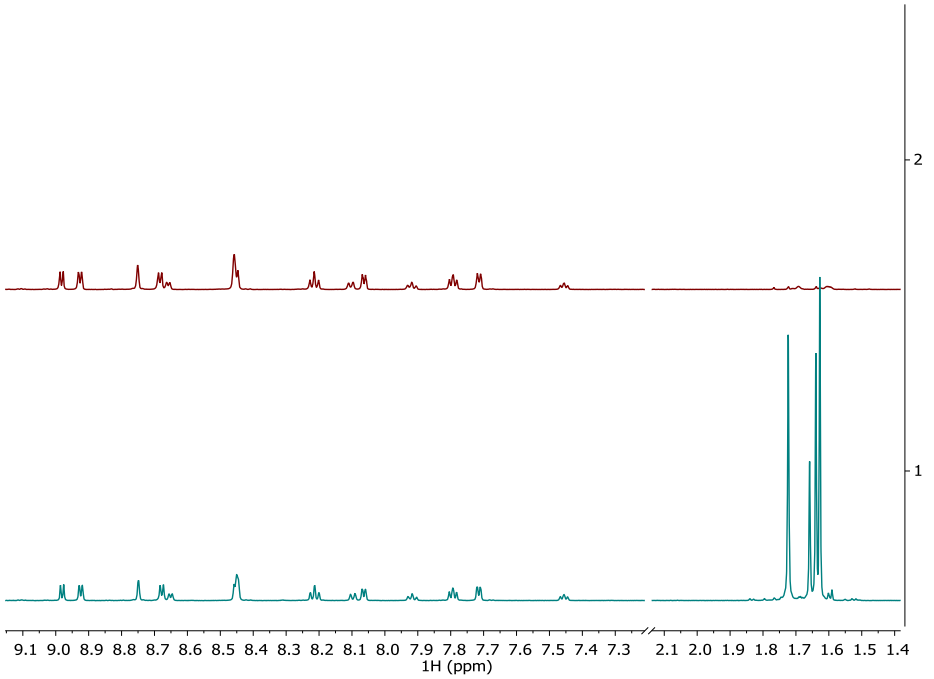

Figure 5.10. ^{1}H NMR spectra showing an equilibrium mixture of $[Cp^*Ir(bpy)(H)]^+$, $[Cp^*Ir(bpy)(Cl)]^+$, $[Cp^*Ir(bpy\text{-}COO)(H)]^-$, and $[Cp^*Ir(bpy\text{-}COO)(H)]^-$ (formed by mixing electrochemically produced $[Cp^*Ir(bpy\text{-}COO)(H)]^-$ with $[Cp^*Ir(bpy)(Cl)][Cl]$)[126] shortly after equilibrium had been achieved (bottom) and 7 weeks later (top). The Cp* peaks have disappeared with no changes to the aromatics indicating per-deuteration of the Cp* protons. Deuteration was also observed by ^{2}H NMR. $[(Cp^*\text{-}d_{15})Ir(bpy)(Cl)]^+$ (m/z = 534.21 (calc), 534.33 (obs)) and $[(Cp^*\text{-}d_{15})Ir(bpy\text{-}COONa)(Cl)]^+$ (m/z = 666.16 (calc), 666.20 (obs)) were also observed by mass spec.

Scheme 5.5 combines our new findings with Fish's original mechanistic proposal[122] to construct an alternative mechanistic hypothesis. Starting from the $[(Cp^*)Rh(bpy)(OH_2)]^{2+}$ precatalyst, a $1H^+/2e^-$ reduction (either by a hydride donor, e.g. formate, or through reduced species **1**) transiently produces $[(Cp^*)Rh(bpy)(H)]^+$. Reductive elimination yields a (Cp*H)Rh moiety. The endo orientation of the proton seems to ideally position the C–H bond to deliver hydride to a bound substrate such as NAD^+ ligating the Rh center. Following

hydride transfer, displacement of NADH by water regenerates the initial state of the catalyst. Several other mechanisms can be envisioned, such as hydride transfer via reversible access to the high energy hydride intermediate $[(Cp^*)Rh(bpy)(H)]^+$. The mechanism in Scheme 5.5 offers an alternative path for substrate binding without invoking an η^5 to η^3 Cp* ring slip.

Scheme 5.5. Proposed mechanism for the reduction of NAD^+ through a (Cp*H)Rh(bpy) intermediate. N∪N is 2,2'-bipyridine.

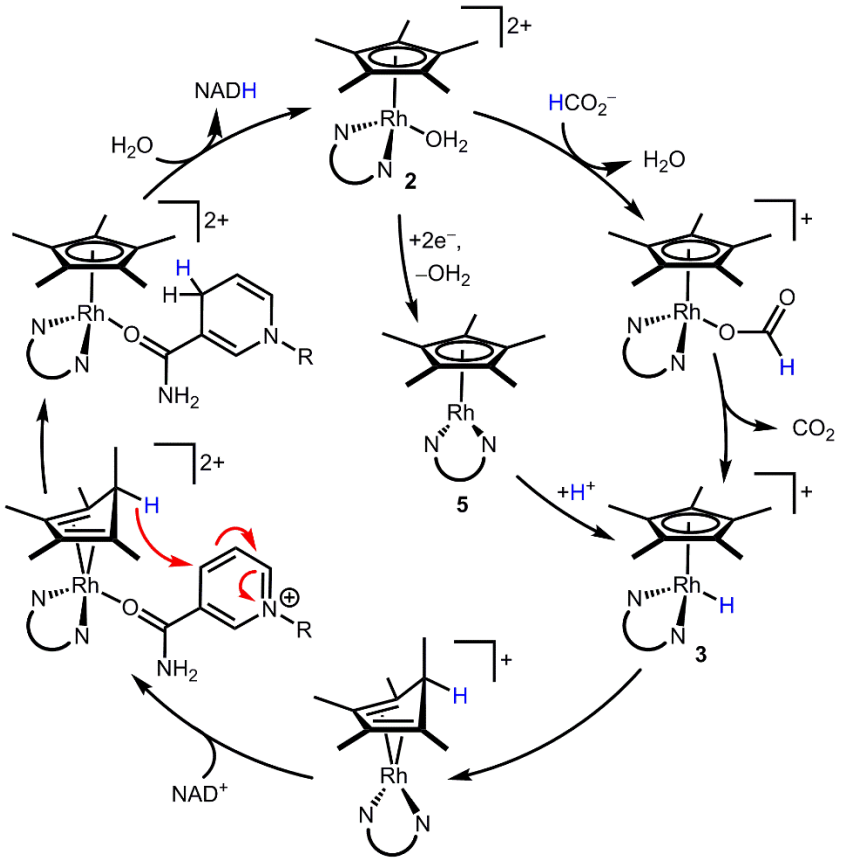

5.3 Conclusions

We have prepared a pentamethylcyclopentadiene complex of Rh that is a plausible intermediate in the selective catalytic reduction of NAD^+ to 1,4-NADH. Hydricity

measurements confirm that diene **1** is thermodynamically capable of hydride transfer to NAD^+. A series of hydride transfer reactions to NAD^+ and other transition metals are consistent with the hydricity value. This surprising ligand-based hydride transfer reactivity, involving the typically innocent pentamethylcyclopentadienyl ligand, suggests new pathways for Cp*Rh-catalyzed management of protons and electrons.

5.4 Experimental Section

General Considerations. Procedures were carried out under nitrogen except where noted. All reagents were commercially available and used without further purification. Commercial HPLC-grade water was used as a solvent, and organic solvents were dried and degassed with argon using a Pure Process Technology solvent system. Deuterated solvents were purchased from Cambridge Isotope Laboratories, Inc. Electrochemical experiments were performed on a Pine WaveNow potentiostat or Pine WaveDriver bipotentiostat controlled by Aftermath software. Details on specific electrochemical experiments are described below. Solution pH was recorded using an OrionStar A111 pH meter with a Beckman-Coulter or Hanna pH probe. UV-Vis spectra were obtained using an Ocean Optics USB2000+ spectrometer with a DT-MINI-2GS deuterium/tungsten halogen light source controlled by OceanView software.

NMR spectra were obtained on 400, 500, or 600 MHz spectrometers. ^{1}H NMR spectra were referenced to the residual solvent signals (or dioxane or NaOTs as an internal standard in D_2O).[78] Spectra were processed using the MestReNova software suite from Mestrelab Research S. L. The solution acidity in NMR experiments is reported as pD,

obtained by addition of +0.4 to the reading of a pH electrode that was calibrated using H_2O standards.[79]

Electrochemistry. Electrochemical experiments were carried out with carbon working electrodes (glassy carbon for cyclic voltammetry and reticulated vitreous carbon for bulk electrolysis), platinum wire counter electrodes, and Ag/AgCl (3M NaCl) reference electrode in a small glass tube fitted with a Vycor glass frit. Solutions were thoroughly degassed by sparging with nitrogen for at least 15 minutes before beginning an experiment or the experiments were carried out in a N_2 filled glovebox. All potentials are reported relative to NHE, with values obtained by adding 0.21 V to the experimentally observed potential *vs.* Ag/AgCl.[81] The glassy carbon working electrode was polished with 0.05 micron alumina powder between scans and cyclic voltammetry was performed in an undivided cell. Controlled potential electrolysis experiments were carried out in a divided H-cell with the working electrode chamber and counter electrode chamber separated by a fine frit.

Synthetic Methods. The complexes $[Cp^*RhCl_2]_2$,[80] [Cp*Rh(bpy)(Cl)][Cl] (**4**),[91] [Cp*Rh(bpy-COOH)(Cl)][Cl],[91] [Cp*Ir(bpy-COOH)(Cl)][Cl],[63] $[(C_6Me_6)Ru(bpy)(H)][Cl]$[126] were prepared according to literature procedures.

*(Cp*H)Rh(bpy)(Cl)* (**1**). To a stirring solution of Cp*Rh(bpy) (10.3 mg, 0.026 mmol) in ether, a dilute solution of $HCl{\cdot}Et_2O$ (50 mM) was added dropwise until a change from a dark purple solution to fine red solids was observed. Typically 1-1.5 eq of HCl were added with the excess acid immediately pumped off after completion of the addition. Alternatively, less than 1 eq of 50 mM HCl in pentane was added to a solution of Cp*Rh(bpy) (10.6 mg, 0.027 mmol) stirring at –30 °C. The red solid that precipitated was filtered off and washed 3× with pentane. Samples of hydride prepared in this way typically contained small amounts

[Cp*Rh(bpy)(Cl)][Cl] (presumably formed by protonation of the diene complex to release H_2). ^{1}H NMR (600 MHz, CD_2Cl_2) δ 8.92 (d, J = 5.2 Hz, 2H), 8.09 (dt, J = 7.9, 1.2 Hz, 2H), 7.87 (td, J = 7.8, 1.6 Hz, 2H), 7.47 (ddd, J = 7.6, 5.3, 1.3 Hz, 2H), 2.50 (q, J = 6.3 Hz, 1H), 1.85 (s, 6H), 0.91 (s, 6H), 0.53 (d, J = 6.2 Hz, 3H). ^{13}C NMR (151 MHz, CD_2Cl_2) δ 154.11, 151.38, 136.47, 125.90, 121.87, 92.17 (d, *J* = 10.1 Hz), 56.10 (d, *J* = 3.7 Hz), 53.26 (br s), 19.38, 12.03, 10.56.

Alternatively, [Cp*Rh(bpy)(Cl)][Cl] (5.8 mg, 0.012 mmol) was dissolved in pH 5 3 M NaO_2CH. After stirring for 30 min, the solution had turned from yellow to dark red, and addition of excess $[NH_4][PF_6]$ resulted in the precipitation of a light green solid. Dissolving this solid in CD_3CN produced a red solution of $[(Cp^*H)Rh(bpy)(NCCD_3)][PF_6]$. ^{1}H NMR (400 MHz, CD_3CN) δ 8.98 (dd, *J* = 5.2, 1.3 Hz, 1H), 8.34 (dt, *J* = 8.3, 1.1 Hz, 1H), 8.10 (td, *J* = 7.9, 1.6 Hz, 1H), 7.67 (ddd, *J* = 7.6, 5.3, 1.2 Hz, 1H), 2.31 (q, *J* = 6.2 Hz, 1H), 1.92 (s, 3H), 0.79 (s, 3H), 0.53 (d, *J* = 6.2 Hz, 1H).

*[Cp*Rh(bpy-COO)]*$^{2-}$ (**5coo**). Electrolysis at –0.89 V of [Cp*Rh(bpy-COOH)Cl][Cl] (4.9 mg, 0.009 mmol) in 1.8 mL 0.1 M Na_2SO_4 electrolyte in D_2O passed –1.67 C (2.0 e^-/Rh) resulting in a royal blue solution of $[Cp^*Rh(bpy\text{-}COO)]^{2-}$. ^{1}H NMR (600 MHz, D_2O) δ 8.85 (br s, 1H), 8.35 (s, 1H), 7.06 (dd, *J* = 6.5, 1.9 Hz, 1H), 1.80 (br s, 7H).

Computational Details.

All calculations were performed using the Gaussian09 software package.[140] The PBE1PBE functional[141] was used for all calculations, with the LANL2DZ basis set[142] and pseudopotential used for Ir and the 6-31G(d,p) basis set[143,144] used for all other atoms. After optimizing the structure, frequency optimizations were performed for each species to compute Gibbs free energy values, ensuring the absence of imaginary frequencies. A

polarizable continuum model (IEFPCM as implemented by Gaussian09) was used to approximate the effects of acetonitrile solvent.

CHAPTER 6: PHOTOCHEMICAL PRODUCTION OF ETHANE FROM AN IRIDIUM METHYL COMPLEX

6.1 Introduction

Photocatalysts capable of mediating C–C bond formation could play an important role in the light-driven generation of energy-dense liquid fuels. Ethane formation from two methyl fragments is the simplest C–C bond forming reaction leading to an alkane, and organometallic methyl complexes have been the subject of photophysical and photochemical inquiry. Though photochemical ethane generation has been observed from metal methyl complexes,[145] such reactivity is notably uncommon.[146]

Many approaches to integrating light absorption with C–C bond formation have been explored. In photoredox catalysis, photosensitizers can trigger C–C bond formation following an excited state electron transfer.[147,148] Photochemical ligand dissociation (which opens a coordination site and triggers migratory insertion) and M–C bond homolysis (leading to radical reactivity) can also lead to formation of C–C bonds.[149] Radicals are a common component of alkyl photochemistry: in the 1980s, Crabtree investigated Hg sensitization, which produces radicals, for various alkane functionalizations.[150] Platinum complexes are also known to couple two alkyl ligands on a single site through a radical mechanism.[151]

In thinking of ways to develop photochemical C–C bond formation, we drew inspiration from our recently discovered, bimolecular mechanism for H–H bond formation from a monohydride.[29] Quantum yields of hydrogen production nearing unity can be achieved when irradiating $[Cp^*Ir(bpy)(H)]^+$ ($[\mathbf{1}]^+$, Cp* is η^5-pentamethylcyclopentadienyl,

bpy is 2,2'-bipyridine) in the presence of acids in CH_3CN. The bond formation is initiated by electron transfer between the excited state $[\mathbf{1}]^{+}$* and the ground state $[\mathbf{1}]^{+}$, producing the reactive species $Cp^*Ir^{II}(bpy)(H)$ and $[Cp^*Ir^{IV}(bpy)(H)]^{2+}$ that together form H_2. This mechanism allows a slightly endergonic excited state electron transfer process to be coupled to an exergonic bond formation.

Given that the Cp*Ir(bpy) scaffold facilitates efficient bimetallic coupling for H_2 evolution, we questioned whether substitution of a methyl group for the hydride could lead to C–C bond formation. Herein we report the synthesis and characterization of the methyl complex, $[Cp^*Ir(bpy)(CH_3)]^{+}$ ($[\mathbf{2}]^{+}$) and our mechanistic investigation of its photochemical C–C bond formation reactivity.

6.2 Results and Discussion

Characterization of an Ir methyl complex. Following the procedure of Chapter 3, the methyl complex $[Cp^*Ir(bpy)(CH_3)][I]$ ($[\mathbf{2}][I]$) was synthesized by electrophilic methylation of the Ir(I) precursor Cp*Ir(bpy) (**3**). The ^1H NMR spectrum in CD_3CN shows the expected four aromatic resonances of bpy, the 15H singlet of Cp*, and an upfield 3H singlet at δ –0.04. The ^{13}C NMR spectrum features a methyl resonance (δ –6.35).

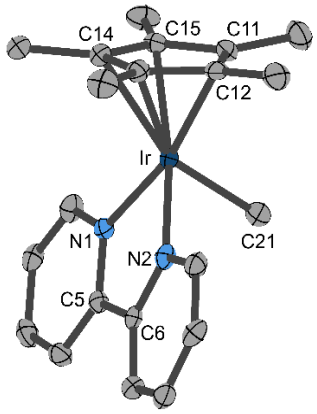

Figure 6.1. Structural representation of [**2**][I] with ellipsoids drawn at the 50% probability level. Hydrogen atoms and iodide counter ion omitted for clarity. Selected distances (Å): Ir–C21 2.147(5), C5–C6 1.458(6)

Table 6.1. Crystal data and structure refinement for [2][I]

Empirical formula	$C_{21}H_{26}N_2IIr$
Formula weight	625.54
Temperature/K	100
Space group	$P2_1/n$
a/Å	11.8894(8)
b/Å	8.9156(6)
c/Å	19.8799(14)
Volume/Å^3	2028.0(2)
Z	4
μ/mm^{-1}	24.725
Crystal size/mm^3	0.171 × 0.105 × 0.043
Radiation	CuKα (λ = 1.54178)
Reflections collected	25601
Independent reflections	3833 [R_{int} = 0.0655, R_{sigma} = 0.0373]
Goodness-of-fit on F^2	1.033
Final R indexes [I>=2σ (I)]	R_1 = 0.0267, wR_2 = 0.0628
Final R indexes [all data]	R_1 = 0.0303, wR_2 = 0.0647

Vapor diffusion of Et_2O into a solution of [**2**][I] in CH_3CN produced yellow crystals suitable for X-ray diffraction (XRD). Complex [**2**][I] takes on a 'piano stool' structure with a methyl ligand and an outer sphere iodide ion (Figure 6.1). Crystallographic data and refinement details are given in Table 6.1. The Ir–CH_3 distance (2.147(5) Å) falls into the

range of other reported Cp*Ir–CH_3 distances (2.03 to 2.22 Å).[152] The Ir atom, however, is not centered below the Cp* ring: the carbons *trans* to methyl ligand form longer bonds to Ir (Ir–C13 2.235(5) Å and Ir–C14 2.236(4) Å) than those *cis* to methyl ligand (Ir–C11 2.186(4) Å, Ir–C12 2.176(4) Å, Ir–C15 2.189(4) Å). The structure of [Cp*Ir(bpy)(Cl)][ClO_4], by contrast, features Ir–C distances that do not vary around the cyclopentadienyl ring (2.163 Å).[66] The structure of [**1**][PF_6][128] displays the same asymmetry found in the structure of [**2**][I], suggesting that this asymmetry is indicative of methyl and hydride ligands acting as strong σ-donors in [**2**][I] and [**1**][PF_6].

The structure of the Ir(III) complex [**2**]$^+$ can be compared to its reduced Ir(I) precursor **3**. The structure of [**2**][I] features a substantially longer C5–C6 distance (1.458(6) Å) than found in **3** (C5–C6 1.403(5) Å**)**. The interpyridyl distance in [**2**][I] is similar to that of [Cp*Ir(bpy)(Cl)][ClO_4] (1.463(11) Å), in which the bpy is not considered to be partially reduced.

In acetonitrile, the UV-vis spectrum of [**2**]$^+$ shows an absorbance with λ_{max} = 418 nm (ε_{max} = 3300 M^{-1} cm^{-1}, Figure 6.2A). The absorbance of [**2**]$^+$ is best fit by two Gaussian curves centered at 413 nm and 476 nm and estimated to have extinction coefficients of 3300 M^{-1} cm^{-1} and 1100 M^{-1} cm^{-1}, respectively. To explore the nature of the orbitals involved in these transitions, we turned to time-dependent density functional theory (TD-DFT). The singlet ground-state structure of [**2**]$^+$ was optimized using the M06 functional (LANL2DZ ECP basis set for the Ir atom and 6-311G** for all other atoms), modeling acetonitrile solvation with a polarized continuum model. Absorption properties in acetonitrile were explored using TD-DFT from the optimized ground-state geometry. The transitions at 450 nm (f = 0.0161) and 442 nm (f = 0.0937) reflect the observed spectrum: both calculation and

experiment feature two transitions under the MLCT with the weaker feature at a longer wavelength. According to TD-DFT, both transitions arise out of mixed HOMO and HOMO–1 states to the LUMO. The HOMO is a bonding interaction between a *d*-orbital of Ir and the C-p_z orbital. HOMO–1, however, is an anti-bonding interaction between Ir-d_{xz} and C-p_x orbitals (Figure 6.2C). The LUMO is primarily bpy π*-based.

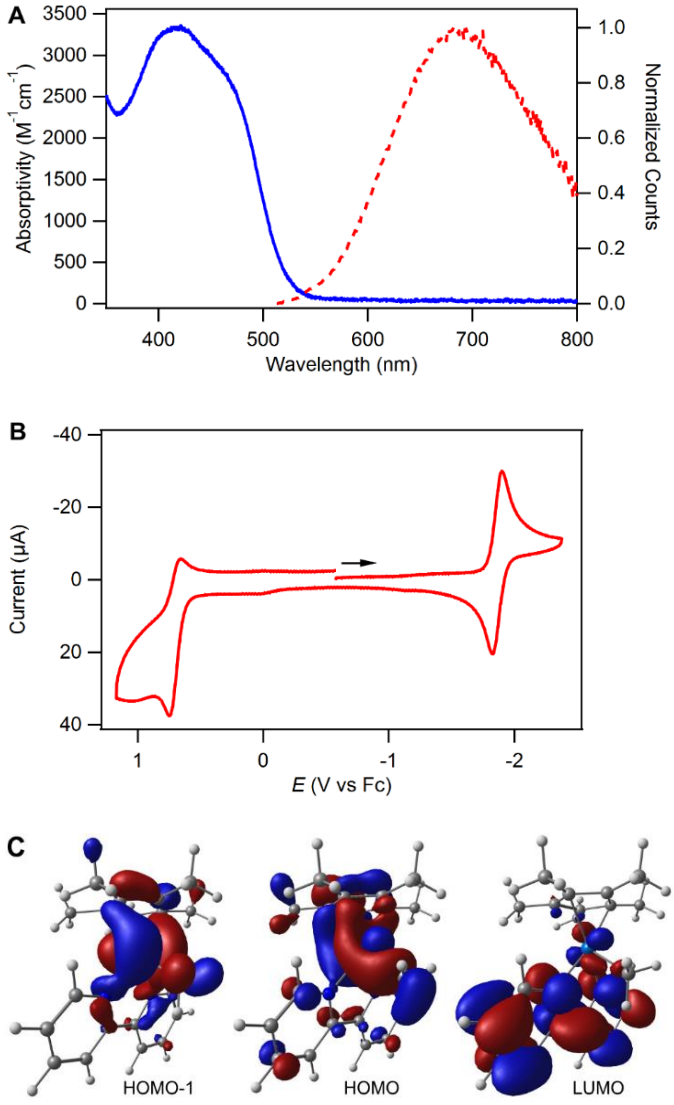

Figure 6.2. A) Absorptivity (solid blue) and normalized emission (dashed red) of $[\mathbf{2}]^+$ in CH_3CN solution. Excitation at 420 nm. B) Cyclic voltammogram of 1 mM $[\mathbf{2}]^+$ in CH_3CN with 0.1 M $[^nBu_4N][PF_6]$ under and an atmosphere of N_2. Scan rate 0.25 $V \cdot s^{-1}$. C) Orbitals from TD-DFT involved in the lowest energy transitions at 450 and 442 nm.

The absorbance spectrum of the analogous Ir hydride $[\mathbf{1}]^+$ in CH_3CN has a Gaussian MLCT transition at 428 (3000 M^{-1} cm^{-1}), ascribed to a charge transfer from a σ bonding HOMO (with Ir *d*-orbital and hydride *s*-orbital character) to a bpy π* LUMO.[73] While the LUMOs of $[\mathbf{1}]^+$ and $[\mathbf{2}]^+$ are similar, the presence of accessible *p*-orbitals in the carbon of the methyl ligand account for the differences in the spectra.

Upon irradiation into the MLCT absorbance of [**2**][I] (excitation at 420 nm), no steady state emission was observed at room temperature in CH_3CN. Hypothesizing that the iodide counter anion was quenching the excited state,[153] counter ion exchange was carried out by addition of excess NH_4PF_6 to a 9:1 H_2O:CH_3OH solution of [**2**][I], resulting in precipitation of [Cp*Ir(bpy)(CH_3)][PF_6] ([**2**][PF_6]) as a light yellow powder.

Metathesized salt [**2**][PF_6] is weakly emissive at room temperature. In CH_3CN solution, excitation at 420 nm produces a broad emission feature at 702 nm with a photoluminescence quantum yield of 0.04% (Figure 6.2A). The excitation spectrum aligns with the MLCT feature of the absorbance spectrum. The energy between the singlet ground state and the triplet excited state (ΔG_{ST}) can be estimated by extrapolation of the high-energy edge of the emission feature to the baseline, giving ΔG_{ST} = 50 kcal·mol^{-1} (Figure 6.3).

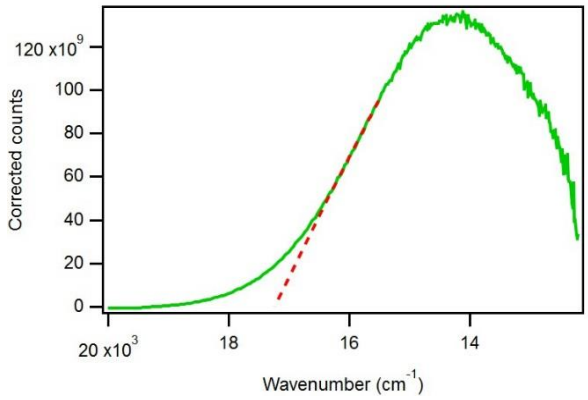

Figure 6.3. Instrument and background corrected emission (green) of [**2**][PF_6] in CH_3CN solution with excitation at 420 nm. The extrapolation of the high energy edge used to measure ΔG_{ST} (dashed red) intercepts the x-axis at 17300 cm^{-1} or 50 kcal·mol^{-1}.

The electronic structure of methyl complex $[\mathbf{2}]^+$ was investigated by cyclic voltammetry. A 1 mM solution of [**2**][PF_6] was prepared in CH_3CN containing 0.1 M [^{n}Bu$_4$N][PF_6]. A reversible reduction (ΔE_p = 77 mV, $i_{p,c}/i_{p,a}$ = 0.94) of $[\mathbf{2}]^+$ was observed at $E_{1/2}$ = –1.82 V and a pseudo-reversible oxidation (ΔE_p = 95 mV, $i_{p,a}/i_{p,c}$ = 0.30, 0.25 V·s^{-1}) was observed at $E_{1/2}$ = 0.74 V (Figure 6.2B). The reduction, formally Ir(III) to Ir(II), may also be described as a bpy-based reduction, $[\mathbf{2}]^+$/Cp*Ir^{III}($bpy^{\bullet-}$)(CH_3). The oxidation, formally $[\mathbf{2}]^+$/[Cp*Ir^{IV}(bpy)(CH_3)]$^{2+}$, extends across the Cp*, Ir, and CH_3 fragments according to our DFT.

Excited state reduction potentials can be calculated from the ground state potentials and ΔG_{ST}. The excited state can be reduced at $E°$(III*/II) = 0.35 V, and it can be oxidized at $E°$(III*/IV) = –1.42 V (Scheme 6.1).

Scheme 6.1. Excited state reduction potentials

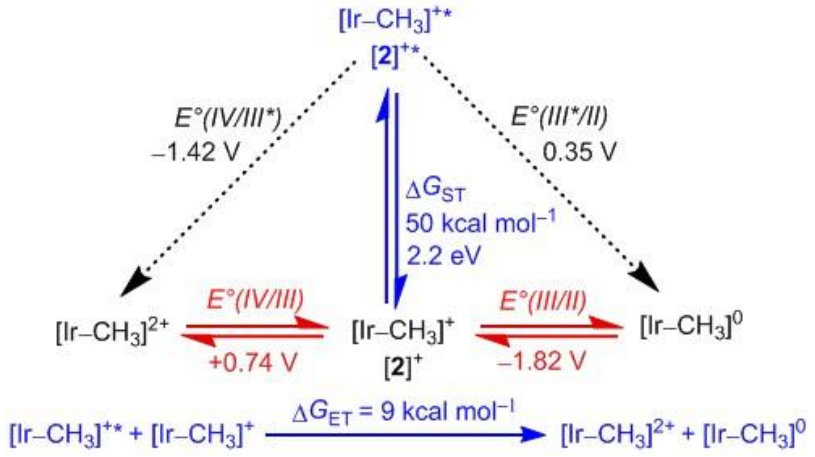

Table 6.2. Comparison of electrochemical and photophysical features of $[\mathbf{1}]^+$ and $[\mathbf{2}]^+$.

Parameter	X = CH_3	X = H
$E°$(III/II)	–1.82 V	–1.80 V[29]
$E°$(IV/III)	0.74 V	0.50 V[29]
λ_{MLCT}, $[Cp^*Ir^{III}(bpy)(X)]^+$	418 nm, (3300 $M^{-1}cm^{-1}$)	428 nm, (3000 $M^{-1}cm^{-1}$)[72]
Emission Max, $[Cp^*Ir^{III}(bpy)(X)]^+$	702 nm	708 nm[29]
ΔG_{ST}	50 kcal·mol^{-1}	47-52 kcal·mol^{-1} [29]
$E°$(III*/II)	0.35 V	0.37 V[29]
$E°$(IV/III*)	–1.42 V	–1.67 V[29]

Our initial hypothesis was that methyl $[\mathbf{2}]^+$ might undergo similar excited state reactivity to hydride $[\mathbf{1}]^+$, which undergoes self-quenching electron transfer from an MLCT excited state. To determine the energetics of self-quenching of $[\mathbf{2}]^+$, the driving force for electron transfer between excited state $[\mathbf{2}]^{+}$* and its ground state $[\mathbf{2}]^+$ ($\Delta G°_{ET}$) can be determined using either an excited state and ground state potential (0.74 V – 0.35 V = 0.39 V) or according to eq. 6.1. $\Delta G°_{ET}$ is determined to be about 9 kcal·mol^{-1} endergonic. Though a sizable barrier, it may be surmountable when coupled to a thermodynamically favorable chemical step, as has been observed for uphill electron transfers with $[Ru(bpy)_3]^{2+}$.[154] Self-

quenching of $[\mathbf{1}]^+$ is ~3 kcal·mol^{-1} endergonic and occurs with high efficiency at high concentration.[29]

$$\Delta G°_{ET} = 23.06(E°(\text{IV/III})) - 23.06(E°(\text{III/II})) - \Delta G_{ST} \qquad (6.1)$$

From the comparison of electrochemical and photophysical properties of hydride $[\mathbf{1}]^+$ and methyl $[\mathbf{2}]^+$ in Table 6.2, and from the structural features discussed above, the electronic similarities of the complexes are apparent. The similarity of the emission features of $[\mathbf{1}]^+$ and $[\mathbf{2}]^+$ gives rise to similar ΔG_{ST}: the value of ΔG_{ST} of 50 kcal·mol^{-1} determined here for $[\mathbf{2}]^+$ falls within the range of 47 kcal·mol^{-1} < ΔG_{ST} < 52 kcal·mol^{-1} previously determined for $[\mathbf{1}]^+$.[29] While the reduction potentials of $[\mathbf{1}]^+$ and $[\mathbf{2}]^+$ are similar, the oxidation of $[\mathbf{2}]^+$ is 240 mV more positive than that of $[\mathbf{1}]^+$. Additionally, this oxidation is noticeably more reversible for $[\mathbf{2}]^+$ than for $[\mathbf{1}]^+$. Fast scan rates (200 V·s^{-1}) were required to observe the re-reduction process for hydride $[\mathbf{1}]^+$,[29] but for methyl $[\mathbf{2}]^+$, a reduction feature is apparent even at a scan rate of 0.05 V·s^{-1}.

Photochemical production of ethane and methane. Encouraged by the similarities in the electronic structures of $[\mathbf{1}]^+$ and $[\mathbf{2}]^+$, we sought to probe for similarities in photochemical reactivity. Inspired by the ability of $[\mathbf{1}]^+$ to undergo light-induced H_2 formation in the presence of a H^+ source, we considered the analogous reaction for C–C bond formation: light-induced ethane formation from $[\mathbf{2}]^+$ and a CH_3^+ source.

A CD_3CN solution of $[\mathbf{2}][PF_6]$, excess CH_3I, and a mesitylene internal standard was illuminated with a 443 nm LED for 3.5 hours. ^{1}H NMR spectroscopic analysis showed the characteristic resonances of ethane, methane, and propionitrile (Figure 6.4). Product yields were determined by measuring gaseous concentrations by GC and by measuring dissolved gasses by ^{1}H NMR spectroscopy. Yields are reported relative to $[\mathbf{2}]^+$ consumed in the

reactions. Ethane, methane, and propionitrile were produced in 19%, 39%, and 9% yield, respectively. *As hypothesized, photolysis of [**2**]$^+$ forms C–C bonds.*

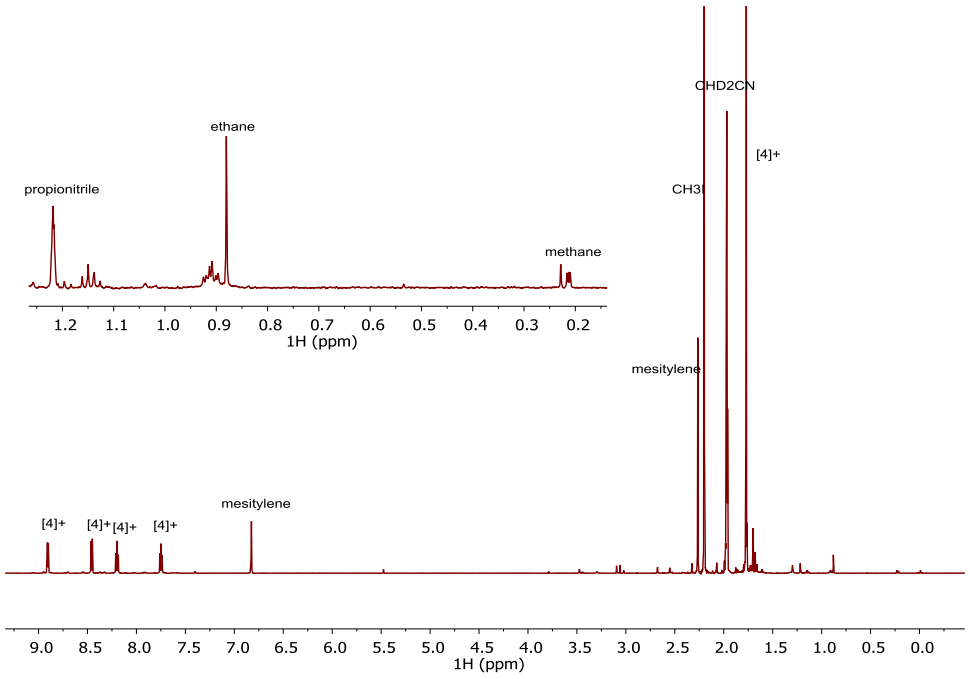

Figure 6.4. Representative ^{1}H NMR spectrum of a 6.7 mM [**2**][PF_6], 0.1 M CH_3I with a 3 mM mesitylene internal standard in CD_3CN after irradiation with a 443 nm light source for 3.5 hours. The iridium species has been converted to [**4**]$^+$ while ethane, methane, and propionitrile have appeared.

The primary Ir-containing species after photolysis was [Cp*Ir(bpy)(I)]$^+$ ([**4**]$^+$, 95%). Iodide [**4**]$^+$ was observed by HR-MS in solutions after photolysis, and [**4**]$^+$ was also independently prepared by addition of 3 equiv NaI to a solution of [Cp*Ir(bpy)(OH_2)][OTf]$_2$ in CD_3CN. The resulting ^{1}H NMR spectrum was consistent with the product of photolysis. The UV-vis spectrum of [**4**]$^+$ in CH_3CN shows and absorbance at $\boldsymbol{\lambda_{max}}$ = 375 nm (2500 M^{-1} cm^{-1}).

Weaker CH_3^+ sources were also investigated. Samples of [**2**][I] with CH_3OTs (OTs is tosylate) in CD_3CN were irradiated with 443 nm light for 22 hours, and ethane and methane, but not propionitrile, were observed by ^{1}H NMR spectroscopy. The appearance of the same

products suggests that the reaction may be proceeding through the same mechanism as with CH_3I.

Scheme 6.2. Possible reaction pathways of metal methyls from the excited state.

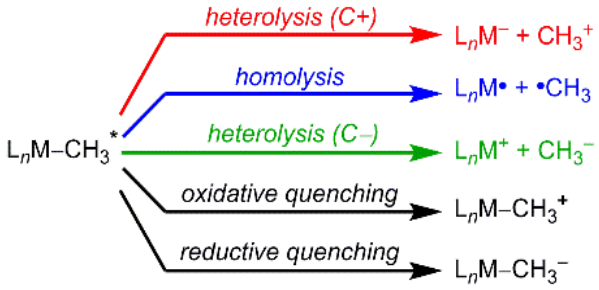

Mechanistic considerations. Scheme 6.2 shows several possible reaction pathways from the excited state of [**2**]$^+$. Reactions that lead to bond breaking are shown in color and electron transfers are shown in black. To probe for CH_3^+ formation, [**2**]$^+$ was irradiated at 443 nm in CD_3CN with 7 equiv pyridine to act as a CH_3^+ trap through the formation of 1-methylpyridinium. No reaction was observed over 5 h of photolysis. To ensure that the reaction was not reversed upon stopping photolysis, Ir(I) complex **3** and 5 equiv 1,4-dimethylpyridinium iodide in CD_3CN were allowed to mix in the dark for 24 h. No methylation of **3** was observed; thus, the red pathway of Scheme 6.2 forming methyl cation is unlikely to be operative.

Scheme 6.3. Pathways for ethane production from [2]$^+$.

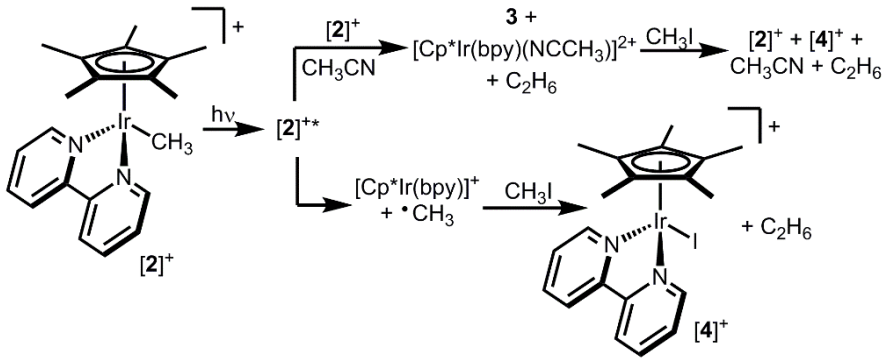

To investigate the other mechanistic possibilities, we examined the intermediates that would lead to ethane formation for two likely reactions: a self-quenching mechanism (Scheme 6.3, top) and a radical homolysis mechanism (Scheme 6.3, bottom). In the case of self-quenching, the methyl ligands of two equivalents of $[\mathbf{2}]^+$ couple in order to make ethane. Further reaction of resultant **3** with CH_3I would regenerate $[\mathbf{2}]^+$. With a radical homolysis pathway, methyl radical reacts with CH_3I to produce C_2H_6 and the resulting iodine atom traps $[Cp^*Ir(bpy)]^+$ to form $[\mathbf{4}]^+$. Though the products of these simplified mechanisms are indistinguishable, reactions from intermediate species can differentiate the two pathways.

Preliminary reactions gave indications of an intermediate methyl radical. In addition to CH_4, partially-deuterated CH_3D was formed (eq. 6.2) along with the distinctive 1:2:3:2:1 pentet (J_{HD} = 1.1 Hz) indicative of propionitrile isotopologue CH_3CD_2CN (eq. 6.3). Both results indicate $D^\bullet$ abstraction from the solvent CD_3CN, which is a thermodynamically favorable reaction for $^\bullet CH_3$ (*vide infra*). Attempts were made to examine the solvent decomposition specifically, but photolysis in the absence of added substrate produced an intractable mixture of products, as occurs for $[\mathbf{1}]^+$.

$$^\bullet CH_3 + CD_3CN \rightarrow CH_3D + {}^\bullet CD_2CN \qquad (6.2)$$

$$^\bullet CD_2CN + CH_3I \rightarrow I^\bullet + CH_3CD_2CN \qquad (6.3)$$

If ethane formation follows a self-quenching mechanism, ethane, **3** and $[Cp^*Ir(bpy)(NCCH_3)]^{2+}$ would likely be the initial products, according to the top pathway of Scheme 6.3. We have shown that acetic acid will readily protonate reduced **3** to form $[\mathbf{1}]^+$.[29,84] In the presence of AcOH, then, a reaction following a self-quenching pathway would be expected to initially form ethane and then form H_2 as the $[\mathbf{1}]^+$ formed *in situ* reacts. Irradiation of $[\mathbf{2}][PF_6]$ in the presence of excess AcOH produced CH_4 and CH_3D, observed

by ^{1}H NMR and GC headspace analysis (Figure 6.5). Methane was detected in 50% yield, but only trace amounts of ethane were observed by ^{1}H NMR spectroscopy and headspace GC analysis, and H_2 was not detected. The primary Ir-containing product was $[Cp^*Ir(bpy)(OAc)]^+$ (86%). The absence of propionitrile in this reaction and in the reaction with CH_3OTs suggests that propionitrile is formed from a reaction between activated solvent and CH_3I. Detecting neither H_2 nor hydride $[\mathbf{1}]^+$ suggests that Ir(I) complex **3** is not produced *in situ*.

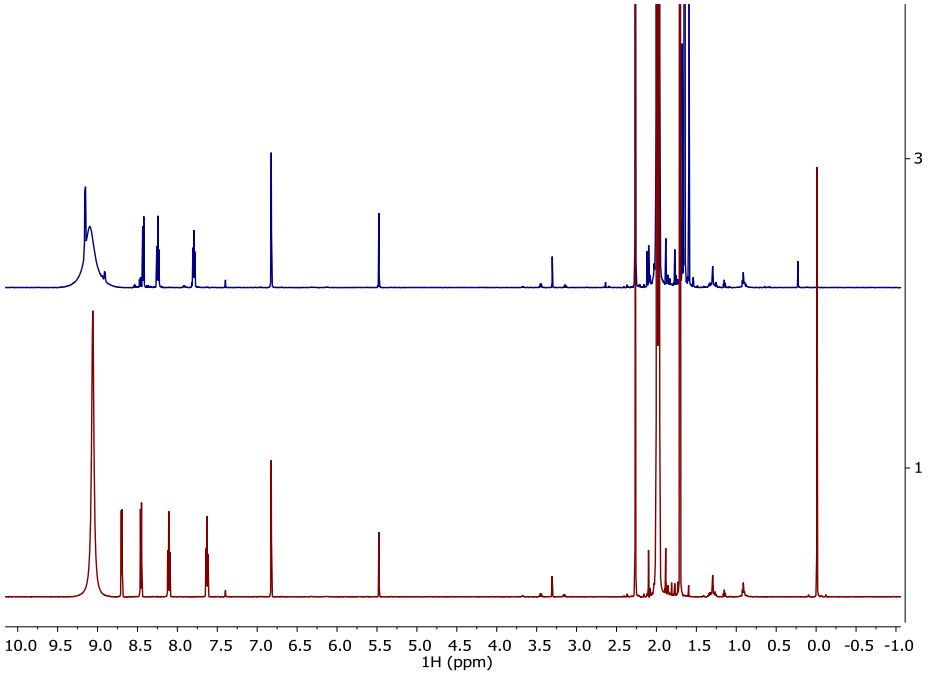

Figure 6.5. ^{1}H NMR spectra of 6 mM [**2**][PF_6] and 0.15 M AcOH in CD_3CN (bottom) photolyzed with 443 nm light for 3.5 hours (top). Methane and $[Cp^*Ir(bpy)(OAc)]^+$ are the primary products.

Evidence for a radical based mechanism. To investigate the mechanism of ethane formation, unlabeled $[Cp^*Ir(bpy)(^{12}CH_3)][PF_6]$ was photolyzed in the presence of labeled $^{13}CH_3I$. The isotope composition was tracked by ^{1}H NMR spectroscopy over the course of a 30 min photolysis of [**2**][PF_6] and $^{13}CH_3I$ with 443 nm light in CD_3CN. In that period, 20%

of methyl [**2**]$^+$ had reacted to form iodide [**4**]$^+$. During photolysis, $^{12}CH_3$ scrambled into the methyl iodide at approximately the same rate as [**2**]$^+$ was consumed, but only a small amount of $^{13}CH_3$ (1% enrichment) was incorporated into [**2**]$^+$. No isotopic scrambling was observed in the dark.

Scheme 6.4. The initial steps of isotope scrambling

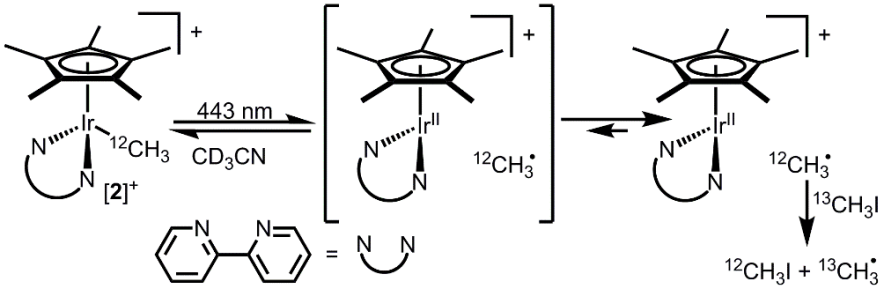

These scrambling rates are telling of the initial steps in the reaction (Scheme 6.4). If Ir(I) complex **3** were formed in the course of the reaction and methyl [**2**]$^+$ were regenerated by methyl iodide (as in Scheme 6.3, top), $^{13}CH_3$ would be expected to be incorporated into [**2**]$^+$ at half the rate with which [**2**]$^+$ is consumed. The observed rates fit a mechanism in which initial cleavage of the Ir–$^{12}CH_3$ bond produces a radical pair that can either separate or recombine. Once separated, the $^{12}CH_3$ radical reacts with $^{13}CH_3I$ to form $^{13}CH_3$ radical, which because of its excess in solution, becomes the dominant radical carrier. Recombination of the radical with [Cp*Ir(bpy)]$^{2+}$ after the pair separates must be rare to account for the minimal ^{13}C enrichment of [**2**]$^+$.

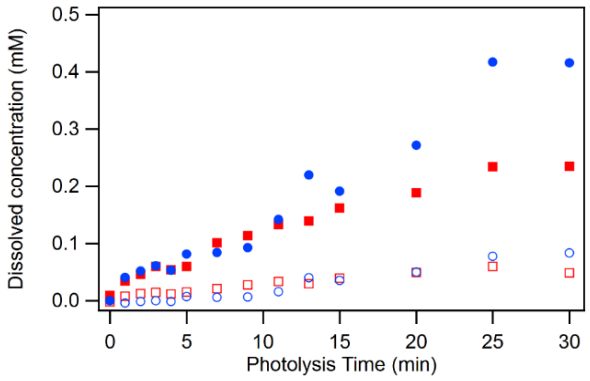

Figure 6.6. Time course of dissolved methane and ethane during photolysis of $[\mathbf{2}]^+$ and $^{13}CH_3I$ in CD_3CN, showing that incorporation of ^{13}C into organic products outpaces that of ^{12}C. $^{13}CH_4$ and $^{13}CH_3D$ (closed red squares), $^{12}CH_4$ and $^{12}CH_3D$ (open red squares), ^{13}C in ethane (closed blue circles), ^{12}C in ethane (open blue circles).

The dominance of $^{13}CH_3$ radical as the primary radical carrier in solution is also seen in the distribution of organic products. Because of the complex ^1H NMR splitting pattern of $^{12}CH_3{}^{13}CH_3$ and overlapping peaks from different isotopologues,[155] precise quantification of the ethane distribution was untenable. Integration of the satellites gives the total concentration of ^{13}C incorporated in ethane either in $^{12}CH_3{}^{13}CH_3$ or $^{13}CH_3{}^{13}CH_3$ (Figure 6.6, closed blue circles) while the center peak gives ^{12}C concentration in $^{12}CH_3{}^{13}CH_3$ or $^{12}CH_3{}^{12}CH_3$ (Figure 6.6, open blue circles). Because this treatment is counting carbons individually, the *ethane* concentration is half the sum of the two measurements. About five times as much ^{13}C is incorporated into ethane than ^{12}C. Consistent with this, $^{13}CH_4$ and $^{13}CH_3D$ were generated at a faster rate than $^{12}CH_4$ and $^{12}CH_3D$ (Figure 6.7). These results suggest that the methyl radical that forms on irradiation undergoes non-productive radical reactions with the excess of $^{13}CH_3I$ before forming methane or ethane.

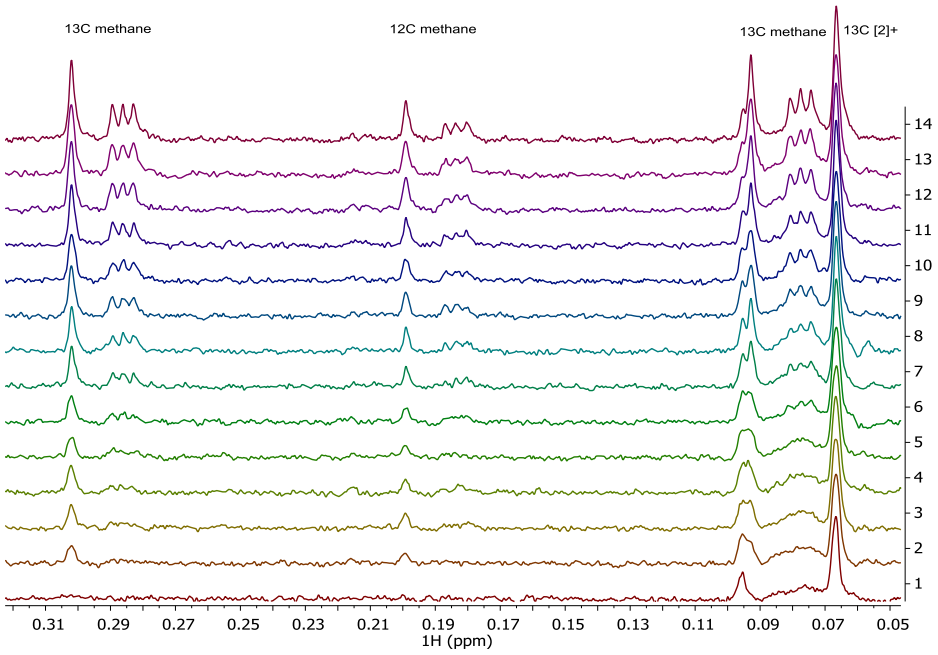

Figure 6.7. Growth of $^{13}CH_4$, $^{13}CH_3D$, $^{12}CH_4$, and $^{12}CH_3D$ over 443 nm 30 min of photolysis of 12.5 mM [**2**][PF_6] and 80 mM $^{13}CH_3I$ in CD_3CN with a 3 mM mesitylene internal standard. The downfield satellite was used for ^{13}C-containing methane integration.

Scheme 6.5. Reaction with radical trap TEMPO.

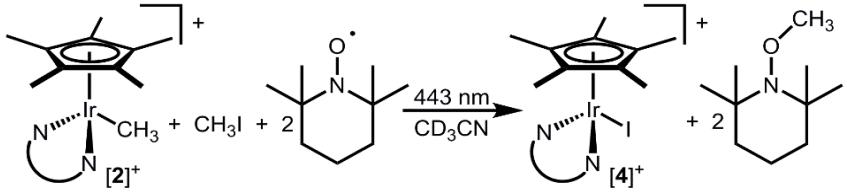

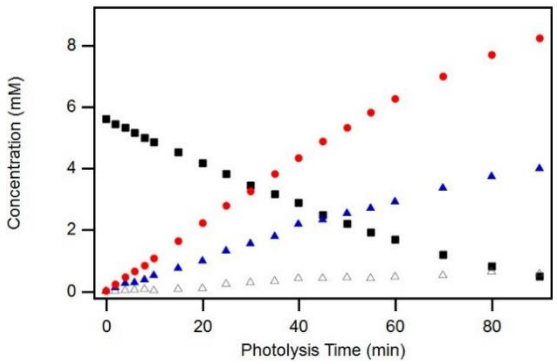

Figure 6.8. Concentrations from ^1H NMR spectroscopy following the irradiation at 443 nm of a solution of 5.6 mM [**2**][PF6] (black squares), 12 mM CH_3I, and 24 mM TEMPO in CD_3CN. TEMPO-CH_3 (red circles) grows in at twice the rate as iodide [**4**]$^+$ (blue triangles).

The decrease in [CH_3I] (not shown) accounts for half of the methyl of TEMPO-CH_3. Methyl [**2**]$^+$ is consumed at a slightly faster rate than [**4**]$^+$ appears: a minor iridium (open triangles, 10%) containing species grows in as evidence of a side reaction.

Radical probes were employed to provide further evidence for the presence of free radicals during photolysis. Photolysis of 5.6 mM [**2**]$^+$ and 12 mM CH_3I in CD_3CN was carried out with 443 nm light for 90 min in the presence of 24 mM radical trap TEMPO. Irradiation exclusively produced TEMPO-CH_3 to the exclusion of methane and ethane. The iridium product was [**4**]$^+$, which was formed at half the rate with which TEMPO-CH_3 appeared (Scheme 6.5). Ir–CH_3 homolysis will produce 1 equiv of TEMPO-CH_3, and to account for rates and electrons, the formed [Cp*Ir(bpy)]$^+$ must cleave CH_3I forming an additional equivalent of TEMPO-CH_3 and the final species [**4**]$^+$.

Scheme 6.6. Reaction of the radical clock complex, [5][Br].

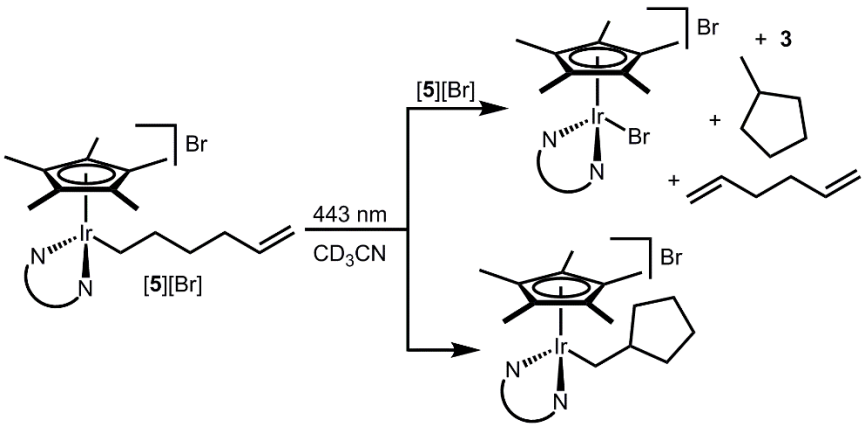

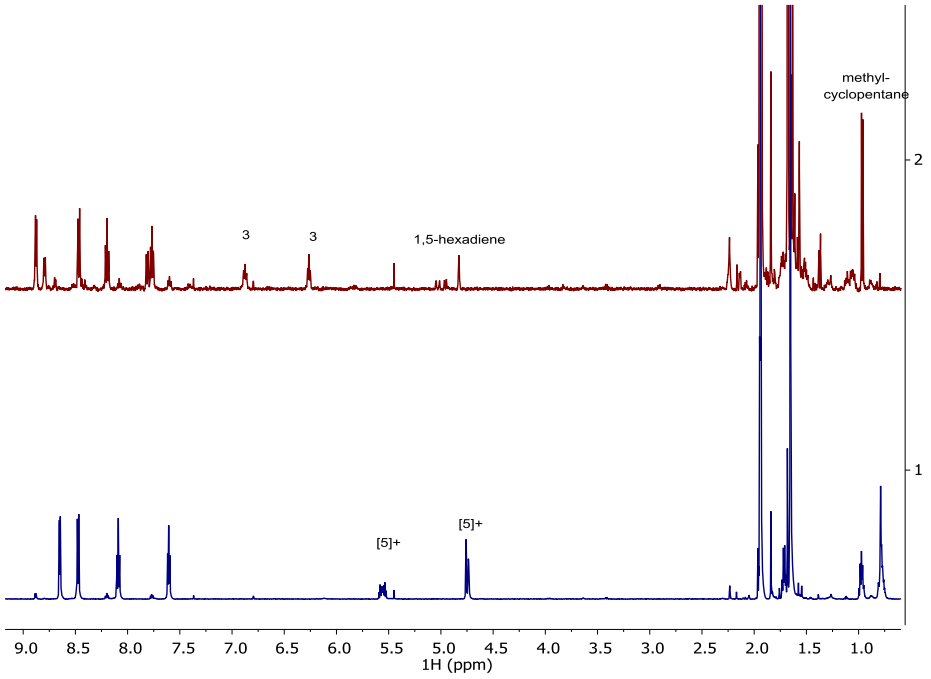

Figure 6.9. ^{1}H NMR spectra of [**5**][Br] in CD_3CN (bottom) photolyzed with 443 nm light for 1 h (top). The consumption of $[\mathbf{5}]^+$ is most clearly identified by the absence of the olefinic protons at 4.75 ppm and 5.55 ppm. The CH_3 doublet of methylcyclopentane is at 0.95 ppm.

An intramolecular alkyl radical clock was also synthesized to probe radical intermediates. 5-hexenyl radical is known to quickly cyclize to form cyclopentylmethyl radical.[156] To access this radical, an excess of 6-bromo-1-hexene was added to a purple solution of Ir(I) complex **3** in Et_2O and allowed to stir in the dark for 2 days. Over that time, a yellow solid precipitated from solution and was isolated by filtration and washed with ether giving [Cp*Ir(bpy)($(CH_2)_4CHCH_2$)][Br] ([**5**][Br]).

Irradiation of a solution of [**5**][Br] in CD_3CN gave methylcyclopentane (confirmed by spiking with an authentic sample) and 1,5-hexadiene (Scheme 6.6). The Ir products were **3**, $[Cp^*Ir(bpy)(Br)]^+$ and a new minor species. ESI-MS of the product mixture showed a peak at m/*z* = 567.23452. This is the same as the starting material $[\mathbf{5}]^+$ (calc m/*z* = 567.2351), but NMR data showed that the starting material was fully consumed (Figure 6.9); the same mass

would also be consistent with a ring-closed product $[Cp^*Ir(bpy)(CH_2C_5H_9)]^+$. The presence of methylcylopentane in the product mixture is evidence for the homolysis of the Ir–C bond. Following homolysis, 1,5-hexadiene is formed by H• abstraction by $[Cp^*Ir^{II}(bpy)]^+$ from the formed 5-hexenyl radical. This produces $[Cp^*Ir^{III}(bpy)(H)]^+$ ($[\mathbf{1}]^+$) which can supply the additional H atom equivalent need to form methylcyclopentane. The final Ir(I) and Ir(III) products could be formed by disproportionation of $[Cp^*Ir(bpy)]^+$. Similar mechanisms for light-induced β-hydride elimination have been previously proposed for Ir,[157] and this is a common mechanism in cobalt alkyl photochemistry.[158,159]

Differentiating mechanisms with excited state lifetime and kinetic order. Ir–C bond homolysis could occur through either monometallic homolysis from the excited state (Scheme 6.2, blue) or following an electron transfer which weakens the Ir–CH_3 bonds (Scheme 6.2, black). Excited state lifetimes and kinetic order were investigated to determine which of these pathways was operative.

Excited state lifetimes and luminescence quantum yields were investigated to look for self-quenching directly. No change in photoluminescent quantum yield was observed in the range of 0.02 mM to 0.6 mM of $[\mathbf{2}]^+$ (Figure 6.10). The lifetime of $[\mathbf{2}]^{+*}$ was found to be 50 ns by time-correlated single photon counting, with no dependence on $[\mathbf{2}]^+$ from 0.02 mM to 0.9 mM (Figure 6.11A). Both results indicate that $[\mathbf{2}]^{+*}$ is not efficiently quenched by $[\mathbf{2}]^+$. Quenching by methyl iodide ($E_{1/2}$ = –2.18 V[160]) was also investigated: no change in lifetime was observed to 1 M CH_3I (Figure 6.11B).

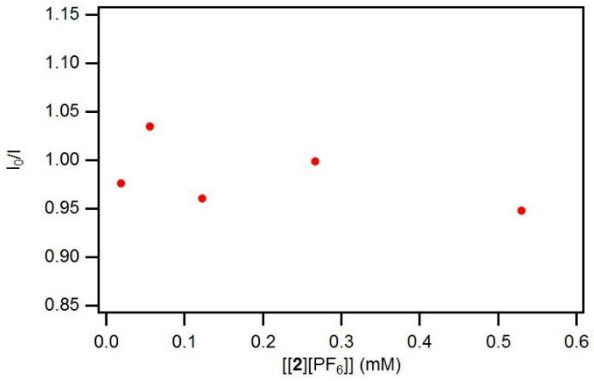

Figure 6.10. Self-quenching Stern-Volmer analysis for [**2**][PF_6] in CH_3CN at room temperature. I_0 is the emission extrapolated to infinite dilution. I is the corrected and normalized emission at a given concentration of [**2**]$^+$. The absence of upward trend indicates the absence of self-quenching.

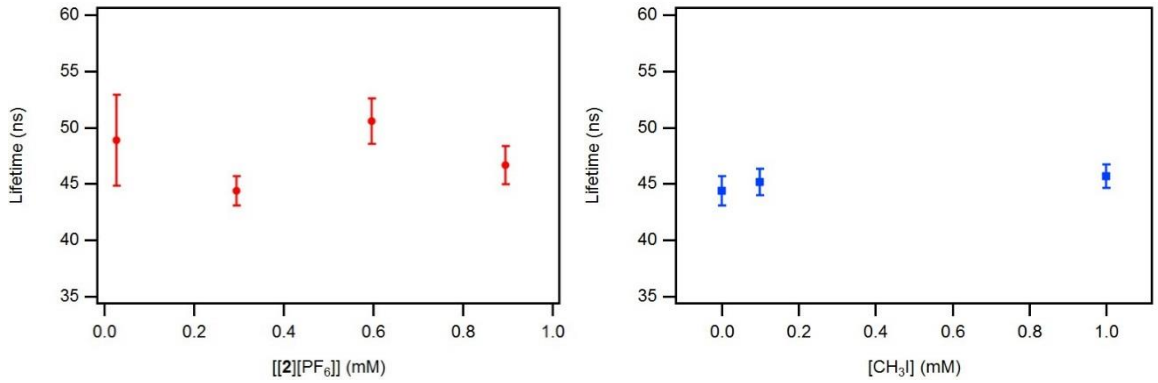

Figure 6.11. A**)** Photoluminescent lifetime of varying concentrations of [**2**][PF_6] in CH_3CN measured by time-correlated single photon counting. B) Photoluminescent lifetime of [**2**][PF_6] in CH_3CN with varying concentration of CH_3I. Laser excitation at 444.2 nm source with 73.3 ps pulse width at 2 MHz pulse rate. Emission detected at 680 nm with a 5 nm bandwidth. The independence of lifetime with concentration indicates the absence of quenching.

The reaction of [**2**]$^+$ and CH_3I in CH_3CN during irradiation with 443 nm light was also monitored by UV-vis spectroscopy in quartz cuvettes. The disappearance of the MLCT feature of [**2**]$^+$ was monitored at 443 nm, and quantum yields for the disappearance of [**2**]$^+$

were calculated over the course of 10% consumption. Samples which were photolyzed until no further change occurred were consistent with the spectrum of $[\mathbf{4}]^+$ (Figure 6.12).

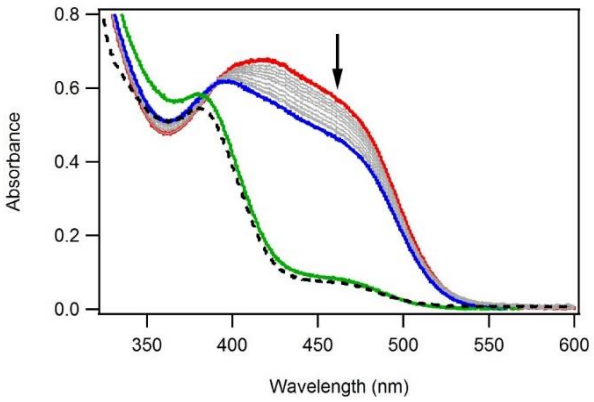

Figure 6.12. Representative experiment following the reaction of [**2**][PF6] with CH_3I in CH_3CN. The sample was irradiated at 443 nm (1.58×10^{-6} moles of photons min^{-1}) in 30 s intervals for the first 5 min (from the red trace to the blue trace) to calculate quantum yield. Photolysis for longer periods produces the green spectrum. The expected spectrum of $[\mathbf{4}]^+$ is shown in the dashed black spectrum.

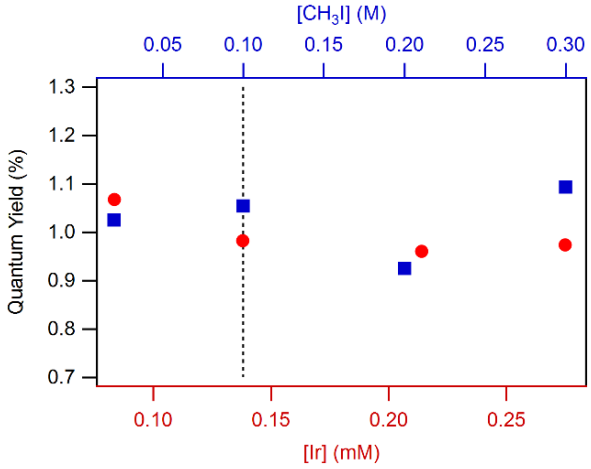

Figure 6.13. Dependence of quantum yield on $[CH_3I]$ (blue squares) and $[[\mathbf{2}]^+]$ (red circles) in CH_3CN photolyzed with 443 nm light. The dashed-line marks the constant concentration of CH_3I and $[\mathbf{2}]^+$ (0.1 M and 0.14 mM respectively) held while the other reagent varied. The lack of dependence in CH_3I indicates the reaction is zero order in substrate, while the lack of dependence on $[\mathbf{2}]^+$ indicates an overall first order as $[\mathbf{2}]^+$ is the chromophore.

Order in Ir was determined using by monitoring the disappearance of $[\mathbf{2}][PF_6]$ in an irradiated quartz cuvette in the presence of 0.1 M CH_3I in CH_3CN. The quantum yield for consumption of starting material remained constant at 1.0(5)% from 0.08 mM to 0.28 mM

[**2**]$^+$ (Figure 6.13). Because calculating quantum yield includes normalizing for sample absorbance, a lack of dependence on the chromophore concentration indicates an overall first order dependence on chromophore [**2**]$^+$. Order in CH_3I was determined by varying the concentration of substrate from 0.02 M to 0.3 M at constant [[**2**]$^+$]. No dependence of quantum yield on substrate concentration was observed, indicating that the reaction is zero-order in CH_3I.

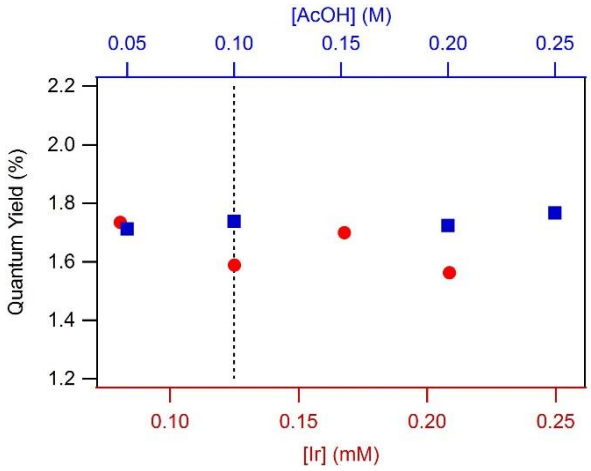

Figure 6.14. Dependence of quantum yield on [AcOH] (blue squares) and [[**2**]$^+$] (red circles) in CH_3CN photolyzed with 443 nm light. The dashed-line marks the constant concentration of AcOH and [**2**]$^+$ (0.1 M and 0.12 mM respectively) held while the other reagent varied. The lack of dependence in AcOH indicates the reaction is zero order in substrate, while the lack of dependence on [**2**]$^+$ indicates an overall first order as [**2**]$^+$ is the chromophore.

Order in Ir and substrate was similarly investigated for the reaction of [**2**]$^+$ in the presence of AcOH to probe the reaction with a different substrate. Variation of [**2**]$^+$ concentration from 0.8 mM to 0.21 mM in the presence of a constant 0.1 M AcOH in CH_3CN resulted in no change in quantum yield (1.7(5)%, Figure 6.14). To probe higher iridium concentrations, solutions of 1 mM to 8 mM [**2**]$^+$ in CD_3CN and 0.1 M AcOH were irradiated in standard NMR tubes with 443 nm light and monitored by ^{1}H NMR spectroscopy. No

change in quantum yield was observed. Varying [AcOH] caused no change in quantum yield, indicating a zero-order dependence on substrate.

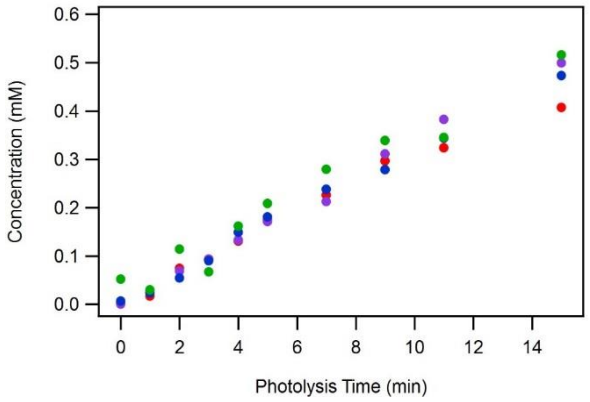

Figure 6.15. Growth of Ir-containing products on 443 nm photolysis of 1 mM (red), 2 mM (purple), 4 mM (blue), and 8 mM (green) [**2**][PF_6] in CD_3CN with 10 mM AcOH. The consistent increases indicate quantum yield is not changing across this concentration range.

Additionally, if a bimolecular reaction of two cationic iridium species were occurring, one might expect an increase in quantum yield on addition of electrolyte. Quantum yields for the disappearance of [**2**]$^+$ with and without 0.1 M [^{n}Bu$_4$N][PF_6] were identical in four trials with concentrations of [**2**]$^+$ at 0.07 and 0.18 mM with 0.05 M AcOH acid, indicating that the reaction does not involve the close approach of two charged species.

From a kinetic analysis indicating that the reaction is first-order in [**2**]$^+$ and zero-order in substrate, several characteristics of the reaction become apparent. The first is that bimolecular self-quenching cannot play a significant role in the reaction. The second is that reactions involving the added organic methyl source must occur after the rate-determining step. Additionally, the radical chain is not significantly propagated through radical attack on [**2**]$^+$ to produce either Ir(II) or methyl radical. Such a process would result in an additional pathway consuming [**2**]$^+$ and typically results in 3/2 order in [**2**]$^+$.[161]

Many of the species that would be formed to continue propagation of methyl radical in solution—ICH_2CN and I_2—have particularly weak bonds (44.7 and 36.4 kcal·mol^{-1}, respectively[162]) and are unlikely to be generated in high concentrations. Indeed, attempts to detect ICH_2CN by photolyzing a solution of [**2**][PF_6] with excess CH_3I in 9:1 CH_3CN:CD_3CN produced no iodoacetonitrile by ^{1}H NMR spectroscopy (Figure 6.16). Instead, evidence for another C–C bond forming event was observed: half an equivalent of succinonitrile ($(CH_2CN)_2$) was detected per [**2**]$^+$, presumably produced by the termination of two acetonitrile radicals. Given that iodide [**4**]$^+$ was formed in this reaction as well, CH_3I must be involved in other radical reactions, and therefore, short chain reactions must occur.

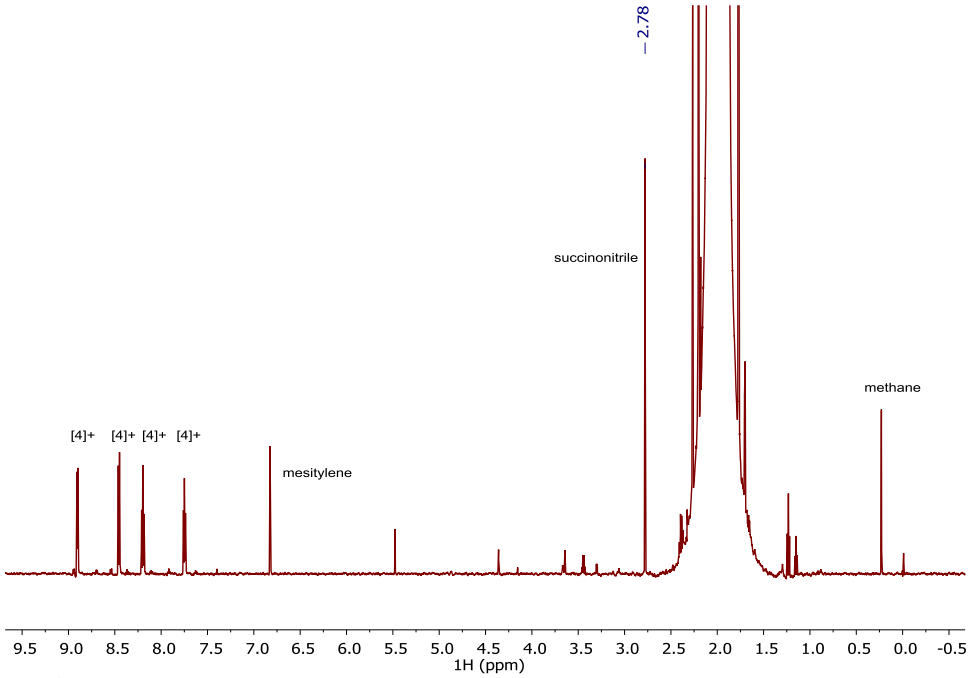

Figure 6.16. ^{1}H NMR spectrum of [**2**][PF_6] and 0.1 M CH_3I in 9:1 CH_3CN:CD_3CN photolyzed with 443 nm light for 3.5 hours. Methane, succinonitrile, and [**4**]$^+$ are formed.

Succinonitrile could not be detected in experiments in CD_3CN because it would be fully deuterated and ^{1}H NMR silent, and it is not volatile for GC detection. Curiously, ethane was not detected in this experiment, which suggests that the slightly more inert C–D bond of

CD_3CN encourages ethane formation. Given the difference in product distribution in *protio* and *deutero* solvent, we investigated the quantum yield for the reaction of $[\mathbf{2}]^+$ in CD_3CN with CD_3I and found no decrease. Therefore, the isotope effect is product-determining, but not rate-determining. Either initial homolysis or solvent separation of the radical pair is likely the rate-determining step.

Table 6.3. Relevant bond dissociation energies.

molecule	ΔH (kcal·mol^{-1})	ref
H–H	104.2	162
H–CH_3	105	162
H–CH_2CN	97	162
I–CH_3	57	162
I–CH_2CN	44.7	162
I–I	36.4	162
H_3C-CH_2CN	83.2	162
$NCCH_2$–CH_2CN	70.6	163
H–Ir(Cp*)(PMe_3)(H)	74	164
H_3C–Ir(Cp*)(PMe_3)(CH_3)	56	164

Understanding the preference for homolysis. The collected data indicate that ethane and methane are produced following monometallic Ir–CH_3 bond homolysis from the excited state. Bond dissociation enthalpies relevant to this discussion are collected in Table 6.3. Deuterium atom abstraction by •CH_3 from CD_3CN forms CH_3D. Methyl radical is thermodynamically capable of abstracting a hydrogen atom from acetonitrile.[162] The absence of propionitrile in reactions with AcOH and CH_3OTs suggests that propionitrile-d_2 results from the reaction of •CD_2CN with CH_3I. Ethane could be formed either in a reaction of •CH_3

with CH_3I or in a termination step upon recombination of two methyl radicals. Addition of I• to the primary Ir photoproduct $[Cp^*Ir^{II}(bpy)]^+$ offers an organometallic termination pathway that affords the observed iodide complex.

To better understand the mechanism change from electron transfer with $[\mathbf{1}]^+$ to homolysis with $[\mathbf{2}]^+$, relevant thermodynamic parameters were considered. One possibility is that homolysis of an Ir–CH_3 bond is thermodynamically favorable relative to homolysis of an Ir–H bond. While the hydrogen atom and methyl radical are almost equally stable (ΔH(H–H) = 104 kcal·mol^{-1} while the ΔH(H_3C–H) = 105 kcal·mol^{-1} [162]), related systems suggest that the bond dissociation enthalpies of Ir–H in $[\mathbf{1}]^+$ and Ir–CH_3 in $[\mathbf{2}]^+$ may differ dramatically. The most similar system for which M–CH_3 and M–H bond strengths have been measured is $Cp^*Ir(PMe_3)X_2$ (where X = H, CH_3). In this system, ΔH(Ir–H) = 74 kcal·mol^{-1} while ΔH(Ir–CH_3) = 56 kcal·mol^{-1}. This ~20 kcal·mol^{-1} decrease in bond dissociation enthalpy from ΔH(Ir–H) to ΔH(Ir–CH_3) is consistent with other Ir systems in which both have been measured.[164] This is a striking difference, especially when considered in light of the overall similarity of $[\mathbf{1}]^+$ and $[\mathbf{2}]^+$.

Homolysis is also consistent with the nature of the orbitals involved in the MLCT transition. The largest contribution to the excitation depopulates a σ bond between Ir and CH_3 (HOMO, Figure 6.2C). Irradiation of this transition would, therefore, be expected to weaken the Ir–C bond.

While a more accessible homolysis pathway explains much of the observed chemistry, the differences in quantum yields for $[\mathbf{1}]^+$ and $[\mathbf{2}]^+$ suggest that there may be other factors. The quantum yields for conversion of $[\mathbf{2}]^+$ are low, especially when compared with quantum yields for H_2 evolution for $[\mathbf{1}]^+$ that approach unity. Homolysis may be out-

competing electron transfer, and low quantum yields could be a result of efficient recombination from the radical pair. Alternatively, the discrepancy may be explained by self-quenching being thermodynamically inaccessible. As discussed above, self-quenching for $[\mathbf{2}]^{+}$* and $[\mathbf{2}]^{+}$ lies 9 kcal·mol^{-1} uphill. This is a larger barrier than for $[\mathbf{1}]^{+}$* and $[\mathbf{1}]^{+}$ (3 kcal·mol^{-1}) and may, indeed, be insurmountable even with a following reaction. Such self-quenching reactions are often kinetically limited as well. Self-quenching of $[Ru(bpy)_3]^{2+}$ with its excited state is thermodynamically favorable, but only occurs when suitable electron donors and acceptors are included in solution.[165,166] In the absence of a viable electron transfer pathway for $[\mathbf{2}]^{+}$, homolysis provides a feasible pathway to dissipate the energy of the excited state.

6.3 Conclusions

A new iridium methyl complex, $[Cp^*Ir(bpy)(CH_3)]^{+}$, was prepared and characterized. Photolysis of this complex forms C–C bonds: ethane, propionitrile, and succinonitrile are all formed. The mechanism of C–C bond formation was shown to proceed through monometallic radical homolysis, rather than the bimetallic electron transfer mechanism that led to H–H bond formation from $[\mathbf{1}]^{+}$. The minor structural change of substituting a methyl ligand for a hydride ligand, despite modifying the electrochemical and photophysical properties of the molecule only slightly, was sufficient to give rise to drastically different reactivity. Comparison of the bond dissociation enthalpies of similar complexes suggests that the change in mechanism can be explained by the weaker Ir–CH_3 bond in comparison to the Ir–H bond. The dramatic differences underscore the changes in reactivity that can be observed on minor synthetic variation.

6.4 Experimental Section

General Considerations. Procedures were carried out under nitrogen except where noted. All solutions containing metal methyl species were protected from ambient light during preparation to prevent excited state reactions. All reagents were commercially available and used without further purification. Organic solvents were dried and degassed with argon using a Pure Process Technology solvent system. Deuterated solvents were purchased from Cambridge Isotope Laboratories, Inc and degassed with three freeze-pump-thaw cycles before storing over sieves in a N_2 glovebox. UV−vis spectra were obtained using an Ocean Optics USB2000+ spectrometer with a DTMINI-2GS deuterium/tungsten halogen light source controlled by OceanView software. NMR spectra were obtained on 400, 500, or 600 MHz spectrometers. ^{1}H and ^{13}C NMR spectra were referenced to the residual solvent signals. Spectra were processed using the MestReNova software suite from Mestrelab Research S. L. Mass spectrometry was carried out with an LTQ FT (ICR 7T) (ThermoFisher, Bremen, Germany) mass spectrometer. Samples (in acetonitrile solution) were introduced via a microelectrospray source at a flow rate of 3 μL/min. Xcalibur (ThermoFisher, Breman, Germany) was used to analyze the data. Molecular formula assignments were determined with Molecular Formula Calculator (v 1.2.3). For ICP-MS, samples were prepared in 2% nitric acid solution diluted with 18.2 MΩ/cm water and were analyzed with an Element XR inductively coupled plasma (ThermoFisher, Bremen, Germany) mass spectrometer (ICP-MS). Samples were introduced via a peristaltic pump connected to an Elemental Scientific SC autosampler (Omaha, Nebraska). Iridium 193 was monitored in low resolution mode for 30 sec for each sample (~300 scans). All UV-vis and photoluminescence samples were prepared in an N_2 glovebox in 1 cm path length 4-sided quartz cuvettes, sealed with

screwcaps, and reinforced with parafilm on removing from the glovebox, unless otherwise noted. Single-crystal X-ray diffraction data were collected on a Bruker APEX-II CCD diffractometer at 100 K with Cu Kα radiation (λ = 1.54175 Å). Using Olex2,[95] the structures were solved with the olex2.solve[96] structure solution program using Charge Flipping and refined with the XL[97] refinement program using least squares minimization. The complex Cp*Ir(bpy) was prepared following literature procedures.[126]

Electrochemistry. Cyclic voltammograms were measured with glassy carbon working electrodes (polished with 0.3 and 0.05 μm alumina powder before use), platinum wire counter electrodes, and a Ag pseudo-reference electrode. An undivided cup cell was used. Experiments were carried out in an N_2 filled glovebox using a Pine WaveNow potentiostat controlled by Aftermath software connected to a computer outside of the glovebox by a custom USB feed through. Ferrocene was added at the end of data collection, and all potentials are reported relative to the $Fc^{0/+}$ couple.

Photoluminescence Studies. Steady-state emission and excitation spectra were recorded at room temperature on a Photon Technology, Inc. Quantamaster 4SE-NIR5 spectrometer PC-controlled by FelixX32 software. Excitation light was provided by a 75 W Xenon light source coupled to a single monochromator outfitted with a 1200 L/mm grating blazed at 400 nm. A 300 nm long pass filter was placed before the sample to prevent deep UV excitation from a second order grating effect. Emission was collected at a right angle relative to excitation, focused into a single monochromator (grating blazed at 500nm with 1200 L/mm) and detected by a Hamamatsu R928P photomultiplier tube used in single photon counting mode. Slit widths for both emission and excitation monochromators were fixed at 0.5 mm. All spectra were corrected for system response.

Absolute photoluminescence quantum yield was measured on an Edinburgh FLS-920 emission spectrophotometer with detection by a Hamamatsu R2658P photomultiplier tube to count photons to 950 nm by which wavelength the phosphorescence had decayed to zero. Photoluminescent lifetimes were measured by time-correlated single photon counting on the Edinburgh instrument with excitation by a 443 nm, 73.3 ps width laser.

Synthesis. *[Cp*Ir(bpy)(CH_3)][PF_6] ([**2**][PF_6]).* In air, complex [**2**][I] (54.1 mg, 0.086 mmol) was dissolved in 75 mL 9:1 H_2O:MeOH. Excess [NH_4][PF_6] (160 mg) was added as a solid resulting in the immediate precipitation of a fine yellow solid. The solid was separated by filtration through a fine frit and flushed with water resulting in 49.8 mg [**2**][PF_6] (0.077 mmol, 89% yield). **^{1}H NMR** (600 MHz, CD_3CN, Figure 6.17) δ 8.67 (d, J = 5.7 Hz, 2H), 8.43 (d, J = 8.1 Hz, 2H), 8.08 (t, J = 7.8 Hz, 2H), 7.60 (t, J = 6.6 Hz, 2H), 1.68 (s, 15H), -0.04 (s, 3H). **^{13}C NMR** (151 MHz, CD_3CN, Figure 6.18) δ 156.01, 152.45, 139.07, 129.00, 125.33, 90.85, 8.70, -6.36. **Anal. Calcd** for $C_{21}H_{26}F_6IrN_2P$: C, 39.19; H, 4.07; N, 4.35. Found: C, 38.94; H, 3.89; N, 4.15.

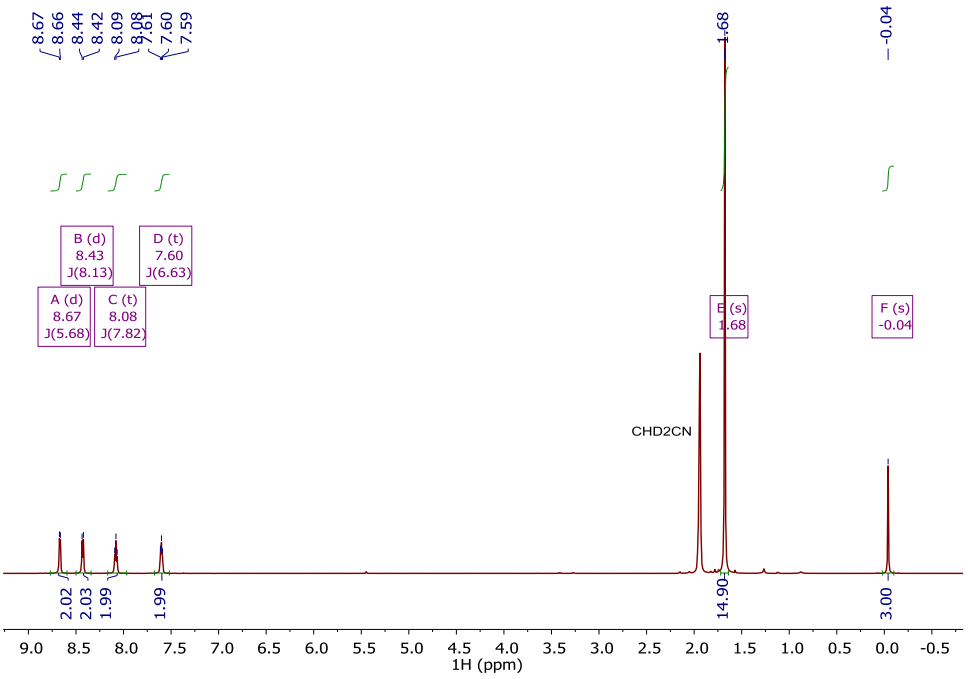

Figure 6.17. ^{1}H NMR spectrum of [Cp*Ir(bpy)(Me)][PF_6] ([**2**][PF_6]) in CD_3CN.

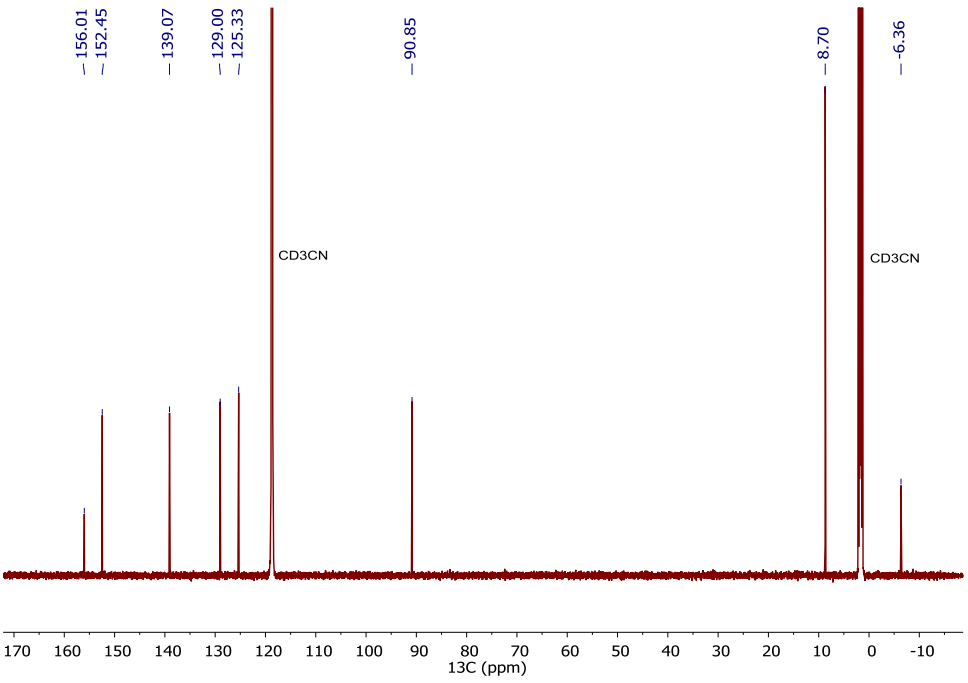

Figure 6.18. $^{13}C\{^{1}H\}$ NMR spectrum of [Cp*Ir(bpy)(Me)][PF_6] ([**2**][PF_6]) in CD_3CN.

*[Cp*Ir(bpy)(I)]$^+$ ([**4**]$^+$).* [Cp*Ir(bpy)(I)]$^+$ was prepared by addition of 3 eq NaI to 3.9 mg [Cp*Ir(bpy)(OH_2)][OTf]$_2$. **^{1}H NMR** (500 MHz, CD_3CN, Figure 6.19) δ 8.88 (d, J = 5.7 Hz, 2H), 8.46 (d, J = 8.1 Hz, 2H), 8.18 (t, J = 8.1 Hz, 2H), 7.75 – 7.71 (m, 2H), 1.74 (s, 15H). $\lambda_{abs,max}$ (CH_3CN, Figure 6.20) = 375 nm (2500 M^{-1} cm^{-1}).

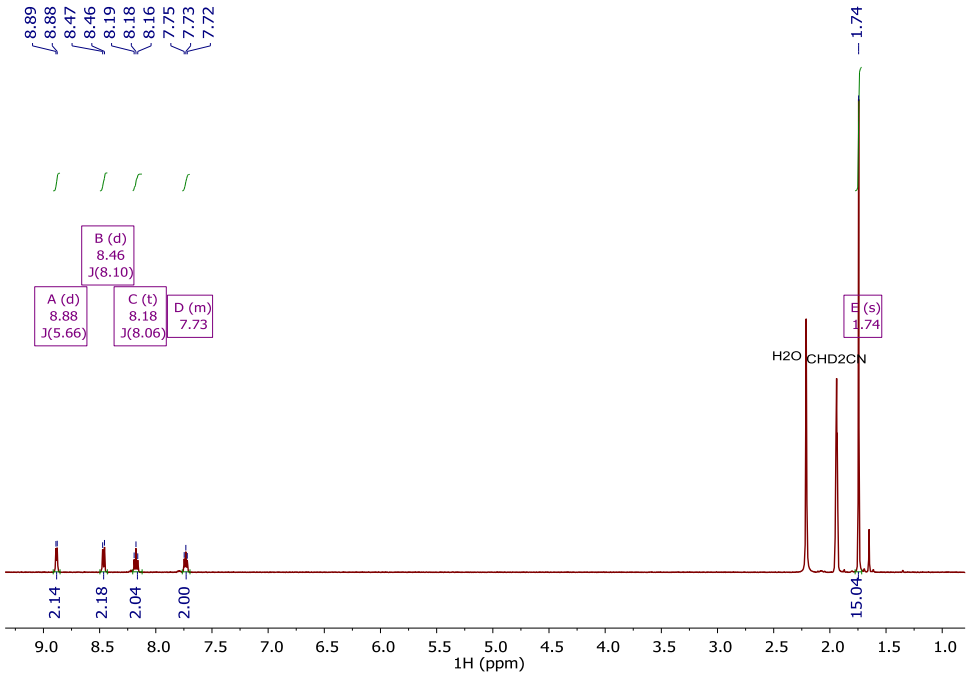

Figure 6.19. ^{1}H NMR spectrum of [Cp*Ir(bpy)(I)]$^+$ ([**4**]$^+$) in CD_3CN.

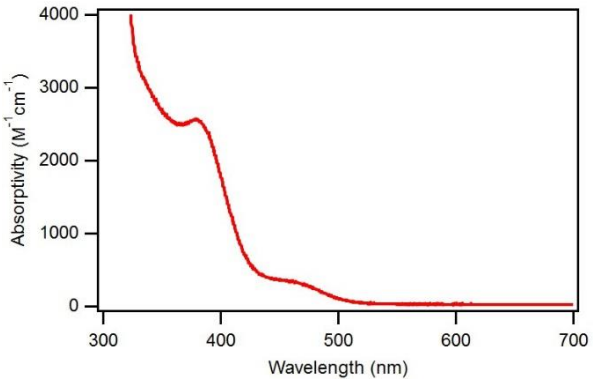

Figure 6.20. Absorptivity of [Cp*Ir(bpy)(I)]$^+$ in CH_3CN. Sample prepared by addition of 3 equiv NaI to a solution of [Cp*Ir(bpy)(OH_2)][OTf]$_2$. Ir concentration determined by ICP-MS.

*[Cp*Ir(bpy)((CH$_2$)$_4$CHCH$_2$)][Br] ([**5**][Br]).* To a purple stirring solution of Cp*Ir(bpy) (5.1 mg, 0.01 mmol) in Et_2O was added excess 6-bromo-1-hexene (20 μL). The solution was allowed to stir for 3 days over which a yellow solid precipitated, which was filtered to separate and washed 3x with ether giving 5.2 mg [**5**][Br]. (0.008 mmol, 77%). The solid was assessed to be 93% pure by ^{1}H NMR. **^{1}H NMR** (600 MHz, CD_3CN, Figure 6.21) δ 8.68 (dt, J = 5.8, 1.1 Hz, 2H), 8.53 – 8.49 (m, 2H), 8.12 (td, J = 7.9, 1.4 Hz, 2H), 7.64 (ddd, J = 7.3, 5.7, 1.4 Hz, 2H), 5.65 – 5.53 (m, 1H, Ir-$CH_2CH_2CH_2CH_2$***CH***CH_2), 4.83 – 4.73 (m, 2H, Ir-$CH_2CH_2CH_2CH_2CH$***CH$_2$***), 1.74 (q, J = 7.3 Hz, 2H, Ir-$CH_2CH_2CH_2$***CH$_2$***$CHCH_2$), 1.68 (s, 15H), 1.00 (p, J = 6.9 Hz, 2H, Ir-CH_2CH_2***CH$_2$***CH_2CHCH_2), 0.85 – 0.77 (m, 4H, Ir-***CH$_2$CH$_2$***$CH_2CH_2CHCH_2$). **^{13}C NMR** (151 MHz, CD_3CN, Figure 6.22) δ 154.98, 151.18, 139.03 (Ir-$CH_2CH_2CH_2CH_2$***CH***CH_2), 137.64, 127.58, 124.06, 113.51 (Ir-$CH_2CH_2CH_2CH_2CH$***CH$_2$***), 89.97, 32.96 (Ir-CH_2CH_2***CH$_2$***CH_2CHCH_2), 32.78 (Ir-$CH_2CH_2CH_2$***CH$_2$***$CHCH_2$), 29.58 (Ir-CH_2***CH$_2$***$CH_2CH_2CHCH_2$), 12.48 (Ir-***CH$_2$***$CH_2CH_2CH_2CHCH_2$), 7.24.

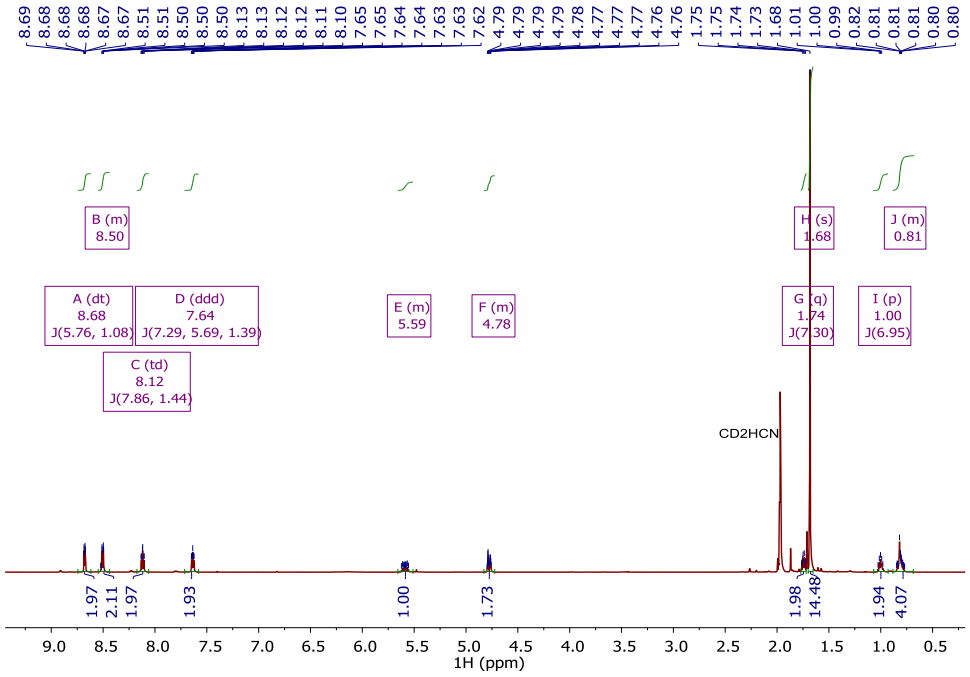

Figure 6.21. ^{1}H NMR spectrum of [Cp*Ir(bpy)((CH$_2$)$_4$CHCH$_2$)][Br] ([**5**][Br]) in CD$_3$CN.

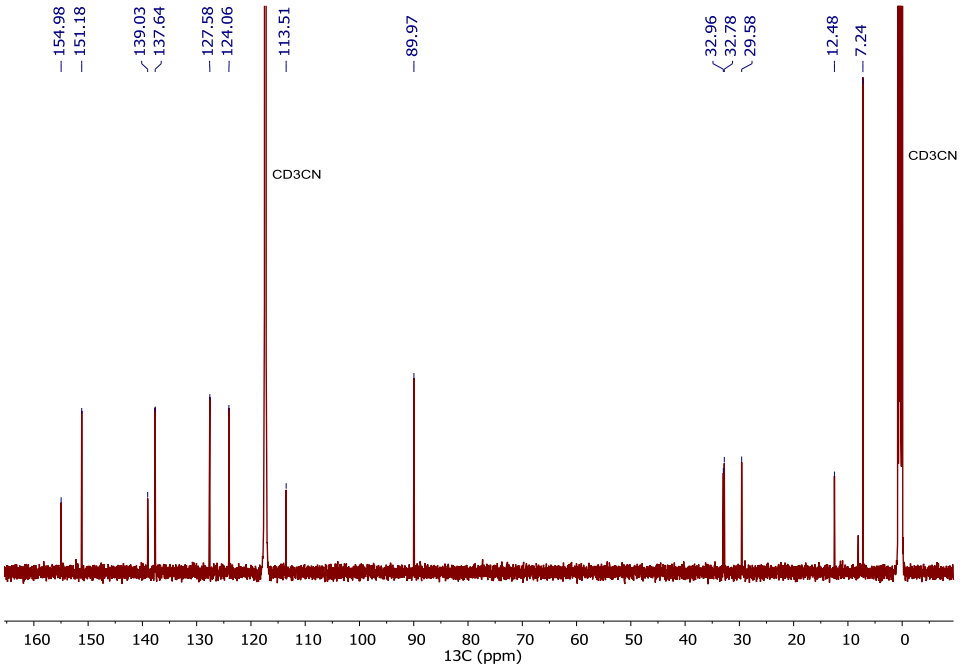

Figure 6.22. ^{13}C{^{1}H} NMR spectrum of [Cp*Ir(bpy)((CH$_2$)$_4$CHCH$_2$)][Br] ([**5**][Br]) in CD$_3$CN.

Representative photolysis monitored by ^{1}H NMR spectroscopy. In a nitrogen filled glovebox, 4.8 mg [**2**][PF_6] was dissolved in 1 mL CD_3CN. 0.98 mL of this solution were transferred to a vial containing 6 μL MeI and 20 μL of a 150 mM mesitylene solution in filtered CD_3CN was added as an internal standard. The solution was split between two screw cap NMR tubes. ^{1}H NMR spectra were recorded after removing the tubes from the glovebox and reinforcing the seal with parafilm. One tube remained wrapped in aluminum foil, while the other was irradiated with 443 nm light (Thor Multi-channel) until [**2**]$^+$ had fully reacted. Using a gas-tight, locking syringe, 0.3 mL of the headspace was removed and analyzed by GC to determine yields of methane and ethane

Representative photolysis monitored by UV-vis spectroscopy. Samples for analysis by UV-vis spectroscopy were typically prepared in sets of four. In a nitrogen filled glovebox, excess CH_3CN was filtered through a pipet filter to remove sieve dust from storage. Stock solutions of [**2**][PF_6] and CH_3I were prepared, and delivered to the cuvettes with volumetric syringes. The total volume of solution was brought to 2 mL by addition of CH_3CN. After capping with screwcap, the samples were removed from the glovebox, parafilmed around the cap, and stored in the dark. Samples were photolyzed sequentially. Each was irradiated in 30 s segments (Thor Multi-channel, 2.37 x 10^{-6} moles of photons min^{-1}, determined by chemical actinometry[29]) followed by collection of a UV-vis spectrum. Samples were photolyzed for a total of 3 min.

Computational Methods. Geometry optimizations, frequency, and time-dependent calculations were done using the hybrid functional M06 as implemented in Gaussian 09[140] with the LANL2DZ ECP basis set[167,168] for the iridium atom and 6-311G** for all other atoms. The PCM implicit solvation models (CH_3CN solvent) was employed for all

calculations. This strategy has been effective for Ir TD-DFT in the literature.[169,170] Calculations were analyzed using the Chemcraft suite.

REFERENCES

(1) Muir, J. *The Yosemite*; 1912.

(2) U.S. Energy Information Administration. International Energy Outlook 2016 http://www.eia.gov/outlooks/ieo/ (accessed Feb 14, 2017).

(3) Sherman, B. D.; Vaughn, M. D.; Bergkamp, J. J.; Gust, D.; Moore, A. L.; Moore, T. A. *Photosynth. Res.* **2014**, *120*, 59–70.

(4) International Energy Agency. Technology Roadmap Solar Thermal Electricity www.iea.org (accessed Feb 14, 2017).

(5) Cook, T. R.; Dogutan, D. K.; Reece, S. Y.; Surendranath, Y.; Teets, T. S.; Nocera, D. G. *Chem. Rev.* **2010**, *110*, 6474–6502.

(6) Seh, Z. W.; Kibsgaard, J.; Dickens, C. F.; Chorkendorff, I.; Nørskov, J. K.; Jaramillo, T. F. *Science* **2017**, *355*, eaad4998.

(7) Zou, X.; Zhang, Y. *Chem. Soc. Rev.* **2015**, *44*, 5148–5180.

(8) McKone, J. R.; Marinescu, S. C.; Brunschwig, B. S.; Winkler, J. R.; Gray, H. B. *Chem. Sci.* **2014**, *5*, 865–878.

(9) Volbeda, A.; Charon, M.-H.; Piras, C.; Hatchikian, E. C.; Frey, M.; Fontecilla-Camps, J. C. *Nature* **1995**, *373*, 580–587.

(10) Peters, J. W.; Lanzilotta, W. N.; Lemon, B. J.; Seefeldt, L. C. *Science* **1998**, *282*, 1853–1858.

(11) Gloaguen, F.; Rauchfuss, T. B. *Chem. Soc. Rev.* **2009**, *38*, 100–108.

(12) Rountree, E. S.; Mccarthy, B. D.; Eisenhart, T. T.; Dempsey, J. L. **2014**.

(13) Artero, V.; Fontecave, M. *Coord. Chem. Rev.* **2005**, *249*, 1518–1535.

(14) Artero, V.; Chavarot-Kerlidou, M.; Fontecave, M. *Angew. Chem., Int. Ed. Eng.* **2011**, *50*, 7238–7266.

(15) Wiedner, E. S.; Chambers, M. B.; Pitman, C. L.; Bullock, R. M.; Miller, A. J. M.; Appel, A. M. *Chem. Rev.* **2016**, *116*, 8655–8692.

(16) Dempsey, J. L.; Brunschwig, B. S.; Winkler, J. R.; Gray, H. B. *Acc. Chem. Res.* **2009**, *42*, 1995–2004.

(17) Helm, M. L.; Stewart, M. P.; Bullock, R. M.; Rakowski DuBois, M.; Dubois, D. L. *Science* **2011**, *333*, 863–866.

(18) Zee, D. Z.; Chantarojsiri, T.; Long, J. R.; Chang, C. J. *Acc. Chem. Res.* **2015**, *48*,

2027–2036.

(19) Karunadasa, H. I.; Montalvo, E.; Sun, Y.; Majda, M.; Long, J. R.; Chang, C. J. *Science* **2012**, *335*, 698–702.

(20) Karunadasa, H. I.; Chang, C. J.; Long, J. R. *Nature* **2010**, *464*, 1329–1333.

(21) Han, Z.; Eisenberg, R. *Acc. Chem. Res.* **2014**, *47*, 2537–2544.

(22) Eckenhoff, W. T.; Eisenberg, R. *Dalton Trans.* **2012**, *41*, 13004–13021.

(23) Esswein, A. J.; Nocera, D. G. *Chem. Rev.* **2007**, *107*, 4022–4047.

(24) Perutz, R. N.; Procacci, B. *Chem. Rev.* **2016**, *116*, 8506–8544.

(25) Delgado-Lieta, E.; Luke, M. A.; Jones, R. F.; Cole-Hamilton, D. J. *Polyhedron* **1982**, *1*, 839–840.

(26) Maguire, J. A.; Boese, W. T.; Goldman, A. S. *J. Am. Chem. Soc.* **1989**, *111*, 7088–7093.

(27) Burk, M. J.; Crabtree, R. H. *J. Am. Chem. Soc.* **1987**, *109*, 8025–8032.

(28) Teets, T. S.; Nocera, D. G. *Chem. Commun.* **2011**, *47*, 9268–9274.

(29) Chambers, M. B.; Kurtz, D. A.; Pitman, C. L.; Brennaman, M. K.; Miller, A. J. M. *J. Am. Chem. Soc.* **2016**, *138*, 13509–13512.

(30) Vincent, K. A.; Parkin, A.; Armstrong, F. A. *Chem. Rev.* **2007**, *107*, 4366–4413.

(31) Dobbek, H.; Svetlitchnyi, V.; Gremer, L.; Huber, R.; Meyer, O. *Science* **2001**, *293*, 1281–1285.

(32) Appel, A. M.; Bercaw, J. E.; Bocarsly, A. B.; Dobbek, H.; DuBois, D. L.; Dupuis, M.; Ferry, J. G.; Fujita, E.; Hille, R.; Kenis, P. J. A.; Kerfeld, C. A.; Morris, R. H.; Peden, C. H. F.; Portis, A. R.; Ragsdale, S. W.; Rauchfuss, T. B.; Reek, J. N. H.; Seefeldt, L. C.; Thauer, R. K.; Waldrop, G. L. *Chem. Rev.* **2013**, *113*, 6621–6658.

(33) Morris, A. J.; Meyer, G. J.; Fujita, E. *Acc. Chem. Res.* **2009**, *42*, 1983–1994.

(34) Cornils, B.; Herrmann, W. A.; Lubineau, A.; Auge, J.; Scherrmann, M.-C.; Kühn, F. E.; Laurenczy, G.; Darensbourg, D. J.; Ortiz, C. G.; Stelzer, O.; Rossenbach, S.; Hoff, D.; Goedheijt, M. S.; Kamer, P. C. J.; Reek, J. N. H.; van Leeuwen, P.; Kalck, P.; Urrutigoity, M.; Papadogianakis, G.; Davis, M. E.; Joo, K.; Bianchini, C.; Meli, A.; Beller, M.; Krauter, J. G. E.; Bryndza, H. E.; Harrelson Jr, J. A.; Grubbs, R. H.; Lynn, D. M.; Mecking, S. *Aqueous-Phase Organometallic Catalysis*; Cornils, B.; Herrmann, W. A., Eds.; 2nd ed.; Wiley-VCH: Weinheim, 2004.

(35) Joó, F. *Acc. Chem. Res.* **2002**, *35*, 738–745.

(36) Warren, J. J.; Tronic, T. A.; Mayer, J. M. *Chem. Rev.* **2010**, *110*, 6961–7001.

(37) Bourrez, M.; Steinmetz, R.; Ott, S.; Gloaguen, F.; Hammarström, L. *Nat. Chem.* **2015**, *7*, 140–145.

(38) DuBois, D. L.; Berning, D. E. *Appl. Organomet. Chem.* **2000**, *14*, 860–862.

(39) Rakowski DuBois, M.; DuBois, D. L. *Chem. Soc. Rev.* **2009**, *38*, 62–72.

(40) Bullock, R. M.; Appel, A. M.; Helm, M. L. *Chem. Commun.* **2014**, *50*, 3125–3143.

(41) Rodriguez-Maciá, P.; Dutta, A.; Lubitz, W.; Shaw, W. J.; Rüdiger, O. *Angew. Chem., Int. Ed.* **2015**, *54*, 12303–12307.

(42) Bard, A. J.; Faulkner, L. R. *Electrochemical Methods: Fundamentals and Applications*; Wiley: New York, 2000.

(43) Buncel, E.; Menon, B. *J. Am. Chem. Soc.* **1977**, *99*, 4457–4461.

(44) Pearson, R. G. *J. Am. Chem. Soc.* **1986**, *108*, 6109–6114.

(45) Wayner, D. D. M.; Parker, V. D. *Acc. Chem. Res.* **1993**, *26*, 287–294.

(46) Ellis, W. W.; Raebiger, J. W.; Curtis, C. J.; Bruno, J. W.; DuBois, D. L. *J. Am. Chem. Soc.* **2004**, *126*, 2738–2743.

(47) Connelly, S. J.; Wiedner, E. S.; Appel, A. M. *Dalton Trans.* **2015**, *44*, 5933–5938.

(48) Creutz, C.; Chou, M. H. *J. Am. Chem. Soc.* **2009**, *131*, 2794–2795.

(49) Taheri, A.; Thompson, E. J.; Fettinger, J. C.; Berben, L. A. *ACS Catal.* **2015**, *5*, 7140–7151.

(50) Tsay, C.; Livesay, B. N.; Ruelas, S.; Yang, J. Y. *J. Am. Chem. Soc.* **2015**, *137*, 14114–14121.

(51) Appel, A. M.; Lee, S.-J.; Franz, J. A.; DuBois, D. L.; DuBois, M. R. *J. Am. Chem. Soc.* **2009**, *131*, 5224–5232.

(52) Fang, J.; Lin, C.-H.; Bradshaw, C. W.; Wong, C. *J. Chem. Soc. Perkin Trans. 1* **1995**, 967.

(53) Lo, H. C.; Fish, R. H. *Angew. Chem., Int. Ed.* **2002**, *41*, 478–481.

(54) Zhao, H.; van der Donk, W. A. *Curr. Opin. Biotechnol.* **2003**, *14*, 583–589.

(55) Chenault, H. K.; Whitesides, G. M. *Appl. Biochem. Biotechnol.* **1987**, *14*, 147–197.

(56) Thoi, V. S.; Sun, Y.; Long, J. R.; Chang, C. J. *Chem. Soc. Rev.* **2013**, *42*, 2388–2400.

(57) Osterloh, F. E. *Chem. Soc. Rev.* **2013**, *42*, 2294–2320.

(58) Kalyanasundaram, K.; Grätzel, M. *Photochem. Photobiol.* **1984**, *40*, 807–822.

(59) Otruba, J. P.; Neyhart, G. A.; Dressick, W. J.; Marshall, J. L.; Sullivan, B. P.; Watkins, P. A.; Meyer, T. J. *J. Photochem.* **1986**, *35*, 133–153.

(60) Deronzier, A.; Essakalli, M. *J. Chem. Soc., Chem. Commun.* **1990**, 242–244.

(61) Ziessel, R. *J. Chem. Soc., Chem. Commun.* **1988**, 16–17.

(62) Ziessel, R. *Angew. Chem., Int. Ed. Eng.* **1991**, *30*, 844–847.

(63) Ziessel, R. *J. Am. Chem. Soc.* **1993**, *115*, 118–127.

(64) Steckhan, E.; Herrmann, S.; Ruppert, R.; Dietz, E.; Frede, M.; Spika, E. *Organometallics* **1991**, 1568–1577.

(65) Caix, C.; Chardon-Noblat, S.; Deronzier, A.; Ziessel, R. *J. Electroanal. Chem.* **1993**, *362*, 301–304.

(66) Dadci, L.; Elias, H.; Frey, U.; Hoernig, A.; Koelle, U.; Merbach, A. E.; Paulus, H.; Schneider, J. S. *Inorg. Chem.* **1995**, *34*, 306–315.

(67) Costentin, C.; Robert, M.; Savéant, J.-M. *Chem. Soc. Rev.* **2013**, *42*, 2423–2436.

(68) Ogo, S.; Makihara, N.; Watanabe, Y. *Organometallics* **1999**, 5470–5474.

(69) Hendry, P.; Sargeson, A. M. *J. Am. Chem. Soc.* **1989**, *111*, 2521–2527.

(70) Hendry, P.; Sargeson, A. M. *Inorg. Chem.* **1990**, *29*, 97–104.

(71) Li, C.; Wang, C.; Villa-Marcos, B.; Xiao, J. *J. Am. Chem. Soc.* **2008**, *130*, 14450–14451.

(72) Sandrini, D.; Maestri, M.; Ziessel, R. *Inorg. Chim. Acta* **1989**, *163*, 177–180.

(73) Suenobu, T.; Guldi, D. M.; Ogo, S.; Fukuzumi, S. *Angew. Chem., Int. Ed.* **2003**, *42*, 5492–5495.

(74) Crabtree, R. H. *Chem. Rev.* **2012**, *112*, 1536–1554.

(75) Limburg, B.; Bouwman, E.; Bonnet, S. *Coord. Chem. Rev.* **2012**, *256*, 1451–1467.

(76) Delahay, P.; Stiehl, G. L. *J. Am. Chem. Soc.* **1952**, *74*, 3500.

(77) Appel, A. M.; Helm, M. L. *ACS Catal.* **2014**, *4*, 630–633.

(78) Fulmer, G. R.; Miller, A. J. M.; Sherden, N. H.; Gottlieb, H. E.; Nudelman, A.; Stoltz,

B. M.; Bercaw, J. E.; Goldberg, K. I. *Organometallics* **2010**, *29*, 2176–2179.

(79) Glasoe, P. K.; Long, F. A. *J. Phys. Chem.* **1960**, *64*, 188–189.

(80) White, C.; Yates, A.; Maitlis, P. M. *Inorg. Synth.* **1992**, *29*, 228–230.

(81) *Handbook of Electrochemistry*; Zoski, C. G., Ed.; Elsevier: Amsterdam, 2007.

(82) Walter, M. G.; Warren, E. L.; McKone, J. R.; Boettcher, S. W.; Mi, Q.; Santori, E. A.; Lewis, N. S. *Chem. Rev.* **2010**, *110*, 6446–6473.

(83) Ladwig, M.; Kaim, W. *J. Organomet. Chem.* **1992**, *439*, 79–90.

(84) Barrett, S. M.; Pitman, C. L.; Walden, A. G.; Miller, A. J. M. *J. Am. Chem. Soc.* **2014**, *136*, 14718–14721.

(85) Pitman, C. L.; Miller, A. J. M. *ACS Catal.* **2014**, *4*, 2727–2733.

(86) Lenges, C. P.; White, P. S.; Marshall, W. J.; Brookhart, M. *Organometallics* **2000**, *19*, 1247–1254.

(87) Nakai, H.; Jeong, K.; Matsumoto, T.; Ogo, S. *Organometallics* **2014**, *33*, 4349–4352.

(88) Blakemore, J. D.; Hernandez, E. S.; Sattler, W.; Hunter, B. M.; Henling, L. M.; Brunschwig, B. S.; Gray, H. B. *Polyhedron* **2014**, *84*, 14–18.

(89) Irwin, M.; Doyle, L. R.; Krämer, T.; Herchel, R.; McGrady, J. E.; Goicoechea, J. M. *Inorg. Chem.* **2012**, *51*, 12301–12312.

(90) Kaim, W.; Reinhardt, R.; Sieger, M. *Inorg. Chem.* **1994**, *33*, 4453–4459.

(91) Kolle, U.; Kang, B.; Infelta, P.; Comte, P.; Gratzel, M. *Chem. Ber.* **1989**, *122*, 1869–1880.

(92) Ogo, S.; Uehara, K.; Abura, T.; Watanabe, Y.; Fukuzumi, S. *Organometallics* **2004**, *23*, 3047–3052.

(93) Creutz, C.; Chou, M. H. *J. Am. Chem. Soc.* **2009**, *131*, 2794–2795.

(94) Dykeman, R. R.; Luska, K. L.; Thibault, M. E.; Jones, M. D.; Schlaf, M.; Khanfar, M.; Taylor, N. J.; Britten, J. F.; Harrington, L. *J. Mol. Catal. A Chem.* **2007**, *277*, 233–251.

(95) Dolomanov, O. V.; Bourhis, L. J.; Gildea, R. J.; Howard, J. A. K.; Puschmann, H. *J. Appl. Crystallogr.* **2009**, *42*, 339–341.

(96) Bourhis, L. J.; Dolomanov, O. V.; Gildea, R. J.; Howard, J. A. K.; Puschmann, H. *Acta Crystallogr. Sect. A Found. Adv.* **2015**, *71*, 59–75.

(97) Sheldrick, G. M. *Acta Crystallogr. Sect. A Found. Crystallogr.* **2008**, *64*, 112–122.

(98) Berning, D. E.; Noll, B. C.; DuBois, D. L. *J. Am. Chem. Soc.* **1999**, *121*, 11432–11447.

(99) Brewster, T. P.; Miller, A. J. M.; Heinekey, D. M.; Goldberg, K. I. *J. Am. Chem. Soc.* **2013**, *135*, 16022–16025.

(100) Miller, A. J. M.; Heinekey, D. M.; Mayer, J. M.; Goldberg, K. I. *Angew. Chem., Int. Ed.* **2013**, *52*, 3981–3984.

(101) Hull, J. F.; Himeda, Y.; Wang, W.-H.; Hashiguchi, B.; Periana, R.; Szalda, D. J.; Muckerman, J. T.; Fujita, E. *Nat. Chem.* **2012**, *4*, 383–388.

(102) Fukuzumi, S.; Kobayashi, T.; Suenobu, T. *Angew. Chem., Int. Ed.* **2011**, *50*, 728–731.

(103) Himeda, Y. *Green Chem.* **2009**, *11*, 2018–2022.

(104) Ogo, S.; Kabe, R.; Hayashi, H.; Harada, R.; Fukuzumi, S. *Dalton Trans.* **2006**, 4657.

(105) Leslie Dutton, P. In *Methods in Enzymology*; 1978; Vol. 54, pp. 411–435.

(106) Pugh, J. R.; Meyer, T. J. *J. Am. Chem. Soc.* **1992**, *114*, 3784–3792.

(107) Seifriz, I.; Konzen, M.; Paula, M. M. S.; Goncalves, N. S.; Spoganickz, B.; Creczynski-Pasa, T. B.; Bonetti, V. R.; Beirith, A.; Calixto, J. B.; Franco, C. V. *J. Inorg. Biochem.* **1999**, *76*, 153–163.

(108) Ciancanelli, R.; Noll, B. C.; DuBois, D. L.; Rakowski DuBois, M. *J. Am. Chem. Soc.* **2002**, *124*, 2984–2992.

(109) Wilson, A. D.; Miller, A. J. M.; DuBois, D. L.; Labinger, J. A.; Bercaw, J. E. *Inorg. Chem.* **2010**, *49*, 3918–3926.

(110) Matsubara, Y.; Fujita, E.; Doherty, M. D.; Muckerman, J. T.; Creutz, C. *J. Am. Chem. Soc.* **2012**, *134*, 15743–15757.

(111) Hu, Y.; Norton, J. R. *J. Am. Chem. Soc.* **2014**, *136*, 5938–5948.

(112) Kolthoff, I. M. *Anal. Chem.* **1974**, *46*, 1992–2003.

(113) Robertson, A.; Matsumoto, T.; Ogo, S.; Takahiro, M.; Ogo, S. *Dalton Trans.* **2011**, *40*, 10304–10310.

(114) de Respinis, M.; Joya, K. S.; De Groot, H. J. M.; D'Souza, F.; Smith, W. A.; van de Krol, R.; Dam, B. *J. Phys. Chem. C* **2015**, *119*, 7275–7281.

(115) Ellis, W. W.; Miedaner, A.; Curtis, C. J.; Gibson, D. H.; DuBois, D. L. *J. Am. Chem. Soc.* **2002**, *124*, 1926–1932.

(116) Bhagan, S.; Wayland, B. B. *Inorg. Chem.* **2011**, *50*, 11011–11020.

(117) Curtis, C. J.; Miedaner, A.; Ellis, W. W.; DuBois, D. L. *J. Am. Chem. Soc.* **2002**, *124*, 1918–1925.

(118) Hansch, C.; Leo, A.; Taft, R. W. *Chem. Rev.* **1991**, *91*, 165–195.

(119) Kanan, M. W.; Nocera, D. G. *Science* **2008**, *321*, 1072–1075.

(120) Joya, K. S.; Subbaiyan, N. K.; D'Souza, F.; de Groot, H. J. M. *Angew. Chem., Int. Ed.* **2012**, *51*, 9601–9605.

(121) van der Donk, W. A.; Zhao, H. *Curr. Opin. Biotechnol.* **2003**, *14*, 421–426.

(122) Lo, H. C.; Leiva, C.; Buriez, O.; Kerr, J. B.; Olmstead, M. M.; Fish, R. H. *Inorg. Chem.* **2001**, *40*, 6705–6716.

(123) Ghosh, T.; Slanina, T.; König, B. *Chem. Sci.* **2015**, *6*, 2027–2034.

(124) Leiva, C.; Christine Lo, H.; Fish, R. H. *J. Organomet. Chem.* **2010**, *695*, 145–150.

(125) Kolle, U.; Gratzel, M. *Angew. Chem., Int. Ed. Eng.* **1987**, *99*, 567–570.

(126) Pitman, C. L.; Brereton, K. R.; Miller, A. J. M. *J. Am. Chem. Soc.* **2016**, *138*, 2252–2260.

(127) Taheri, A.; Berben, L. A. *Inorg. Chem.* **2016**, *55*, 378–385.

(128) Abura, T.; Ogo, S.; Watanabe, Y.; Fukuzumi, S. *J. Am. Chem. Soc.* **2003**, *125*, 4149–4154.

(129) Quintana, L. M. A.; Johnson, S. I.; Corona, S. L.; Villatoro, W.; Goddard, W. A.; Takase, M. K.; VanderVelde, D. G.; Winkler, J. R.; Gray, H. B.; Blakemore, J. D. *Proc. Natl. Acad. Sci.* **2016**, *113*, 6409–6414.

(130) Jones, W. D.; Kuykendall, V. L.; Selmeczy, A. D. *Organometallics* **1991**, *10*, 1577–1586.

(131) Pedersen, A.; Tilset, M. *Organometallics* **1993**, *12*, 3064–3068.

(132) Matsubara, Y.; Hightower, S. E.; Chen, J.; Grills, D. C.; Polyansky, D. E.; Muckerman, J. T.; Tanaka, K.; Fujita, E. *Chem. Commun.* **2014**, *50*, 728–730.

(133) McSkimming, A.; Bhadbhade, M. M.; Colbran, S. B. *Angew. Chem., Int. Ed.* **2013**, *52*, 3411–3416.

(134) McSkimming, A.; Colbran, S. B. *Chem. Soc. Rev.* **2013**, *42*, 5439–5488.

(135) Warren, J. J.; Tronic, T. A.; Mayer, J. M. *Chem. Rev.* **2010**, *110*, 6961–7001.

(136) Rodkey, F. L. *J. Biol. Chem.* **1955**, *213*, 777–787.

(137) Polkowska, J.; Bastkowski, F.; Schrader, T.; Klärner, F.-G.; Zienau, J.; Koziol, F.; Ochsenfeld, C. *J. Phys. Org. Chem.* **2009**, *22*, 779–790.

(138) Kang, J. W.; Maitlis, P. M. *J. Organomet. Chem* **1971**, *30*, 127–133.

(139) Ciancaleoni, G.; Bolaño, S.; Bravo, J.; Peruzzini, M.; Gonsalvi, L.; Macchioni, A. *Dalton Trans.* **2010**, *39*, 3366–3368.

(140) Frisch, M. J.; Trucks, G. W.; Schlegel, H. B.; Scuseria, G. E.; Robb, M. A.; Cheeseman, J. R.; Scalmani, G.; Barone, V.; Mennucci, B.; Petersson, G. A.; Nakatsuji, H.; Caricato, M.; Li, X.; Hratchian, H. P.; Izmaylov, A. F.; Bloino, J.; Zheng, G.; Sonnenberg, J. L.; Hada, M.; Ehara, M.; Toyota, K.; Fukuda, R.; Hasegawa, J.; Ishida, M.; Nakajima, T.; Honda, Y.; Kitao, O.; Nakai, H.; Vreven, T.; Montgomery, J. A. J.; Peralta, J. E.; Ogliaro, F.; Bearpark, M.; Heyd, J. J.; Brothers, E.; Kudin, K. N.; Staroverov, V. N.; Kobayashi, R.; Normand, J.; Raghavachari, K.; Rendell, A.; Burant, J. C.; Iyengar, S. S.; Tomasi, J.; Cossi, M.; Rega, N.; Millam, N. J.; Klene, M.; Knox, J. E.; Cross, J. B.; Bakken, V.; Adamo, C.; Jaramillo, J.; Gomperts, R.; Stratmann, R. E.; Yazyev, O.; Austin, A. J.; Cammi, R.; Pomelli, C.; Ochterski, J. W.; Martin, R. L.; Morokuma, K.; Zakrzewski, V. G.; Voth, G. A.; Salvador, P.; Dannenberg, J. J.; Dapprich, S.; Daniels, A. D.; Farkas, O.; Foresman, J. B.; Ortiz, J. V.; Cioslowski, J.; Fox, D. J. *Gaussian 09, Revision D.01*; Gaussian, Inc: Wallingford, CT, 2009.

(141) Perdew, J. P.; Burke, K.; Ernzerhof, M. *Phys. Rev. Lett.* **1996**, *77*, 3865–3868.

(142) Hay, P. J.; Wadt, W. R. *J. Chem. Phys.* **1985**, *82*, 270.

(143) McLean, A. D.; Chandler, G. S. *J. Chem. Phys.* **1980**, *72*, 5639.

(144) Krishnan, R.; Binkley, J. S.; Seeger, R.; Pople, J. A. *J. Chem. Phys.* **1980**, *72*, 650.

(145) Hill, R. H.; Puddephatt, R. J. *Organometallics* **1983**, *2*, 1472–1474.

(146) Alt, H. G. *Angew. Chem., Int. Ed. Eng.* **1984**, *23*, 766–782.

(147) Ravelli, D.; Protti, S.; Fagnoni, M. *Chem. Rev.* **2016**, *116*, 9850–9913.

(148) Paul, A.; Smith, M. D.; Vannucci, A. K. *J. Org. Chem.* **2017**, *82*, 1996–2003.

(149) Geoffroy, G. L.; Wrighton, M. S. *Organometallic Photochemistry*; Academic Press: New York, 1979.

(150) Brown, S. H.; Crabtree, R. H. *J. Am. Chem. Soc.* **1989**, *111*, 2946–2953.

(151) van Slageren, J.; Klein, A.; Záliš, S. *Coord. Chem. Rev.* **2002**, *230*, 193–211.

(152) Groom, C. R.; Bruno, I. J.; Lightfoot, M. P.; Ward, S. C. *Acta Cryst.* **2016**, *B72*, 171–179.

(153) Clark, C. C.; Marton, A.; Meyer, G. J. *Inorg. Chem.* **2005**, *44*, 3383–3385.

(154) Bock, C. R.; Connor, J. A.; Gutierrez, A. R.; Meyer, T. J.; Whitten, D. G.; Sullivan, B. P.; Nagle, J. K. *J. Am. Chem. Soc.* **1979**, *101*, 4815–4824.

(155) Alemany, L. B.; Malloy, T. B.; Nunes, M. M.; Zaibaq, N. G. *J. Mol. Struct.* **2012**, *1023*, 176–188.

(156) Griller, D.; Ingold, K. U. *Acc. Chem. Res.* **1980**, *13*, 317–323.

(157) Bradley, P.; Suardi, G.; Zipp, A. P.; Eisenberg, R. *J. Am. Chem. Soc.* **1994**, *116*, 2859–2868.

(158) Schrauzer, G. N.; Sibert, J. W.; Windgassen, R. J. *J. Am. Chem. Soc.* **1968**, *90*, 6681–6688.

(159) Debuigne, A.; Poli, R.; Jérôme, C.; Jérôme, R.; Detrembleur, C. *Prog. Polym. Sci.* **2009**, *34*, 211–239.

(160) Occhialini, D.; Daasbjerg, K.; Lund, H. *Acta Chem. Scand.* **1993**, *47*, 1100–1106.

(161) Espenson, J. H. *Chemical Kinetics and Reaction Mechanisms*; 2nd ed.; McGraw Hill: New York, 1981.

(162) Luo, Y. R. *Comprehensive Handbook of Chemical Bond Energies*; CRC Press: Boca Raton, FL, 2007.

(163) Afeefy, H. Y.; Liebman, J. F.; Stein, S. E. In *NIST Chemistry WebBook, NIST Standard Reference Database Number 69*; Linstrom, P. J.; Mallard, W. G., Eds.; National Institute of Standards and Technology: Gaithersburg MD, 20899.

(164) Simoes, J. A. M.; Beauchamp, J. L. *Chem. Rev.* **1990**, *90*, 629–688.

(165) Nagle, J. K.; Young, R. C.; Meyer, T. J. *Inorg. Chem.* **1977**, *16*, 3366–3369.

(166) Creutz, C.; Sutin, N. *J. Am. Chem. Soc.* **1977**, *99*, 241–243.

(167) Schuchardt, K. L.; Didier, B. T.; Elsethagen, T.; Sun, L.; Gurumoorthi, V.; Chase, J.; Li, J.; Windus, T. L. *J. Chem. Inf. Model.* **2007**, *47*, 1045–1052.

(168) Feller, D. *J. Comput. Chem.* **1996**, *17*, 1571–1586.

(169) Hintermair, U.; Sheehan, S. W.; Parent, A. R.; Ess, D. H.; Richens, D. T.; Vaccaro, P. H.; Brudvig, G. W.; Crabtree, R. H. *J. Am. Chem. Soc.* **2013**, *135*, 10837–10851.

(170) Brereton, K. R.; Pitman, C. L.; Cundari, T. R.; Miller, A. J. M. *Inorg. Chem.* **2016**, *55*, 12042–12051.